A molecular approach to the ultimate friction response of confined fluids

Alejandro Porras Vazquez

N°d'ordre NNT : 2019LYSEI087

THESE de DOCTORAT DE L'UNIVERSITE DE LYON
opérée au sein de
INSA de Lyon

Ecole Doctorale N° 162
Ecole doctorale des Sciences pour l'Ingénieur de Lyon : Mécanique, Energétique, Génie Civil, Acoustique (MEGA)

Spécialité/ discipline de doctorat :
Génie Mécanique

Soutenue publiquement le 29/10/2019, par :
Alejandro Porras Vázquez

A molecular approach to the ultimate friction response of confined fluids

---

Devant le jury composé de :

Echeverri, Sebastián	Chercheur (SKF RTD)	Invité
Fillot, Nicolas	Maître de Conférences – HDR (INSA-Lyon)	Directeur
Galliero, Guillaume	Professeur (Université de Pau)	Rapporteur
Joly, Laurent	Professeur (Université Claude Bernard Lyon 1)	Examinateur
Martens, Kirsten	Chargée de Recherche (Université Grenoble Alpes)	Examinatrice
Martini, Ashlie	Professeure (University of California Merced)	Rapporteure
Martinie, Laetitia	Maître de Conférences (INSA-Lyon)	Co-directrice
Vergne, Philippe	Directeur de Recherche – HDR (INSA-Lyon)	Invité

Département FEDORA – INSA Lyon - Ecoles Doctorales – Quinquennal 2016-2020

SIGLE	ECOLE DOCTORALE	NOM ET COORDONNEES DU RESPONSABLE
CHIMIE	**CHIMIE DE LYON** **http://www.edchimie-lyon.fr** Sec. : Renée EL MELHEM Bât. Blaise PASCAL, 3e étage **secretariat@edchimie-lyon.fr** INSA : R. GOURDON	M. Stéphane DANIELE Institut de recherches sur la catalyse et l'environnement de Lyon IRCELYON-UMR 5256 Équipe CDFA 2 Avenue Albert EINSTEIN 69 626 Villeurbanne CEDEX **directeur@edchimie-lyon.fr**
E.E.A.	**ÉLECTRONIQUE, ÉLECTROTECHNIQUE, AUTOMATIQUE** **http://edeea.ec-lyon.fr** Sec. : M.C. HAVGOUDOUKIAN **ecole-doctorale.eea@ec-lyon.fr**	M. Gérard SCORLETTI École Centrale de Lyon 36 Avenue Guy DE COLLONGUE 69 134 Écully Tél : 04.72.18.60.97 Fax 04.78.43.37.17 **gerard.scorletti@ec-lyon.fr**
E2M2	**ÉVOLUTION, ÉCOSYSTÈME, MICROBIOLOGIE, MODÉLISATION** **http://e2m2.universite-lyon.fr** Sec. : Sylvie ROBERJOT Bât. Atrium, UCB Lyon 1 Tél : 04.72.44.83.62 INSA : H. CHARLES **secretariat.e2m2@univ-lyon1.fr**	M. Philippe NORMAND UMR 5557 Lab. d'Ecologie Microbienne Université Claude Bernard Lyon 1 Bâtiment Mendel 43, boulevard du 11 Novembre 1918 69 622 Villeurbanne CEDEX **philippe.normand@univ-lyon1.fr**
EDISS	**INTERDISCIPLINAIRE SCIENCES-SANTÉ** **http://www.ediss-lyon.fr** Sec. : Sylvie ROBERJOT Bât. Atrium, UCB Lyon 1 Tél : 04.72.44.83.62 INSA : M. LAGARDE **secretariat.ediss@univ-lyon1.fr**	Mme Emmanuelle CANET-SOULAS INSERM U1060, CarMeN lab, Univ. Lyon 1 Bâtiment IMBL 11 Avenue Jean CAPELLE INSA de Lyon 69 621 Villeurbanne Tél : 04.72.68.49.09 Fax : 04.72.68.49.16 **emmanuelle.canet@univ-lyon1.fr**
INFOMATHS	**INFORMATIQUE ET MATHÉMATIQUES** **http://edinfomaths.universite-lyon.fr** Sec. : Renée EL MELHEM Bât. Blaise PASCAL, 3e étage Tél : 04.72.43.80.46 **infomaths@univ-lyon1.fr**	M. Luca ZAMBONI Bât. Braconnier 43 Boulevard du 11 novembre 1918 69 622 Villeurbanne CEDEX Tél : 04.26.23.45.52 **zamboni@maths.univ-lyon1.fr**
Matériaux	**MATÉRIAUX DE LYON** **http://ed34.universite-lyon.fr** Sec. : Stéphanie CAUVIN Tél : 04.72.43.71.70 Bât. Direction **ed.materiaux@insa-lyon.fr**	M. Jean-Yves BUFFIÈRE INSA de Lyon MATEIS - Bât. Saint-Exupéry 7 Avenue Jean CAPELLE 69 621 Villeurbanne CEDEX Tél : 04.72.43.71.70 Fax : 04.72.43.85.28 **jean-yves.buffiere@insa-lyon.fr**
MEGA	**MÉCANIQUE, ÉNERGÉTIQUE, GÉNIE CIVIL, ACOUSTIQUE** **http://edmega.universite-lyon.fr** Sec. : Stéphanie CAUVIN Tél : 04.72.43.71.70 Bât. Direction **mega@insa-lyon.fr**	M. Jocelyn BONJOUR INSA de Lyon Laboratoire CETHIL Bâtiment Sadi-Carnot 9, rue de la Physique 69 621 Villeurbanne CEDEX **jocelyn.bonjour@insa-lyon.fr**
ScSo	**ScSo*** **http://ed483.univ-lyon2.fr** Sec. : Véronique GUICHARD INSA : J.Y. TOUSSAINT Tél : 04.78.69.72.76 **veronique.cervantes@univ-lyon2.fr**	M. Christian MONTES Université Lyon 2 86 Rue Pasteur 69 365 Lyon CEDEX 07 **christian.montes@univ-lyon2.fr**

*ScSo : Histoire, Géographie, Aménagement, Urbanisme, Archéologie, Science politique, Sociologie, Anthropologie

Preface

This thesis is submitted in partial fulfillment for the requirements of a Ph.D. degree in mechanical engineering from the “Institut National des Sciences Appliquées” (INSA) de Lyon. The contained research has been carried out from September 2016 to October 2019 at the Contacts and Structural Mechanics laboratory (LaMCoS) of CNRS and INSA de Lyon, in straight collaboration with the company SKF through the industrial research chair “Lubricated interfaces for the future”.

I would like to express my gratitude to my two supervisors Dr. Nicolas Fillot and Dr. Laetitia Martinie for the very interesting discussions and for the support during the last three years. I would also like to thank SKF for the financial support, and especially to Dr. Guillermo Morales-Espejel, Dr. Sebastián Echeverri-Restrepo, Dr. Yhves Mahéo and Dr. Alexandre Mondelin for the continuous feedback on the project. My gratitude also goes to Dr. Philippe Vergne, for closely following with interest the thesis and for the experimental data (very important for the validation of the atomistic simulations). Finally, I am also thankful to anyone who directly or indirectly participated in this thesis, to my friends and to my family. Without them I wouldn’t be here today.

Abstract

In order to control energy losses in mechanical systems, a thin film of lubricant is often introduced between the solids in contact. The lubricated point contacts operate in the elastohydrodynamic regime, characterized by high pressures (of the order of GPa) and thin film thicknesses (of the order of 100 nanometers). At high shear rates, the fluid may exhibit a limiting shear stress whose physical origin is still uncertain. At present, the empirical models available for the prediction of friction fail to describe the ultimate response of lubricants at these severe operating conditions. In addition, in-situ experimental analysis is very difficult to achieve due to confinement and high pressures. Thus, in this thesis, the problem is approached from the angle of modeling at the atomic scale. The shear behavior of three fluids (a traction fluid, a model lubricant and an industrial lubricant for the aerospace industry) is analyzed by Molecular Dynamics Simulation. The numerical results are then compared qualitatively and quantitatively with experimental tests. The friction response is independent of the velocity profile in the confinement thickness, the latter appearing rather as a consequence of boundary conditions at the surfaces. The limiting friction regime naturally occurs when the lubricant is subjected to thermodynamic conditions characteristic of a solid state. In this case, the dynamics of the molecules is strongly slowed down. The activation energy increases rapidly with the pressure, so that the diffusion becomes negligible at high pressure, even at the severe shear rates imposed in the Molecular Dynamics simulations. The macroscopic response to this phenomenon is thus a saturation of the value of friction. This work ends by laying the foundations of a modeling that will allow the prediction of lubricated friction under severe conditions.

Keywords: Elastohydrodynamic lubrication, Molecular Dynamics, Limiting Shear Stress, Phase transition, Molecular mobility.

Résumé

Afin de contrôler les pertes d'énergie dans les systèmes mécaniques, un film mince de lubrifiant est souvent introduit entre les solides en contact. Les contacts lubrifiés ponctuels fonctionnent en régime élastohydrodynamique, caractérisé par des pressions élevées (de l'ordre du GPa) et des épaisseurs de film minces (de l'ordre de 100 nanomètres). A des taux de cisaillement élevés, le fluide peut présenter une contrainte de cisaillement limite dont l'origine physique est encore incertaine. Actuellement, les modèles empiriques disponibles pour la prédiction du frottement ne décrivent pas la réponse ultime des lubrifiants dans ces conditions sévères. De plus, l'analyse expérimentale in-situ est très difficile à réaliser en raison du confinement et des fortes pressions. Ainsi, dans cette thèse, le problème est abordé sous l'angle de la modélisation à l'échelle atomique. Le comportement en cisaillement de trois de fluides (un fluide de traction, un lubrifiant modèle et un lubrifiant industriel pour le secteur aérospatial) est analysé par simulation Dynamique Moléculaire. Les résultats numériques sont ensuite comparés qualitativement et quantitativement à des essais expérimentaux. La réponse en frottement est indépendante du profile de vitesse dans l'épaisseur du confinement, ce dernier apparaissant plutôt comme une conséquence des conditions limites aux surfaces. Le régime de frottement limite apparaît naturellement lorsque le lubrifiant est soumis à des conditions thermodynamiques caractéristiques d'un état solide. Dans ce cas, la dynamique des molécules est fortement ralentie. L'énergie d'activation augmente rapidement avec la pression, de sorte que la diffusion devient négligeable à forte pression, même aux taux de cisaillement sévères imposés dans les simulations Dynamique Moléculaire. La réponse macroscopique à ce phénomène est donc une saturation de la valeur du frottement. Ce travail s'achève en jetant les bases d'une modélisation qui pourra permettre la prédiction du frottement lubrifié sous conditions sévères.

Mots-clés : Lubrification Elastohydrodynamique, Dynamique Moléculaire, Contrainte Limite Tangentielle, Transition de Phase, Mobilité Moléculaire.

Résumé étendu

i. Introduction générale et contexte

Le frottement est un mécanisme de dissipation commun rencontré dans de nombreux systèmes lubrifiés tels que les roulements à billes ou les systèmes came/suiveur, où deux solides en contact sont en mouvement relatif. Le frottement entraîne une consommation d'énergie plus élevée dans les systèmes mécaniques. Ainsi, en introduisant un film mince de lubrifiant entre les surfaces frottantes, de nombreux systèmes verraient leur efficacité améliorée. Le film de lubrifiant évite le contact direct entre les surfaces et génère de faibles valeurs de frottement et d'usure, garantissant ainsi une durée de vie maximale des composants. Bien qu'il existe des modèles précis de prédiction d'épaisseur de film [1], la théorie ne permet pas de prédire les mesures expérimentales de frottement dans le régime élastohydrodynamique (EHD), caractérisé par des surfaces de contact petites et des fortes pressions. Ceci est dû principalement à un manque de compréhension du comportement du lubrifiant dans le contact, où les propriétés physiques du lubrifiant sont susceptibles de varier avec la température et la pression [2]. En effet, un comportement purement Newtonien du fluide tend à surestimer le frottement à des vitesses de glissement moyennes et élevées.

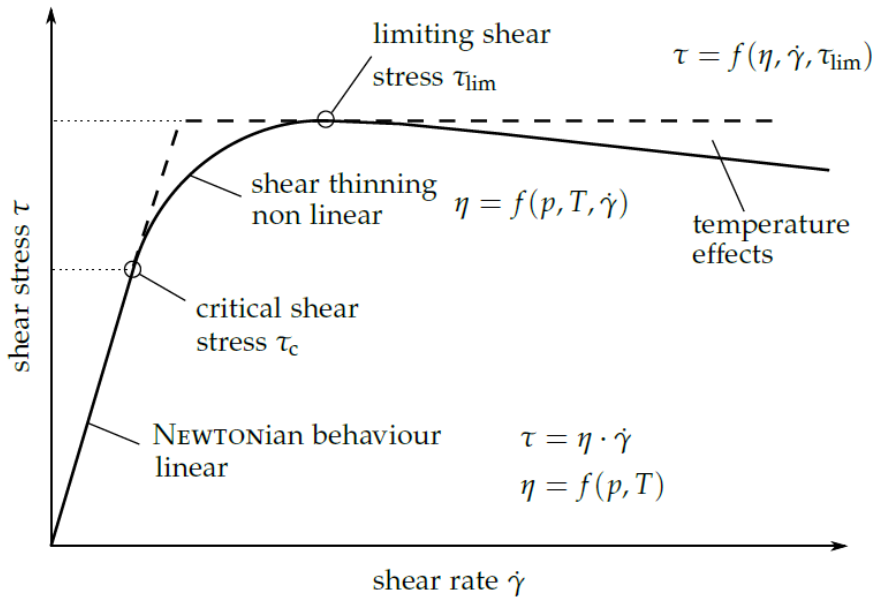

Figure 1. Modèle du frottement lubrifié décrit par Bair [3], où la contrainte de cisaillement est représentée en fonction du taux de cisaillement. Le comportement ultime du lubrifiant apparaît avec une contrainte de cisaillement maximale τ_{lim}.

Le lubrifiant subit, à pression constante, trois régimes successifs de frottement dans le contact en fonction de la vitesse de glissement (voir Figure 1). Initialement, pour des faibles vitesses, le comportement du lubrifiant est Newtonien et la contrainte de cisaillement dépend linéairement du taux de cisaillement. Ensuite, il suit un régime non linéaire rhéofluidifiant à des

vitesses plus élevées. Finalement, lorsque la vitesse et la charge appliquée sont suffisamment élevées, la contrainte de cisaillement peut atteindre une valeur maximale : la contrainte de cisaillement limite τ_{lim} (LSS). Dans ce régime plateau, la contrainte de cisaillement n'augmente plus avec la vitesse, les mécanismes physiques déclenchant ce comportement ultime du lubrifiant n'étant pas encore complétement compris. C'est en fait Smith [4] vers 1960 qui proposait l'idée d'une valeur maximale de frottement pouvant être atteinte pour un lubrifiant (τ_{lim} correspond à une contrainte limite sur la Figure 1). Cela conduirait à un écoulement semblable à un solide plastique, avec quelques couches solidifiées du lubrifiant se déplaçant à la vitesse imposée aux surfaces solides [5]. Toutefois, au-delà de l'apparition de la LSS, le fluide est sensible aux effets thermiques qui, d'autre part, diminueraient la viscosité du lubrifiant et, par conséquent, la valeur limite de la contrainte de cisaillement.

De nombreuses approches phénoménologiques ont été proposées dans la littérature pour décrire à la fois le phénomène de LSS et le comportement du lubrifiant dans des conditions typiques du régime EHD [6, 7, 8], dont une transition de phase liquide-solide du lubrifiant, du glissement localisé à l'interface surface/lubrifiant, ou l'apparition de bandes de cisaillement. Les modèles empiriques donnent maintenant une image complète des caractéristiques du lubrifiant sur une large plage de pressions et de températures, de temps de transit courts et de taux de cisaillement élevés. Néanmoins, même si les modèles sont précis, aucun dispositif rhéométrique ne permet d'atteindre les conditions sévères de la région hertzienne du contact. En effet, ils sont limités aux faibles taux et contraintes de cisaillement [9, 3], qui sont parfois très éloignés des conditions réelles du régime EHD. De plus, les modèles empiriques sont encore incomplets et doivent donner de meilleures prévisions dans des conditions extrêmes de pression et de taux de cisaillement. En outre, des questions restent en suspens sur les mécanismes physiques à l'origine du phénomène de LSS, ainsi que sur l'influence de la pression et de la température [3]. C'est pour cela que des méthodes computationnelles ont été de plus en plus utilisées pour la meilleure compréhension des lubrifiants.

Parmi les différentes méthodes de calcul existantes, les simulations Dynamique Moléculaire (DM) représentent une technique idéale pour étudier et analyser le comportement en frottement et l'écoulement de lubrifiants fortement confinés. À partir de ces simulations, il est possible de fournir des informations sur le comportement local du fluide, difficilement accessible par expérimentation. Cependant, bien que les simulations DM donnent un aperçu précis du comportement des fluides dans des différentes conditions de fonctionnement, ils doivent encore être comparés quantitativement aux données expérimentales, tâche peine à être accomplie en raison des différentes échelles spatiales et temporelles. Des progrès substantiels ont été réalisés dans ce domaine, qui permettent à présent d'obtenir des résultats quantitatifs et qualitatifs semblables [10, 11]. Par ailleurs, plusieurs hypothèses sont constamment formulées en simulation, que ce soit en ce qui concerne le fluide ou les parois utilisées pour créer le confinement. En effet, seule une petite aire de contact peut être simulée, qui doit représenter toute la région hertzienne avec tous les phénomènes thermiques et mécaniques. Malgré toutes les limitations, les simulations atomistiques peuvent permettre de mieux comprendre les phénomènes sous-jacents à la lubrification, en particulier dans des conditions extrêmement difficiles à reproduire et à exploiter par le biais d'expériences.

ii. Objectifs de la thèse

Le frottement a un impact important sur la performance globale des systèmes mécaniques, d'où l'inquiétude croissante des fabricants de roulements de réduire les pertes d'énergie dues au frottement avec l'objectif d'améliorer leur efficacité, mais aussi de réduire les coûts de fabrication associés. En fait, le potentiel d'économie d'énergie que cela pourrait permettre est considérable en raison de la vaste gamme d'applications où les roulements sont utilisés. De plus, les émissions de CO_2 seraient réduites. Pour ce faire, des modèles mis à jour et fiables permettant de prévoir les pertes par frottement dans les systèmes mécaniques lubrifiés sont nécessaires.

L'objectif de ce travail est donc d'améliorer la prévision du frottement dans les contacts lubrifiés, tels que ceux rencontrés dans les roulements, dans le scénario le plus extrême, c'est-à-dire lorsqu'ils sont exposés à des conditions sévères de pression et de cisaillement. Il existe encore un débat ouvert sur les différents phénomènes se produisant dans un contact lubrifié lorsqu'on travaille dans ces conditions extrêmes, d'où la nécessité de développer des modèles prédictifs du frottement local et de la rhéologie des lubrifiants. Actuellement, divers modèles empiriques permettant de prédire les régimes classiques de frottement sont disponibles mais il n'existe encore aucun modèle prédictif du comportement ultime des lubrifiants à fort cisaillement. En outre, les outils expérimentaux ne permettent pas d'accéder aux échelles locales au niveau du contact. Par conséquent, l'approche choisie pour ce travail est axée sur des simulations atomistiques visant à déterminer la réponse à l'écoulement de fluides confinés dans des conditions lubrifiées élastohydrodynamiques. En particulier, des simulations Dynamique Moléculaire à l'équilibre (EMD) et hors équilibre (NEMD) sur trois fluides de différentes natures (fluides de traction, lubrifiants modèles, et lubrifiants industriels pour des applications aérospatiales) sont réalisées dans ce travail. Ces fluides sont représentatifs des huiles de base qui peuvent être rencontrés dans l'industrie.

iii. Simulations Dynamique Moléculaire

La Dynamique Moléculaire est une méthode de calcul déterministe [12] selon laquelle les équations du mouvement de Newton qui régissent chacun des atomes du système sont résolues de manière explicite, en calculant ainsi les trajectoires des particules dans le temps. Pour chaque pas de temps, les forces agissant sur chaque particule peuvent être calculées à l'aide d'un champ de force (FF), décrivant les différentes interactions des particules. Une intégration ultérieure des accélérations fournit les positions atomiques pour les étapes suivantes. Le temps étant calculé explicitement, la durée d'une simulation est généralement limitée à quelques dizaines de nanosecondes. Il est également possible d'explorer des phénomènes tels que les distributions de vitesse et de température, la structuration des molécules, etc. sur cette plage de temps. Des quantités physiques supplémentaires peuvent être déduites, telles que la viscosité, la conductivité thermique et électrique, le frottement ou même l'énergie totale du système atomique.

iii.1. Modèle et méthodes

iii.1.1. Simulations en volume

La configuration initiale des systèmes moléculaires en volume est créée à l'aide du logiciel Moltemplate [13] et l'évolution au cours du temps est calculé par le logiciel LAMMPS [14]. L'environnement de simulation consiste en une région de 5,0 x 5,0 x 5,0 nm approximativement à la pression ambiante, contenant généralement environ 10 000 atomes (voir Figure 2). Toutes les molécules sont affectées par une version adaptée [15] du champ de force L-OPLS-AA [16, 17], qui prend en compte les interactions inter et intra-atomiques.

Les interactions interatomiques des molécules comprennent à la fois les interactions de Lennard-Jones (LJ) et de Coulomb à longue portée, les premières étant établies avec une distance de coupure de 12 Å. De plus, les règles de mélange de Lorentz-Berthelot sont appliquées pour les paramètres de LJ entre des atomes de nature différente. Les interactions électrostatiques, quant à elles, sont déterminées par l'algorithme PPPM. Les conditions aux limites périodiques sont appliquées dans les trois directions du système.

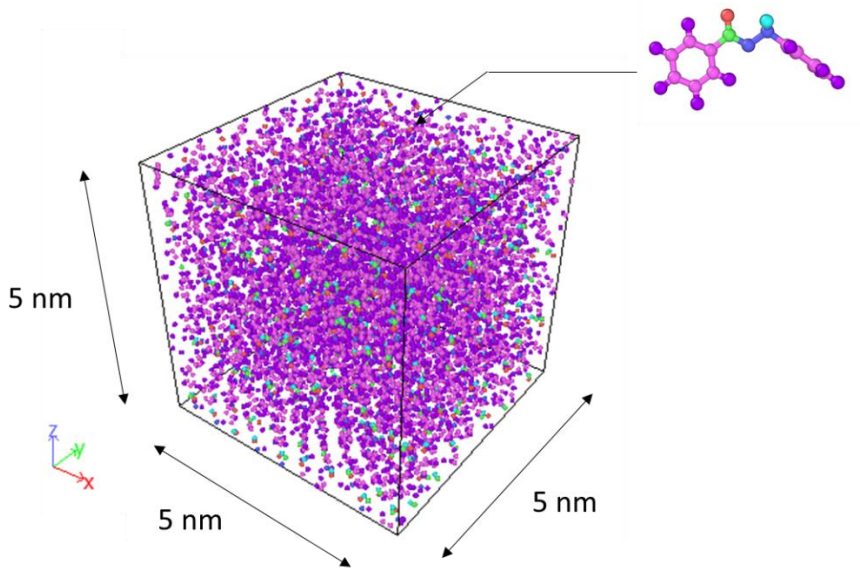

Figure 2. Exemple d'un système en volume de molécules. Ici, le système est composé de 360 molécules de benzoate de benzyle.

iii.1.2. Simulations en confinement

Les molécules du lubrifiant sont modélisées, comme pour les systèmes moléculaires en volume, avec le champ de force L-OPLS-AA. La configuration initiale des systèmes confinés est créée avec le logiciel open source LAMMPS_builder [18], qui utilise des modules de Moltemplate [183] et ASE [19]. Les calculs s'exécutent toujours sur le logiciel LAMMPS [14]. Ces systèmes représentent des molécules du fluide confinées entre deux surfaces solides soit atomiquement lisses en oxyde de fer (α-Fe2O3 [100]) soit rugueuses en fer avec des aspérités aléatoires (α-Fe [100]).

Le but principal de ces simulations DM est de caractériser complètement les phénomènes de frottement et d'écoulement du lubrifiant confiné en s'affranchissant des effets que les surfaces provoquent sur le fluide. En effet, les surfaces atomiquement lisses échouent parfois à représenter les interactions à la frontière entre les molécules de fluide et les surfaces solides [20, 21], d'où l'intérêt d'inclure également dans cette étude les surfaces rugueuses, qui sont une représentation plus proche de la réalité. De plus, des paramètres tels que le potentiel de corrugation [22] ou même la géométrie de la surface [20, 23] peuvent avoir un impact important sur l'écoulement.

En ce qui concerne les systèmes conçus avec des surfaces lisses, les surfaces en oxyde de fer ont des dimensions approximatives de 5,0 x 5,0 x 1,5 nm dans les dimensions x, y et z respectivement. Les atomes de fer et d'oxygène sont retenus dans la structure cristalline par des liaisons harmoniques, dont la constante de rappel est égale à 25 $kcal.mol^{-1}$ [24]. Quant aux interactions interatomiques, elles sont modélisées avec des interactions LJ et électrostatiques. Des informations supplémentaires sur les paramètres LJ pour les atomes de fer et d'oxygène utilisés pour la surface lisse en oxyde de fer sont présentées dans le Tableau 1 et sont basées sur la littérature de Savio et al. [24] et Berro et al. [25]. Dans le Tableau 1, le paramètre ε de LJ des atomes de fer est réglé artificiellement afin de prendre en compte différents degrés d'adhérence.

Tableau 1. Paramétrage des atomes d'oxyde de fer utilisés pour la surface lisse en oxyde de fer. Les deux valeurs différentes de ε pour les atomes de fer représentent deux degrés différents d'adhérence aux surfaces.

Groupe	Type d'atome	Description	q / e	σ / Å	ε^+ / $kcal.mol^{-1}$	ε^- / $kcal.mol^{-1}$
Oxyde de fer (Fe_2O_3)	FE	Surface Fe	0.771	2.320	9.518	0.945
	OX	Surface O	-0.514	2.960	0.210	

Il est également possible d'insérer des profils de rugosité à l'échelle nanométrique dans la structure cristalline des surfaces. Les surfaces rugueuses en fer sont créées en utilisant une loi d'échelle auto-fractale avec la méthodologie exposée par [10], et en réglant l'exposant de Hurst et la rugosité moyenne quadratique (RMS) à 0,8 et 0,8 nm respectivement. Les surfaces en fer créées mesurent environ 5,0 x 5,0 nm dans les directions x et y et ont une épaisseur comprise entre 3,0 et 5,0 nm dans la direction z. Les atomes de fer sont affectés par le FF empirique EAM [26], largement utilisé pour les systèmes métalliques [27, 28].

Les simulations sont exécutées à l'aide d'un ensemble thermodynamique NVE, ce qui implique que le nombre total de molécules contenues dans le système, le volume et l'énergie totale sont maintenus constants pendant la durée de la simulation. Les conditions aux limites périodiques ne sont appliquées que dans les directions x et y, empêchant ainsi l'écoulement des molécules de fluide en dehors le contact. Ce choix est approprié du fait qu'au centre d'un contact lubrifié EHD typique, l'épaisseur de film est inférieure aux autres dimensions du

système. De plus, l'intégrité du modèle DM est assurée car le flux de sortie des molécules de lubrifiant lors des étapes de simulation est empêché.

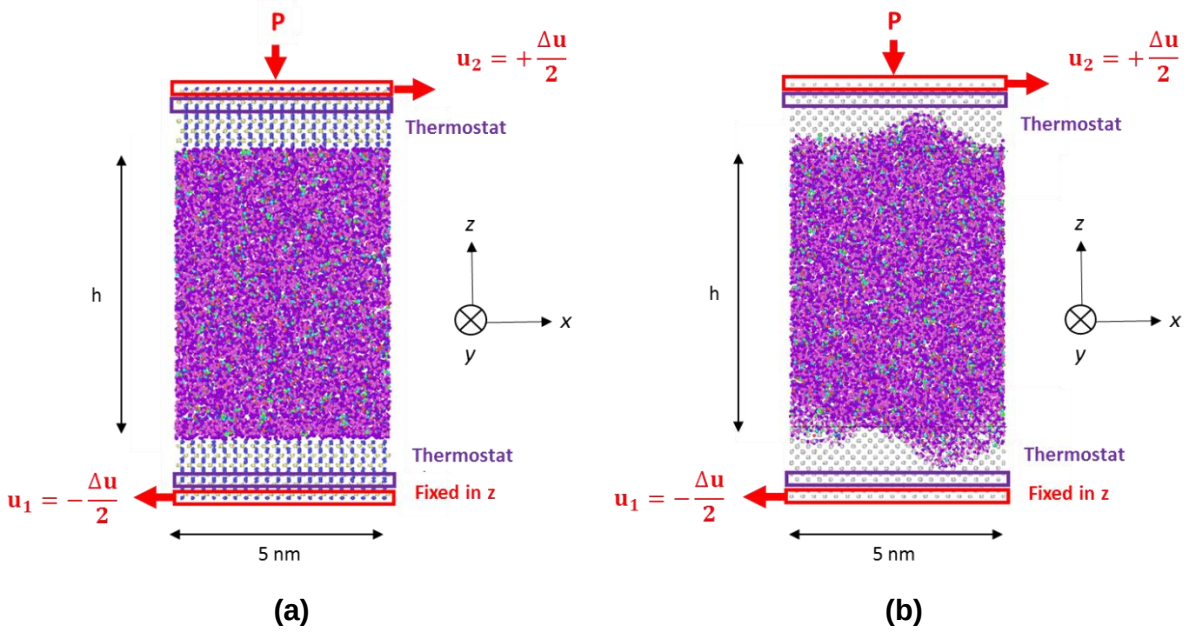

Figure 3. Configuration représentative du système de molécules de benzoate de benzyle confinées entre (a) des surfaces lisses en oxyde de fer et (b) des surfaces rugueuses en fer, après compression et avant de glisser dans la direction x. La vitesse de glissement est définie comme $u_2 = -u_1 = +\Delta u/2$.

Trois étapes sont définies pour une simulation : relaxation des molécules de fluide, compression et cisaillement. Le système est d'abord minimisé en énergie et relâché car les molécules, initialement assignées aléatoirement dans l'espace, doivent être disposées dans une configuration telle que celle trouvée à l'équilibre. La pression est ensuite appliquée au système en définissant une pression normale P sur la couche externe d'atomes dans la surface solide supérieure, conformant une région de contrôle (voir Figure 3). La pression est uniformément répartie sur tous les atomes de la région de contrôle. Chaque atome supporte une force égale à :

$$F_{z,i} = \frac{PS}{N_c} \tag{1}$$

avec S la section de la surface du nano-patch égale à $S = L_x \times L_y$ (L_x et L_y étant la longueur des côtés de la section) et N_c le nombre d'atomes dans la région de contrôle. La surface solide inférieure est maintenue fixe dans la direction z, sans aucune pression appliquée. La plage de valeurs de pression choisie (de 0,5 à 2 GPa) est représentative d'un contact lubrifié EHD.

La compression est effectuée pendant environ 2 ns, pour laquelle l'épaisseur de film évolue de manière progressive avec le temps jusqu'à sa stabilisation. Lorsque l'épaisseur de film atteint une valeur constante, l'étape de cisaillement commence.

Au cours de la phase de cisaillement (voir Figure 3), un gradient de vitesses constant dans la direction x est imposé en appliquant une vitesse constante sur les couches extérieures des atomes dans les surfaces solides supérieure et inférieure, mais dans des directions opposées. Sur la surface supérieure, la vitesse de cisaillement est égale à $u_2 = +\Delta u/2$, tandis que dans la surface inférieure, elle est $u_1 = -\Delta u/2$. On préfère que le cisaillement soit imposé par les couches solides plutôt que d'être directement imposé sur le fluide. En effet, il a été confirmé que la dynamique du fluide confiné est modifiée si le cisaillement agit directement sur les molécules du fluide [29, 30]. L'excès de chaleur généré est dissipé par un thermostat de Langevin [31] dans la direction y, qui est la direction perpendiculaire au mouvement et à la compression. Le thermostat est appliqué juste au-dessous des conditions limites mécaniques de la surface solide afin de ne pas interférer avec le fluide ou l'interface fluide/surface [22]. De cette façon, la température dans le système fluide est laissée évoluer indépendamment. Enfin, il convient de noter que la régulation de la température du fluide à partir de la température aux limites du système s'est révélée être un moyen efficace de contrôler la température du fluide confiné [32, 33, 34]. Cependant, pour des vitesses de cisaillement supérieures à 10^{10} s^{-1}, les températures dans le contact commencent à s'écarter de leur état isotherme [35, 22].

Le régime permanent était généralement atteint pour des temps de cisaillement supérieurs à 1 ns et dépendant du taux de cisaillement appliqué. Des taux de cisaillement plus élevés entraînent des temps inférieurs pour atteindre un écoulement stable. Les profils moyens de vitesse et de densité sur l'épaisseur du film, et la contrainte de cisaillement au niveau des surfaces ont été obtenus à partir d'une moyenne avec le temps.

iii.2. Modèle des fluides

La modélisation du fluide dans son ensemble implique un défi de taille pour la représentation de chacun des composants : la tâche est trop longue, imprécise et, dans la plupart des cas, impossible à réaliser car la formulation du lubrifiant est inconnue. Par conséquent, les modèles présentés ici ne prennent en compte que les molécules de fluide de base, qui sont représentatives de l'ensemble du lubrifiant et qui seront paramétrées pour les simulations DM ultérieures. Un choix de trois molécules d'huile de base sera tout d'abord présenté.

iii.2.1. Fluides de traction : benzoate de benzyle

La molécule choisie pour représenter un fluide caractéristique de type traction est le benzoate de benzyle (BB), un fluide organique de formule $C_6H_5COOCH_2C_6H_5$, qui est l'ester de l'alcool benzylique et de l'acide benzoïque (voir Figure 4). Ce fluide a été sélectionné car il existe déjà de nombreuses données rhéologiques et de frottement [36]. De plus, le BB est une molécule intéressante pour les études expérimentales car elle présente des anneaux, permettant une caractérisation spectroscopique [8]. Les paramètres de LJ du benzoate de benzyle sont définis dans le Tableau 2.

(a) **(b)**

Figure 4. Représentation schématique (a) de la molécule de benzoate de benzyle et (b) de son modèle DM. Dans (b), les particules vertes représentent les atomes d'hydrogène, les oranges les atomes de carbone et les bleues les atomes d'oxygène.

Tableau 2. Paramètres de LJ et charges électroniques partielles de la molécule de benzoate de benzyle [15]. Les types d'atomes du groupe ester marqués d'un * ont des charges partielles modifiées afin d'assurer une charge nette neutre de la molécule.

Groupe	Type d'atome	Description	q / e	ε / Å	σ / kcal.mol^{-1}
Ester (glycéride)	C	C=O	0,795*	3,750	0,150
	O	O=C	-0,380*	2,960	0,210
	OS	ROR	-0,200*	3,000	0,170
Anneau aromatique	CA	C	-0,115	3,550	0,066
	HA	H-C	0,115	2,420	0,023
Benzoate	CB	C-COO-	-0,100	3,550	0,066
Alkyle	CT	-CH2-	-0,148	3,500	0,066
	HC	H-C CH2	0,074	2,500	0,026

iii.2.2. Lubrifiants modèles : squalane

Le squalane (SQ) est un lubrifiant organique de formule $C_{30}H_{62}$ (voir Figure 5). Cette molécule a déjà été largement étudiée et caractérisée dans la littérature [10, 37, 38] et sera davantage utilisée dans ce travail pour les simulations de DM. Les paramètres de LJ du squalane sont définis dans le Tableau 3.

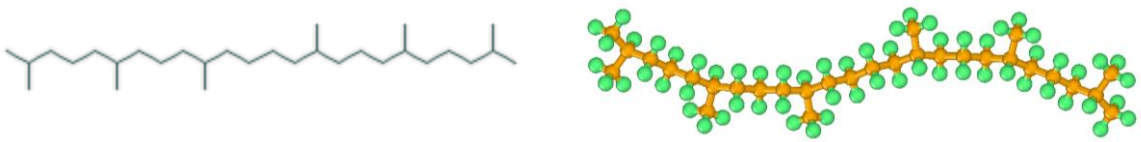

(a) **(b)**

Figure 5. Représentation schématique (a) de la molécule de squalane et (b) de son modèle DM. Dans (b), les particules vertes représentent les atomes d'hydrogène, et les orange les atomes de carbone.

Tableau 3. Paramètres de LJ et charges électroniques partielles de la molécule de squalane [181].

Groupe	Type d'atome	Description	q / e	ε / Å	σ / kcal.mol^{-1}
Alkyle	CT	-CH3-	-0,222	3,500	0,066
	HC	H-C CH3	0,074	2,500	0,026
	CT	-CH2-	-0,148	3,500	0,066
	HC	H-C CH2	0,074	2,500	0,026
	CT	-CH-	-0,074	3,500	0,066
	HC	H-C CH	0,074	2,500	0,026

iii.2.3. Lubrifiants pour des applications aérospatiales

Le lubrifiant modèle aérospatial utilisé dans ce travail est la Nycobase 5750 (NPE), une huile de base fournie par la société Nyco (Paris, France) à base de molécules de polyol ester (PE) (voir Figure 6). Le modèle DM considère donc uniquement les molécules de PE, dont les paramètres de LJ et les charges électroniques partielles sont présentés dans le Tableau 4 [15].

Le modèle choisi dans ce travail pour représenter ce lubrifiant est un mélange binaire de proportion 1: 4 entre des molécules de différentes longueurs. En fonction de la longueur n_C de la chaîne alcane radicalaire, la molécule de PE aura une formulation différente. La formule sera $C_9O_8H_8$ et constante pour le «noyau», tandis que 4x [(n_C-1) CH_2 - CH_3] et variable pour les ramifications n-alcanes (voir Figure 6). Ici, le fluide est composé par 20% de molécules de longueur n_C=8 et 80% de molécules de longueur n_C=4.

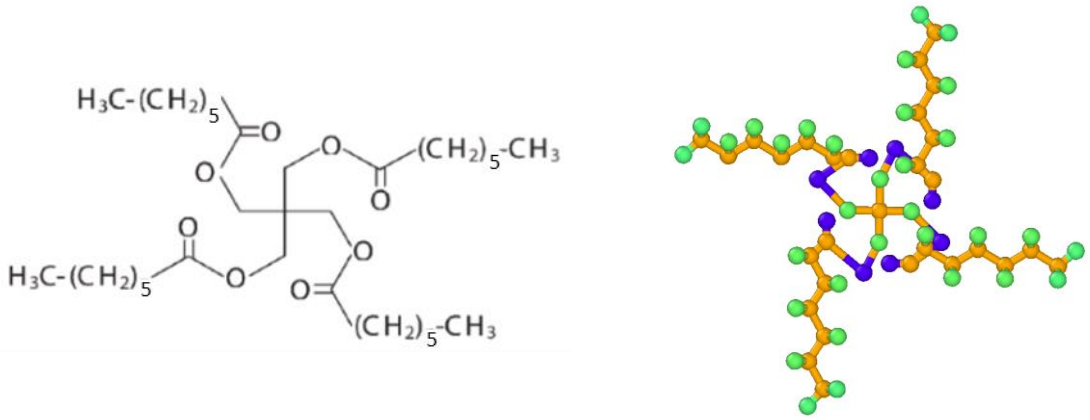

(a) **(b)**

Figure 6. Représentation d'une molécule de PE utilisée pour les simulations DM. En particulier, la molécule représentée est une molécule de PE avec n_C=6. Dans (b), les particules vertes représentent les atomes d'hydrogène, les oranges les atomes de carbone et les bleues les atomes d'oxygène.

Tableau 4. Paramètres de LJ et charges électroniques partielles de la molécule de PE [181]. Les types d'atomes du groupe ester marqués d'un * ont des charges partielles modifiées afin d'assurer une charge nette neutre de la molécule.

Groupe	Type d'atome	Description	q / e	ε / Å	σ / kcal.mol^{-1}
Ester (glyceride)	C	C=O	0,710*	3,750	0,150
	O	O=C	-0,380*	2,960	0,210
	OS	ROR	-0,330	3,000	0,170
Alkyle	CT	-CH3-	-0,222	3,500	0,066
	HC	H-C CH3	0,074	2,500	0,026
	CT	-CH2-	-0,148	3,500	0,066
	HC	H-C CH2	0,074	2,500	0,026
Atome central	CT	>C<	0,000	3,500	0,066

iv. Mécanismes d'écoulement et de frottement de fluides moléculaires confinés

Le frottement est généralement représenté par le coefficient de frottement C_f, défini macroscopiquement comme le rapport entre la force de frottement tangentielle moyenne dans la direction principale d'entraînement F_x et la charge normale appliquée F_z:

$$C_f = \frac{F_x}{F_z} \quad (2)$$

Le frottement varie avec la vitesse de glissement $\Delta u = u_1 - u_2$, qui est la différence de vitesse des deux parois de confinement suivant la direction de cisaillement, où u_1 et u_2 sont respectivement les vitesses des surfaces 1 et 2. De là, un taux de cisaillement apparent $\dot{\gamma}$ peut être défini à partir de l'épaisseur centrale du film de lubrifiant h_c comme :

$$\dot{\gamma} = \frac{\Delta u}{h_c} \tag{3}$$

L'état physique du fluide a été présenté comme l'un des principaux acteurs possibles de l'apparition du phénomène LSS. Afin de prouver ces hypothèses, une série de simulations NEMD ont été réalisées dans les conditions de pression et de température spécifiées au Tableau 5, pour une large plage de valeurs de taux de cisaillement allant de 10^8 à 10^{11} s^{-1}. Ces conditions sont sélectionnées à l'aide des diagrammes de phases de chaque fluide, développés dans ce travail avec des simulations EMD (voir Figure 7). Les modèles DM présentés ci-après prennent en compte les molécules de lubrifiant confinées entre deux plaques solides afin de reproduire les conditions de confinement d'un contact EHD réel.

Tableau 5. Conditions expérimentales et des simulations NEMD pour le benzoate de benzyle, le squalane et le mélange de PE, représentant les deux conditions dans lesquelles le fluide devrait être dans un état liquide ou solide.

	Etat liquide		Etat solide	
Fluide	P_m / GPa	T / K	P_m / GPa	T / K
BB	0,5	313	2	313
SQ	2	353	1,2	313
NPE	0,8	300	1,2	300

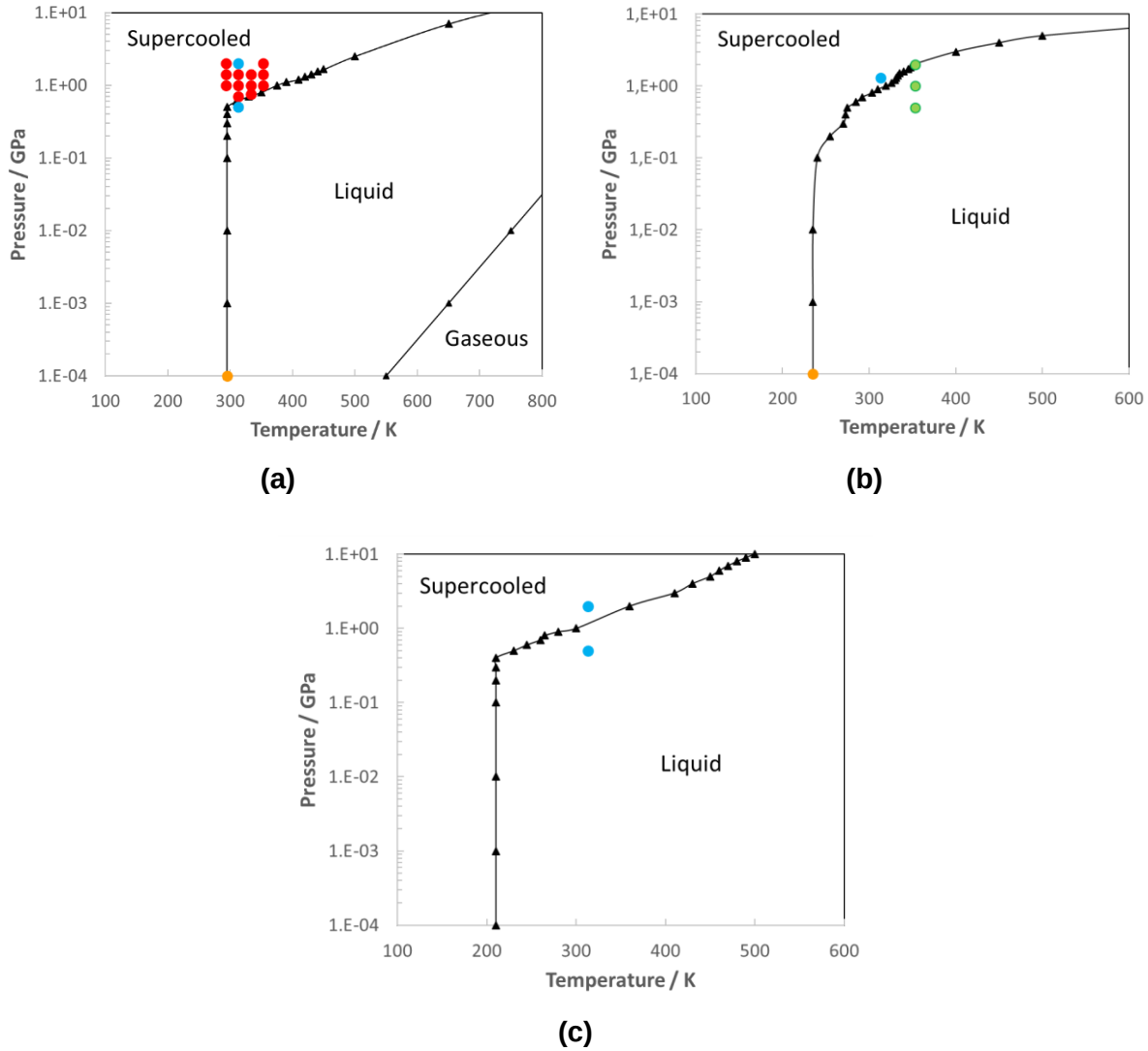

Figure 7. Diagrammes de phases pour (a) BB, (b) SQ et (c) NPE, où les triangles noirs représentent des résultats DM de ce travail. Les points bleus correspondent aux conditions de pression et de température des simulations NEMD effectuées dans ce travail. Les marques rouges en (a) représentent les mesures expérimentales de BB [36] où la LSS a été capturée. En (b), les marques vertes représentent les conditions thermodynamiques dans lesquelles le squalane a été évalué sous confinement en [10]. La LSS n'a pas été capturée ici. Pour (a) et (b), les marques en orange symbolisent les mesures expérimentales de la température de fusion prises de [39] et [40] respectivement.

iv.1. Influence des surfaces sur l'écoulement

Le comportement de l'écoulement résulte d'une compétition continue entre la rhéologie du fluide, pilotée par la pression et la température du système, et la résistance interfaciale solide/fluide, contrôlée par le paramètre LJ des atomes de fer de la surface. Le cisaillement s'initierait donc dans la région où ces interactions sont les plus faibles. Le Tableau 6 synthétise la réponse obtenue de l'écoulement aux différentes conditions imposées au fluide confiné et aux conditions de fonctionnement appliquées.

Tableau 6. Synthèse du comportement de l'écoulement pour des pressions inférieures et supérieures à la pression de transition liquide-solide, où le profil de vitesse dans la direction de cisaillement (en rouge) et le profil de densité (en bleu) sont représentés.

Surface	α-oxyde de fer [100] (lisse)		α-fer [100] (rugueuse)
ε / kcal.mol^{-1}	Cas 1 ε^-	Cas 2 ε^+	Cas 3 ε^-
$P < P_t$	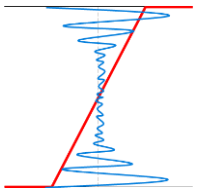	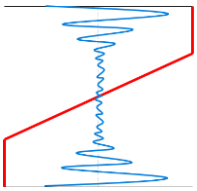	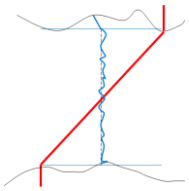
$P > P_t$	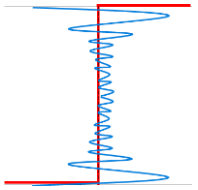	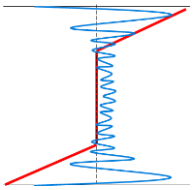	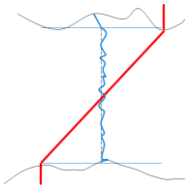

L'influence des surfaces, et donc la physique qui régit la dissipation d'énergie dans la région de contact, est bien représentée dans le Tableau 6. Ici, deux contributions distinctes entrent en jeu : d'un côté la nature géométrique de la surface représentée par sa rugosité [25], et de l'autre l'énergie surfacique, qui représente l'adhérence des molécules de fluide sur les surfaces solides. Ce dernier paramètre en particulier est piloté par le paramètre ε de LJ des atomes de fer [41] et induit des interfaces faibles ou fortes, c'est-à-dire, il permet de modifier la mouillabilité de l'interface solide/fluide. Par conséquent, du glissement ou du verrouillage aux niveau des parois apparaît respectivement. Dans les deux premiers cas (voir les deux premières colonnes du Tableau 6), grâce à l'utilisation d'une surface lisse, la structuration en couches est induite sur l'épaisseur du film, créant des points de faiblesse entre les couches moléculaires. Cependant, dans le cas 2, les surfaces de confinement sont très adhésives, de sorte que le verrouillage s'étend sur quelques couches moléculaires. Il en résulte que le cisaillement est localisé dans la région loin des surfaces, dont la résistance au cisaillement dépend fortement de la pression. De plus, le comportement de l'écoulement du fluide confiné change radicalement lorsque la pression de transition est dépassée, passant d'un profil d'écoulement classique de Couette à un écoulement fortement bouchon. Dans ce dernier cas, l'accommodation de la vitesse a lieu près des surfaces, entre des couches denses de molécules de fluide [42, 43, 44]. Enfin, dans le cas 3, les surfaces rugueuses empêchent la structuration en couches près de la surface (voir la troisième colonne du Tableau 6), de sorte qu'aucune zone plus faible ne puisse être définie sur l'épaisseur. Ainsi, le cisaillement s'étend sur l'ensemble du contact et présente un profil de Couette presque pur. De manière surprenante, ce profil de vitesse ne dépend que très légèrement de la charge normale appliquée, de telle sorte que le profil ne semble pas affecté par l'effet de la pression.

Les différentes conclusions tirées jusqu'à présent soulèvent plusieurs questions quant aux origines du frottement concernant i) quel profil de vitesse est le plus susceptible d'être généré pendant l'expérimentation et ii) si les différentes distributions de vitesse affectent le coefficient de frottement. En effet, on pourrait s'attendre à une influence significative sur le frottement, car il se traduit macroscopiquement par la dissipation de la chaleur hors du contact. Cette corrélation entre les profils de vitesse et le frottement devrait fournir des réponses à ces questions.

iv.2. Une comparaison quantitative du frottement

Pour chaque condition aux limites appliquée aux systèmes fluides, différents profils de vitesse et de densité ont été mesurés même s'ils convergent tous vers des valeurs de frottement similaires (voir Figure 8). Cela ne suggère aucun lien apparent entre le comportement de l'écoulement et le comportement du frottement. En effet, le comportement de l'écoulement provient des conditions de pression et température rencontrées dans le contact, ainsi que des caractéristiques des parois solides (rugosité et mouillabilité). Cependant, la valeur du frottement est indépendante du choix des surfaces solides et donc du régime d'écoulement, pour autant que le film de lubrifiant soit suffisamment épais. En effet, le frottement se stabilise autour d'une valeur définie identique pour toutes les surfaces pour une épaisseur de film supérieure à une valeur critique. Pour les simulations ci-mentionnées, cette épaisseur est supérieure à 10 nm.

Sur la Figure 8.a et 8.b, les mesures de frottement du BB obtenues expérimentalement par Ndiaye et al. [36] sont comparées aux résultats numériques des simulations NEMD du même fluide dans les mêmes conditions de température et pression (313 K et à la fois à 0,5 et à 2 GPa). Des données de frottement expérimentales et de simulation NEMD sont également disponibles pour le SQ à 353 K et 2 GPa (Figure 8.c) fournies par [10]. Elles sont comparées à des nouvelles simulations de SQ confiné entre des surfaces rugueuses, soumis aux mêmes conditions de pression et de température. En outre, le comportement en frottement du SQ à 313 K et 1,2 GPa est étudié (Figure 8.d). L'analyse est enfin complétée par la comparaison directe des données de NPE pour des expériences et des simulations avec des surfaces rugueuses dans la Figure 8.e et 8.f. Toutes les nouvelles données expérimentales proviennent du LaMCoS et de P. Vergne et ont été fournies en suivant la procédure détaillée dans [36]. Pour les six cas présentés, les valeurs numériques des coefficients de frottement calculés à partir de la DM correspondent bien aux expériences, même si les échelles temporales et spatiales diffèrent de plusieurs ordres de grandeur. Un résultat similaire a été obtenu par [10] pour des fluides de traction et pour un alcane linéaire.

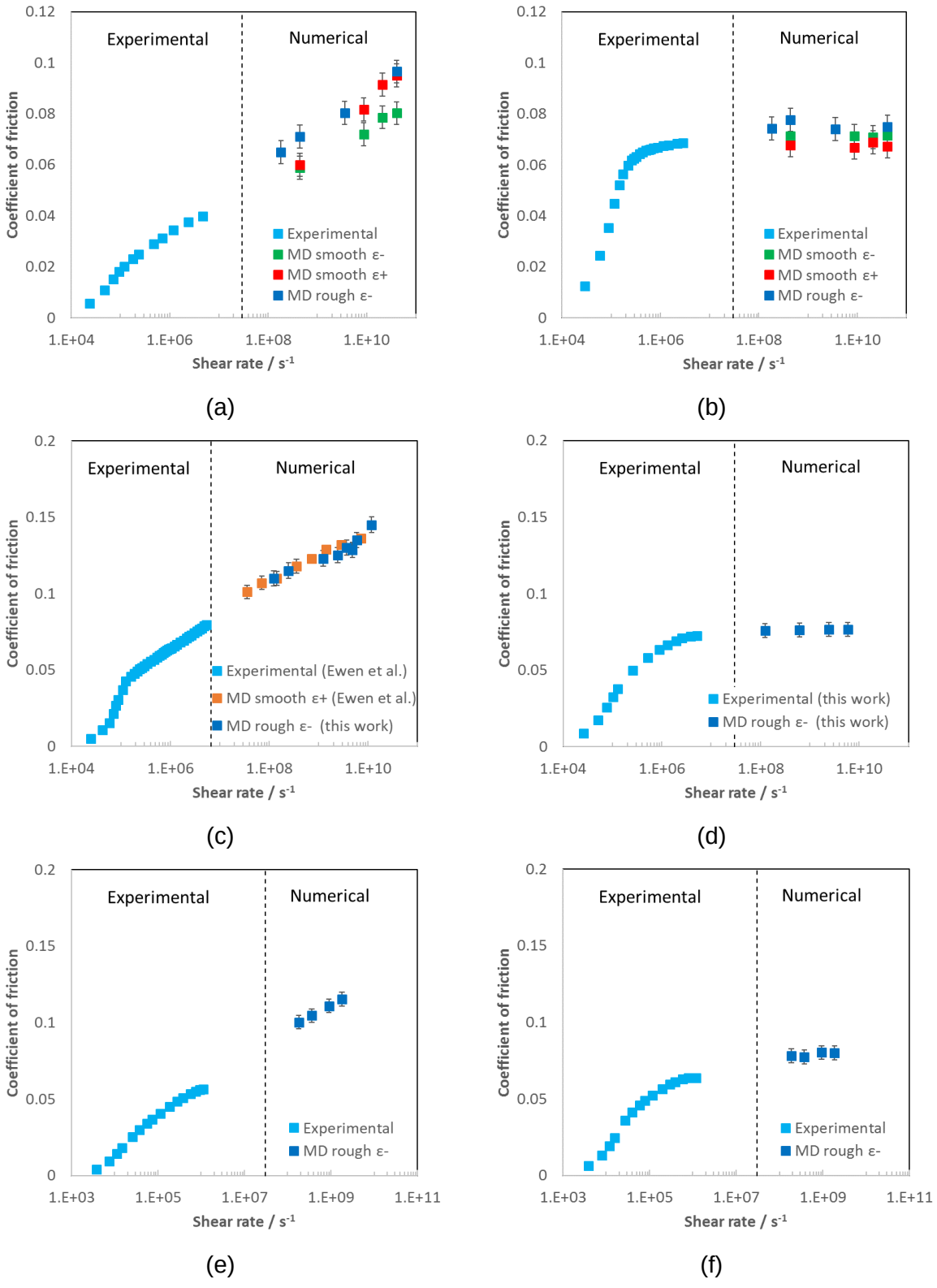

Figure 8. Coefficient de frottement en fonction du taux de cisaillement pour BB à 313 K et (a) 0,5 GPa et (b) 2 GPa, pour SQ à (c) 353 K et 2 GPa, et à (d) 313 K et 1,2 GPa, et NPE à 300 K et (e) 0,8 GPa et (f) 1,4 GPa. Pour la figure (c), les données expérimentales et numériques à surfaces lisses proviennent de [10]. Pour les figures (d), (e) et (f), les nouvelles mesures expérimentales effectuées conformément à la procédure de [36] sont confrontées à des données numériques.

En ce qui concerne le comportement de la LSS, le régime plateau est correctement prédit quantitativement à partir des simulations NEMD du BB confiné une fois que la pression de transition du fluide (selon le diagramme de phases de la Figure 7) est dépassée. Cette corrélation entre l'état physique et la réponse au frottement est aussi reproduite avec succès pour le SQ et pour le NPE lors du cisaillement quand le fluide est soumis à des conditions nominales de l'état solide. En effet, il convient de noter que pour SQ soumis à 353 K et 2 GPa, aucun régime plateau n'est à prévoir, le fluide étant supposé être à l'état liquide (marques vertes dans la Figure 7.b), aspect qui n'avait pas été pris en compte auparavant dans [10]. Ainsi, pour les structures moléculaires étudiées dans ce travail, on peut conclure que la LSS et la transition de phase sont deux concepts fortement interconnectés, même si aucune causalité directe entre les deux phénomènes n'est prouvée. En effet, les profils de vitesse homogènes obtenus pour des fluides confinés entre des surfaces rugueuses (voir Tableau 6) et l'ordre de grandeur de la viscosité effective (<< 1 Pa.s) en pouvant être déduite excluent la possibilité d'un véritable comportement solide lors du cisaillement à des taux élevés. Cela implique que la sensibilité du fluide à la pression et à la température est affectée de manière significative par sa déformation (cisaillement) et que la réponse de la LSS provient d'un mécanisme plus sophistiqué, possiblement liée à son comportement dynamique. En outre, l'application de cartes de frottement, telles que [45, 46, 47], basées exclusivement sur des systèmes fluides confinés entre des surfaces lisses, serait limitée à des cas très particuliers, sans une influence significative sur les phénomènes macroscopiques.

Finalement, on peut conclure que le comportement plateau des fluides confinés dans des conditions d'EHD et la transition de phase sont des concepts interdépendants. Il existe des preuves substantielles démontrant qu'il existe pour chaque fluide une combinaison donnée de pression et de température pour laquelle il subit une transition de phase d'un état liquide à un état solide. A l'état liquide, les molécules de fluide ont suffisamment de liberté pour réagir et s'adapter aux contraintes générées, de sorte que le frottement puisse évoluer avec des taux de cisaillement croissants. À des taux très élevés, la LSS est atteinte.

v. Mécanismes de dissipation dans de systèmes moléculaires confinés

Dans les simulations DM, le chemin suivi par le flux d'énergie lors du cisaillement d'un fluide confiné est composé de trois étapes différentes. L'énergie est d'abord ajoutée au système par la compression et le mouvement relatif de la surface de confinement. L'énergie est ainsi absorbée par le lubrifiant sous forme d'énergie mécanique et transformée pendant le processus de cisaillement en chaleur. Cette transformation entraîne une augmentation de la température globale du fluide et la création d'un gradient de température à travers le film avec les surfaces thermostatées. Il en résulte finalement la dissipation de l'énergie thermique à travers les surfaces solides.

Plusieurs auteurs attribuent aux méthodes de thermostatisation un impact significatif sur la température globale du fluide lorsque le lubrifiant est susceptible de s'échauffer [35, 48]. Eventuellement, le thermostat n'est qu'un aspect à prendre en compte lorsque de l'échauffement est considéré, l'autre aspect étant le type de fluide confiné lors de la simulation. De plus, il a déjà été constaté pour des nombreux systèmes moléculaires [35, 48] l'existence d'un seuil de taux de cisaillement au-dessus duquel apparaît de l'échauffement significatif. Bien que des efforts ont été déployés pour établir une loi universelle pour la prédiction de

l'échauffement à l'intérieur du fluide, aucun progrès n'a encore été réalisé [35], l'échauffement étant dépendant du type de fluide utilisé. Jusqu'à maintenant, seulement les fluides de Lennard-Jones ont été considérés [46, 45, 47], ainsi que des n-alcanes simples [35, 48]. Cependant, dans ce travail, des systèmes moléculaires plus complexes avec plus de degrés de liberté sont utilisés.

v.1. Echauffement visqueux

Des simulations utilisant du BB, du SQ et du NPE ont été effectuées avec des surfaces en α-Fe [100] rugueuses à une large plage de vitesses de glissement, donnant des taux de cisaillement entre 10^8 s^{-1} et 10^{11} s^{-1}. En ce qui concerne les conditions de pression et de température utilisées, les deux cas étudiés pour chaque fluide conduisent soit à un état solide ou liquide (voir Tableau 5), entraînant respectivement l'apparition d'un régime plateau ou d'un régime de rhéofluidification. Pour la suite, l'algorithme de Langevin avec un coefficient d'amortissement de 100 fs est utilisé pour toutes les simulations ultérieures afin de contrôler la température dans le contact.

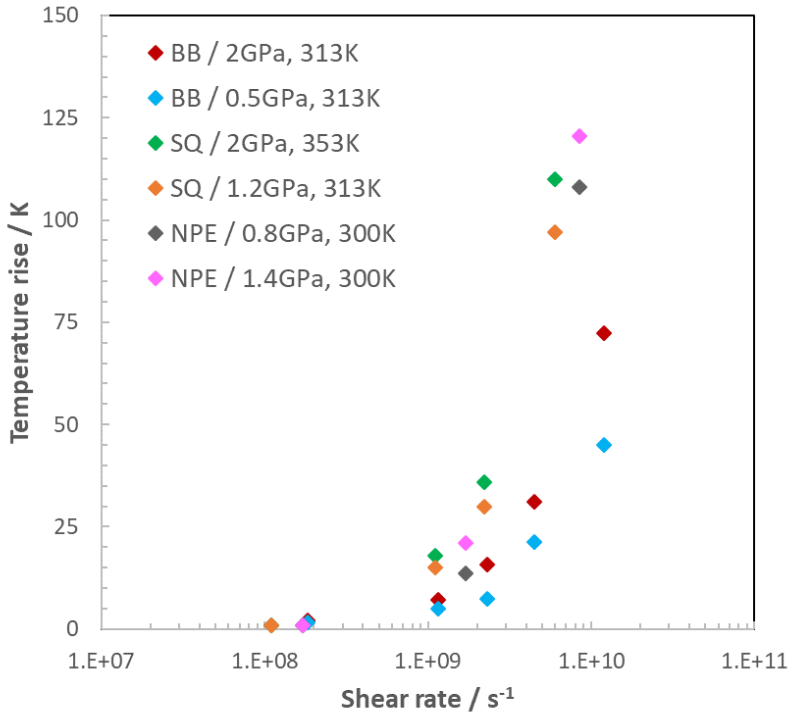

Figure 9. Augmentation de la température à l'intérieur d'un film confiné de BB, SQ et NPE entre deux surfaces rugueuses de α-Fe [100] et dans différentes conditions de pression et de température, correspondant à des conditions thermodynamiques liquides ou solides. Le thermostat Langevin avec un coefficient d'amortissement de 100 fs est utilisé.

Les résultats concernant l'augmentation de la température dans le film de lubrifiant sont présentés dans la Figure 9, où le début de l'échauffement par cisaillement est visible à partir d'un taux de cisaillement critique proche de 10^9 s^{-1}. Cependant, le point de départ de l'échauffement visqueux et sa magnitude semblent dépendre fortement de la nature du fluide.

En effet, les lubrifiants tels que le SQ présentant des structures de type alcane sont généralement plus sensibles à la température que les fluides de type traction tels que le BB. Les températures augmentent d'un facteur deux à quatre fois plus pour le SQ que pour le BB, en fonction des conditions de fonctionnement. Le comportement thermique du fluide NPE ressemble le plus au SQ, même si la composition du fluide est complètement distincte.

v.2. Mobilité moléculaire : le déplacement quadratique moyen

Le comportement en frottement d'un fluide donné, et donc sa réponse à la dissipation thermique, est également étroitement lié au comportement diffusif des molécules formant le fluide [35]. Afin de quantifier le comportement diffusif moyen des molécules de lubrifiant, l'approche classique consiste à définir le déplacement quadratique moyen (MSD) des particules de fluide. Le MSD mesure la distance moyenne au carré parcourue par des particules diffusantes à partir de leur position initiale [12]. Il est exprimé par :

$$MSD = \frac{1}{N}\sum_{i=1}^{N}\langle|r_i(t) - r_i(0)|^2\rangle \quad (4)$$

où N représente le nombre de molécules de fluide dans le système et $|r_i(t) - r_i(0)|$ est la distance parcourue par une molécule i sur un intervalle de temps t. Dans la même expression, $r_i(t)$ représente ainsi la position d'une molécule spécifique i à un instant t et $r_i(0)$ la position de la même molécule au pas de temps initial pris comme temps de référence. $\langle \dots \rangle$ est la moyenne d'ensemble dans l'espace et dans le temps pour l'ensemble des particules du système.

À partir de la définition donnée par la formule (4), il est possible de quantifier une série de régimes dynamiques du fluide, résultant des diverses interactions entre les particules au cours du temps. À très court terme, l'inertie des particules devient importante, ce qui conduit à un régime appelé balistique dominé par l'inertie. Dans ce régime, les molécules, après avoir reçu une impulsion des particules environnantes, se déplacent en lignes droites à vitesse constante avant d'entrer en collision avec les molécules de fluide voisines. Les molécules sont ainsi ralenties et leur mouvement devient aléatoire [49]. Le MSD a ici une dépendance quadratique avec le temps (une pente de deux sur un graphique log-log) [50]. A des temps intermédiaires, un régime de formation de cages suit, caractérisé par un plateau dans le graphique MSD vs temps. Les molécules collisionnent aléatoirement les unes contre les autres et se retrouvent temporairement piégées dans des cages formées par leurs plus proches voisins, ce qui limite leur mobilité et leurs réarrangements. De plus, dans ces circonstances, le fluide se comporte comme un solide. Le mouvement devient ainsi collaboratif jusqu'à ce qu'une énergie suffisante soit acquise pour surmonter les barrières d'énergie associées à l'échappement des cages et diffuser. Le temps caractéristique auquel les molécules commencent à diffuser à des échelles de temps longues est appelé temps de relaxation t_{rel}. Le MSD dans ce dernier régime dynamique montre une reprise avec la diffusion des molécules. Il augmente presque linéairement avec le temps (une pente unitaire sur un graphique log-log), étant directement proportionnel au coefficient de diffusion (la vitesse à laquelle les molécules diffusent) et à la viscosité du fluide [50]. Le fluide se comporte comme un liquide sous ces conditions.

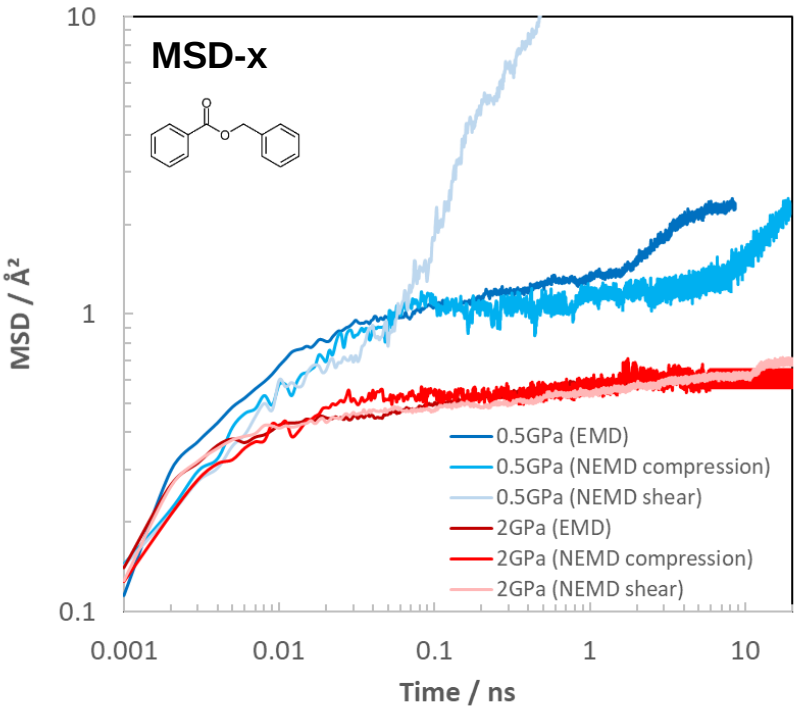

(a)

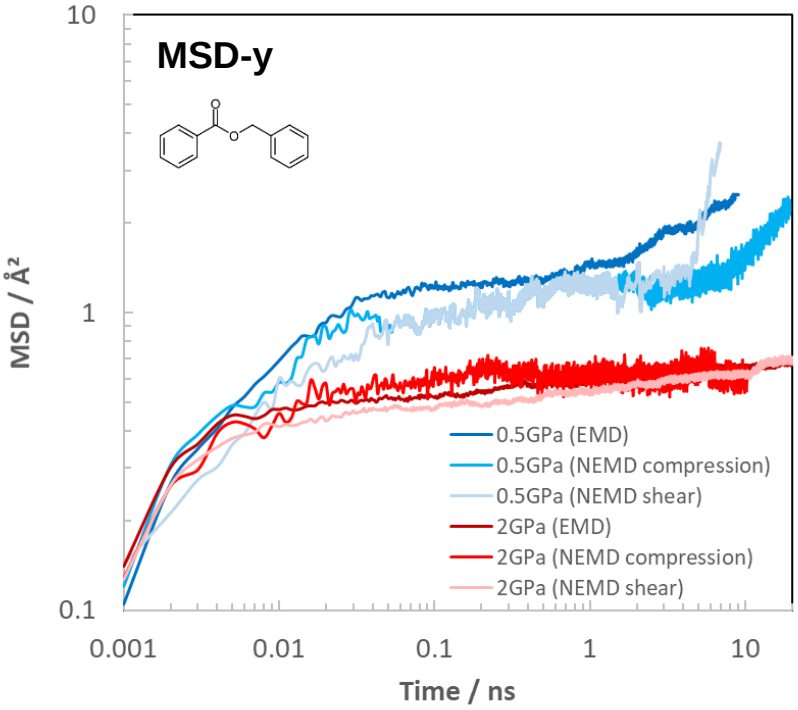

(b)

Figure 10. MSD pour les simulations NEMD en volume et confinées de BB à 313 K à 0,5 GPa et à 2 GPa. Différentes conditions aux limites sont considérées : fluide statique en volume, compression statique sous confinement et cisaillement sous confinement. Dans (a) la composante x du MSD et en (b) la composante y du MSD sont représentées.

Le paramètre MSD pour le BB à 313 K est représenté en fonction du temps sur la Figure 10. Sur cette figure, une pression inférieure (0,5 GPa) et supérieure (2 GPa) à la pression de transition liquide-solide à cette température (0,65 GPa) est considérée, ainsi que différentes conditions aux limites (systèmes statiques en volume, compression statique de molécules de fluide sous confinement, et cisaillement sous confinement). Le MSD est calculé dans les directions x et y.

Les conditions thermodynamiques prises en compte dans l'analyse du MSD (pression, température, confinement et cisaillement) sont toutes interconnectées et influencent la dynamique du fluide, soit en réduisant la mobilité, soit en modifiant la réponse en relaxation du système fluide. Premièrement, pour les systèmes de BB en volume (voir la Figure 10) à 0,5 GPa, le MSD subit les trois régimes dynamiques décrits précédemment, en commençant par le mouvement balistique à des temps bas et en échappant du régime cage vers 1 ns, point auquel les molécules commencent à diffuser à nouveau. Au contraire, si la pression est augmentée à 2 GPa, une fois que le régime de formation de cages est en place, aucune diffusion des molécules n'est réalisée pendant la durée de la simulation. En effet, la pression (comme indiqué à la section iv) détermine l'état physique du lubrifiant, ce qui définit par conséquent les propriétés rhéologiques du fluide. À 313 K et 2 GPa, le système BB en volume devrait présenter des caractéristiques similaires à celles des solides, c'est-à-dire des valeurs de viscosité élevées et des temps de relaxation élevés. De plus, la cohésion des molécules dans le système augmente avec la pression, accompagnée d'un changement radical du mouvement des particules. Cela se traduit par une dynamique ralentie et par la présence d'un plateau dans le graphique MSD vs temps, au cours duquel les molécules expérimentent le régime de cage pendant toute la simulation. Sur cette plage de temps, les molécules de BB n'ont pas le temps suffisant pour répondre aux sollicitations.

Si le fluide est alors confiné entre deux plaques rugueuses parallèles, dans les mêmes conditions de pression et de température qu'auparavant, alors qu'aucun cisaillement n'est appliqué, peu ou pas de variation dans le mouvement des molécules de BB est observée (voir Figure 10) : les valeurs du MSD sont similaires, et les mêmes régimes dynamiques sont présents.

Enfin, le fluide est cisaillé. Pour ce dernier scénario, les systèmes considèrent des surfaces rugueuses en fer et un taux de cisaillement d'environ 10^8 s^{-1}. Cette valeur du taux de cisaillement a été choisie pour la très faible réponse à l'échauffement par cisaillement du BB prévue à la Figure 9. En effectuant des simulations sur la base de ces hypothèses, si un phénomène devait se produire concernant la mobilité moléculaire du lubrifiant confiné, il ne serait que de nature mécanique, la température ne jouant pas un rôle significatif dans la réponse dynamique du fluide. La réponse observée du BB cisaillé dans des conditions nominales solides à 313 K et 2 GPa ressemble à celle de son homologue statique. Néanmoins, à des pressions plus basses, le fluide soumis au cisaillement présente également un comportement similaire au scénario de compression, mais avec un passage presque immédiat du mouvement balistique au mouvement diffusif dans la direction x. Cela est dû à l'énergie ajoutée au système en imposant un cisaillement aux surfaces dans cette direction. Dans la direction y, le temps de relaxation correspond à la valeur trouvée dans le cas en volume et dans le cas de la compression sous confinement. Par conséquent, en imposant du cisaillement, la barrière énergétique est abaissée, c'est-à-dire l'énergie nécessaire pour diffuser les molécules est plus petite. Ainsi, le fluide quitte le régime de formation de cages à

des temps plus bas. Autrement dit, l'énergie ajoutée au fluide implique un échappement beaucoup plus facile des molécules de BB de leurs voisins, ce qui conduit à la diffusion à des temps de relaxation plus courts.

L'influence de l'état physique du fluide sur sa dynamique est cruciale, car pour les hautes pressions, la cohésion élevée empêche la diffusion moléculaire, même si de l'énergie est ajoutée au système par cisaillement. La mobilité est également réduite par rapport aux pressions plus basses. La formation de cages serait ici associée à la réponse ultime en frottement du lubrifiant et se manifesterait macroscopiquement à travers le plateau de la LSS lors d'essais de frottement. Par exemple, pour BB soumis à 313 K et 2 GPa, le temps de relaxation est tellement élevé (plus de 20 ns dans la Figure 10) que, même si la valeur du taux de cisaillement est élevée (ici à 10^8 s^{-1}), la diffusion n'aura pas lieu et la LSS sera toujours présent pour des simulations de DM. De plus, il convient de mentionner l'impact négatif des effets thermiques sur l'étude de la mobilité moléculaire par des simulations DM. En effet, le BB a un taux de cisaillement critique d'environ 10^9 s^{-1} au-dessus lequel la température augmente même à basse pression. Par conséquent, les simulations sont limitées à un petit nombre de valeurs possibles du taux de cisaillement avant que ne se produise un échauffement par cisaillement, ce qui implique qu'une LSS pourrait éventuellement se produire à des taux de cisaillement supérieurs à 10^9 s^{-1} pour le BB à 313 K et 0,5 GPa. Cependant, en raison de l'échauffement par cisaillement du fluide dans le contact, la diffusion serait favorisée et aucune LSS ne serait perçue dans les simulations.

vi. Conclusion générale

Le comportement en frottement de trois fluides (benzoate de benzyle, squalane et une mixture de polyol ester) a été étudié. Initialement, une image complète de l'état physique des trois fluides a été obtenue à l'équilibre avec le développement d'un diagramme de phases pour chaque lubrifiant. Le diagramme a ensuite été utilisé pour déterminer les conditions thermodynamiques menant aux lubrifiants à l'état liquide et solide pour des simulations DM hors équilibre et en confinement. Des conditions aux limites supplémentaires ont été mises en œuvre sur le modèle DM pour tenir compte de différents degrés de rugosité ou de mouillabilité. Les profils d'écoulement sont conditionnés par les conditions de fonctionnement et limites appliquées lors du cisaillement, présentant soit des distributions de vitesse non linéaires (avec des surfaces lisses), soit des profils de vitesse de type Couette (avec des surfaces rugueuses). De plus, le gradient de vitesse développé lors du cisaillement est une conséquence directe des conditions imposées à l'interface solide/liquide, le cisaillement émergeant à l'interface la plus faible (près des parois de confinement ou à l'intérieur du film fluide, en fonction des détails de la simulation). En outre, le régime de frottement plateau s'est naturellement créé lorsque les molécules de fluide ont été soumises à des conditions thermodynamiques solides, et indépendamment des profils de vitesse du lubrifiant pendant le cisaillement.

Le frottement étant directement liée à l'agitation thermique des atomes, un plateau en frottement implique une limite de la capacité des fluides à dissiper de la chaleur. Or, même si cette limite en frottement était obtenue dans des conditions solides, les valeurs de viscosité déduites des distributions de vitesse étaient trop basses pour supposer une mécanique vitreuse (<< 1 Pa.s). En particulier, la réponse dynamique du BB a été étudiée en observant l'influence de la pression sur le déplacement quadratique moyen des molécules de fluide. Le

déplacement quadratique moyen a mis en évidence une dynamique ralentie avec une pression croissante, avec la restriction des degrés de liberté du fluide une fois l'état solide est atteint. En supprimant les degrés de liberté du fluide, les molécules ont tendance à former des cages dynamiques avec les molécules voisines, n'ayant plus la capacité de répondre rapidement aux sollicitations mécaniques. Cependant, même si le régime de formation de cages peut être surmonté en injectant une énergie suffisamment élevée au système par cisaillement, le seuil d'énergie potentielle nécessaire pour briser les cages augmente rapidement avec la pression, d'où l'absence de diffusion même aux vitesses de cisaillement très élevées rencontrées dans les simulations DM. La réponse macroscopique à ce phénomène s'observe donc comme une valeur limite en frottement lorsque le fluide est cisaillé dans des conditions de pression et de taux de cisaillement sévères.

Les résultats présentés dans cette thèse peuvent aider les fabricants industriels à mieux comprendre la réponse au frottement des lubrifiants lorsque des conditions de pression et de taux de cisaillement deviennent sévères. On constate l'universalité du comportement ultime en frottement en tant que propriété inhérente au fluide, apparaissant comme une conséquence de la dynamique ralentie du lubrifiant une fois qu'il subit une transition à un état solide. Par conséquent, le temps de relaxation du fluide confiné augmente considérablement et ne peut donc plus réagir assez rapidement aux contraintes générées dans le contact. Par conséquent, une valeur limite de frottement est atteint : la contrainte de cisaillement limite ou LSS.

Contents

Main abbreviations

BB	**B**enzyl **B**enzoate
EHD	**E**lasto**h**ydro**d**ynamic
EHL	**E**lasto**h**ydrodynamic **L**ubrication
FF	**F**orce **F**ield
LSS	**L**imiting **S**hear **S**tress
MD	**M**olecular **D**ynamics
MSD	**M**ean **S**quared **D**isplacement
NEMD	**N**on **E**quilibrium **M**olecular **D**ynamics
NPE	**N**eopolyol **E**ster
PEC	Mono**p**enta**e**rythritol
SQ	**Sq**ualane

Introduction

Introduction

Context

Friction is a common dissipation mechanism encountered in many lubricated systems such as rolling element bearings or cam-follower systems, where two contacting solids are in relative motion. It is typically expressed as a friction coefficient, representing several phenomena: the lubricant viscosity, the applied pressure, etc. Friction leads to a higher energy consumption in mechanical systems. Hence, by introducing a thin film of lubricant in between the rubbing surfaces, many systems would see their efficiency improve. Consequently, the interest in the lubricant market is to develop lubricant formulations that provide low friction and wear, avoiding the direct contact between the solid surfaces. Lubricant viscosity has a significant impact on the ability of a lubricant to reduce friction and wear too. For car engine oils, for example, the difference between the optimized low-friction oil and the standard oil can be as high as 5% [51].

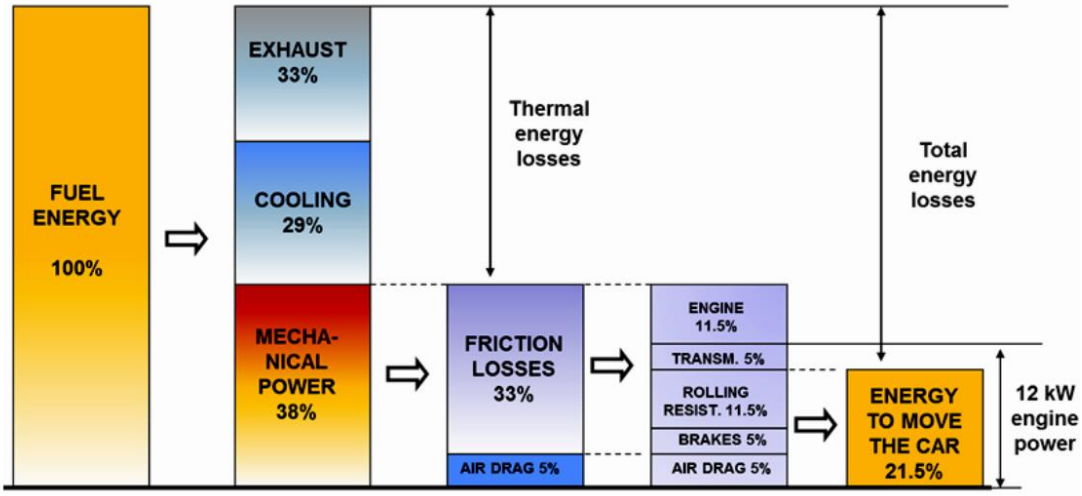

Figure 1. Distribution of the energy consumption of passenger cars, as analyzed by Holmberg et al. [52].

In recent studies, Holmberg et al. [52] showed that about one third of the total fuel energy is used to overcome friction in passenger cars (see Figure 1). Indeed, the direct losses due to friction, excluding those that come from braking, make up to 28% of the fuel energy. Conversely, only 21.5% of the total energy consumption is spent to move the car. It is thus evident how big of an impact friction losses have in the energy efficiency of passenger cars. At present, significant efforts are put together to reduce global energy losses, not only because of economic reasons but also because of the environmental impact they have on the greenhouse effect. Friction losses in cars could be reduced by about 18% within the upcoming 5 to 10 years by adapting more friction control technologies, a feat that would represent annual fuel savings of around 117,000 million liters. Within 15 to 25 years, however, 61% of the total

energy losses due to friction could be reduced, representing an overwhelming 385,000 million liters per year [53]. Consequently, CO_2 emissions in passenger cars would be decreased by 290 million tons per year in the upcoming years, and by 960 million tons per year in the long run. This would allow to consolidate the objective the European Union (EU) has set for 2020 to limit the carbon dioxide emissions in cars to less than 95 $gCO_2.km^{-1}$ [54].

Motivation

The fast progress of lubrication technology and all the recent worries about the environmental impact have led bearing manufacturers to introduce in the market gradual and substantial improvements to their products. In 2015, the global rolling element bearing market was valued at USD 81.6 billion, and is expected to significantly grow in the upcoming years (see Figure 2), mainly due to the increasing demand of the heavy machine industry.

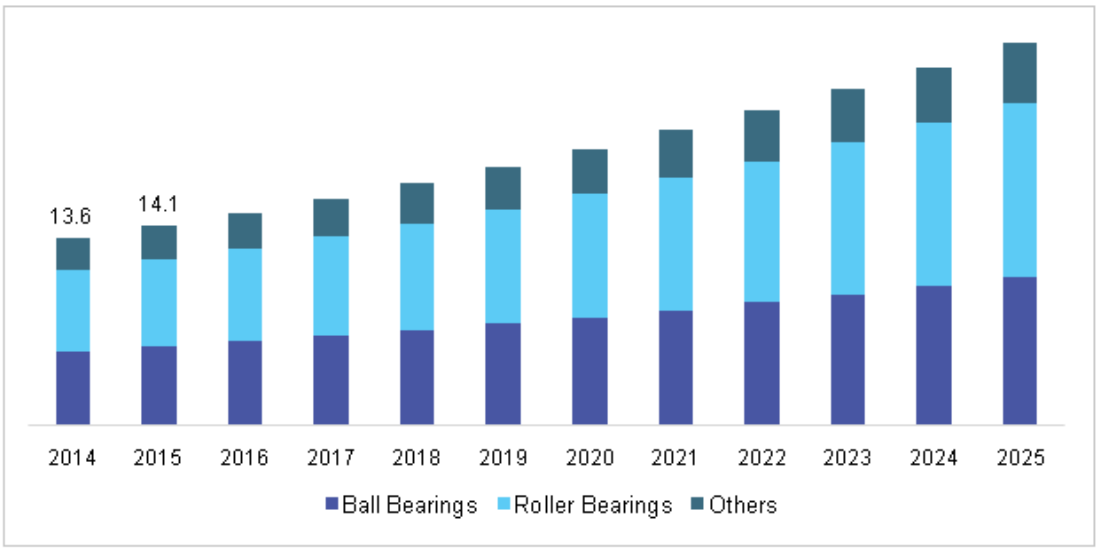

Figure 2. U.S. rolling element bearings market by product, from 2014 to 2025 (expected), in USD Billion [55].

With mechanical systems supporting progressively heavier charges, friction in such systems have a big impact in the global performance of industrial systems. Hence the increasing worry of bearing manufacturers to reduce friction energy losses to, first and foremost, improve their efficiency, but also to reduce the associated operating costs. In fact, the potential of energy savings that could be accomplished by this is significant due to the wide range of applications rolling element bearings are used for. In addition, the CO_2 gas emissions would be reduced. However, in order to do so, updated and reliable models to predict friction losses in lubricated mechanical systems are needed.

Friction constitutes one of the principal performance indicators in roller bearings. Much of the current efforts are put to reduce it, as the life expectancy, the performance and the maintenance of these elements are all impacted by the degree of friction and wear in the contact. Thus, the presence of a thin lubricant film is necessary. However, the latter also

transforms the contact problem into a multiphysical problem with multiple agents and phenomena that need to be accounted for, and for which current physical models are incomplete.

Objectives

The objective of this work is thus to improve the prediction of friction in lubricated contacts, such as those found in rolling element bearings, when operating in the most extreme scenario i.e. when they are exposed to severe conditions of pressure and shear. There is still some open debate regarding the different phenomena occurring in a lubricated contact when operating under these severe conditions, hence the need to develop local models for the prediction of friction and the rheology of lubricants. At present, various models allow the prediction of classic regimes but, as of now, no predictive model of the ultimate behavior of lubricants exists. Consequently, the approach chosen for this work focuses on atomistic simulations to determine the friction and flow response of fluids at the molecular scale under elastohydrodynamic lubricated conditions.

Outline

The present work consists of a total of five chapters.

Chapter I presents an introduction to the basic concepts needed in order to understand the following chapters. First, a brief historical review of the main advances and challenges in the field of Tribology are shown, with special interest in elastohydrodynamic lubricated contacts. These kinds of contacts are present in various industrial applications, such as roller bearings, gears, or cam-follower systems. In particular, attention will be put at the limiting behavior of friction when the lubricants are submitted to severe conditions of pressure and shear rate, introducing the current hypotheses behind its apparition as well as the challenges its investigation poses.

The ultimate behavior of lubricants is then studied at the atomic scale with Molecular Dynamics simulations. The method is detailed in **Chapter II**, where the advantages of using this tool are detailed. In order to understand flow and friction behavior at the molecular scale, two models are introduced: the fluid bulk system (equilibrium simulations) and the fluid molecules confined and sheared between two solid walls (non-equilibrium simulations). At the end of the chapter, the main computed quantities of interest are described.

In **Chapter III**, the molecular models for three test fluids are introduced, two of which representing model lubricants, and the third one with direct application in the aerospace industry. The models of the three fluids are first validated for density and viscosity, then their respective phase diagrams are established. These phase diagrams, identifying the different physical states of the fluids, will be subsequently used in the following chapters.

Data from previous experiments of confined fluids have shown that the ultimate behavior of lubricants in industrial contacts appears when the conditions are such that the fluid undergoes thermodynamic conditions leading to a solid state. In **Chapter IV** this hypothesis

will be further investigated with a direct comparison between experimental and numerical results from non-equilibrium Molecular Dynamics simulations. The molecular model is bound to illustrate a representative classic steel-steel lubricated contact, where different solid/liquid interface conditions are established in order to assess the dynamics of the confined fluid. The validity of the results is also analyzed with regards to the size of the system.

To complete the analysis, a possible structuration and orientation of the fluid molecules is studied in **Chapter V**. Additionally, thermal dissipation and molecular mobility are analyzed in this chapter. Here, possible thermal effects are studied as potential mechanisms behind the saturation of friction. On the other hand, the molecular mobility is directly related with the viscosity and the diffusion of fluid molecules. Finally, an underlying physical mechanism behind the ultimate response of lubricants is proposed, providing the opportunity to better design lubricated systems for applications that require severe operating conditions.

Chapter I

State of the art

Chapter I
State of the art

Tribology is the science of friction, wear, and lubrication between two contacting bodies in relative motion. Since the beginning of human existence, tribology has played a key role in every-day life: water, animal fat or sand were used as a primitive way to lubricate; stones or pieces of wood were rubbed together to generate fire by friction [56]. Since then, the number of applications including friction has increased exponentially with the development of civilizations and their technologies. In the present day, tribology is studied in order to reduce the impact of friction and thus optimize the performance of mechanical systems where two elements are rubbing against each other.

Interest in tribology appeared during the Renaissance (circa the XV century) with Leonardo Da Vinci. Da Vinci [56] conducted quantitative experiments to elucidate how two contacting bodies behaved under dry friction. It was him who introduced the notion of coefficient of friction, which is calculated as the ratio between the tangential force resisting relative motion of the two solid bodies sliding against each other and the applied normal load holding these two bodies in contact. He corroborated the independence of friction with the apparent area of contact. His work was later rediscovered and confirmed by Amontons [57] in the XVII century. Coulomb, better known for his work on electrostatic forces, completed the theory of friction by testing the influence of the surface roughness and demonstrating that, generally, the solid-to-solid coefficient of friction is invariant with the sliding velocity [58]. Even though tribology was not yet considered as a separate science, there were sporadic attempts to better understand the nature of a contact [56].

Lubrication gained significance at the start of the XIX century with the beginning of the first industrial revolution, which came alongside the development of new transportation means and the rise of the energy and manufacturing industries. Important studies concerning tribology started during this era because the central question was to optimize the performance of machinery. In 1847, preliminary experimental studies by Hirn [56] introduced a lubricant between two solid moving bodies to study friction. Remarkably, Hirn highlighted a significant variation of the coefficient of friction with the sliding speed for lubricated contacts. Around the same time, Tower, with the support of the results presented by Hirn, demonstrated that the two solid bodies in a hydrodynamic bearing were completely separated by a film of lubricant [59], and that it was this thin layer of oil that exclusively controlled the friction forces generated in the contact.

Later in 1886, a milestone occurred in the field of lubrication. Reynolds, by simplifying the Navier-Stokes equations [60], developed his eponymous equation [61], which is even today the starting point for all modern lubrication theories. The Reynolds equation describes viscous laminar flow of incompressible Newtonian fluids in a contact and allows relating the body kinematics and the geometry of the contact to the build-up of pressure in the lubricant film, which results in a hydrodynamic lift, as represented in Figure I.1. This phenomenon is critical in the understanding of the formation of the lubricant film, avoiding direct contact between surface asperities, reducing friction and, finally, preventing wear.

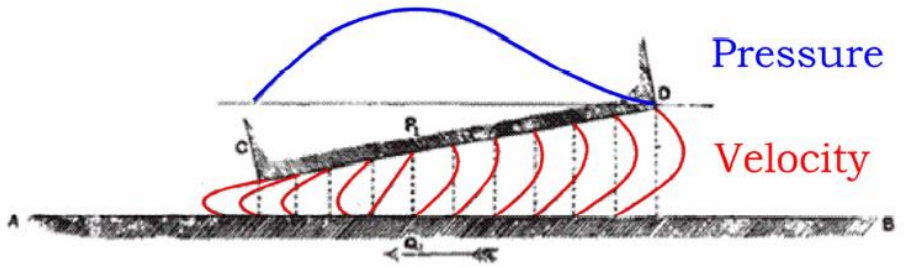

Figure I.1. Velocity and pressure fields in a thrust pad, resulting from the moving surfaces and the geometry of the surfaces. Results from Reynolds [61].

I.1. Lubrication regimes

Stribeck, in 1902, proposed a diagram to describe friction with respect to the sliding velocity, the lubricant viscosity, and the applied load, which is related to the lubricant film thickness [62]. The diagram, as shown in Figure I.2, qualitatively differentiates three lubrication regimes, which accounts for the various scenarios that may be encountered during lubricated friction.

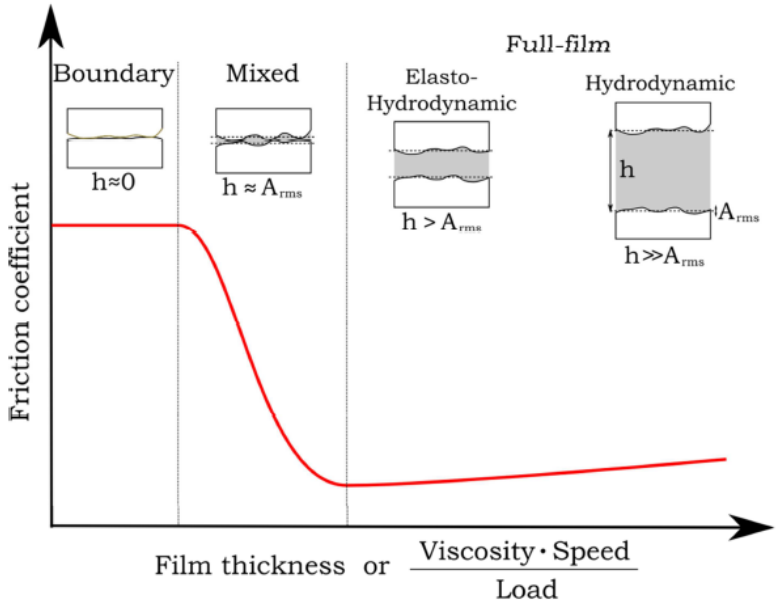

Figure I.2. Stribeck curve, showing the direct qualitative dependence of friction with the film thickness or the operating conditions of the lubricated contact. In the same diagram, a relation is drawn between the oil film thickness, the root mean square roughness amplitude of the contacting bodies, and the lubrication regime.

Three regimes of lubrication can thus be identified, which are generally represented in the Stribeck diagram (Figure I.2): boundary lubrication, mixed lubrication, and full-film lubrication. At low sliding speeds, low viscosity values, and/or high loads, a boundary regime takes place: the direct contact between solids governs friction. Friction, as suggested by Coulomb, is independent from the sliding velocity. However, higher speeds, viscosities and/or

lower loadings lead some of the lubricant to be dragged in between the sliding surfaces. A partial fluid film is therefore generated, entering a new regime called mixed lubrication regime. In this case, the film thickness is increased, reaching the size of the asperities of the surfaces. The thicker the film becomes, the more the friction is reduced until it reaches a minimum. This minimum corresponds to the point where the film thickness is higher than the amplitude of the roughness asperities. The load is then entirely supported by hydrodynamic lift accessing to a full-film lubrication regime. From this regime forward, friction only experiences a slight increase with the entrainment speed. There is no direct contact between both sliding surfaces, and wear becomes negligible. It is thus evident that this regime is desired for most lubricated mechanisms, allowing the maximum performance with minimum energy losses.

The full-film lubrication regime can also be subdivided into two independent lubrication regimes depending on the configuration of the contact geometry. On one hand, for surfaces of conforming bodies (like those present in journal bearings, see Figure I.3.a), local pressures are small (pressures are of the range of 0.1 to 10 MPa) so that no significant deformations on the contacting bodies result. The lubrication is then called hydrodynamic (HD) and the friction increases linearly with the sliding speed in the case of Newtonian fluids. On the other hand, contrary to HD lubrication, non-conforming surfaces (see Figure I.3.b) do present high local pressures (from 500 MPa to 5 GPa) that induce important deformation on the confinement surfaces in the contact [63]. This impacts the nature of the fluid, modifying its viscosity and its density due to high pressure, as well as inducing an increase of the temperature in the contact [64, 65, 66, 67]. Consequently, the fluid flow in the contact is altered [68, 69, 70, 71, 72], and so does friction [73, 74, 75]. The lubrication regime is then defined as elastohydrodynamic (EHD). The multiple contributions and alterations of the nature of the fluids makes it necessary to develop and apply multiphysical methods for its study [75, 74, 76, 77, 78]. Many lubricated industrial systems operate in the EHD regime, so that it becomes essential to understand the underlying process of lubrication in order to better predict and control the dynamics and the global performance of the mechanism.

(a) **(b)**

Figure I.3. Schematic representation of the geometries of: (a) a conformal contact in a journal bearing, and (b) a non-conforming contact in a roller bearing [79].

The lubrication regime undergone by a lubricated contact is usually determined by the film thickness ratio R_h, defined as:

$$R_h = \frac{h}{A_{rms}} \tag{I.1}$$

where h is the central film thickness of ideally smooth surfaces and A_{rms} the root mean square roughness (RMS) or standard deviation of the roughness profiles [80]. In spite of the different existing criteria, it is well established that full-film lubrication occurs when R_h > 3 [81, 82, 83], which corresponds to the case where 99.3% of roughness asperities of the solid bodies are not in contact between each other. On another note, surfaces employed for tribological contacts present roughness of the order of a tenth of a micrometer or less after running in. Based on equation (I.1) and on the criterion for full-film lubrication, this leads to lubricant films operating in the EHD regime to present thicknesses at least three times larger than roughness.

I.2. Ultimate behavior of confined fluids

Industrial mechanical systems such as rolling element bearings are generally designed to function under EHD conditions, and thus in the full-film lubrication regime. The mixed and the boundary regimes, with higher levels of wear and friction, are only found in particular situations of startup and stopping, or in abnormal cases rapidly leading to the failure of the system. In this section, friction is investigated in the elastohydrodynamic lubrication (EHL) regime.

I.2.1. Friction regimes in EHL

Lubricated contacts operating in the EHL regime are characterized by elevated normal loads distributed over a small area of the contact. Pressures typically reach values ranging between 1 and 3 GPa which involve, amongst other, the deformation of the contacting solid surfaces and a significant increase of the fluid viscosity [84]. In combination with the imposed entrainment velocity during shearing, a thin oil film of around a tenth of a micron is generated. In the early days, pioneering research was focused on ensuring full-film lubrication [70, 68, 85, 64] in order to prevent fatal failure and damage of mechanical components, a topic that is still avidly researched nowadays [9, 86].

Although accurate models for film thickness prediction [1] exist, the theory fails to quantitatively predict experimental measurements of friction in highly loaded contacts (EHL) [87, 88, 89]. This is primarily due to a lack of understanding of the lubricant behavior in the contact, where the physical properties of the lubricant are very susceptible to vary with temperature and pressure [2]. Indeed, a purely Newtonian behavior of the fluid tends to overestimate friction at medium to high sliding velocities. In reality, friction experiences three to four stages as a function of the sliding velocity, at constant pressure and film thickness.

At low sliding speeds, the lubricant behavior can be considered as Newtonian, where the shear stress (and thus friction) evolves almost linearly with the shearing rate, in relationship with the following expression:

$$\tau = \eta \cdot \dot{\gamma} \tag{I.2}$$

where τ is the shear stress, $\dot{\gamma}$ the shear rate and η the viscosity at low shear rates. The linear dependence between stress and rate continues until the shear stress reaches a critical value τ_c, usually associated to the Eyring stress τ_E [89], above which the apparent lubricant viscosity

decreases (see Figure I.4). Indeed, the lubricant abandons the linear regime and enters the so-called shear-thinning regime.

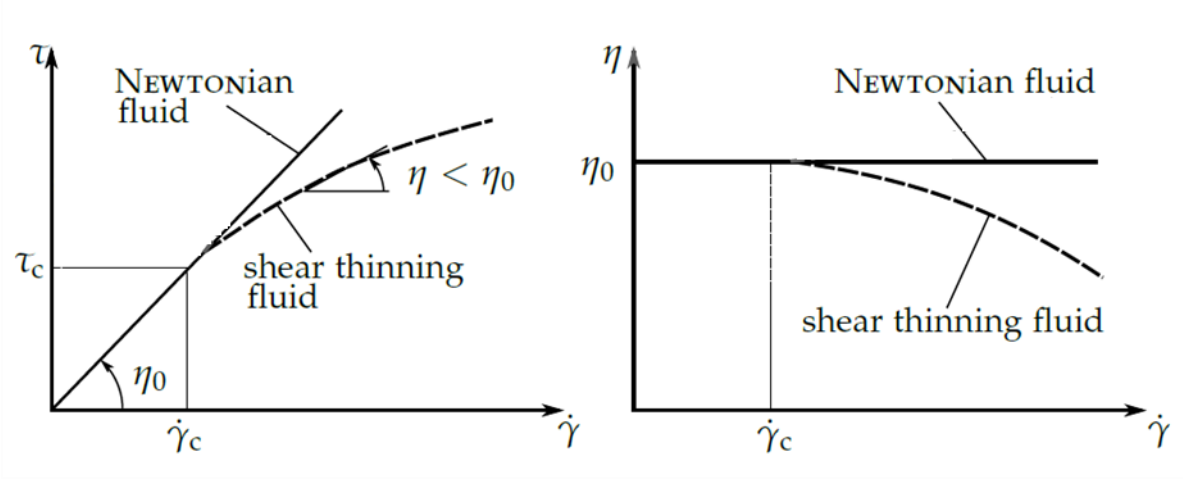

Figure I.4. Evolution of the shear stress (left) and the dynamic viscosity (right) at constant pressure and temperature with the applied shear rate. A Newtonian fluid presents a constant viscosity, which translates into a constant slope in the shear stress-shear rate plot. Adapted from [90].

Shear-thinning is generally attributed to an alignment of the fluid molecules during shearing, which makes it to be dependent on the shear rate and, more generally, on the internal organization of the lubricant. This leads to a decrease in viscosity [3, 91]. Thus, viscosity depends on pressure, temperature, and shear rate:

$$\eta = \eta(\dot{\gamma}, P, T) \tag{I.3}$$

At the onset of shear-thinning (at τ_c in Figure I.4), the dimensionless Weissenberg number Wi reaches unity [3, 91]. The Weissenberg number describes the relationship between the elastic and the viscous forces in the contact and is given by:

$$Wi = \lambda \cdot \dot{\gamma} \tag{I.4}$$

In this equation, λ accounts for the relaxation time, a characteristic time needed for a liquid molecule to realign through Brownian motion and reach a state of thermodynamic equilibrium. If Wi is superior to unity, the fluid molecules do not have time to realign and the fluid enters the shear-thinning regime, leading to a decrease of the fluid viscosity. For Wi values lower than unity, the relaxation time is sufficient to ensure molecular realignment and thus viscosity remains constant. The behavior in the latter case is therefore Newtonian.

Some authors have attributed shear-thinning to thermal effects [92]. However, although viscous heating may lead to a drop in friction, isothermal shear-thinning has been observed and measured in viscometers [93]. Nonetheless, temperature in the contact needs to be controlled efficiently in order to avoid ambiguous data where some phenomena could be falsely attributed to other sources.

When the applied load is sufficiently high, and for high shear rates, the shear stress reaches a maximum value: the limiting shear stress τ_{lim} (LSS). In this plateau-like regime, the shear stress does not increase anymore with the shear rate, in other words, stress becomes rate-independent, as seen in Figure I.5. It was actually Smith [4], circa 1960 who proposed a maximum value of friction attainable for a lubricant, which he explained would appear once a critical shear stress value was reached, leading to a plastic solid-like flow behavior. He later completed his explanation by implying that the entrainment velocity would be accommodated in a molecularly thin shear plane within the lubricant film thickness, surrounded by some solidified layers of the lubricant moving at the imposed sliding speed of the solid surfaces [5]. Beyond the onset of LSS, however, the fluid is susceptible to thermal effects that would otherwise decrease the lubricant viscosity and, consequently the limiting value of the shear stress.

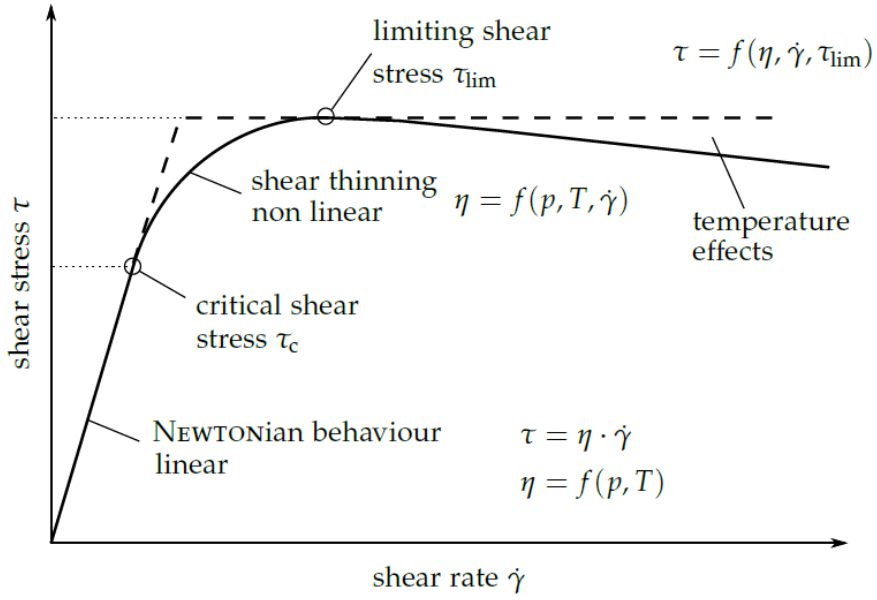

Figure I.5. Model for lubricated friction described by Bair [3], where the shear stress is plotted against the shear rate. The ultimate behavior of a lubricant appears with a maximum shear stress τ_{lim}.

Some explanations on the friction behavior of lubricants have been given based on their rheological characteristics [94, 95]. For instance, Dyson [95] divided the friction curve into three regimes: an isothermal regime where the Newtonian behavior of the lubricant would dominate and where the shear stress depends linearly with the shear rate, followed by a non-linear regime characterized by non-Newtonian shear-thinning behavior, and finally a thermal regime where thermal effects would predominate in the contact. The effective viscosity is here determined in the isothermal region as the slope of the plot at the origin. On another note, Plint [96] discussed that the limiting shear stress value is reached at high shear rates if the lubricant flows like a plastic solid. Understanding this plateau behavior becomes crucial as it represents the maximum level of friction a mechanism is able to transmit in an EHD contact and, according

to Bair and Winer [9], corresponds to the main characteristic to be evaluated when choosing an oil.

Many phenomenological approaches have been proposed in literature to describe both the LSS phenomenon and the lubricant behavior under typical EHD conditions [6, 7, 8]. Models now give a full picture of the lubricant characteristics over a wide range of pressures and temperatures, short transit times and high shear rates. Nevertheless, however precise the empirical models may be, no rheometric device allows reaching the severe conditions of the high-pressure region of the contact. Indeed, twin-disc machines and high-pressure devices suffer from several technical limitations. They are restricted to low shear rates and shear stresses [9, 3], which sometimes are far away from the real EHD conditions. In addition to this, empirical models are still incomplete and need to give better predictions at severe conditions of pressure and shear rate. Furthermore, there are still pending questions around the physical mechanisms behind the LSS phenomenon, as well as on the influence of pressure and temperature [3].

I.2.2. Hypothetical scenarios of LSS

In the following section, a review of the main hypotheses responsible for the apparition of LSS is presented. Namely, the solid-to-liquid phase transition of the lubricant, slip at the solid/liquid interface, shear localization, or plug flow will be discussed.

I.2.2.1. Lubricant phase change

Despite the many experimental and numerical studies carried out, it is still unclear as to the exact state of lubricants when they are submitted to very high pressures and very high shear rates. Some authors, like Alsaad et al. [97] have supported the idea that lubricants are near a glassy state when EHD conditions apply. Defining a glass transition, however, is troublesome, as this transition would depend not only on thermodynamic but also on kinetic aspects. Today, it is generally accepted to be the point from which the molecular structure present in a fluid starts to behave as a solid due to the slowed-down Brownian motion. The glassy-state transition modifies the lubricant properties, dependent on both thermodynamic conditions (pressure and temperature) as well as on the oil kinetics (how the fluid undergoes the transition). Moreover, even when in the liquid state, the lubricant can be affected by the glass transition dynamics, as suggested by the WLF viscosity model [98], where either a critical pressure or a critical temperature explicitly appear in the formulation. Therefore, even if the viscosity is investigated at low pressures in rheological studies, the glass transition could still have an impact that cannot be neglected in the case of EHD contacts. It can also have an important effect on the predicted film thickness.

The notion of “glassy” or “solid-like” state must be treated with caution when discussing the phenomena under EHD conditions. Indeed, under this regime of lubrication, the lubricant microstructure is typically amorphous. On the contrary, many Molecular Dynamics studies have come to opposite conclusions, reporting some degree of crystallization at high pressures and under static conditions. It should be noted, nonetheless, that crystallization is here promoted by the low fluid complexity, by the structuration of the fluid close to the solid/liquid interface and by the initial configuration of the fluid molecules [99, 100, 101, 102]. This is not

the case for EHD contacts, where the fluid complexity and short transit times lead to amorphous microstructures [6].

Recently, measurements of the velocity profiles under pure rolling conditions in an EHD contact have been performed by the image-based fluorescence recovery after photobleaching (FRAP) technique [103]. They found out that the resulting velocity profile diverged with respect the predictions of the Reynolds equation, relating the phenomenon to a possible transition to a solid state at elevated pressures. Other authors, like Johnson et al. [104], link this solid-like behavior to the contact mechanics [105]. In particular, they measured the fluid viscosity of the commercial oil Turbo33 for different pressures, low sliding speeds and isothermal conditions [104], and noticed that above 10^3 Pa.s the slope of the viscosity with respect to pressure presented a marked change in trend, indicating a clear change in the lubricant properties. These critical pressures were in good agreement with the glass transition pressures of the Turbo33 oil under the specific conditions tested when compared to dilatometry measurements [97]. This behavior was also later confirmed for other fluids [94]. Indeed, above a critical pressure, the fluid no longer behaves like a viscoelastic material but rather like an elastoplastic material [106].

Barlow et al. [107] later on demonstrated that this elastoplastic behavior could also be attained by soliciting a fluid in such a way that the soliciting period is inferior to the Maxwell relaxation time of the fluid i.e. the fluid has not enough time to respond to the generated shear stresses and hence freezes. The solid-like state, however, appears to be a necessary condition for LSS appearance, but not sufficient. Indeed, Briscoe and Tabor [108] attempted to map the EHD contact under different conditions of pressures and shear rates. They suggested that, when lubricants are sheared at high shear rate values when they display a glassy state, they would experience fracture. This phenomenon has not yet been confirmed by experiments.

I.2.2.2. Wall slip

The no-slip boundary condition has always been widely accepted in fluid mechanics and specifically for bearing design and similar systems. However, its validity is questionable, as recent experiments have shown that indeed slippage can be reproduced under specific operating conditions [109, 110]. It has even been validated by Molecular Dynamics simulations [111]. Schnell [112], for instance, experimentally observed wall-slip of water sliding over a hydrophobic surface. His experiments have been the precursor for later observations, demonstrating that this phenomenon is not only restrained to simple fluids [112, 113], but also extends to complex fluids like polymers [114] and to different types of surfaces [115]. Slippage can occur within the fluid film [116] or at the solid/liquid boundary when the interfacial critical shear stress is smaller than the limiting shear stress of the confined oil [117, 116]. The preferred experimental techniques for boundary slip observation include the fluorescence recovery after photobleaching [113], the use of the surface force apparatus (SFA) [118], and the atomic force microscope [109].

Li and co-workers [117] stated that the slip length evolves in a non-linear way with increasing shear rate and increases exponentially with the presence of pressure. Wong et al. [119] studied a polybutene oil (PB1300) in contact with a SiO_2-coated glass disc and a steel ball under different conditions. They captured the impact dimple by observing various

interferograms of the contact area, as can be appreciated from Figure I.6. They concluded that the displacement of the dimple only depended on the movement of the glass disc. In addition, when the velocity of the ball was below 75 μm/s, the dimple velocity was constant and equal to roughly the average velocity of the disc. Above this threshold value, the velocity of the dimple increased with increasing ball velocities. Wong et al. [119] attributed this phenomenon to slip at the lubricant/steel and lubricant/disc boundaries. When performing the same tests with 5P4E at a maximum pressure of 1.33 GPa and at room temperature, the dimple appeared not to move, which was assumed to be due to the transition of the lubricant to a glassy state [120, 121].

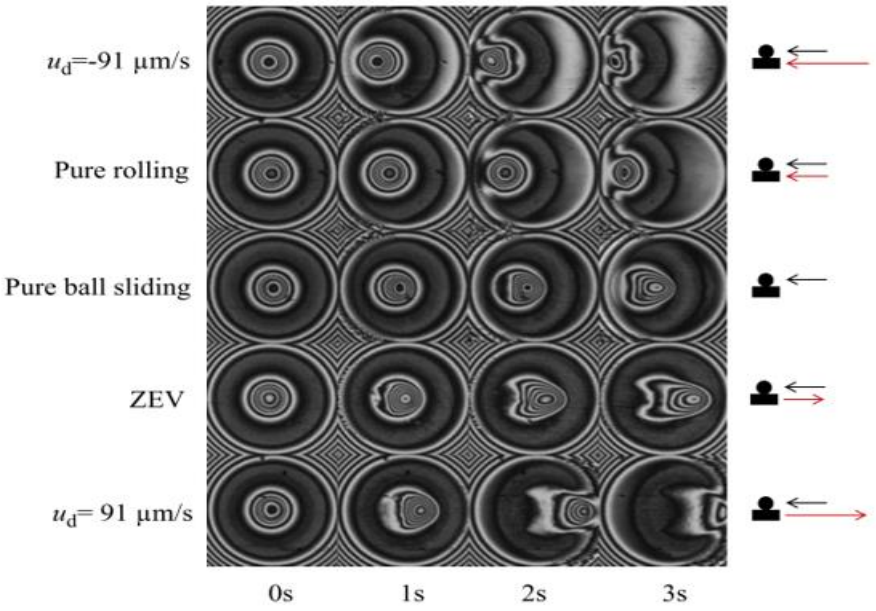

Figure I.6. Interferograms showing the displacement of the impact dimple at different configurations for constant ball velocity during the first 4 s of the test. Reproduction from Wong et al. [119]. On the left side are listed the particular test conditions, on the right side the black and red arrows represent the direction and the magnitude of velocity of the solid bodies.

Kaneta et al. [122], by later measuring the lubricant under pure rolling conditions, found out that the oil exhibited a solid-like behavior. For very thin oil films, slip occurred close to or at the surface, where the slip velocity was found to be equal to one half of the entrainment velocity. As for the slip length, it was expected to be of the same order of magnitude as the molecular size [114], which was later confirmed through Molecular Dynamics simulations by Thompson and co-workers [111]. Finally, Pit et al. [113] observed slip of hexadecane in contact with sapphire discs using the total internal reflection-fluorescence recovery after photobleaching (TIR-FRAP) technique. They concluded wall-slip to be the originator of the limiting behavior of friction. Nevertheless, slippage has never been directly observed under EHD conditions because of the very short transit times, the thin lubricant film thickness, and the motion of the confining bodies.

I.2.2.3. Shear localization

In order to explain friction behavior of lubricants in a highly loaded contact, Evans and Johnson [30] suggested a mechanism by which the non-linear shear-thinning regime is attributed to Eyring's thermal activation model [123] and the ultimate behavior of friction to the formation of shear bands across the oil film, the same way bands are formed during the deformation of solid polymers [124]. Under certain conditions, viscous heat can be generated in the contact, leading to temperature gradients across the film thickness and shear softening of the lubricant oil. The lubricant properties are strongly impacted by temperature, specially the viscosity, so that eventually the shear stress may not distribute homogeneously through the confined fluid, becoming thus localized. Two types of shear localization have been identified [125]: isothermal (mechanical), and thermal shear localization.

On the one hand, for the case of isothermal localization, shear bands originate within the lubricant film when exposed to pressures close to the glass transition pressure, when subjected to high shear stresses and low shear rates, avoiding this way significant temperature gradients in the contact. On the other hand, thermal shear localization was also predicted and observed by Bair and co-workers [93] due to viscous shear heating. Plint [96] also suggested LSS being originated from thermally softened regions within the fluid, leading to shear localization. Bair et al. [126] used a high-pressure cell to capture the flow mechanisms of different fluids. In particular, they found formation of multiple mechanical shear bands for 5P4E, MCS1218 and LVI260 when exposed to certain conditions of pressure, temperature and shear rate. The shear bands presented different inclinations, as can be seen in Figure I.7. In the case of 5P4E, bands had an angle between 19 and 20 degrees with respect to the solid surface, while the angle was 23 degrees for MCS1218 and comprised between 16 and 19 degrees for LVI260. In all, the inclination of shear bands appears to be a material-based property and directly related to the pressure-limiting stress coefficient.

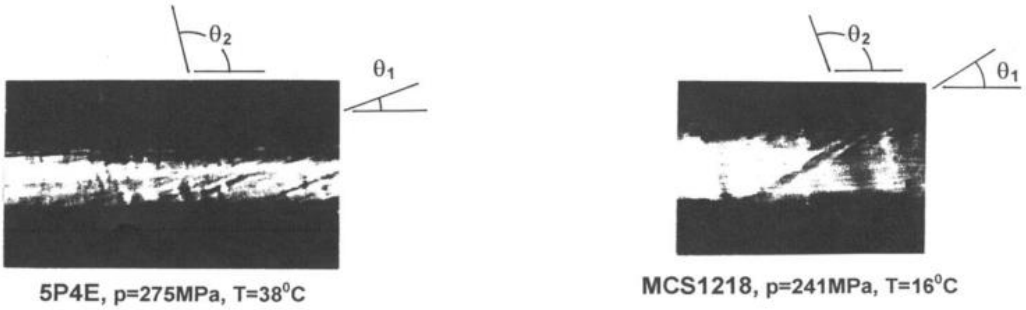

Figure I.7. Observations of mechanical shear bands in confined 5P4E and MC1218, performed by Bair et al. [93].

Shear bands only emerge once the fluid has reached the non-linear regime. Indeed, Bair et al. [93] observed the formation of the first band at the onset of shear-thinning. Beyond this limit, the number of shear bands multiplies with increasing shear rate until the whole contact is filled. Thus, the limiting behavior of the lubricant would appear to be an aggregate effect of these mechanical shear bands in the area of contact. This would result in two types

of shear bands: shear bands that are aligned to the direction of flow, and shear bands that are aligned with the cross-film direction.

Bair et al. [126] since then concluded that shear bands emerge when the pressure developed within the bulk lubricant film is close to the glass transition pressure, something that has been predicted by the Mohr-Coulomb slip model [126]. Nevertheless, shear bands have still to be observed in a living EHD contact.

I.2.2.4. Plug flow

With respect to the dynamics of lubricants under the operating conditions of an EHD contact, flow behavior is still an open question. It was Jacobson [127] who first theorized about the idea of the lubricant not behaving completely as a fluid under EHD conditions, suggesting that only a thin layer of oil near the contacting solid surfaces is actually sheared while the rest of the lubricant remains in a solid-like state creating a core or a plug. This core of the lubricant would be extremely viscous at either a liquid or a glassy state. Figure I.8 presents a schematic representation of how flow would look like when this mechanism is active. Various techniques have been proposed since then in order to visualize flow behavior.

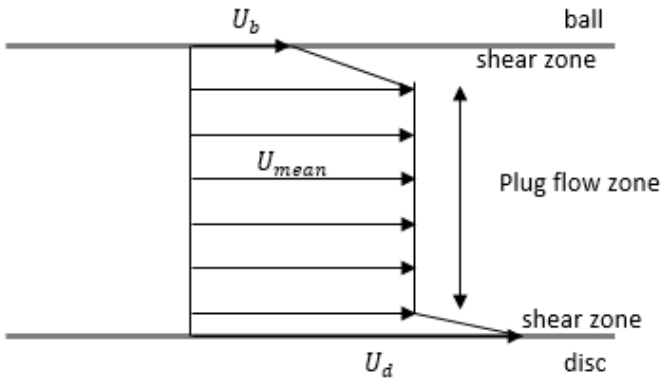

Figure I.8. Schematic representation of a plug flow profile in a ball-to-disc contact. Reproduction from Šperka [128].

Šperka and co-workers [128], for example, used the particle tracking velocimetry (PTV) technique with a mineral oil mixed with graphite nano-particles as their tracking particles. The advantage of this method resides in the small size of these nano-particles, which do not affect lubricant flow and thus allows measuring the velocity profile in the contact under sliding conditions. Indeed, when the particles enter the contact, they do so with different velocities. However, after a certain time, their velocity becomes uniform and equal to about the mean velocity of the lubricant. This phenomenon has been attributed to the plug flow mechanism and could explain the LSS. Around the same time, Ponjavic and co-workers [129] used photo bleached-fluorescence imaging velocimetry to visualize the shearing flow of polybutene in contact with a sphere and a flat surface. They found that below a critical pressure, the velocity profile was nearly linear. However, once this pressure was surpassed, the lubricant could

behave like a plug. This critical pressure was found out to be dependent on the molecular weight of the oil.

Finally, plug flow presents itself as an interesting scenario allowing to make a link between the different mechanisms explaining the limiting shear stress. For instance, plug flow can be considered a particular case of shear localization, where the core of the lubricant film is supposed to be glassy and shear is localized in very thin layers close to the confining solid surfaces. Brought to the extreme, if the thickness of the sheared region becomes infinitely small, then the wall-slip scenario would be considered.

I.3. Numerical investigation methods at the molecular scale

In this section, a series of numerical tools to study the EHD regime at the molecular scale are presented. Special attention is given to the Molecular Dynamics simulation method.

The exponential growth and the parallel progress of computational performance to experimental tools has opened the possibility to a fast development of numerical tools for the study of lubrication at the molecular scale. They allow investigating problems that otherwise experiments alone cannot probe. At the nanoscale, fluids are best described by a set of elementary and discrete elements: the atoms. Generally, classic simulations consist of some millions of atoms extending in space over a wide range of units that go from some Angstroms to up to some tens of nanometers. With regards to the time scale, these simulations are bound to operate from a few picoseconds to a fraction of a microsecond. Thus, atomistic simulations provide a glimpse of the state, phenomena and mechanisms acting at the nanoscale in either a steady or in an ultra-fast transient state. In this subsection, a listing of the most used atomistic methods is presented in the scope of the present project.

Modelling of materials at the atomic scale is typically approached by two methods: Monte-Carlo (MC) simulations, and Molecular Dynamics (MD) simulations. MC is a stochastic method specifically designed to determine the equilibrium properties and the atomic configuration of a molecular system in a defined thermodynamic ensemble [130, 131]. The atomic positions at each time step are randomly assigned and are only kept if specific conditions based on their energy states are verified. Thus, in MC simulations, the potential energy is computed at each step, but not the time. This has a direct impact on the performance of this approach as there is theoretically no limit on how to model the different material properties with quasi-infinite characteristic times. Hence, only a few time steps are typically needed to reach the equilibrium state, making it possible to simulate for very large systems of particles. This makes MC simulations the preferred method to analyze structuration and arrangement of particles over time and space. However, non-equilibrium behavior cannot be studied with this approach because time is not considered explicitly. In addition to this, the kinetic Monte Carlo (kMC) method [132], derived from the MC method, allows to address kinetics of slow processes, but needs to know the energy barriers beforehand. Consequently, Molecular Dynamics simulations are preferred to the study of fluids at the molecular scale, allowing to compute time-dependent material properties. This can be done by either considering all the atoms of the system with an All-Atom (AA) formulation, or by simplifying the molecular model by grouping atoms into “pseudo-atoms”. This is known as a United-Atoms (UA) formulation [133].

Molecular Dynamics is a deterministic computational method [12] by which Newton's equations of motion governing each one of the system's atoms are explicitly solved, calculating this way the trajectories of the particles over time. For each time step, the forces acting on each particle can be computed through the force field (FF), describing the different particle interactions. A subsequent integration of the accelerations provides the atomic positions for the following steps. Because time is computed explicitly, the duration of a simulation is usually restricted to a few tens of a nanosecond. It is also possible to explore non-equilibrium phenomena (such as structuration, velocity and temperature distributions, segregation of molecules, etc.) on this range of time. Additional physical quantities can be derived like the viscosity, the thermal and the electrical conductivity, friction or even the total energy of the atomic system. The potential and computational aspects of MD will be further explored in the following Chapter II of this work. Among the different existing computational methods, MD simulations is one of the preferred techniques to study and analyze friction and flow behavior of confined lubricants. From these simulations, shear can be supplied to the system either directly on the fluid or by transferring momentum from the sliding solid surfaces to the confined fluid, providing valuable information not easily accessible through experimentation. In the following sections, a brief review of some of the main aspects of bulk and confined MD simulations is given.

I.3.1. Bulk MD simulations

MD simulations of fluids have experienced an important development over the last decades. Initially focused on simple Lennard-Jones (LJ) fluids [46, 32], the recent advancements have allowed the leap to short-chain n-alkanes using united-atoms (UA) formulations [22], and most recently lubricant-sized molecules with more complex models [134, 10]. Bulk simulations of fluids give extensive insights into the behavior of parameters such as the density or the viscosity over a vast range of pressure, temperature, or even shear rate values.

The first nonequilibrium bulk simulations of lubricant-sized fluid molecules were performed in the early 1990s by Morriss et al. [135]. They used a UA model of n-eicosane (C_{20}) with a repulsive Weeks-Chandler-Andersen (WCA) potential [136], obtaining acceptable viscosities at low shear rate. However, they predicted an unphysical shear-thickening behavior at high rates, probably associated to the simplified potential. Khare et al. [137] tested additional linear n-alkanes (C_{16}, C_{22}, and C_{28}), as well as branched molecules (5,12-dipropylhexadecane) using an OPLS-UA force field. They qualitatively measured the Newtonian viscosity plateau, with deviations of about 45% with respect to experimentation, and concluded that the addition of branches to the molecules enhances the viscosity by a few orders of magnitude. Furthermore, Moore et al. [138] and McCabe et al. [139, 140] also encountered lower Newtonian viscosities by 40-60% with respect to experiments for bulk C_{30} isomers, and for bulk 9-cotylheptadecane respectively, submitted to different pressure and temperature conditions. However, despite the large deviation of viscosity simulation values with experiments, the pressure-viscosity coefficient for the latter case was within 4% with experiments.

Later in 1998, Cui et al. [141] studied the fluid properties of linear n-alkanes (C_{10}, C_{16}, C_{24}) and branched n-alkanes (squalane, 10-n-hexylnonadecane) using a UA potential developed by Siepmann et al. [142]. At low shear rates, the Newtonian viscosity plateau value

could be directly compared with Green-Kubo [143, 144] simulation results, while for higher shear rates, a shear-thinning behavior was observed over a wide range of rate values. It was found that the continuous decrease of viscosity with shear rate, at constant pressure and temperature, was closely related to the ordering of the fluid molecules.

More recently, Bair and co-workers [37, 145] compared experimental and bulk nonequilibrium simulations of a UA model [142] of squalane submitted to pressure and temperature conditions typically found in the EHL regime, comprising both the Newtonian as well as the shear-thinning regimes. The data, despite being separated by several orders of magnitude in shear rate, perfectly collapsed into a single master curve under the assumption of the time-temperature superposition. Jadhao and Robbins [11], using a similar MD model of squalane, performed a series of simulations to study the influence of viscosity with pressure, temperature, and shear rate. The simulation results were extrapolated using the Eyring model [123] and extended down to shear rates of the order of 10^5 s^{-1} to directly compare with the Newtonian plateau, giving a good accordance with experiments.

I.3.2. Confined MD simulations

Additional information of the fluid can be gained by studying its response when it is confined between two solid plates and submitted to EHL conditions. The observed behavior then differs with respect to that of the bulk fluid. Thus, the continuum approximations no longer hold i.e. the Navier-Stokes hydrodynamics [146], and new laws are needed to describe the dynamics of the fluid. In the following subsections, a series of phenomena susceptible to appear in nonequilibrium simulations of confined fluid films are presented.

I.3.2.1. Viscosity, structuration, and phase transition of the confined fluid

The first simulations of fluids confined between two parallel walls were performed by Bitsanis et al. [147] around 1987 by using the method developed by Ashurst and Hoover [148], and by using a 10-4 LJ potential for the confining solid walls. Through the simulations, they developed the local average density model (LADM), by which the fluid, divided into a set of successive layers, had a density (and thus a local viscosity) assigned to each one of these layers. The LADM model fairly predicted the flow behavior of simple confined fluids, but drastically failed to predict other properties, such as the viscosity, under stronger confinement [149]. Typically, the resistance of a fluid to flow is expressed by the shear viscosity. For bulk molecular systems, this parameter depends only on the nature of the fluid and on the operational conditions (the applied load, the temperature, and the shear rate). However, for fluid systems confined between two solid plates, additional parameters need to be considered (the fluid film thickness and the physico-chemical properties of the solid/fluid interface amongst others).

The fluid film thickness significantly influences the dynamic behavior of the confined system by inducing particular structures, which depend on the level of confinement. For example, when using atomically smooth surfaces, fluid films thicker than approximately ten molecular layers display a structureless region at the center of the film, with the appearance of strong density peaks close to the solid/fluid boundary. These first densely packed layers can reach density values several times higher than those encountered for the bulk, and can extend

to a distance from the solid surfaces up to ten molecular diameters if the operating conditions are favorable [150]. While this first density peaks are located at the point where the solid/liquid interactions (coming from both the Van der Waals and Coulomb forces) are equilibrated [151, 150], the intensity of these density peaks lose power the farther from the solid walls. For thick enough lubricant films, the fluid becomes isotropic and classical fluid dynamics models can again be applied for the prediction of bulk properties. This phenomenon was first observed through Monte Carlo simulations of simple LJ fluids [152, 153]. Later in 1981, Horn and Israelachvili [100] used a surface force apparatus to conduct experiments on octamethylcyclotetrasiloxane (OMCTS) confined between two smooth silica surfaces. They found that the measured force between the two surfaces did not evolve smoothly with distance, as opposed to the predictions by the Van der Waals theory, but rather they oscillated between attractive and repulsive forces with a periodicity that was close to the molecular diameter of the fluid. The phenomenon was baptized as solvation force.

The degree in which layering appears depends upon many factors, mainly on the size and form of the molecules, as well as on the degree of smoothness of the surface. For instance, Horn and co-workers [100] found out experimentally that the size of the fluid molecules influences the layers density and width. Thompson and co-workers [154], on the other hand, carried out Molecular Dynamics simulations of simple LJ fluids identifying a relation between the surface topography and the geometry of the molecule. Additionally, they observed that at high pressure values, crystallization was favored when the surface structure and the fluid can interpenetrate, a condition that is often encountered when the solid density reaches values close to the fluid one and the solid/fluid interactions are strong. Various additional numerical works have shown that the presence of nanometer scale roughness can frustrate the structuration of fluid molecules into layers [41, 133, 42, 155, 156, 154, 157] and the glass transition [133, 42, 155]. However, high shear rates [149, 154, 158, 159, 147] and the temperature [100] have no significant impact on the formation of dense layers of lubricant molecules. In the regions where structuration is more accused, layering can locally change the mobility of the lubricant molecules and modify the classical isotropic interactions inside the fluid. Hence, viscosity amongst other transport properties can vary upon layering [160, 161].

When the film thickness is reduced, both experiments and simulations have proven that the effective viscosity of simple LJ fluids [149, 159], linear n-alkanes [155, 162], and some organic compounds [163] start to experience a strong increase. When the film thickness is further reduced to just about five to six molecular layers, the viscosity brutally increases by several orders of magnitude [155, 162, 163]. An explanation can be given on the basis of the results obtained for the LJ fluids, where the whole fluid crystallizes. However, the molecular complexity of the linear n-alkanes makes them less inclined to go through crystallization but rather to undergo a second order glass transition [164] or the formation of “crystal bridges” [155], which have been attributed as the main reason for the experimented rise of the fluid viscosity. Recently, new MD simulations of fluid cyclohexane and n-decane [165] suggest first order phase transitions into crystalline structures, supporting the sudden change from liquid-like to solid-like structures with stronger confinements recorded during experiments. Pressure can have a similar effect for thicker films [164].

In MD simulations of confined fluids, the induced transitions from a liquid-like state to a solid-like state greatly depend on the molecular shape of the fluid molecules and on the structure of the confining walls. Thus, branched or long flexible molecules tend to remain in a

liquid state under more severe conditions of pressure and confinement than small rigid molecules [166]. Atomically rough confining surfaces, on the other hand, frustrate the ordering of molecules into layers as opposed to smooth surfaces, so that under these circumstances a transition to a solid-like state is prevented [42, 167].

I.3.2.2. Boundary slip

In confined environments, fluid flow can be influenced by slip at the solid/liquid interface. Wall-slip typically occurs when the cohesion of the bulk fluid is relatively stronger than the adhesion to the solid walls [137]. Hence, the solids are not capable of transferring enough momentum to the fluid in order to completely shear it [24]. There are several parameters that are accounted for promoting slip at the solid/fluid interface. For instance, the use of atomically-smooth surfaces in NEMD simulations greatly increases the chances of wall-slip [24, 168, 169, 170]. In addition, slip increases with increasing pressures and sliding velocities [24, 168, 169], as well as for longer and branched molecules. Bulkier and inflexible molecules that can conform to the solid confining surfaces can display significant slip close to or at the solid/fluid interface too [171]. On the contrary, molecular slip decreases with increasing film thicknesses and solid/fluid interaction strength, i.e. wettability [168, 169]. It can even be eliminated by adding atomic-scale roughness to the confining surfaces [42]. The latter is of notorious importance, as surfaces used for experimentation contain fractal roughness down to the atomic scale [79], which frustrate slip and thus validate the extended no-slip boundary condition of the Reynolds equation. Early in 2017, a large-scale NEMD simulation of a 430 nm thick film of n-hexane confined between two atomically-smooth iron surfaces and submitted to EHL conditions (a normal load of 1 GPa, a temperature of 350 K, and a shear rate of about 10^5 s^{-1}) was performed [172]. No slip was encountered for this system under the tested conditions.

Nevertheless, wall-slip has indeed been observed in experiments. For instance, boundary slip was detected for n-hexadecane on oleophobic smooth surfaces, and for polybutadiene on glass surfaces with oleophobic coatings, leading in each case to a reduction of the fluid film thickness and friction [113]. However, at present, boundary slip has not yet been observed experimentally for realistic lubricants in contact with conventional surfaces and submitted to EHL conditions [173].

I.3.2.3. Temperature and pressure control

High shear rates can lead to important viscous shear heating in fluid systems. This excess heat needs to be removed from the system with a thermostat in order to reach a steady state. In particular, for bulk fluid systems, the thermostat is applied to all the atoms of the system. There are several thermostating algorithms (rescaling of atomic velocities, addition of a random force and a friction force, coupling of atoms to an external heat bath, etc.), which will be further discussed in Chapter V, but the most extended method for this kind of systems is the Nosé-Hoover (NH) thermostat [174].

In the case of confined fluid systems, there is a larger collection of thermostats and techniques to control temperature [175]. Indeed, the thermostat is typically applied to some or

all of the atoms conforming the solid confining surface, allowing for a temperature gradient to form across the film thickness, the same way as in experiments [32]. Moreover, direct thermostating has been concluded to generate unphysical phenomena [176]. For the confined scenario, the Langevin thermostat [31] is more popular than the NH algorithm, evacuating viscous shear heat more effectively [35]. Nevertheless, alternative thermostas (virtual atoms) can be envisaged depending on the particularities of the system [35].

Pressure in bulk fluid systems is generally controlled by the Nosé-Hoover barostat [174]. On the contrary, for confined fluid systems, pressure can be controlled following one of two methods: either a fixed separation between the two confining walls is set, or a constant normal load is applied to either one or the two confining walls [177]. In fact, the latter technique is desired for confined systems as fixing a specific film thickness can lead to unphysical phenomena [177]. Lastly, in the case of uncompressible systems, a damping term in the barostat may be needed in order to avoid excessive oscillations of the friction force [177].

I.3.2.4. Friction transitions

In the last decades, simulations of confined LJ fluids submitted to EHL conditions have evidenced the appearance of nonequilibrium phases at high shear rates, suggesting that the generation of linear flow profiles assumed for EHL friction may no longer be supported [46, 45, 47]. Nonlinearities can emerge in two forms, either by presenting sheared regions localized in the central region of the film while close to the walls the fluid remains in a solid-like state or, inversely, the sheared region is found close to the solid walls and the solid-like region is in the center of the film thickness. Ewen et al. [10] evidenced the appearance of nonequilibrium flow phases for 2,3-dimethyl-2-[(3-methylbicyclo[2.2.1]hept-2-yl)methyl]bicycle[2.2.1]heptane (DM2H) and for 2-methyl-2,4-dicycloheylpentane (DCMP), two traction-like fluids, when they were submitted to EHD conditions under confinement between two atomically smooth iron oxide surfaces. The LJ parameter ε for the Fe atoms in the surface was artificially increased in order to avoid wall-slip. However, for squalane and for diethylhexyl sebacate, which have an alkane-like structure, and for similar pressure, temperature, and shear rate conditions, a Couette velocity profile was generated, with the presence of locking close to the confining walls for the higher pressures and the lower speeds. They linked the divergence from the pure Couette velocity profile in the traction-like fluids to the friction plateau regime. At present, shear localization has been observed during some experiments of polybutadiene, polyphenyl ether, and of mineral oils [93, 178], but not yet on more realistic lubricants at high pressures and shear rates.

I.3.3. Nanoscale study of lubrication: pending questions

The following pages of this work will further explore one particular phenomenon found in confined lubricants exposed to high confinement pressures and severe shear rates. This phenomenon is known as the limiting shear stress.

All the previously described scenarios for LSS appearance attempt to give an explanation about the physical origins that lie behind the phenomenon. However, no direct

measurements of friction have been carried out at the same time as said scenarios where present. Interesting work has been achieved with regards to the ultimate behavior of lubricants, be it experimentally or numerically, trying to elucidate the influence of pressure, temperature and rate of deformation on the lubricant characteristics. Since the last two decades, the interest to go beyond the already existing empirical models in order to improve the understanding of the EHD contact has encouraged the use of computational methods. Among the different tools available, Molecular Dynamics simulations appears to be the most practical one, allowing to access phenomena and parameters that experiments are not capable to capture at the present time. Additionally, the control of pressure and temperature is an important asset that cannot be experimentally achieved.

Multiple Molecular Dynamics studies of nano-confined fluids submitted to high pressures and high shear rates have been published. Initially, simple Lennard-Jones fluids [47, 46, 45, 99, 179, 180] where analyzed, but recent studies have considered more complex and realistic molecules [10, 41, 134, 181]. It is noteworthy to remark the latest attempts to map out the friction behavior of confined oils under EHD conditions. Indeed, Heyes et al. [46] first developed a non-equilibrium phase diagram for monoatomic argon where different friction regimes were qualitatively identified and plotted with respect the normal load and the shearing velocity. Later, Gattinoni et al. [45] and Mackowiack et al. [47] refined the diagram considering different types of surfaces with more or less wettability, as well as the influence of temperature. Martinie et al. [173] redefined the map in terms of shear rate and attempted to elucidate the physical origin of LSS by plotting in the same diagram multiple experimental test conditions from literature with the observed shearing behavior (see Figure I.9).

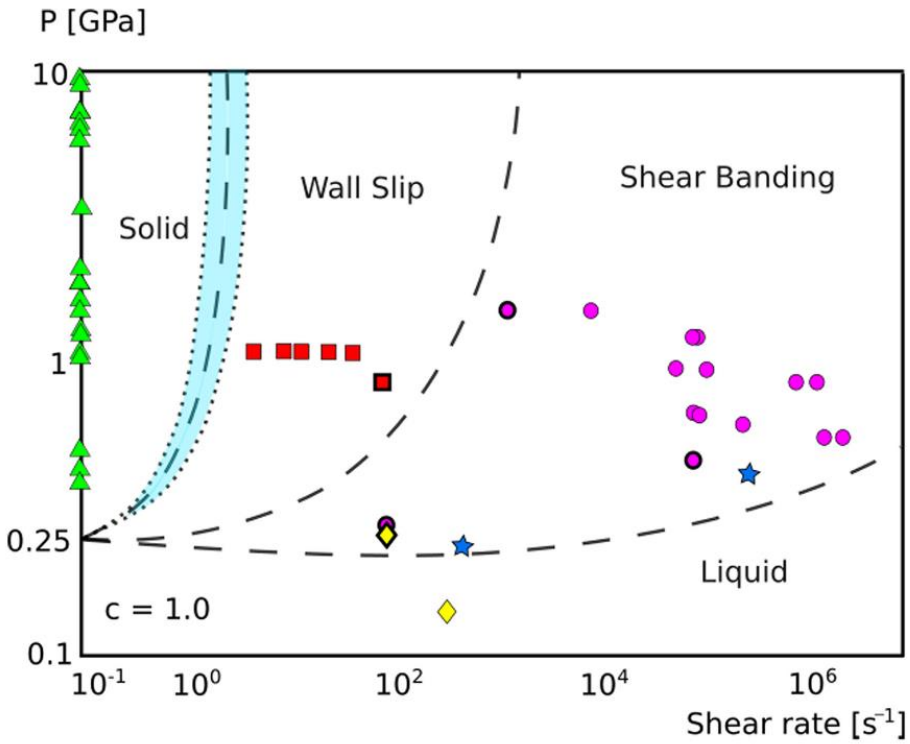

Figure I.9. Experimental phase diagram of the behavior of an ideal confined fluid, with direct comparison of both experimental and simulation data [173]. Bold symbols represent conditions where LSS has been captured experimentally.

The diagram in Figure I.9 gives an overview of the possible mechanisms that can be encountered in a highly loaded and highly sheared lubricant. It first identifies a critical pressure below which the lubricant can be found in a liquid state. Above this critical pressure, the behavior becomes more complex and depends on the shearing rate. Indeed, low rates give rise to a solid-like behavior, which can manifest as a crystal or just a glassy phase. Here, parameters like the fluid complexity or the initial configuration of the fluid, which accounts for the history of the lubricant, have a strong impact on the overall dynamics. For intermediate pressures, slip starts to appear at the solid/liquid boundaries or within the film. In the first case, observations of an intermittent stick-slip motion at the boundary with the confining solid have been made. Nevertheless, as the shear rate increases viscous heating impacts the fluid behavior, creating softened regions close to the solid boundary or even molten layers within the lubricant film. In the first case wall-slip appears, while in the latter different configurations of banding can develop depending on the coexisting regions of crystal and liquid. Butler and Harrowell [99], for instance, confirmed that the nonequilibrum coexistence of phases was determined by the nonlinear response of the crystal/liquid interface under shear. Therefore, the fluid endures a transition from a complete glassy state under static or low shearing conditions to a state where the fluid separates into one or multiple shear bands and unsheared layers [179]. In all, after comparison with experimental data, Martinie et al. [173] concluded shear bands to be behind the LSS behavior.

A last remark is to be made with respect to Molecular Dynamics simulations. Indeed, while they give precise insights into the fluid behavior under different operational conditions, they still need to be quantitatively compared to experimental data, a task that is hardly accomplished due to the different spatial and time scales. However, substantial progress is being made in this field, now being able to get quantitative and qualitative similar results [10, 11]. On another note, several assumptions are constantly being made in simulation, either with respect to the fluid or to the confining walls. Indeed, only a small nano-patch can be recreated which is bound to represent the whole pressurized region of the contact with all the respective thermal and mechanical phenomena. In spite of all the limitations, atomistic simulations can give a better understanding of the underlying phenomena in thin film lubrication, especially under conditions that are extremely difficult to replicate and access through experiments.

Understanding the intrinsic relation between the wetting strength and the interfacial friction would allow to have a better prediction of the rheological mechanisms in a tribological contact. Slip was also found to increase with increasing shear rate, but a better prediction of how it evolves would allow increasing the performance of the response of the contact. Finally, the temperature has been seen to have a direct impact on the nanorheology and the appearance of chemical reactions.

Chapter II

Molecular Dynamics simulations

Chapter II
Molecular Dynamics simulations

The previous Chapter highlighted the recent advancements made in the Tribology community in the search for the mechanisms that lie behind the limiting shear stress or LSS, a phenomenon that appears when a confined fluid is subjected to severe conditions of load and shear rate. Some insights were given as to why and how present studies of the elastohydrodynamic contact can benefit from numerical simulation methods and, specifically, how they can enlighten the path towards the understanding of the LSS phenomenon. In this Chapter, the panorama of multiscale simulations is presented, and special attention is given to Molecular Dynamics simulations, the method that will be employed in the following chapters of this Thesis. Following the basic theory behind MD simulations and after reviewing the main concepts related to force fields, the Chapter will conclude by introducing the MD models of lubricated systems for both the bulk fluids and the fluids confined between surfaces, and the basic outputs that can be analyzed.

II.1. Model theory

II.1.1. Numerical context

Computational modeling is gaining progressively more importance with time along the increased power and capabilities of computers. Engineering and scientific problems in general can now be thoroughly studied numerically, either at the atomic-scale or at the continuum, overall avoiding the limitations inherent to experimentation. The range of scales at which nano-lubricated films can be studied is wide, hence the different types of simulation methods available. Nevertheless, every scale has some constraints associated that need to be overcome during the modeling process of the problem. Figure II.1 briefly depicts some simulation methods for different time and length scales.

On the one end of Figure II.1, at long time and length scales, macroscopic continuum methods (finite element analysis, finite differences analysis or computational fluid dynamics) make use of conservative equations coupled with constitutive equations. However, the validity of these approaches is subjected to the material properties being constant across the volume occupied by the elements, which is the usual case for most engineering applications. There are some other limitations that need to be accounted for. For instance, macroscopic models tend to be oversimplified models based on empirical studies, making the models only valid under very specific conditions. Additionally, transport coefficients need to be implemented into the model.

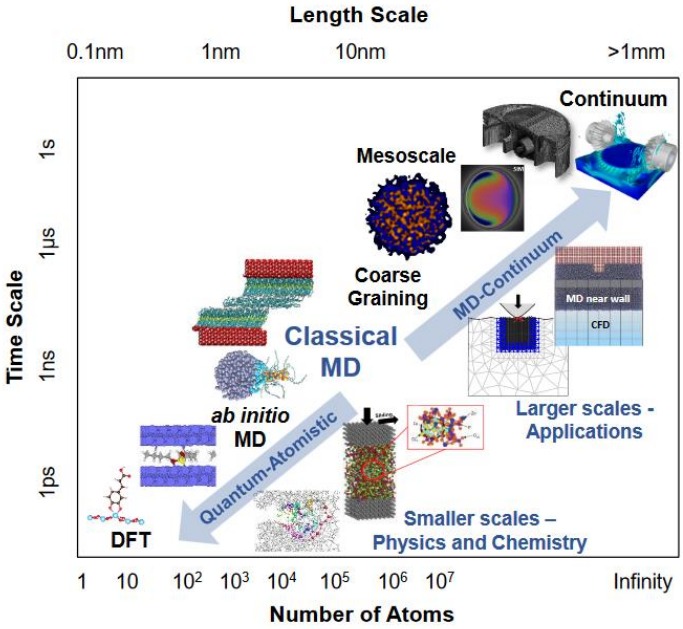

Figure II.1. Simulation through the different scales, from first principle simulations (quantum) to continuum simulations [182].

All these drawbacks can be avoided by using smaller scales in simulation, such as Molecular Dynamics simulations. The MD method originates from the late 1950's by Alder and Wainwright, who introduced a new method to solve Newton's equations of motion on a system composed primarily by particles designed as hard spheres. Originally conceived for the study of phase transitions and interfacial behavior of simple molecular systems, it is now applied to more complex and intricate problems from various domains, ranging from physics [12, 183, 143, 164], chemistry [184, 185, 186] and biology [187, 188, 189, 190] to systems where molecular scale effects play a key role [20, 29, 25]. The power of MD simulations resides in the fact that new sets of parameters of structural, chemical and dynamic nature can be calculated, which are not accessible on larger scale simulations (at the mesoscale with coarse graining techniques, or with continuum models, for example). In the field of Tribology in particular, MD simulations constitute a powerful approach allowing, amongst other, to have a full picture of the mechanisms that take place in highly confined liquid films, otherwise very difficult to attain experimentally [173].

MD results need, however, to be validated with experimental data, a task that is not always accomplished. Indeed, the problem originates from the fact that both experiments and simulation operate in different time and length regimes: MD simulations only consider lubricant film thicknesses of some nanometers (the equivalent of a few molecular layers) sheared for only a few nanoseconds, leading to deformation rates several orders of magnitude higher than those found in experiments [22]. Moreover, only a small nano-patch of a few nm^2 can be simulated at constant pressure and temperature conditions. This, eventually, differs from a real elastohydrodyamic lubricated contact, where temperature and pressure act in gradients. Nevertheless, simulations at the atomic scale are considered to be a value tool for the analysis of nano-confined fluids, not only allowing to control temperature and pressure independently [35], but also capturing phenomena like phase transitions [181, 164].

II.1.2. Basic principles of Molecular Dynamics

Molecular Dynamics is an explicit method that allows calculating directly the evolution of a system of interacting particles through time by the resolution of Newton's equations of motion [12]. For a given time t, the position r_i of every particle i is well known. A potential energy V can consequently be defined as a function of the interatomic distances as well as of the different interactions described by force fields. It accounts for the interaction between a single particle and its neighbors. The force f_i acting on each one of the system's particles is computed as the gradient of the total potential energy [12] as follows:

$$f_i = -\nabla_{r_i} V \tag{II.1}$$

Eventually, the acceleration $\ddot{r}_i$ of particle i can also be computed from Newton's second law of motion once the force acting on that particle is known. The parameter m_i represents the atomic mass.

$$\ddot{r}_i = \frac{f_i}{m_i} \tag{II.2}$$

Generally, the Verlet algorithm [12] is used to compute the new position of the particle at the updated time $t + \delta t$ through a double integration, δt being the time step length. In order to do so, the trajectory of the particles has to be known at the time $t - \delta t$.

$$r_i(t + \delta t) = 2r_i(t) - r_i(t - \delta t) + \delta t^2 \ddot{r}_i(t) \tag{II.3}$$

This algorithm has an easy implementation and is reversible in time. It does not even require any velocity as input. Eventually, the choice of the value of the time step will determine the accuracy of the integration. If the velocity value wants to be evaluated, it is then determined through finite differences:

$$\dot{r}_i(t) = \frac{r_i(t + \delta t) - r_i(t - \delta t)}{2\delta t} \tag{II.4}$$

However, expression (II.3) has an error or the order of δt^4 associated, while the error in (II.4) is of the order of δt^2 [12, 22]. Consequently, the time step δt is critical to ensure the stability of the solution and the conservation of the total energy of the system [12, 22]. Additionally, the Verlet algorithm as presented in (II.3) makes the supposition that the position of atoms and their respective forces do not vary significantly with every successive time step. Consequently, the typical value for time steps used is or the order of the femtosecond (10^{-15} s), which is several orders of magnitude below the time scale for which thermal agitation occurs (10^{-12} s). Thus, the conservation of the total energy of the molecular system is ensured [12].

A set of new algorithms has been developed with the objective of minimizing the errors related to (II.3) and (II.4) while searching to improve the overall stability of the final solution. These are, for example, the leapfrog algorithm or a modified version of the standard Verlet algorithm, best known as the velocity-Verlet algorithm. In particular, this integration method

requires first for the acceleration to be evaluated at a time t with equation (II.2) in order to calculate the new atomic trajectories for the next successive times.

$$r_i(t+\delta t) = r_i(t) + \dot{r}_i(t)\delta t + \frac{1}{2}\delta t^2 \ddot{r}_i(t) \quad \text{(II.5)}$$

From the new position, the velocity at $t+\delta t$ can then be computed by applying the following equation:

$$\dot{r}_i(t+\delta t) = \dot{r}_i(t) + \frac{1}{2}[\ddot{r}_i(t) + \ddot{r}_i(t+\delta t)]\delta t \quad \text{(II.6)}$$

Figure II.2 schematically represents the steps followed during a time step of a simulation.

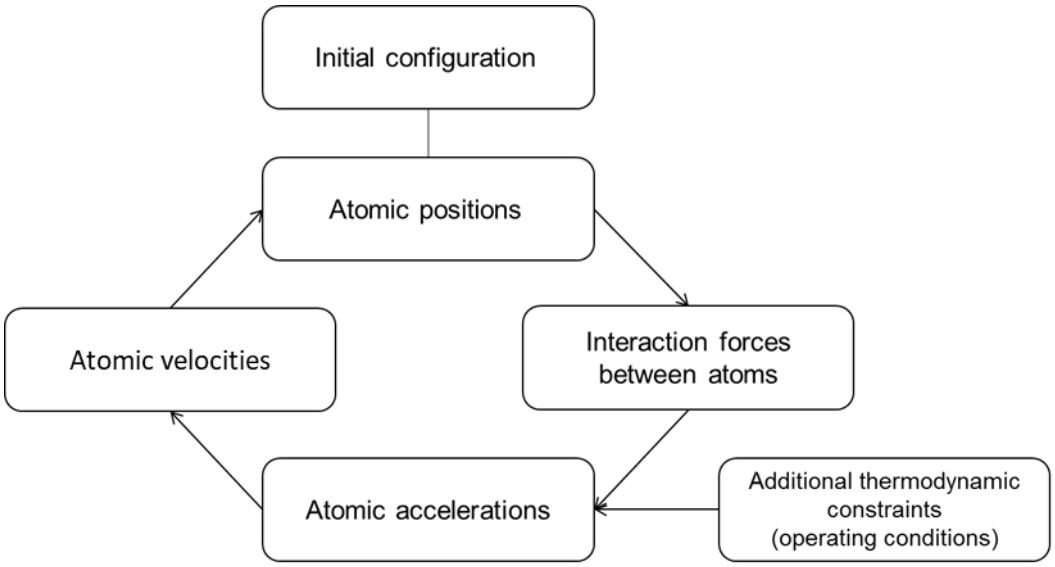

Figure II.2. Flow chart of the Molecular Dynamics method during a time step of the simulation.

II.1.3. Classical force field theory

Force fields describe the behavior of molecules by representing all the interactions occurring between all the atoms constituting a molecule and between atoms of other neighboring molecules, as a function of their respective positions in the system [12, 192, 193]. They contain both the functional form of the potential energy of these interactions and a set of parameters for their coefficients. The correct choice of the force field becomes critical to correctly predict the material properties. As such, a vast set of different force fields exists in literature, derived from either experimental data or quantum-mechanical calculations.

Classical force fields can be classified into three groups depending on how the molecular structure is represented. An All-Atom formulation describes the molecule by

representing every atom in the molecule. On the other hand, a United-Atom [133] formulation represents a simpler version of the molecule by defining “pseudo-atoms”. A pseudo-atom may be either a methyl (CH_3) or a methylene (CH_2) group, for example. They allow for faster computations as the degrees of freedom of the system are drastically reduced. However, they sometimes lead to false predictions of thermodynamic parameters, underpredicting the viscosity for long chained n-alkanes. Coarse-grained (CG) models go beyond these simplifications and replace atom groups by larger sets of pseudo-atoms [194], leading to an even higher computational efficiency. They are primarily used in the biochemistry industry for the design and study of proteins. In this work, an All-Atom formulation of the force field is chosen to model the fluid lubricant systems.

The functional form of the potential energy expressed by the force field can be decomposed into two terms [12] (see equation (II.7)). The first one describes the intramolecular interactions of a molecule of bonded terms, in other words, the interactions between atoms composing a single molecule that are linked together by covalent bonds. The second term describes intermolecular interactions or non-bonded terms. Here, atoms are not linked with each other.

$$V_{total} = V_{bonded} + V_{non-bonded} \tag{II.7}$$

The different interactions, bonded and non-bonded, are described hereon.

II.1.3.1. Bonded interactions

In classical force field formulation, bonded interactions between atoms of a same molecule are represented by harmonic springs. This allows for a correct representation of the flexibility and of all the degrees of freedom of the molecule. These bonded interactions can be of three natures: bond stretching accounting for elongations of the covalent bonds, angle bending, and dihedral interaction or torsion [12]. Figure II.3 presents a graphical depiction of the bonded interactions using the AA formulation for a simple linear n-alkane molecule.

$$V_{bonded} = V_{bond} + V_{angle} + V_{dihedral} \tag{II.8}$$

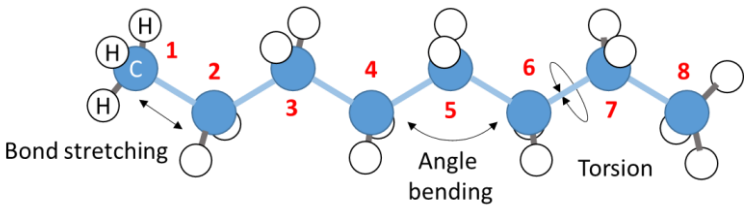

Figure II.3. Schematic representation of a linear n-alkane with an all-atom formulation. The all-atom formulation model highlights the different intramolecular degrees of freedom.

Bond stretching

Bond stretching interactions are modelled by a harmonic spring to take into consideration all elongations and compressions of the covalent bond. They are represented by atoms 1 and 2 in Figure II.3, and by the following formula:

$$V_{bond} = K_b(r - r_0)^2 \quad \text{(II.9)}$$

where K_b represents the stiffness of the bond and $(r - r_0)$ its elongation, with r the distance and r_0 the equilibrium distance.

Angle bending

As for angle bending, like for bond stretching interactions, they are also accounted by harmonic springs. They are represented by atoms 4 to 6 in Figure II.3 and by:

$$V_{angle} = K_\theta(\theta - \theta_0)^2 \quad \text{(II.10)}$$

where K_θ is the angle stiffness and $(\theta - \theta_0)$ is the deviation from the equilibrium position, with θ the angle and θ_0 the angle at the equilibrium position. In this work, for both bond stretching and angle bending, the stiffness corresponds to the classic factor of ½ coming from Hooke's law.

Dihedral torsion

Finally, the last bonded interaction considers proper dihedrals between groups of four atoms pertaining to two planes of the same molecule, represented by atoms 5 to 8 in Figure II.3 and by the formula:

$$V_{dihedral} = \sum_{i=1}^{m} K_i[1 + cos(n_i\varphi - d_i)] \quad \text{(II.11)}$$

with n_i the multiplicity, φ the angle created during torsion and d_i the phase angle. Eventually, if more precision is desired for the dihedral interaction, torsion can be described by a sum of m terms. For example, the OPLS dihedral potential [192] is given by the first three to four initial terms of the series in formula (II.11) so that:

$$V_{dihedral}(OPLS) = \frac{1}{2}V_1[1 + cos\varphi] + \frac{1}{2}V_2[1 - cos(2\varphi)] + \frac{1}{2}V_3[1 + cos(3\varphi)] \quad \text{(II.12)}$$

In some cases, in order to include the effect of improper dihedrals, additional terms to equation (II.12) may be added to enforce the planarity of molecular groups or to prevent molecules from flipping over the boundary conditions.

II.1.3.2. Non-bonded interactions

Non-bonded interactions include two contributions: those coming from Pauli repulsive forces and Van der Waals attractive forces (described by the Lennard-Jones potential), and Coulomb interactions, of electric nature.

$$V_{non-bonded} = V_{Coulomb} + V_{LJ} \tag{II.13}$$

Lennard-Jones interaction

The Lennard-Jones potential is taken into account to model both the attraction (Van der Waals) as well as the repulsion (Pauli) forces between two atoms [12]. For distances smaller than the predefined cutoff distance, the LJ interaction between an atom i with its neighbor j is given by:

$$V_{LJ}(r_{ij}) = 4\varepsilon_{ij}\left[\left(\frac{\sigma_{ij}}{r_{ij}}\right)^{12} - \left(\frac{\sigma_{ij}}{r_{ij}}\right)^{6}\right] \tag{II.14}$$

where ε_{ij} is the LJ energy equal to the depth of the potential well, dependent on the nature of the two interacting atoms, while σ_{ij} is the distance between atoms i and j for which the potential is equal to zero. Atoms i and j are at equilibrium when the distance separating them is equal to $2^{1/6}\sigma_{ij}$. The first term in equation (II.14) represents the repulsive contribution of the LJ potential while the second term is the attractive one. In particular, the formula given in equation (II.14) corresponds to the 12-6 LJ potential, called this way after the exponents used.

Values for ε_i and σ_i are assigned to each atom i. The Lorentz-Berthelot mixing rules define the coefficients ε_{ij} and σ_{ij} as in equation (II.15):

$$\begin{aligned} \varepsilon_{ij} &= \sqrt{\varepsilon_i \varepsilon_j} \\ \sigma_{ij} &= \frac{\sigma_i + \sigma_j}{2} \end{aligned} \tag{II.15}$$

To reduce the computational cost, the LJ potential can be cut off at some limiting distance ($r_{ij} > r_{cut}$), beyond which the interatomic interactions become negligible. It is usually set to a distance of $2.5\sigma_{ij}$ or to less than half of the simulation box length [12]. For the simulation models presented in this work, this cutoff distance is equal to 12 Å.

Coulomb interaction

The Coulomb interaction potential allows considering electrostatic interactions between two bonded or two non-bonded partially charged atoms. The long-range Coulomb potential is represented by equation (II.16):

$$V_{Coulomb}(r_{ij}) = \frac{q_i q_j}{4\pi\varepsilon_0 r_{ij}} \quad \text{(II.16)}$$

with q_i and q_j being the partial charges of atoms i and j respectively, r_{ij} the atomic distance between said atoms, and ε_0 a constant expressing the vacuum permittivity, which is equal to 8.85×10^{-12} F/m.

As it can be appreciated from equation (II.16), long-range Coulomb interactions decrease as the distance between atoms increases by r^{-1}. When compared to Van der Waals attractive interactions in (II.14), which decrease by r^{-6}, it becomes patent that electrostatic interactions become non-negligible at long distances, hence the need to consider them even beyond the cutoff distance. When this occurs, electrostatic interactions can be estimated by applying the particle-particle particle-mesh (PPPM) algorithm [174, 195]. This algorithm results useful for systems with periodic boundary conditions, as it is impossible to compute the electrostatic interactions between the infinite particles of the periodic images of the simulation box. By using the PPPM algorithm, a 3-dimensional mesh is assigned to the simulation cell. The electrostatic potential is then calculated by solving Poisson's equation with the Fast Fourier Transform. Finally, the force of each particle coming from the contribution of the Coulomb interaction at each one of the points of the mesh is determined by interpolation.

Non-bonded interactions scaling

It is possible to exclude or to partially include the contribution of the non-bonded interactions between atoms pertaining to the same molecule. Indeed, in most force fields, non-bonded interactions between atoms of the same molecule separated by either one bond (interaction between atoms 1 and 2 in Figure II.3) or two bonds (interaction between atoms 1 and 3 in Figure II.3) are ignored. For non-bonded interactions separated by more than two bonds (interaction between atoms 1 and 4 in Figure II.3 and beyond), interactions are buffered by a scaling factor in order to better match the behavior to the experimental properties.

For instance, for the OPLS potential and its variants [192, 17], the intramolecular scaling factor for interactions between atoms 1 and 4 and beyond is set to 0.5 for both the LJ potential and for the electrostatic interactions in the Coulomb potential.

II.2. Simulation of bulk fluids

II.2.1. Simulation setup

A choice of three different molecular systems is discussed in Chapter III. The initial configuration of the bulk molecular systems is created using the Moltemplate software [13] and run on the LAMMPS package [14]. The simulation environment consists of a region of 5.0 x 5.0 x 5.0 nm approximately at ambient pressure, generally containing around 10000 atoms (see Figure II.4). All molecules are affected by an updated version [15] of the L-OPLS-AA force field [16], which considers both bonded and non-bonded interactions. This new version of the L-OPLS-AA force field has been evidenced to give more accurate results than the original force field [17] in systems composed primarily by linear n-alkanes [10].

Non-bonded interactions within the molecules include both the 12-6 LJ potential and the long-range Coulomb interactions, the former of which set with a cutoff distance of 12 Å. In addition to this, the Lorentz-Berthelot mixing rules are applied for LJ parameters between atoms of different nature in a same molecule. Electrostatic interactions, on the other hand, are determined by the PPPM algorithm. Periodic boundary conditions are applied in the three directions of the system.

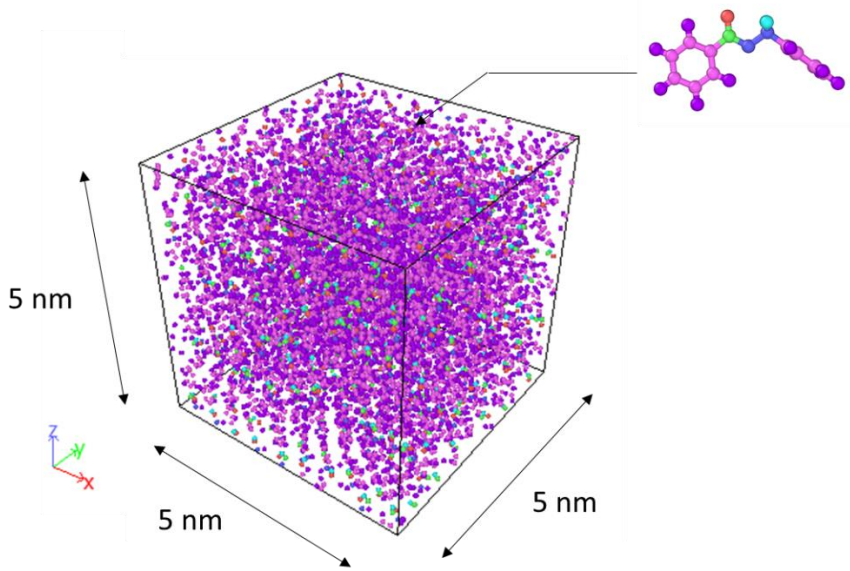

Figure II.4. Example of a bulk system of molecules. Here, the system is composed of 360 benzyl benzoate molecules.

II.2.2. Simulation procedure

The Verlet algorithm is used to integrate Newton's equations of motion. The time step is set to 1 fs. Bulk systems are first equilibrated and then the energy is minimized. Then, a thermodynamic microcanonical (NVE) ensemble is considered in order to equilibrate the temperature of the system with a Nosé-Hoover thermostat [174] and a damping coefficient of 0.1 ps [10]. Once the temperature has reached its stable value, pressure is applied at constant temperature in an isobaric-isothermal (NPT) ensemble for the different pressure conditions of interest. No shear is applied at this stage.

II.2.3. Quantities of interest

A set of various thermodynamic parameters can be computed from the bulk model of the fluids in order to evaluate their rheological behavior for different pressure and temperature conditions.

II.2.3.1. Density

The density ρ of the lubricant characterizes its thermodynamic nature and is easy and fast to compute. It is defined as the total mass of the molecules divided by the volume V of the system by the following formula:

$$\rho = \frac{\langle \sum_{i=1}^{N} m_i \rangle}{V} \tag{II.17}$$

where N is the number of molecules in the bulk system and m_i is the mass of molecule i. The symbol $\langle ... \rangle$ represents the ensemble average. Because formula (II.17) depends on the volume of the system, the NPT ensemble (entraining a constant number of particles, constant pressure, and constant temperature during the whole simulation run) is needed to study the density parameter. Thus, the volume is not fixed to a set value and can vary. Once density stabilizes, an average over the next 0.5 ns is calculated.

II.2.3.2. Viscosity

The bulk viscosity can be determined via two approaches: either by equilibrium Molecular Dynamics (EMD) simulations to determine the Newtonian rheology of the lubricants (viscosity is independent of the shear rate at low shear), or either by nonequilibrium Molecular Dynamics (NEMD) simulations in order to characterize the transition from a Newtonian to a non-Newtonian behavior.

The Newtonian viscosity η_N at equilibrium is estimated within the linear response theory through EMD simulations by using a Green-Kubo relationship [143, 144]. The Green-Kubo relationship integrates the autocorrelation of the five independent components $P_{\alpha\beta}$ of the traceless stress tensor [196]:

$$\eta_N = \frac{V}{5k_B T} \int_0^{\infty} \langle P_{\alpha\beta}(t) P_{\alpha\beta}(0) \rangle \, dt \tag{II.18}$$

In equation (II.18), k_B represents the Boltzmann constant, T the temperature of the fluid, and $P_{\alpha\beta}$ the different independent components of the traceless stress tensor, here being equal to P_{xy}, P_{yz}, P_{zx}, $\frac{1}{2}(P_{xx} - P_{yy})$, and $\frac{1}{2}(P_{yy} - P_{zz})$. As the accuracy of the value of viscosity is directly dependent on the computation time, by averaging viscosity over these five components, the computation time is significantly reduced. In order to ensure convergence of the viscosity, the simulation runs exceed 20 ns.

In a non-equilibrium system, viscosity is determined with the Müller-Plathe (MP) algorithm [197]. The Müller-Plathe algorithm has the particularity that, even though viscosity is calculated for a sheared system, there is no need to apply any shear nor any additional external energy to the system. Indeed, the algorithm artificially exchanges momenta p between particles of different regions of the system, thus generating a velocity profile through the film thickness. In other words, the shear rate $\dot{\gamma}$ is not an input by itself but the number of particles

swapping their momenta, as well as the frequency of the swaps occurring. This method allows reaching shear rate values ranging from 10^7 s^{-1} to 10^{11} s^{-1} for momenta exchanges going from one exchange every picosecond to 1000 exchanges every picosecond respectively. The values of shear rate that can be calculated through this method are, however, bound to limits: for low shear rates, a longer computation time is needed to yield the shear rate through thermal noise; on the other hand, at high shear rates, a very fast swapping rate of momenta induces noise in the velocity profile signal, impeding the establishment of a linear velocity gradient.

The viscosity η is finally calculated as the ratio between the shear stress τ coming from the exchanged momenta, and the shear rate $\dot{\gamma}$.

$$\eta = \frac{\tau}{\dot{\gamma}}$$
$$\tau = \frac{1}{2S}\frac{\delta p}{\delta t} \quad \text{(II.19)}$$

S is the surface perpendicular to the flux direction.

II.3. Simulation of confined fluids

The fluid lubricant molecules are modeled, as with the bulk molecular systems, with the L-OPLS-AA force field. The lubricant molecules used, as well as their parametrization will be presented in detail in the following Chapter III.

II.3.1. Surface modeling

The initial configuration of the confined systems are created with the open source software LAMMPS_builder [18] that utilizes modules from Moltemplate [13] and ASE [19], and runs through the LAMMPS package [14]. These systems represent confined fluid molecules between two solid surfaces of different nature: an atomically smooth iron oxide surface (α-Fe_2O_3 [100]) or a randomly rough iron surface (α-Fe [100]). Both surfaces are made out of materials representative of a real EHD contact and are referred to in Figure II.5.

Although the main aim of these MD simulations is to fully characterize the friction and flow phenomena of the confined lubricant, the choice of the confining surfaces is crucial if physicochemical events occurring like fluid adsorption were to be analyzed. Overall, the goal of this work is to focus on the lubricant flow in the thickness of an EHL contact rather than in surface effects on ultra-thin films. Indeed, although atomically smooth surfaces are modeled in this Chapter and are successfully used in both Chapter IV and Chapter V, they sometimes fail to represent the interactions at the boundary between fluid molecules and solid surfaces [20, 21], hence the interest to also include rough surfaces in this study, which are a closer representation of reality. Moreover, parameters such as the corrugation potential [22] or even the geometry of the surface [20, 23] may have a large impact in flow.

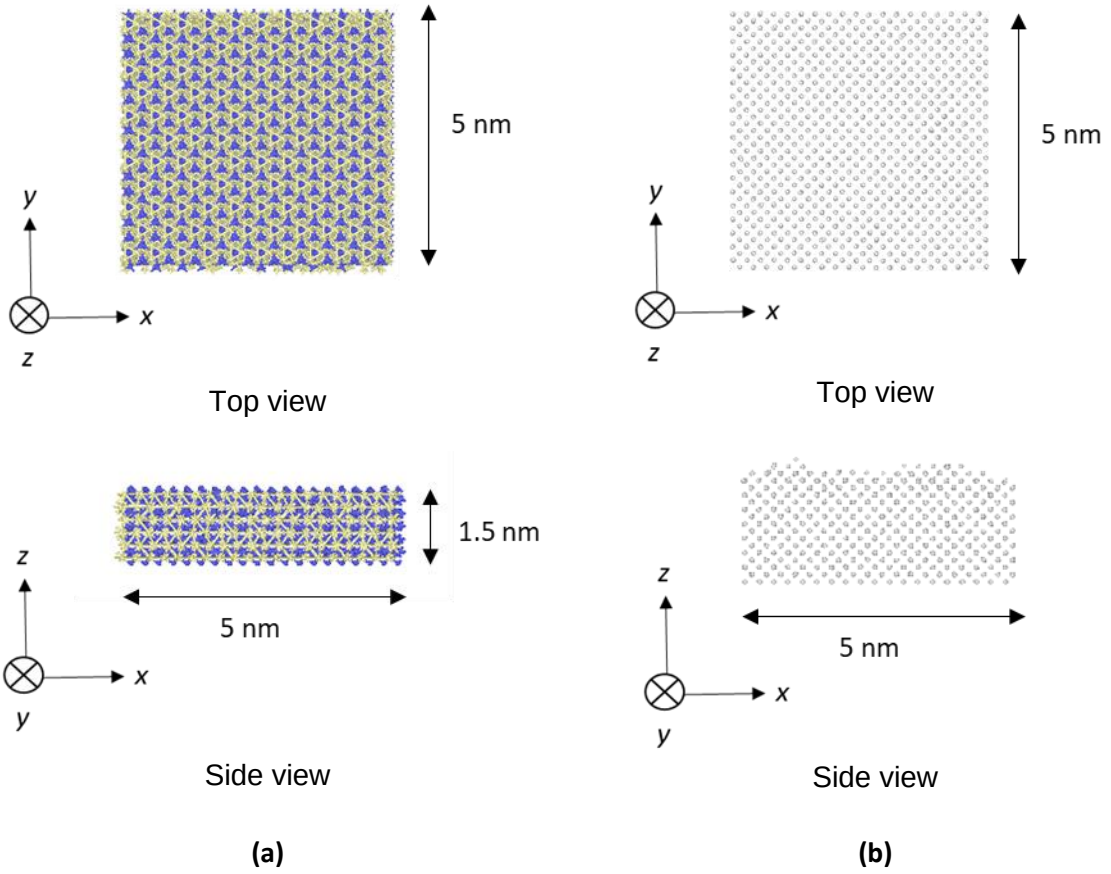

Figure II.5. Examples of surfaces used for the confined simulations: (a) atomically smooth iron oxide and (b) randomly rough iron surfaces. In (a), yellow particles are O atoms and blue particles are Fe atoms.

With respect to the systems conformed with smooth surfaces, the solid iron oxide slabs have approximate dimensions of 5.0 x 5.0 x 1.5 nm in the x-, y- and z- dimensions respectively. Iron and oxygen atoms are restrained in the crystalline structure with harmonic bonds, whose spring constant is equal to 25 kcal.mol^{-1} [24]. As for pairwise interactions, they are modeled with LJ and electrostatic interactions. Additional information on the LJ parameters for both iron and oxygen atoms used for the smooth iron oxide surface are presented in Table II.1, and are based on literature from Savio *et al.* [24] and Berro *et al.* [25]. In Table II.1, ε^- is the reference value of the FF for Fe, while ε^+ is the artificially tuned value of the LJ parameter ε, accounting for a higher adhesion.

Table II.1. Parametrization of iron oxide atoms used for the atomically smooth iron oxide surface. The two different values of ε for the iron atoms account for two different degrees of surface adhesion.

Group	Atom type	Description	q / e	σ / Å	ε^+ / kcal.mol^{-1}	ε^- / kcal.mol^{-1}
Iron oxide (Fe_2O_3)	FE	Surface Fe	0.771	2.320	9.518	0.945
	OX	Surface O	-0.514	2.960	0.210	

It is also possible to carve nano-scale roughness profiles into the crystalline structure of the surfaces (Figure II.5.b). Nano-rough iron surfaces are created using a self-fractal scaling law, using the methodology exposed by [10]. In order to parametrize the roughness of the surface, the Hurst exponent and the root mean square (RMS) roughness are presented. They both are set to 0.8 and 0.8 nm respectively. The iron slabs created measure 5.0 x 5.0 nm in the x- and y-directions approximately, and have a thickness ranging between 3.0 and 5.0 nm in the z-direction. Iron atoms are affected by the classical empirical Embedded Atom Method (EAM) force field [26], which is widely used for metallic systems [27, 28].

II.3.2. Simulation procedure

The confined fluid is submitted to the applied pressure through the solid walls, as well as to shearing. Thermodynamic constraints are considered in the system in order to implement load, entrainment speed and temperature on the confined surfaces, thus recreating the operational conditions one may find in an EHL contact. Periodic boundary conditions are only applied along the x- and y-axis directions, preventing outflow of fluid molecules from the contact. This choice results appropriate due to the fact that in the center of a regular EHL contact, the film thickness is far smaller than the other dimensions of the system. In addition, the integrity of the MD model is assured because the outflow of lubricant molecules during the simulation steps is prevented.

Three main steps are defined for one simulation run: relaxation of the fluid molecules, compression, and shearing. The system is first energy minimized and relaxed, as the molecules, initially randomly assigned in space, need to be disposed in a configuration such as found at equilibrium. Then, pressure is applied to the system by setting a normal pressure P to the outer layer of atoms in the upper solid surface, defining a control region (see Figure II.6). The pressure is uniformly distributed on all the atoms of the control region. Each atom supports the force equal to:

$$F_{z,i} = \frac{PS}{N_c} \tag{II.20}$$

with S the surface section of the nano-patch equal to $S = L_x \times L_y$ (L_x and L_y being the length of the sides of the section) and N_c the number of atoms in the control region. The bottom solid

surface is kept fixed in the z-direction, with no applied pressure on it. The range of pressure values chosen (from 0.5 to 2 GPa) is representative of an EHL contact.

Compression is performed for around 2 ns, for which film thickness evolves in a dumping manner with time until it stabilizes. When the film thickness reaches a constant value, the shearing step starts.

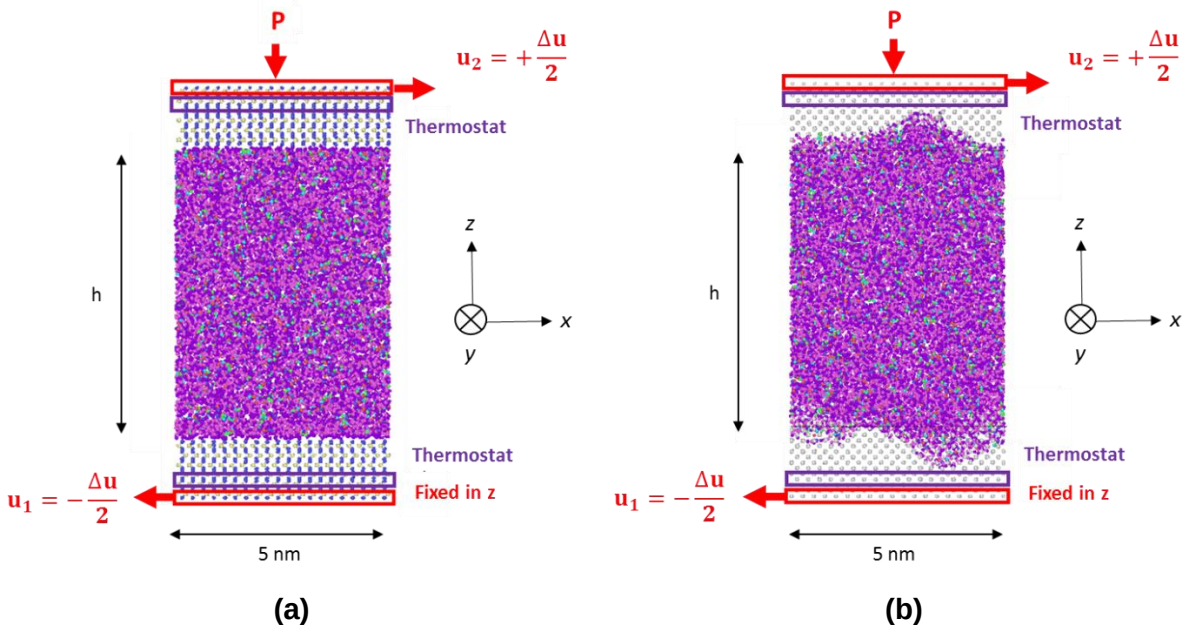

Figure II.6. Representative system setup of confined benzyl benzoate molecules between (a) atomically smooth iron oxide surfaces and (b) randomly rough iron surfaces, after compression and before sliding in the x-direction. The sliding speed is $u_2 = -u_1 = +\Delta u/2$.

During the shearing step (see Figure II.6), a constant velocity gradient in the x-direction is imposed by applying a constant velocity on the outer layers of atoms in both the top and bottom slabs, but in opposite directions. On the top solid surface slab, the shearing velocity is equal to $u_2 = +\Delta u/2$ while in the bottom surface slab it is $u_1 = -\Delta u/2$. Shear is preferred to be boundary-driven instead of being directly imposed in the bulk of the fluid. Indeed, it has been confirmed that the dynamics of the confined fluid are modified in the latter case [29, 30].

Mechanical energy is brought to the system by shearing. This energy is then transformed into heat. On the other hand, he interactions acting on the system are conservative. It thus becomes crucial to evacuate the excess heat created during sliding in order to avoid an unrealistic temperature increase. It is dissipated by a Langevin thermostat [31] in the y-direction, which is the direction perpendicular to motion and to compression. The thermostat is applied just below the mechanical boundary conditions of the solid surface in order to not interfere with the fluid or the fluid/surface interface [22]. This way, temperature in the fluid system is let to evolve independently. It should finally be noted that boundary thermostating has been proven to be an effective way of controlling the temperature of the confined fluid [32, 33, 34]. However, for shear rates above 10^{10} s^{-1} the temperatures in the contact begin to deviate from their isothermal state [35, 22].

A steady state was generally reached for shearing times above 3 ns and depended on the applied shear rate. Higher shear rates entrain lower times to reach a stable flow. Results were obtained from time averaging, such as the velocity and density profiles through the film thickness, or the shear stress at the surfaces.

II.3.3. Quantities of interest

Through statistical analysis, local parameters such as the film thickness, the tangential force at the solid confining walls or the density can be calculated from the MD model described in the previous section. It has to be noted that these parameters may deviate from the typical bulk behavior of the fluid, mainly due to structural and dynamic phenomena.

II.3.3.1. Film thickness

The film thickness h in confined systems is calculated for lubricated systems with smooth surfaces by calculating the distance existing between both solid surfaces once the system enters the steady state regime (Figure II.7.a). However, in the case of molecules confined between rough surfaces (Figure II.7.b), film thickness is calculated as the minimum distance existing between the highest roughness peaks in each one of the solid surfaces in the steady state regime.

$$h = \langle z_2^{min} - z_1^{max} \rangle \tag{II.21}$$

where z_1^{max} and z_2^{min} represent the maximum and minimum z-coordinates for the bottom and upper solid surface respectively. The difference in peak heights is averaged through time.

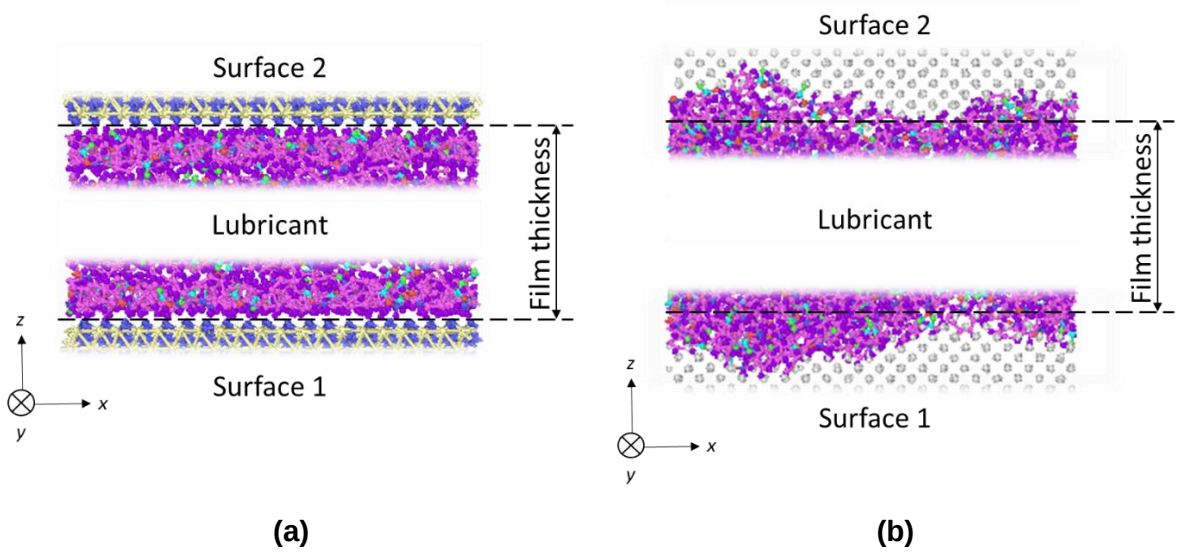

Figure II.7. Schematic representation of the determination of the film thickness for a lubricant system confined between (a) smooth surfaces and (b) rough surfaces.

II.3.3.2. Lubricant density

The lubricant density ρ is calculated from the film thickness [198] as follows:

$$\rho = \frac{\langle \sum_{i=1}^{N} m_i \rangle}{Sh} \tag{II.22}$$

with N the number of fluid molecules, m_i the mass of each fluid molecule i, S the area of the nano-patch and $\langle \ldots \rangle$ the ensemble average. The lubricant density obtained this way can be directly compared to available experimental data. An example of density calculation for a confined fluid is given in Figure II.8, where the average density in the central region of the thickness equals $\rho = 1004$ kg/m^3. The density value is calculated in the central region of the thickness in order to avoid the influence of local structuration near the walls. The values obtained are comparable to empirical bulk laws, such as those proposed by Dowson and Higginson [68] or by Tait [199].

Density profiles can also be derived from MD simulations by considering the atomic positions. Indeed, if the film thickness is divided into a series of slabs with thickness δh containing N_{slab} molecules, the density in each slab can be time averaged along the steady state regime, leading to a density profile similar to the one shown in Figure II.8.

$$\rho_{slab}(z) = \frac{\langle \sum_{i=1}^{Nslab} m_i \rangle}{S\delta h} \tag{II.23}$$

The peaks near the solid walls correspond to regions where molecular layers are well defined. This structuration is lost far from the solid walls. As will be discussed in Chapter IV, this phenomenon is mainly predominant for atomically smooth surfaces [167].

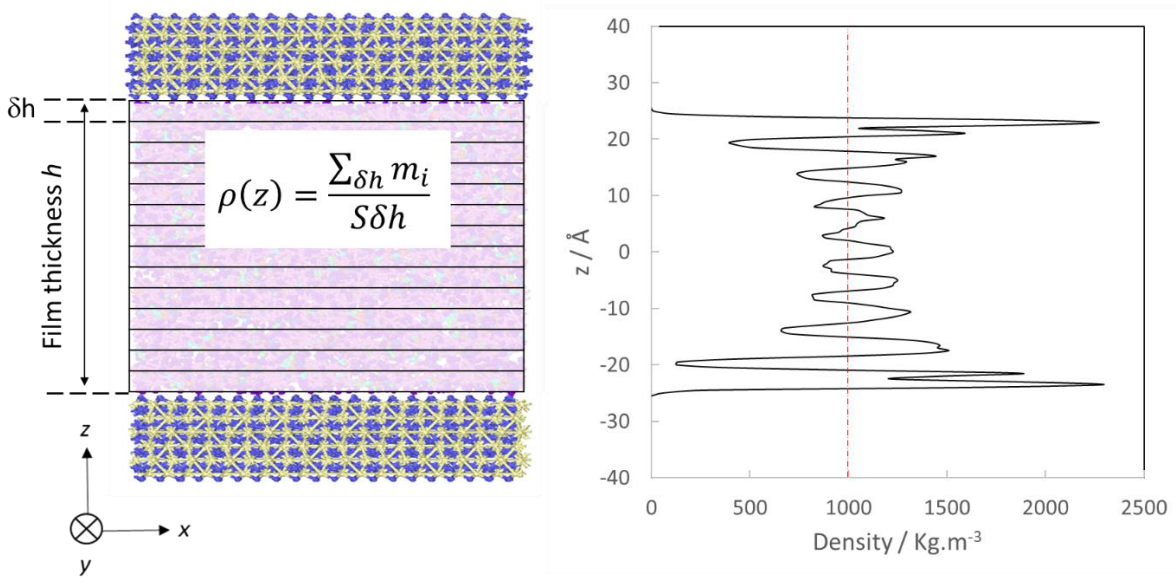

Figure II.8. Representation of the methodology employed for the calculation of the fluid density across the film thickness, leading to a density profile (benzyl benzoate confined

between smooth iron oxide surfaces, P = 0.5 GPa, T = 313 K). The red dashed line on the right image represents the average density of the fluid.

II.3.3.3. Velocity distribution

The method used to obtain the velocity distribution of the fluid across the film thickness follows a similar procedure than the one employed for the density profiles. The film thickness is divided into a series of slabs with thickness equal to δh. For each slab, the velocity of every particle within the slab in the shearing direction is time averaged when the steady state conditions are met. A velocity profile, such as the one in Figure II.9 is generated.

In the specific case presented in Figure II.9, the flow displays at the center of the fluid film a linear-like or Couette-like profile, typical of a liquid-like behavior. This linear region allows the identification of an effective shear rate $\dot{\gamma}_{eff}$, which is none other than the velocity gradient following the z-direction $\partial u(z)/\partial z$, i.e. the ratio between the velocity in the shearing x-direction and the film thickness. The effective shear rate is determined in the center of the film in order to ignore boundary effects.

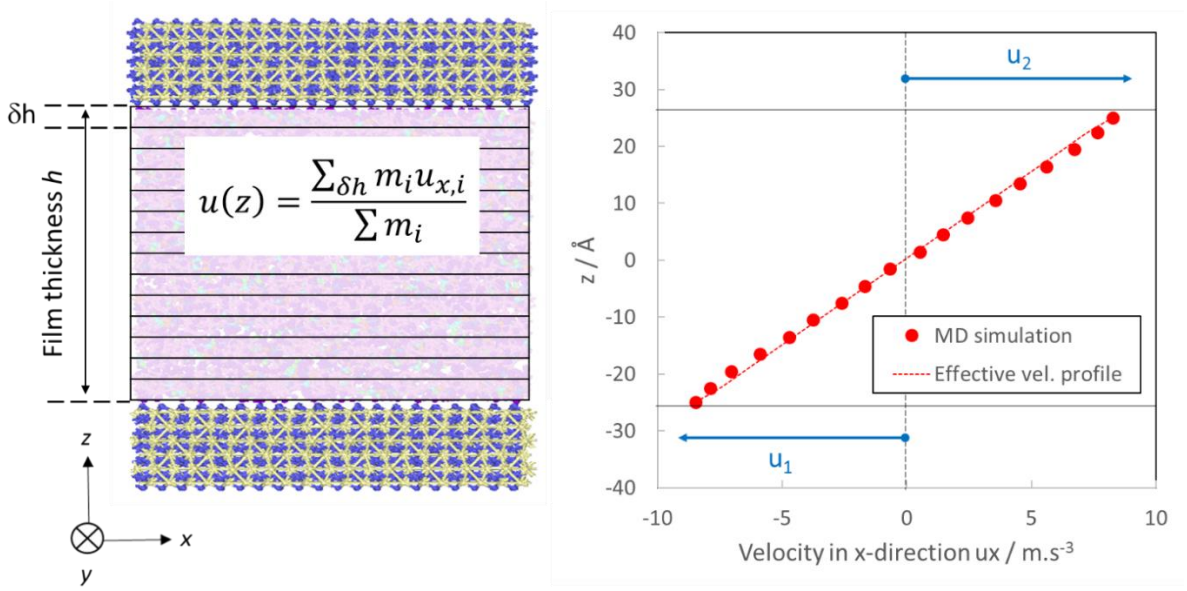

Figure II.9. Representation of the methodology employed for the calculation of the fluid velocity across the film thickness, leading to a velocity profile (benzyl benzoate confined between smooth iron oxide surfaces, P = 0.5 GPa, T = 313 K, $u_2 = -u_1 = 10$ m.s^{-1}). A Couette-like profile is obtained.

The characterization of the flow behavior of lubricants will be further exploited in Chapter IV, with the aim to comprehend the physical origins of friction.

II.3.3.4. Shear stress, friction and viscosity

The shear stress τ_{zx} is related to the force $F_{x,i}$ acting on each atom i that is opposing the movement in the shearing x-direction [198]:

$$\tau_{zx} = \frac{\langle \sum_{i=1}^{N_c} F_{x,i} \rangle}{S} \tag{II.24}$$

where N_c is the number of atoms in the control region where the velocity in the wall is applied, S is the surface area of the solid walls and $\langle \dots \rangle$ is the ensemble average. The friction coefficient can be classically determined as the ratio between said shear stress and the applied normal load P. Furthermore, the rheological response of the lubricant can also be derived from the effective viscosity η_{eff} [198]:

$$\eta_{eff} = \frac{\tau_{xy}}{\dot{\gamma}_{eff}} \tag{II.25}$$

As a final remark, it should be remembered that the parameters presented in this Chapter, such as the viscosity, present values that have been averaged over time (some nanoseconds) and space (some nanometers) and, even though local variations of these parameters are not captured [200], they are appropriate for the study of friction and flow behavior in nano-confined lubricated contacts.

II.4. Conclusion

In this Chapter, a Molecular Dynamics model has been presented in order to study the behavior of lubricants in their bulk state or in a confined environment. The first model, representing only the bulk lubricant, aims to analyze and describe the static behavior of the fluids. The results obtained from these simulations are the focus of Chapter III. On the other hand, the model of the lubricant molecules entrapped between two parallel solid plates allow obtaining the dynamic properties of the lubricants. It only represents a small nano-patch inside a real contact area. The different elements that have been presented for this model replicate the realistic properties of the materials used in a real EHD contact. As for the operating conditions (normal load, applied temperature and shearing speed), they are all implemented in the system through a set of thermodynamic constraints and techniques.

The main outputs that can be extracted from a typical Molecular Dynamics simulation are the positions of the atoms and their variation with time. They are averaged over time and space to calculate the resulting film thickness during shearing, the density and velocity profiles, as well as the viscosity and the local friction in the contact. All these parameters serve to characterize the local behavior of the lubricated EHD contact and are studied in detail in Chapter IV and V.

Furthermore, the main molecular models presented in this Chapter can be further exploited to characterize phenomena like shear thinning or thermal dissipation that appear in a real tribological contact. In the following chapters, a detailed description of the flow behavior

and its implication on friction will be given. In particular, some insights of the physical mechanisms behind the limiting shear stress behavior of the lubricants will be given with respect to the dynamic response of the fluid molecules during shearing.

Chapter III

Rheology of lubricants

Chapter III
Rheology of lubricants

In the introductory Chapter, the benefits of lubrication in the performance of mechanical systems under industrial operating conditions were presented, as well as the different phenomena occurring during shearing. The limiting shear stress was hinted out to be related to a change in the behavior of the lubricant film. In Chapter II, the basic concepts related to the Molecular Dynamics method were reviewed at high pressure and a model for both the bulk and confined situations of the lubricant were developed. In this Chapter, the MD simulation model will be completed by focusing on the lubricant molecules. Generally, lubricants are made of a base oil (which makes up for 70-99% of the composition) to which various additives are included to enhance or modify a property of the fluid, such as its viscosity or its integrity to thermal stresses. In particular, fluids used for lubrication can be separated into two main categories: traction fluids and lubricants, each one with its own formulation, properties and specific applications.

However, modeling the whole fluid would imply an enormous challenge in representing each one of the components: the task is too time-consuming, imprecise and, in most cases, impossible to carry out because the lubricant formulation is unknown. Therefore, the models presented hereon only account for the base fluid molecules, which are representative of the whole lubricant, and which will be parametrized for subsequent MD simulations. A choice of three base oil molecules will be first characterized under different pressure and temperature conditions for their density and viscosity behavior. The Chapter will then end by introducing the phase diagrams for each one of the three base oils.

III.1. Lubricant molecules

III.1.1. Traction-like fluids: benzyl benzoate

III.1.1.1. Description

Traction drive fluids (TDFs), commonly known as traction fluids, are lubricant fluids used for applications that require a high traction coefficient for high power transmission at elevated shear rates and pressures. Such applications include traction drive mechanisms or continuous variable transmissions (CVT). They are characteristic of entering a regime of shear-independent friction at high shear rates for sufficiently high pressures, which is related to the limiting shear stress value [201, 173] and which constitutes the main topic of this work.

Traction-like molecules are small and rigid [201]. Research has been conducted in order to elucidate the reasons behind the high values of friction for these kind of compounds, but it is agreed that the saturated rings in their structure are a relevant factor in their behavior to traction [202]. Indeed, the difficulty of rotation of the saturated rings, combined with the small molecular size and the stiffness of the molecule, leads TDFs to higher traction forces. In addition, TDFs are also required to be able to form high viscosity oil films between contact elements under high pressure, as well as low viscosity films at low temperatures. Table III.1

succinctly summarizes the main characteristics traction fluids are required to have for a correct performance.

Table III.1. Specifications for traction fluids. Inspired from [202].

Specification	Properties	Requirements
Power transmission	High traction coefficient	No degradation Slight dependence of T
Lubrication	Integrity at high P Anti-wear property Long fatigue life	Film thickness at high T
Hydraulic fluid properties	Integrity between -30 °C and 140 °C	Adequate viscosity High viscosity index Low temperature fluidity
Maintenance free	Long life Long drain	Good oxidation stability

III.1.1.2. Model

The molecule chosen to represent a characteristic traction-like fluid is benzyl benzoate (BB), an organic compound with formula $C_6H_5COOCH_2C_6H_5$, which is the ester of the benzyl alcohol and benzoic acid (see Figure III.1). This fluid has been selected because there already exists extensive rheological and friction data for it [36]. Furthermore, BB is an interesting molecule for experimental studies as it presents rings that allow spectroscopic characterization [8].

(a) **(b)**

Figure III.1. Schematic representation of the (a) benzyl benzoate molecule and (b) its MD model. In (b), green particles stand for hydrogen atoms, orange for carbon atoms and blue for oxygen atoms.

The MD model is affected by the updated version of the L-OPLS-AA force field [15]. LJ parameters and partial electric charges are presented in Table III.2. Partial electric charges of

the ester group have been modified in order to ensure a neutral net charge of the molecule, as done in [10].

Table III.2. LJ parameters and partial electric charges of the benzyl benzoate molecule, from [15]. Atom types in the ester group marked with * have modified partial charges in order to ensure a neutral net charge of the molecule.

Group	Atom type	Description	q / e	σ / Å	ε / kcal.mol^{-1}
Ester (glyceride)	C	C=O	0.795*	3.750	0.150
	O	O=C	-0.380*	2.960	0.210
	OS	ROR	-0.200*	3.000	0.170
Aromatic ring	CA	C	-0.115	3.550	0.066
	HA	H-C	0.115	2.420	0.023
Benzoate	CB	C-COO-	-0.100	3.550	0.066
Alkyl	CT	-CH2-	-0.148	3.500	0.066
	HC	H-C CH2	0.074	2.500	0.026

III.1.2. Model lubricants: squalane

III.1.2.1. Description

Most base oil molecules in model lubricants are manufactured from petroleum and thus classically present a linear alkane structure, with some or no ramifications at all. They are long and flexible, as opposed to the small and rigid traction fluid molecules [203].

Lubricants provide a protective film between the contacting surfaces, significantly reducing the level of friction in the contact. There are many specifications which need to be ensured in order for the lubricant to perform correctly. For instance, they need to be viscous in order to develop and maintain a lubricant film thickness but, at the same time, not too viscous in order to not increase friction significantly. They also need to exhibit good stability to oxidative and thermal stresses as well as an adequate heat capacity.

III.1.2.2. Model

Squalane (SQ) is an organic lubricant with formula $C_{30}H_{62}$ (see Figure III.2). This molecule has already been largely studied and characterized in literature [10, 37, 38] and will be further used in this work for MD simulations. Squalane is parametrized by the updated version of the L-OPLS-AA force field [15], where the LJ parameters are set as shown in Table III.3.

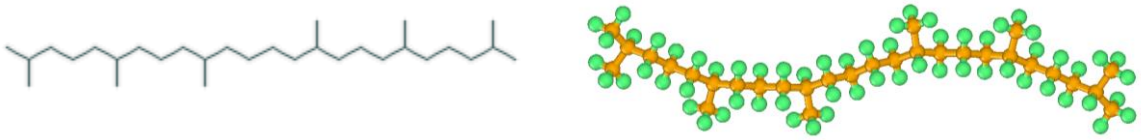

(a) **(b)**

Figure III.2. Schematic representation of the (a) squalane molecule and (b) its MD model. In (b), green particles stand for hydrogen atoms, and orange for carbon atoms.

Table III.3. LJ parameters and partial electric charges of the squalane molecule, from [15].

Group	Atom type	Description	q / e	σ / Å	ε / kcal.mol^{-1}
Alkyl	CT	-CH3-	-0.222	3.500	0.066
	HC	H-C CH3	0.074	2.500	0.026
	CT	-CH2-	-0.148	3.500	0.066
	HC	H-C CH2	0.074	2.500	0.026
	CT	-CH-	-0.074	3.500	0.066
	HC	H-C CH	0.074	2.500	0.026

III.1.3. Aerospace model lubricants: commercial blends

III.1.3.1. Description

Lubricants in the aerospace industry are primarily used to cool bearings that make part of the compressor or the turbine of aircraft engines. Various specifications have to be met in order to comply the demanding constraints. First and foremost, the lubricants are commonly exposed to the extreme operating conditions experienced in an aircraft, where temperatures reach values as high as 1200 °C. These very high solicitations lead to thermal and oxidative stresses in the lubricant. Furthermore, the exposure to high temperatures inside bearings can also lead to rapid oxidation and cocking of the residual oil entrapped in the bearing chamber. Eventually, this would lead to failure and possibly to a catastrophic fate for the aircraft. Second of all, these oils need a low temperature-viscosity coefficient due to standard regulations. Indeed, aircrafts and engines need the ability to start at temperatures comprised between -54 and 40 °C. Globally, oils for these kinds of applications are submitted to a wide range of temperatures, which require a very complex formulation.

These precise requirements regarding performance and integrity of the aerospace oil lead to very specific oil compositions. Lubricants are composed of a quality polyol ester base

fluid (about 93 to 95% of its composition) to which a set of additives of different natures are mixed into, primarily with anti-oxidant, anti-wear and corrosion inhibiting properties. Currently, neopolyol esters are the only base fluids that appear to deliver the required levels of thermal and oxidative stability, cleanliness and low-temperature rheology. They are produced by a process called catalytic esterification from polyol fluids, as seen in Figure III.3. At present, only three types of neopolyols are typically used to produce such esters: neopolyol glycol (NPG), trimethyol propane (TMP), and monopentaerythritol (PE).

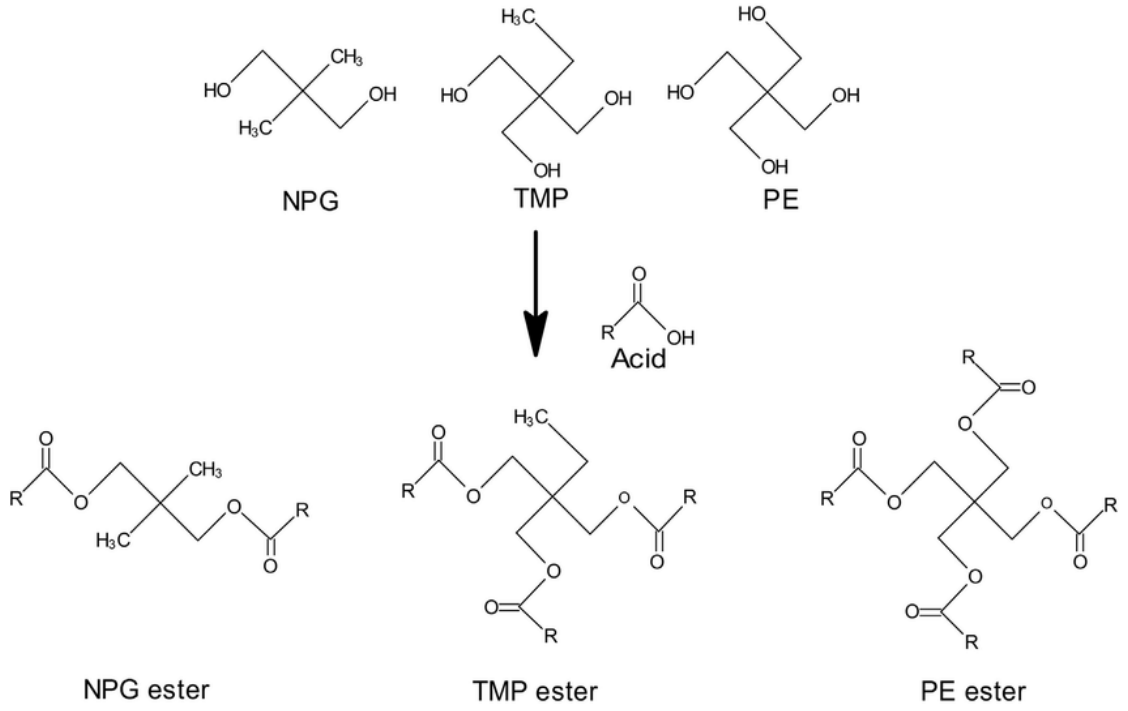

Figure III.3 Catalytic esterification of acid and polyol to polyol ester. Reproduced from [204].

The use of polyol ester-based fluids can also be extended to other applications where the operating conditions are extreme. For example, ground turbines, high compression rate compressors or even turbochargers in some passenger car engines may find benefit from the large stability of this lubricant.

III.1.3.2. Model

The aerospace model lubricant used in this work is the Nycobase 5750 (NPE), a base oil supplied by the company Nyco (Paris, France) made of PE ester molecules. A PE ester is also known as monopenthaerythritol tetra-A_{nC} or just PEC-(n_C+1), where A_{nC} stands for the n-alkane radical chain with n_C carbon atoms. For example, the polyol ester PEC7 has a radical alkane chain length of six carbon atoms and is also called monopentaerthtitol tetrahexane. In the following pages, generic polyol esters will be referred to as PEC.

Two parameters are initially unknown at the start of this investigation:

1) How many types of PEC molecules are mixed together in the base oil, i.e. the composition of the Nycobase 5750.
2) The concentration of each PEC in the base oil, in the case of it not being a monomolecular fluid.

The MD model thus considers only PEC molecules, whose LJ parameters and partial electric charges are presented in Table III.4 from [15]. The L-OPLS-AA force field is also chosen. Eventually, depending on the length of the radical alkane chain, the PEC molecule will have a different formulation. The formula will be $C_9O_8H_8$ (constant) for the "core", and 4x[(n_C-1) CH_2 – CH_3] (with variable n_c) for the n-alkane branches.

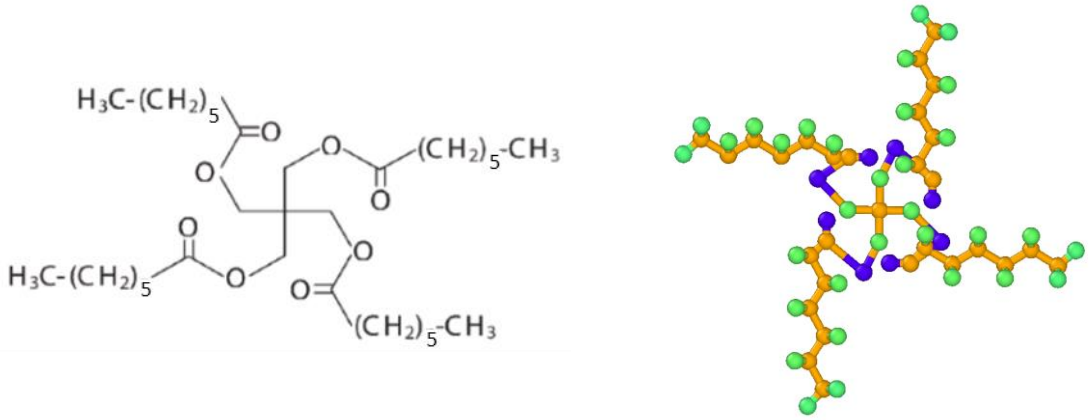

(a) **(b)**

Figure III.4. Representation of a polyol ester molecule used for MD simulations. In particular, it represents a PEC7 molecule. In (b), green particles stand for hydrogen atoms, orange for carbon atoms and blue for oxygen atoms.

Table III.4. Parametrization of the atom types in the PEC molecule from [15]. Atom types in the ester group marked with * have modified partial charges in order to ensure a neutral net charge of the molecule.

Group	Atom type	Description	q / e	σ / Å	ε / kcal.mol^{-1}
Ester (glyceride)	C	C=O	0.710*	3.750	0.150
	O	O=C	-0.380*	2.960	0.210
	OS	ROR	-0.330	3.000	0.170
Alkyl	CT	-CH3-	-0.222	3.500	0.066
	HC	H-C CH3	0.074	2.500	0.026
	CT	-CH2-	-0.148	3.500	0.066
	HC	H-C CH2	0.074	2.500	0.026
Central atom	CT	>C<	0.000	3.500	0.066

Different scenarios can be envisaged relatively to the composition of the Nycobase. PEC5 [205], PEC7 and PEC9 [206] molecules for instance, are already explored in literature as well as the binary mixture of PEC5 and PEC9 [207] (hereon PEC5-9). However, for this last fluid, no details are given on the concentrations of each molecule. Internal research on the Nycobase 5750 base oil has been made, testing it experimentally [208], and properties such as the density, the viscosity and the refraction index were extracted for different temperature and pressure conditions. An analysis by steric exclusion chromatography was performed in order to determine the composition of the base fluid (see Table III.5 for the conditions of the analysis). Steric exclusion chromatography is a technique that separates compounds solely on the basis of size by letting the solution go through a series of progressively thinner porous beads. Thus, larger molecules are separated from the solution at the first beads while smaller molecules are let through. The pore sizes of these beads are used to estimate the dimensions of the molecules of the solution. The results give strong evidence about the binary molecular nature of the base oil. Indeed, in Figure III.5 two peaks are observed at retention volumes of 20.73 ml and 21.78 ml, which correspond to the two compounds in the formulation of the base oil. The type of PEC molecules cannot be derived from this test, but rather an estimation of their masses, with the first peak giving the larger (heavier) molecule and the second peak the smallest (lightest) molecule. This estimation is calculated as a ratio of areas under the curve of the chromatogram (Figure III.5). The area under the first peak is equal to 4.91 mV.ml and for the second peak 21 mV.ml, which leads to a ratio of roughly 1:4. This means that the heavier molecule (with longer radical n-alkane chains) entrains around 20% of the mass of the fluid.

Table III.5. Analysis conditions for the steric exclusion chromatography of the Nycobase 5750.

Solvent	Tetrahydrofuran (THF)
Pump flow	1 ml/min
Injected volume	100 μm
Sample concentration	4.8 mg/ml
Detector	Refraction index
Columns	3 Waters columns
Calibration	Polystyrene standards

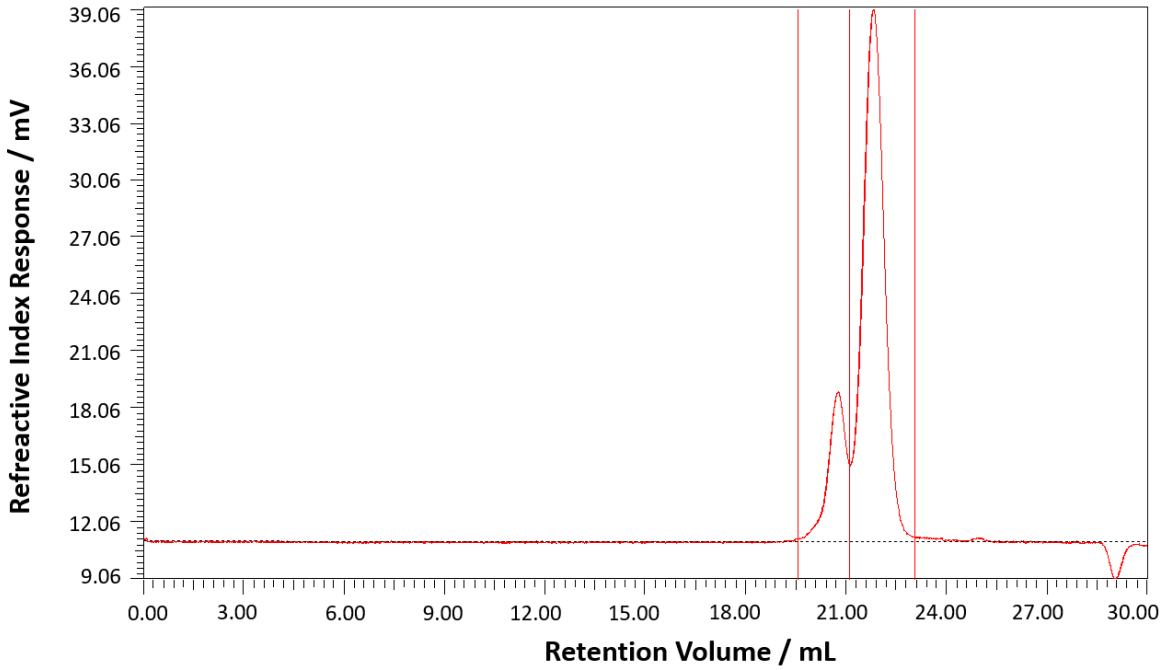

Figure III.5. Chromatography results showing the composition of Nycobase 5750. The first intensity peak represents the heaviest PEC atoms while the second peak the lightest. The area under the curve gives a rough estimation of the ratio in mass of each component. Reproduced from [208].

MD simulations of different PEC-based fluids are performed at different temperatures and at ambient pressure. The MD systems are composed of a total of 100 molecules. If the models represent binary mixtures, the 1:4 proportion is respected: 20 molecules represent PEC with the highest n-alkane chain length while the lightest molecules make up the rest of the fluid. The simulation procedure for the bulk systems is described in Chapter II.

First, density is evaluated, as it is easy to compute and allows to have a first estimation of the composition of the fluid. The deviation of masses with respect to experimental Nycobase 5750 measures estimates the veracity of the model and elucidates the possible composition. For the possible candidates, Green-Kubo viscosity calculations (see Chapter II) are then performed. The results are summarized in Table III.6 for density and Table III.7 for viscosity values, where PEC5, PEC7 and PEC9 base oils are only considered as a reference for evaluating the precision of the force field. It should be further noted that in Table III.6 and Table III.7 the relative concentration of the binary mixture PEC5-9 used in experiments is unknown [207]. Therefore, MD results and experiments cannot be directly compared between each other as they may not be the same fluid. This would consequently justify the differences in density and viscosity between experiments and simulation for this binary mixture.

Table III.6. Density values for different polyol ester base oils from experiments and MD simulations. In parenthesis the relative error in percentage value calculated as $^{(Commercial\ NPE - PEC)}/_{Commercial\ NPE} \times 100$ is indicated. Values calculated from regression of experimental data are specified in italics. Experimental data of the commercial NPE are provided by [208], of PEC 5 by [205], of PEC 7 and PEC 9 by [206] and of PEC5-9 by [207].

T / K	Commercial NPE / g.cm^{-3}		PEC5 / g.cm^{-3} (%)	PEC7 / g.cm^{-3} (%)	PEC9 / g.cm^{-3} (%)	PEC5-9 / g.cm^{-3} (%)	PEC7-9 / g.cm^{-3} (%)
293	0.9869	Exp	*1.0187 (-3.22)*	0.9843 (+0.26)	0.9606 (+2.66)	0.9774 (+0.96)	-
		MD	-	0.9353 (+5.23)	-	0.9698 (+1.73)	0.9496 (+3.78)
313	0.9717	Exp	*1.007 (-3.59)*	0.9692 (+0.26)	0.9464 (+2.61)	0.9625 (+0.95)	-
		MD	-	0.9185 (+5.47)	-	0.9601 (+1.19)	0.9348 (+3.80)
333	0.9565	Exp	0.9867 (-3.14)	0.9541 (+0.27)	0.9319 (+2.59)	0.9477 (+0.94)	-
		MD	-	0.9052 (+5.36)	-	0.9411 (+1.61)	0.9251 (+3.28)

Table III.7. Viscosity values for different polyol ester base oils from experiments and MD simulations. In parenthesis the relative error in percentage value calculated as $^{(Commercial\ NPE - PEC)}/_{Commercial\ NPE} \times 100$ is indicated. Values calculated from regression of experimental data are specified in italics. Experimental data of the commercial NPE are provided by [208], of PEC 5 by [205], of PEC 7 and PEC 9 by [206] and of PEC5-9 by [207].

T / K	Commercial NPE / mPa.s	/	PEC5 / mPa.s (%)	PEC7 / mPa.s (%)	PEC9 / mPa.s (%)	PEC5-9 / mPa.s (%)	PEC7-9 / mPa.s (%)
293	55.55	Exp	-	-	-	-	-
		MD	-	33.70 (+39.33)	-	42.10 (+24.28)	-
313	23.90	Exp	16.60 (+30.6)	20.80 (+13.00)	30.90 (-29.30)	32.10 (-34.30)	-
		MD	-	13.40 (+43.93)	-	17.18 (+25.52)	-
333	12.47	Exp	9.09 (+27.1)	11.50 (+7.80)	15.40 (-23.40)	15.10 (-21.00)	-
		MD	-	5.35 (+53.09)	-	8.81 (+29.52)	-

Among the monomolecular fluids, PEC7 presents the closest rheological behavior to the Nycobase 5750. However, the commercial base oil is a binary mixture. For the two tested mixtures, PEC5-9 presents the most similar behavior to the Nycobase. Therefore, this fluid is selected for later MD simulations as a representative base oil of the aerospace industry. It will be labeled as NPE.

III.2. Density

The density allows to have a first estimation of the precision and validity of the L-OPLS-AA force field at different pressure and temperature conditions. The density was evaluated with MD simulations on a 5.0 x 5.0 x 5.0 nm^3 static volume. The volume contained either 360 benzyl benzoate molecules, or 92 squalane molecules.

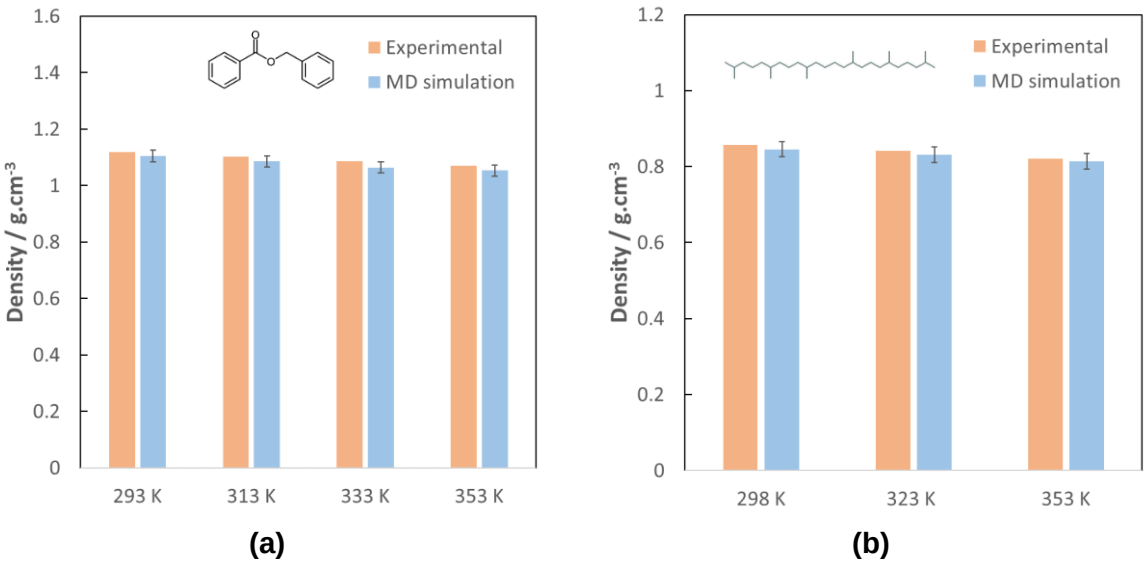

Figure III.6. Comparison between experimental and MD simulation values of density for (a) benzyl benzoate and (b) squalane at ambient pressure and different temperatures. Experimental data of BB and squalane are given by [8] and [209] respectively.

Figure III.6 shows a direct comparison between experimental and numerical values of the density at ambient pressure for different temperatures. Only the results corresponding to BB and squalane are represented as Nycobase density values have already been discussed in the previous section. The MD simulation results were accurate within 2% of the experiments. The density for both fluids is underpredicted for the temperatures studied.

The influence of pressure was evaluated in MD at constant temperature and compared to a Tait equation of state parametrized for BB [8],and squalane [209] as presented in Figure III.7. In the case of BB (Figure III.7.a), MD values are close to experiments up to 400 MPa, where the relative error starts to slightly increase. Squalane shows a similar behavior to BB, with a deviation of the empirical curve starting at about 300 MPa. In both cases, this range of pressures corresponds to values for which experiments have been performed. Data beyond these pressures are extrapolated through the empirical model.

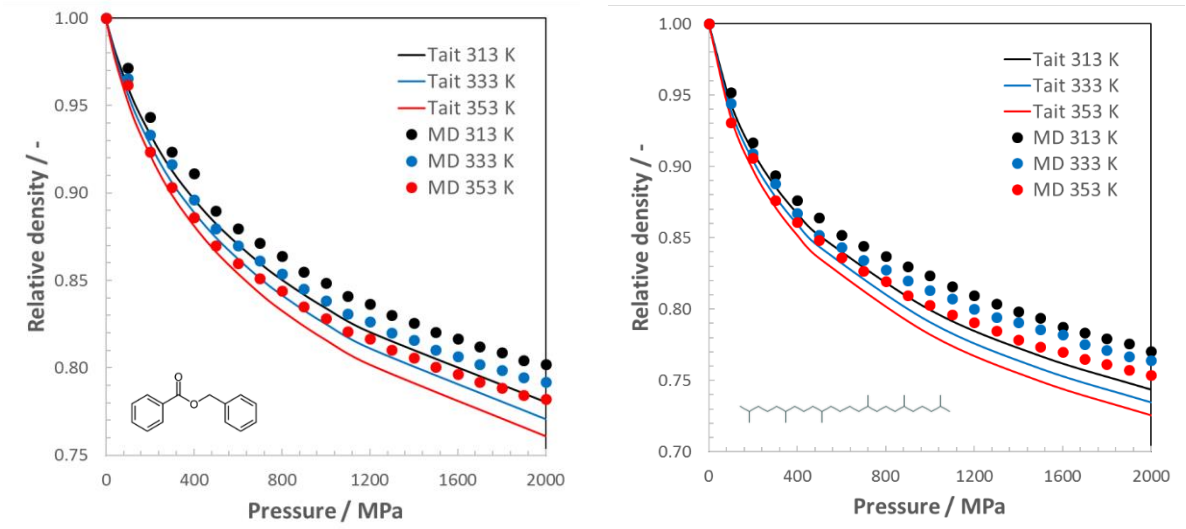

Figure III.7. Relative density of (a) benzyl benzoate and (b) squalane at three different temperatures (313 K, 333 K, and 353 K) and pressures ranging from 0.0001 to 2 GPa. Numerical data for (a) and (b) is compared to a Tait equation of state [209, 8].

III.3. Viscosity

The Newtonian viscosity is evaluated through a Green-Kubo equation of state, as specified in the previous Chapter II. In combination with the density calculations, the FF is validated for the three test fluids. Even though the relative error between experiments and simulations goes up to values around 19% (see Figure III.8) for the case of squalane, the L-OPLS-AA force field still gives reasonable values of Newtonian viscosity. Unfortunately, there is a lack of experimental viscosity data at high pressures for both BB and SQ.

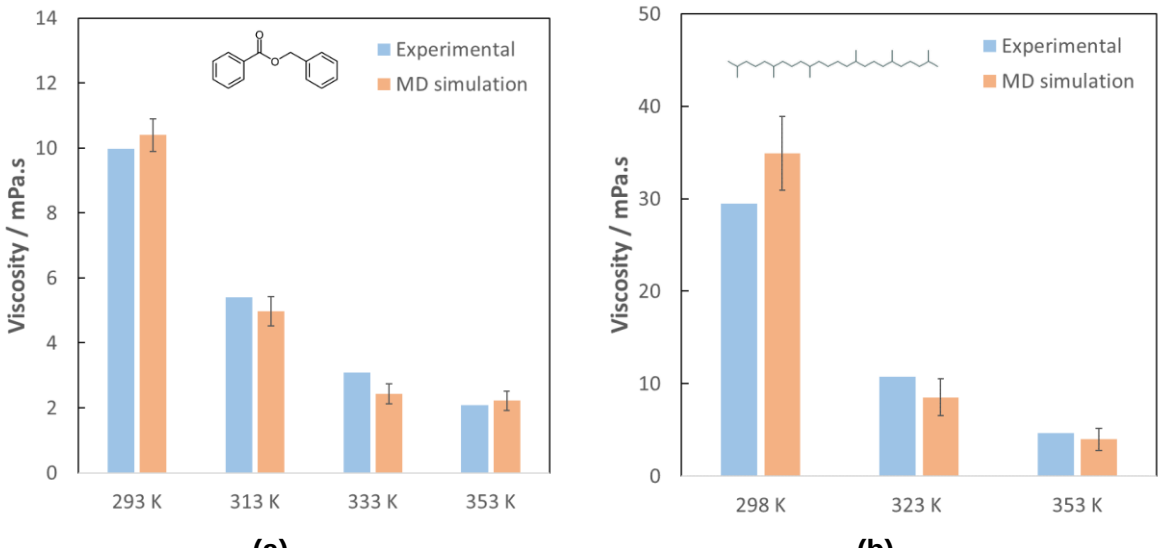

Figure III.8. Comparison between experimental and MD simulation values of Newtonian viscosity for (a) benzyl benzoate and (b) squalane at ambient pressure for different temperatures. Experimental data of BB and squalane are given by [8] and [209] respectively.

The error bars for the simulation data are computed from the standard deviation of the Green-Kubo viscosity during the last 5 ns of the simulation.

III.4. Phase diagram

A phase diagram for each fluid was established for pressures between 0.0001 and 10 GPa. For every simulation run, the pressure was set constant through a Nosé-Hoover barostat. Initially set to 1000 K with a Nosé-Hoover thermostat, the temperature was progressively decreased in steps of 25 K until reaching 100 K. The evolution of the volume of the molecular system with temperature at constant pressure was captured, identifying a point of inflexion related to a change in the nature of the fluid. An example is given in Figure III.9, where BB is cooled down at 0.0001 GPa. In this figure, two transition points are found at 300 K (supercooled-liquid transition) and at 550 K (liquid-gas transition). Additional information on these diagrams for BB, SQ, and the NPE mixture are given in Appendix A. The thermodynamic state at which this change of slope appears corresponds to a phase transition [210], and is represented in a pressure versus temperature plot such as in Figure III.9. In this figure, different regimes can be identified, be it a gaseous state, a liquid state or a supercooled state. The supercooled state corresponds to the physical state that originates when the liquid cools down below the melting temperature without crystalizing. Due to the very rapid cooling rates imposed during the EMD simulation runs, the molecular fluid system is unable to crystallize, resulting in amorphous structures.

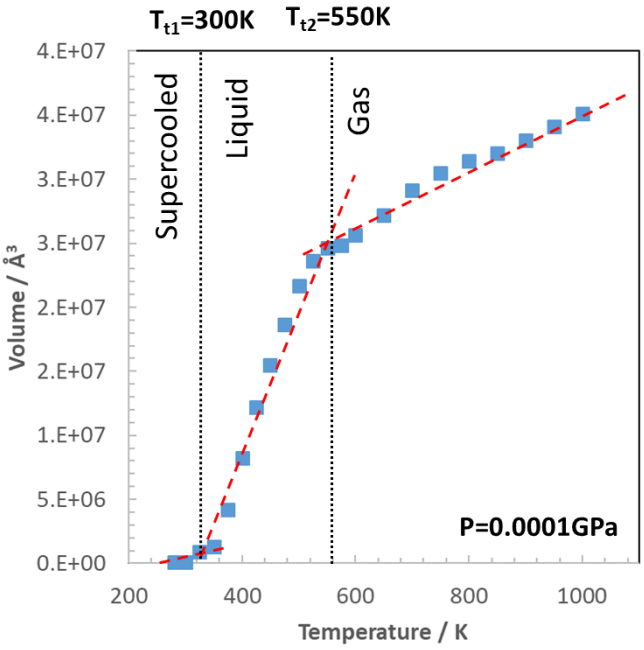

Figure III.9. Evolution of the volume of BB with temperature at a constant pressure of 0.0001 GPa during one simulation run. The difference in slopes marks the transition points reported in the phase diagrams in Figure III.10.

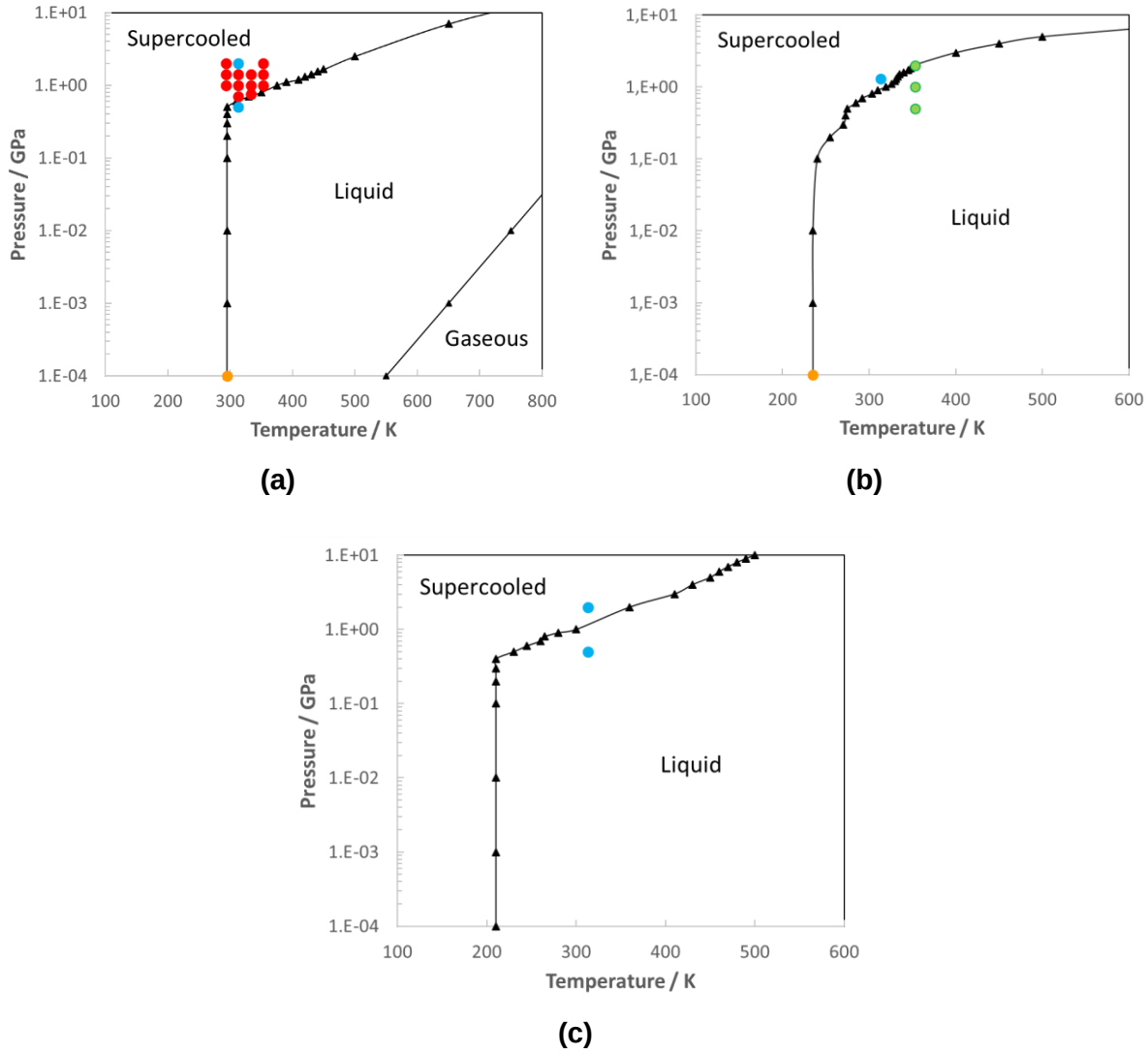

Figure III.10. Phase diagrams for (a) benzyl benzoate, (b) squalane and (c) NPE. Blue points correspond to the pressure and temperature conditions confined NEMD simulations are run in this work (Chapter IV and Chapter V). Black triangles are MD results from this work. Red marks in (a) represent experimental measurements of BB [36] where LSS was captured. In (b), green marks represent the thermodynamic conditions at which squalane was evaluated under confinement [10]. No LSS was captured here. For both (a) and (b), orange marks symbolize experimental measures of the melting temperature taken from [39] and [40] respectively.

For the three fluids tested, a constant melting temperature with pressure is found up to a critical pressure, for which the transition evolves exponentially. For BB, the melting temperature remains close to 300 K for pressures below 0.6 GPa, while for squalane the temperature is around 240 K below 0.65 GPa. As for the binary mixture NPE, the melting temperature is around 210 K for pressures under 0.4 GPa. Orange marks in Figure III.10 symbolize the experimental measures of the melting temperature from benzyl benzoate [39] and squalane [40] respectively. Additionally, with this method, no liquid-to-gas transition has been found for squalane and NPE.

Furthermore, in the BB phase diagram (see Figure III.10.a), red marks are drawn to represent the thermodynamic conditions at which LSS was captured during experimental tests [36]. No experiences for squalane (see Figure III.10.b) have been conducted over the transition line in the literature. Green marks corresponding to the simulating conditions of Ewen et al. [10] (in liquid state) have been drawn. It was pointed out in [10] that model lubricants such as squalane experience a continuous increase in their shear stress with increasing values of shear rate, without any evidence of a plateau behavior, and which drastically contrasts with the friction behavior of BB [36]. In the following chapters, NEMD confined simulations of the lubricants under the conditions specified by the blue marks in the diagrams in Figure III.10 will be performed in order to see if there is a link between the physical state of the lubricant and its friction behavior.

III.5. Conclusion

In this Chapter, the rheological behavior and characteristics of lubricants were reviewed in the scope of this work. Commercial lubricants present very complex formulations which hinder the modeling of every component for atomic-scale simulations. In particular, only the base oils are chosen to be simulated in MD simulations, being the most abundant constituent in the formulation of a lubricant (over 90% in most cases). Three molecules were in total selected: benzyl benzoate as a characteristic traction-like fluid, squalane as a characteristic model lubricant, and the commercial Nycobase 5750, a base oil used for aerospatial applications. The Nycobase 5750, after an exhaustive analysis, was considered to be a binary mixture composed of two polyol esters, where 20% of the constituents are PEC9 molecules and 80% PEC5 molecules. Each one of these base oils are affected by the L-OPLS-AA force field to model the atomic interactions.

The force field was validated by direct comparison between already existing experimental data and MD simulation results of both density and viscosity. The values obtained from numerical analysis are in good agreement with experiments and give a good estimation of the precision that can be expected from this FF. Relative errors for density are below 2%, while viscosity measurements are more susceptible to deviate from experiments. However, the accuracy of the MD simulations is sufficient to accept this FF for subsequent analysis. Additionally, phase diagrams were performed for the three fluids, on the basis of MD simulations, and partially validated by experiments. They allow to establish a starting point for the discussion on the frictional behavior of these fluids considering their thermodynamic state.

Chapter IV

Flow and friction of confined fluids

Chapter IV
Flow and friction of confined fluids

Friction reduction has become an important concern for the saving of natural resources and energy, especially in lubricated systems. Amongst the phenomena to be expected under the severe operating conditions is the limiting shear stress phenomenon, which has yet to be associated with a specific physical origin. Various scenarios have been proposed in literature, but each one of them fails to completely explain this ultimate behavior of the lubricants. In recent years, the idea that the confined lubricant undergoes a transition from a liquid state to solid-like state has gained notable support [8]. In this Chapter, this theory will be approached and analyzed by direct comparison between experimental and NEMD simulation results. A link with the physical state at equilibrium of the three test fluids introduced in Chapter III will be established. In addition to this, the flow behavior of the fluid molecules under confinement will be examined. The results presented in this Chapter have been partially published in Physical Chemistry Chemical Physics (reference [211]).

IV.1. Friction at high pressure and high shear rates

At present, the prediction of friction still constitutes a challenge in industry. Not only a combination of extreme pressures and shear rates has to be reproduced in a controlled environment, but also care has to be taken in order to not generate unexpected temperature increases. Friction in EHL contacts is also significantly affected by the molecular structure of the base fluid, so that the prediction of friction needs to account on how the testing conditions will affect the behavior of the lubricant molecules. Severe shear rates, for example, will lead to a non-linear rheology of the lubricant, a viscosity variation due to shear heating and to non-equilibrium phase transitions of flow behavior [212].

Friction is typically represented by the coefficient of friction C_f, which is macroscopically defined as the ratio of the average tangential friction forces in the main entrainment direction F_x and the applied normal load F_z:

$$C_f = \frac{F_x}{F_z} \tag{IV.1}$$

Friction varies with the sliding velocity $\Delta u = u_1 - u_2$, which is the difference in velocity of the two confining solid walls following the shearing direction, where u_1 and u_2 are respectively the velocities of surfaces 1 and 2. From here, an apparent shear rate $\dot{\gamma}$ can be defined as:

$$\dot{\gamma} = \frac{\Delta u}{h_c} \tag{IV.2}$$

with h_c the central film thickness of the contact. These magnitudes are representative of the macroscopic solicitations applied to the lubricant and have an impact on its response. This is why friction is represented with respect to the shear rate in this work.

Under the severe conditions of pressure and shear rate encountered in EHL, the lubricants experience the different friction stages presented in Chapter I, dominated in each case by either a viscous, a non-linear or a plastic-like response of the confined lubricant. In particular, the plastic-like response appears at high contact pressures and very high shear rates and is characterized by a plateau regime. In this regime, friction becomes rate-independent. An illustration depicting this phenomenon appears in Figure IV.1, where friction measurements for benzyl benzoate at 313 K and for squalane at 353 K at different pressures are plotted against the experimental shear rate given by equation (IV.2). Figure IV.1.a evidences a saturation of the coefficient of friction once a critical pressure and a critical shear rate value are surpassed. For benzyl benzoate at 313 K, this critical pressure is equal to 0.67 GPa and the critical shear rate is around 3.10^6 s^{-1}. With respect to squalene, however, Figure IV.1.b does not show any plateau regime under the conditions studied by [10].

When the plateau regime is reached, the mean shear stress measured in the contact (obtained from the ratio between the mean frictional forces and the contact area) is related to the limiting shear stress phenomenon. It represents the ultimate response of the confined lubricant to the applied operating conditions [4]. There are still many questions pending as to what causes this phenomenon to appear [173], but there is much consensus that this behavior is an inherent property of the fluid. Bair et al. [213] even go to the point as to affirm that the physical mechanisms of LSS encountered in polymers are virtually the same for fluids. Moreover, the ultimate behavior of the lubricant would originate as a consequence of the fluid undergoing a glass transition through the passage across the contact [214]. It would thus be linked to the yield stress of the newly created amorphous material, which would entrain extremely high viscosities [87]. Nevertheless, the mechanisms originating LSS are still open to debate, as many phenomena (interfacial wall-slip, shear banding or solidification) have been captured experimentally [173] and possibly falsely attributed to this phenomenon [178]. They have not yet been confirmed with simultaneous friction measurements.

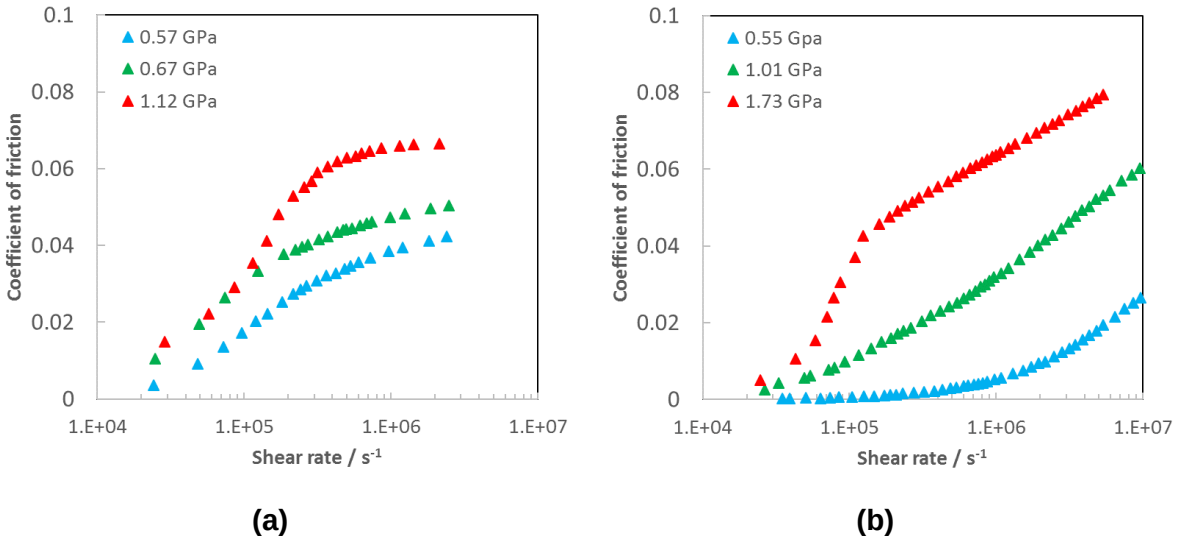

Figure IV.1. Friction measurements of (a) benzyl benzoate at 313 K [36] and of (b) squalane at 353 K [10] at different mean normal pressures.

High shear rates are reported to also have a crucial impact in the behavior of confined lubricants in an EHD contact. Indeed, atomistic simulations have revealed a series of different flow regimes that deviate from the typical Couette behavior with increasing rates of deformation [47, 46, 45, 215, 128]. These modifications in the lubricant flow can occur near the solid confining walls in the form of a certain structuration of the fluid molecules, giving rise to a local increase of the fluid density [160, 216, 99]. Moreover, they may also appear concentrated in the central region of the film thickness or across the whole lubricant film [101, 42, 100, 179]. All these local molecular arrangements are suspected to be associated to the appearance of the LSS regime [173], in spite of the inability to simultaneously perform in-situ measurements of friction and observations of the flowing behavior [217, 214]. Hence, the aforementioned reasons make atomistic simulations attractive for the study of the frictional nature of nano-confined fluids submitted to EHD conditions. The results detailed in this Chapter are inspired from the experiments of Figure IV.1 and attempt to give insights into the mechanisms of the LSS apparition.

IV.2. Methodology

The physical state of the fluid has been hinted as one of the main possible actors in the apparition of the LSS phenomenon. In order to prove these assumptions, a series of NEMD simulations were performed under the pressure and temperature conditions specified in Table IV.1, for a wide range of shear rate values, going from 10^8 up to 10^{11} s^{-1}. The MD models hereon presented consider lubricant molecules confined between two solid plates in order to replicate the confinement conditions of a real EHL contact. The molecular model considers either smooth iron oxide plates with either low or strong adhesion energies, or a rough surface with low adhesion energies. The surface models are detailed in Chapter II. The proposed values of normal loading and temperature are derived from the phase diagrams from Figure III.10 and allow to investigate the nature of the fluid state when there is shearing, and its response to friction.

Table IV.1. Experimental and NEMD simulation test conditions for benzyl benzoate, squalane and the neopolyol ester mixture, representing both conditions where the fluid is expected to be in either a liquid-like or a solid-like state. Report to Figure III.10 in Chapter III for additional information.

	Liquid-like state		Solid-like state	
Fluid	P_m / GPa	T / K	P_m / GPa	T / K
BB	0.5	313	2	313
SQ	2	353	1.2	313
NPE	0.8	300	1.4	300

The presence of two solid surfaces leads to the application of a new set of hypotheses, generally related to the geometry of the surface and to the adhesion energy at the solid/fluid

interface, both aspects associated to the corrugation and the commensurability [24] of the respective surfaces. The characteristics of the surfaces have been chosen so as to avoid any artifact due to the simulating conditions, and specifically to avoid slip at the solid/fluid interface, which is generally favored in the case of atomically smooth surfaces. The strategies chosen in this section to avoid these artifacts follow two directions: the chemical nature of the material used for the surface, and its degree of roughness. Regarding the first aspect, the LJ parameter ε of the iron atoms conforming the solid surfaces [24] can be artificially tuned, thus modifying the solid/fluid interfacial interactions and enabling to frustrate slip at the interface of the contact. Consequently, the influence of the surfaces on the flow and friction behavior would derive from the molecular arrangement of the fluid molecules induced by the smooth surfaces. On the other hand, the roughness degree of the confining surfaces can be altered while keeping the representative LJ parameters of the material conforming it [42, 43, 44], leading to a similar response to slip as with high interfacial adhesive energies. However, one key aspect has to be pointed out with respect to this strategy. Indeed, the roughness implementation is realistic only up to a certain extent. In fact, both the size and the distribution of the asperities are arbitrarily chosen with the sole purpose to frustrate slip and do not correspond to typical measured values in experiments (of the order of 0.1μm in experiments against the order of the nm in MD simulations). By adding roughness to the otherwise atomically smooth solid surfaces, a new constraint emerges into the system by impeding the fluid molecules to align parallel to the walls. On a final note, the film thickness has been fixed to a high enough value to ensure the independence of the friction value with the size of the simulation box, an aspect that will be further discussed in section IV.4.

IV.3. Influence of the surfaces on the flow behavior

Many questions are still revolving around the true nature of lubricants in a typical EHL contact, primarily due to the inability to simultaneously perform friction measurements and capturing the different flow phenomena in the contact region when both severe contact pressures and shear rates are in place. Regardless of some of the advances that have turned up in the last decades in this field [218], no conclusive answer has been given yet.

In this section, we focus on the surface effects on the molecular structure of the fluids and on flow, so mostly one fluid is considered: benzyl benzoate. Confined benzyl benzoate at 313 K is simulated at pressures above and below the transition pressure following the phase diagram in Figure III.10. The confined molecular system is analyzed with three different surfaces: atomically smooth iron oxide slabs with either low or high adhesion energies, and rough iron surfaces with low adhesion energy. Squalane is studied only considering rough surfaces as smooth surfaces have already been approached in [10]. Finally, the NPE mixture will be treated just with rough surfaces too.

Case 1. Shear between smooth surfaces with low surface energy (smooth ε^-)

With this first case, benzyl benzoate molecules are confined between two atomically smooth iron oxide plates with the lowest adhesion energy (corresponding to the reference value for Fe in the FF). In Figure IV.2, both the atomic mass density profile and the x-velocity profile across the film thickness are represented for two pressures: a pressure equal to 0.5 GPa (below the transition pressure of 0.65 GPa at the simulated temperature) and a pressure

equal to 2 GPa (above the transition pressure). The density profiles present layering, with strong peaks close to the confining walls and propagating towards the center of the film. Regarding the flow behavior, at low pressure values, the system presents a Couette-like profile in the central part of the thickness with some localized slip at the solid/fluid boundary (see Figure IV.2.a). If the pressure in the system is increased, the cohesion of the fluid molecules is increased and hence slip is favored at the level of the solid surfaces. At high pressure, the resulting velocity profile in the shearing direction corresponds to a plug flow, where a strong degree of slip is present at each surface (see Figure IV.2.b).

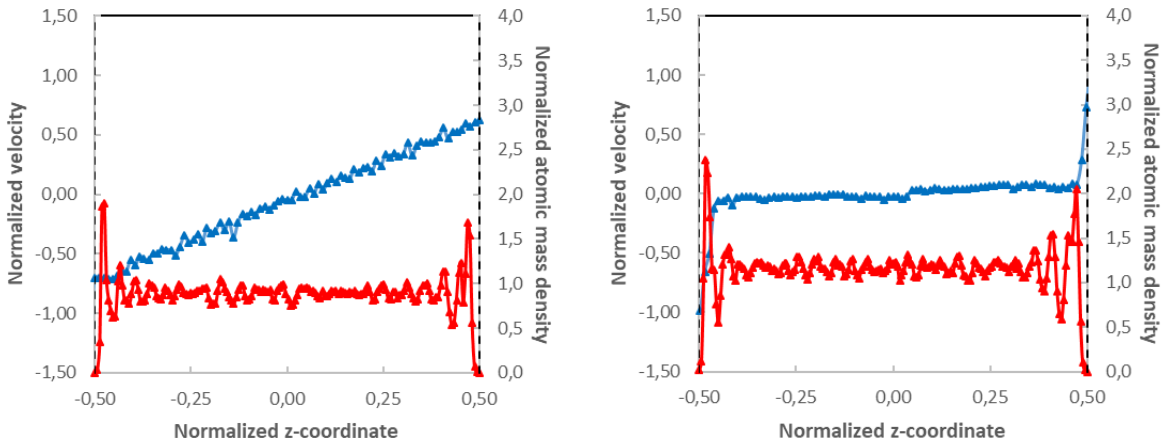

(a) (b)

Figure IV.2. Velocity (blue) and atomic mass density (red) profiles for benzyl benzoate at 313 K, 50 m.s^{-1}, and (a) 0.5 GPa and (b) 2 GPa. The velocity profile has been normalized with respect to the imposed sliding wall velocity, and the density profile with respect to the bulk density value at the given pressure and temperature conditions. They are represented versus the normalized z-coordinate $^{z}/_{h}$, where the origin is considered in the center of the film thickness. The film thickness is about 13 nm. Atomically smooth iron oxide surfaces with low adhesion energy (smooth ε^{-}) are used.

Case 2. Shear between smooth surfaces with high surface energy (smooth ε^{+})

The response to shear changes drastically with respect to the preceding case when the interfacial interactions are increased, although similar trends are observed. As reported with case 1, the density profile presents a succession of peaks distributed across the film thickness. This kind of behavior has already been observed for simple LJ fluids [45] and for more complex fluids [10] when they are confined between two parallel smooth surfaces. Figure IV.3 shows the velocity and the atomic mass density profiles across the film thickness for benzyl benzoate for the same simulated conditions as case 1, but with higher adhesion energies at the solid/fluid interface by artificially changing the ε parameter of Fe (see Chapter II). At low pressure, for 0.5 GPa (Figure IV.3.a), the velocity profile in the shearing direction slightly deviates from a Couette flow by presenting two to three molecular layers locked to the solid slabs. It thus results in a velocity profile where molecular layers close to the solid surfaces are entrained at the same sliding velocity imposed at the walls, while only the central region of the film is actually

sheared. The results shown in Figure IV.3 are consistent with NEMD simulations of confined n-alkanes sheared at high pressures and shear rates [41]. When the pressure is elevated to values superior to the transition pressure, shear can neither take place in the central region of the film because of the increased viscosity, nor at the solid/fluid interface due to the high adhesion energies. Shear thus can only localize in between these two regions (see Figure IV.3.b), generating a flow regime defined as plug-slip by Ewen and co-workers [10] for simulations performed on similar fluids.

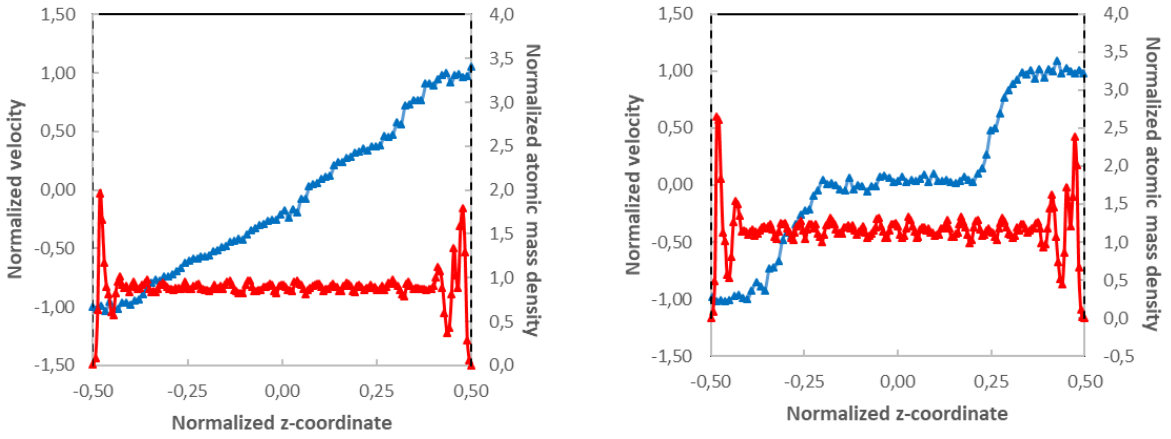

(a) (b)

Figure IV.3. Velocity (blue) and atomic mass density (red) profiles for benzyl benzoate at 313 K, 50 m.s^{-1}, and (a) 0.5 GPa and (b) 2 GPa. The velocity profile has been normalized with respect to the imposed sliding wall velocity, and the density profile with respect to the bulk density value at the given pressure and temperature conditions. They are represented versus the normalized z-coordinate $^{z}/_{h}$, where the origin is considered in the center of the film thickness. The film thickness is about 13 nm. Atomically smooth iron oxide surfaces with high adhesion energy (smooth ε^{+}) are used.

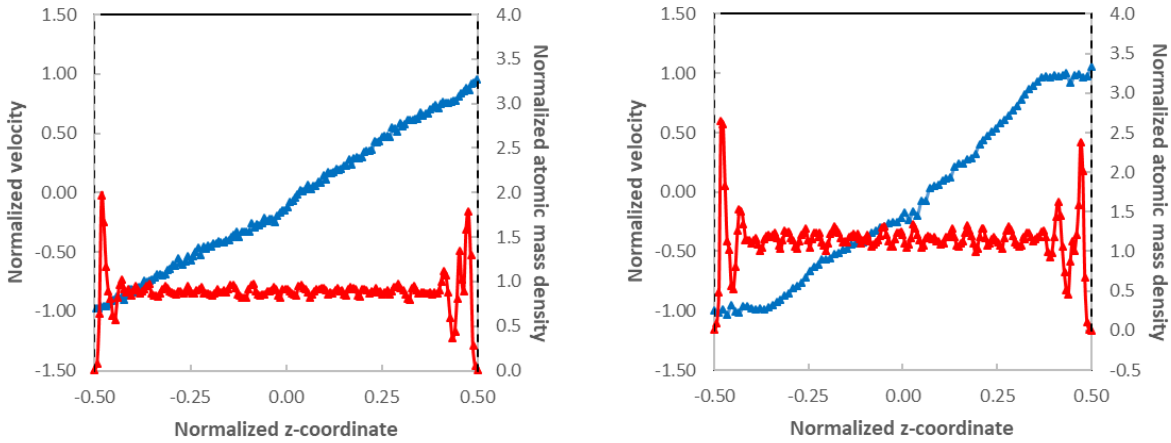

(a) (b)

Figure IV.4. Reproduction of the results from [10] with squalane. Velocity (blue) and atomic mass density (red) profiles for squalane at 353 K, 50 m.s^{-1}, and (a) 0.5 GPa and (b) 2 GPa.

The velocity profile has been normalized with respect to the imposed sliding wall velocity, and the density profile with respect to the bulk density value at the given pressure and temperature conditions. They are represented versus the normalized z-coordinate $^{z}/_{h}$, where the origin is considered in the center of the film thickness. The film thickness is about 13 nm. Atomically smooth iron oxide surfaces with high adhesion energy (smooth ε^{+}) are used. The results obtained with our simulations are similar to those presented by [10].

In particular, regarding the squalane molecule, it has already been studied in literature by [10] at 2 GPa and 353 K, but confined between two parallel atomically-smooth iron oxide plates with high adhesion energies. This was done, they discussed, in order to avoid wall slip. Figure IV.4 reproduces the velocity and atomic mass densities encountered under these pressure and temperature conditions, obtaining similar outputs than the ones presented by [10]. The profiles that were measured correspond to those encountered in Figure IV.3.a, which are found at pressures below the transition pressure.

Case 3. Shear between rough surfaces with low surface energy (rough ε^{-})

Finally, rough iron surfaces have been considered as boundary conditions for benzyl benzoate, squalane, and the neopolyol ester mixture. In Figure IV.5, both scenarios with pressures lower and higher than the transition pressure are presented for the three simulated fluids. Little to no variation is seen with respect to the velocity profiles, where some locking is present at higher pressures. With respect to the density profiles, practically no molecular layering is measured, a response that strongly contrasts with smooth surfaces.

In this case 3, by modifying the confinement conditions, the fluids display an almost pure Couette velocity profile, independently of the applied normal load. The density profiles also remain unaffected by pressure, where layering is not present across the film thickness, and density is kept around bulk values.

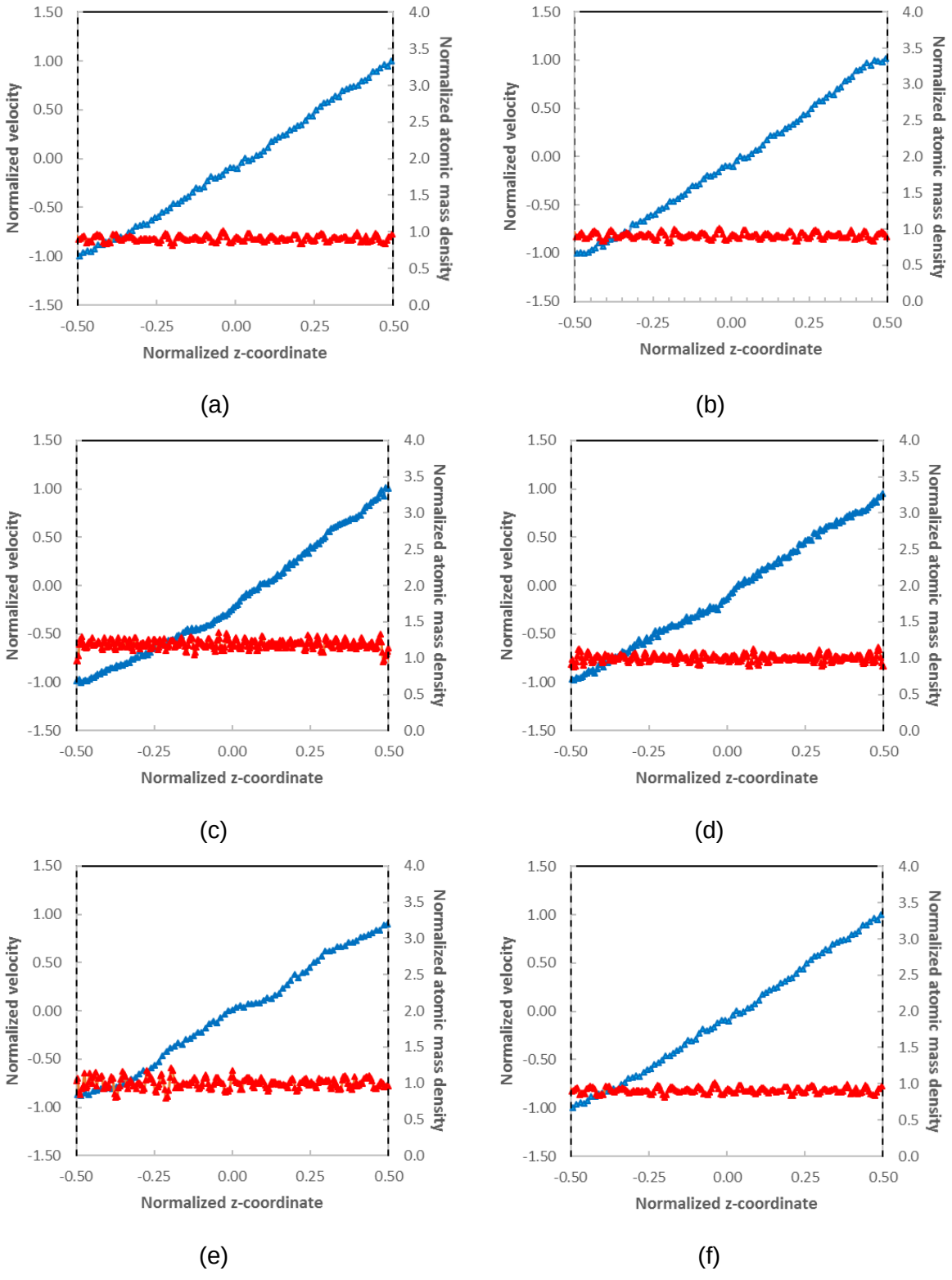

Figure IV.5. Velocity (blue) and atomic mass density (red) profiles for benzyl benzoate at 313 K, 50 m.s^{-1}, and (a) 0.5 GPa and (b) 2 GPa, squalane at 50 m.s^{-1}, (c) 353 K and 2 GPa, and (d) 313 K and 1.2 GPa, and finally the NPE mixture at 50 m.s^{-1}, 300K, and (e) 0.8 GPa and (f) 1.4 GPa. The velocity profile has been normalized with respect to the imposed sliding wall velocity, and the density profile with respect to the bulk density value at the given pressure and temperature conditions. They are represented versus the normalized z-

coordinate $^{z}/_{h}$, where the origin is considered in the center of the film thickness. The film thickness is about 13 nm in each case. Atomically smooth iron surfaces with low adhesion energy (rough ε^{-}) are used.

Synthesis

Table IV.2 synthetizes the expected flow response to the different boundary conditions imposed on the confined fluid, and on the applied operating conditions.

Table IV.2. Synthesis of flow behavior for pressures below and above the transition pressure, where the velocity profile in the shearing direction (red) and the density profile (blue) are represented.

Surface	α-iron oxide [100] (smooth)		α-iron [100] (rough)
ε / kcal.mol^{-1}	ε^{-}	ε^{+}	ε^{-}
$P < P_t$	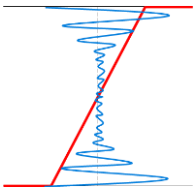	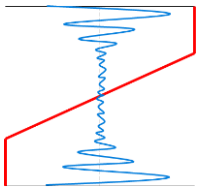	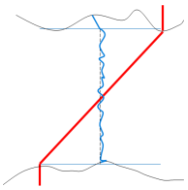
$P > P_t$	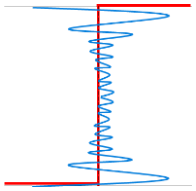	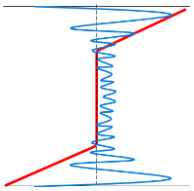	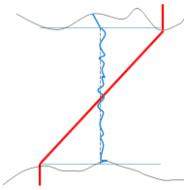

Figures IV.2 to IV.5 evidence how flow behavior results from a continuous competition between the fluid bulk interactions, piloted by the pressure and the temperature on the system, and the solid/fluid interfacial strength, which is driven by the LJ parameter of the surface atoms. Shear would thus originate in the region where these interactions are the weakest, where accommodation of the velocity can take place.

The influence of the surfaces, and hence the physics that govern the dissipation of energy in the contact region, is well represented Table IV.2. Here, there are two distinct contributions that come into play: on one side there is the geometric nature of the surface represented by the smoothness or roughness of the solid confining walls [25], and on the other side there is the surface energy, which accounts for the adhesion of the fluid molecules to the solid slabs. This last parameter in particular is piloted by the LJ parameter ε of the iron atoms [41] and induces either weak or strong interfaces i.e. it allows modifying the wettability of the

solid/fluid interface. Consequently, wall-slip or locking to the solid slabs originates respectively. In cases 1 and 2, because a smooth surface is used, layering is induced across the film thickness, creating weakness spots between molecular layers. However, because in case 2 the confining surfaces are highly adhesive, the weak regions are overcome so that locking extends over a few molecular layers. It thus results in shear to be localized in the bulk region of the confined fluid, whose shear strength is strongly dependent on pressure. Moreover, the flow behavior of the confined fluid changes drastically when the transition pressure is surpassed, transitioning from a classical Couette flow profile to strong plug flow. In the latter case, the accommodation of the solid wall velocity takes place close to the surfaces, in between dense layers of fluid molecules [42, 43, 44].

Finally, in case 3, rough surfaces prevent layering from occurring next to the surface (see Figure IV.5) so that no weakest area can be defined over the thickness. Thus, shear spreads across the whole contact displaying an almost pure Couette profile. Surprisingly, this velocity profile very slightly depends on the applied normal load, so that the profile appears unaffected by pressure effects.

The different conclusions that have been reached until now raise several questions with respect to the origins of friction regarding i) which velocity profile is most likely to be generated during experimentation and ii) whether the distinct velocity distributions affect the coefficient of friction. Indeed, the reader could expect a significant influence on friction, as it macroscopically translates into heat being dissipated out of the contact. The aforementioned correlation should clarify if indeed the LSS can originate from the shear distribution.

IV.4. A quantitative experimental/numerical comparison of friction

Friction was accounted for by the friction coefficient C_f which was calculated in simulations from the tangential stress response τ_{xy} from the outer layer of atoms of the top and bottom solid surfaces to the sheared fluid. It can be expressed as the ratio between τ_{xy} and the applied normal load P, time and spatially averaged over the two confining surfaces:

$$C_f = \frac{\langle \tau_{xy} \rangle}{P} \tag{IV.3}$$

The friction coefficient was initially measured for confined BB at 313 K and 2 GPa for different film thickness values, resulting in the diagram of Figure IV.6.a, where friction has been plotted against the gap between surfaces for the three tested boundary conditions. Friction has also been measured for SQ at 313 K and 1.2GPa, and for NPE at 300K and 1.4 GPa, for different film thicknesses but only considering iron rough surfaces (see Figure IV.6.b and c). Large oscillations of friction are visible as the film thickness is reduced to a few nanometers [41]. For large film thickness values, on the contrary, friction stabilizes around a set value, which is the same for every given surface nature (see Figure IV.6).

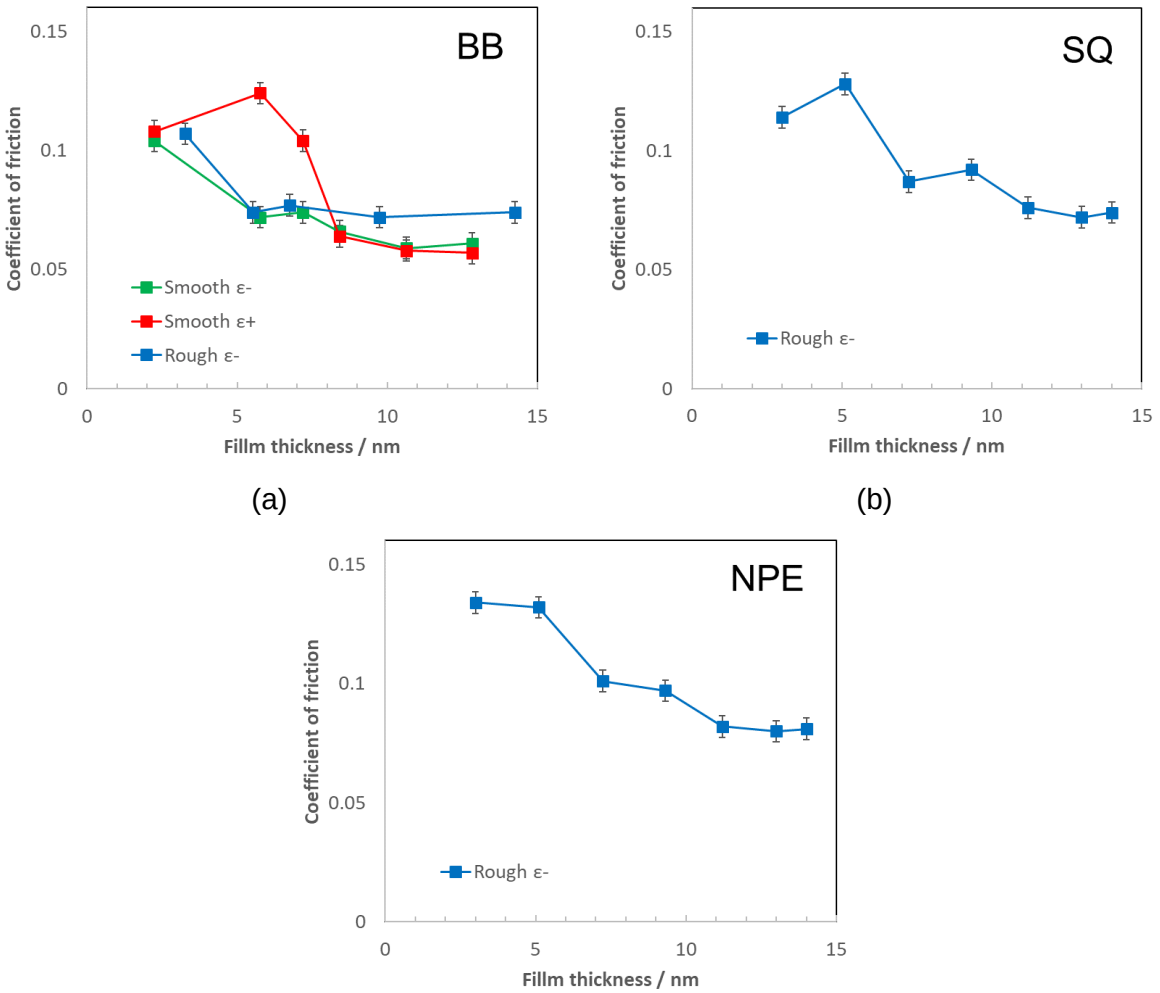

Figure IV.6. Film thickness dependence of friction for confined systems of (a) BB at 313 K and 2 GPa, (b) SQ at 313K and 1.2 GPa, and (c) NPE at 300 K and 1.4 GPa. Only rough surfaces are used for the SQ and NPE systems. The apparent shear rate is, in each case, about 10^9 s^{-1}.

Figure IV.6 depicts how friction decreases with increasing film thickness in an oscillating manner until it reaches a stable value, a behavior that has already been reported with MD simulations for confined systems of n-alkanes [41]. From hereon, two conclusions can be highlighted. First, a minimum film thickness exists for which friction becomes invariable i.e. friction becomes independent of the size of the system. Secondly, a quantitative comparison between experimental and simulation data is possible.

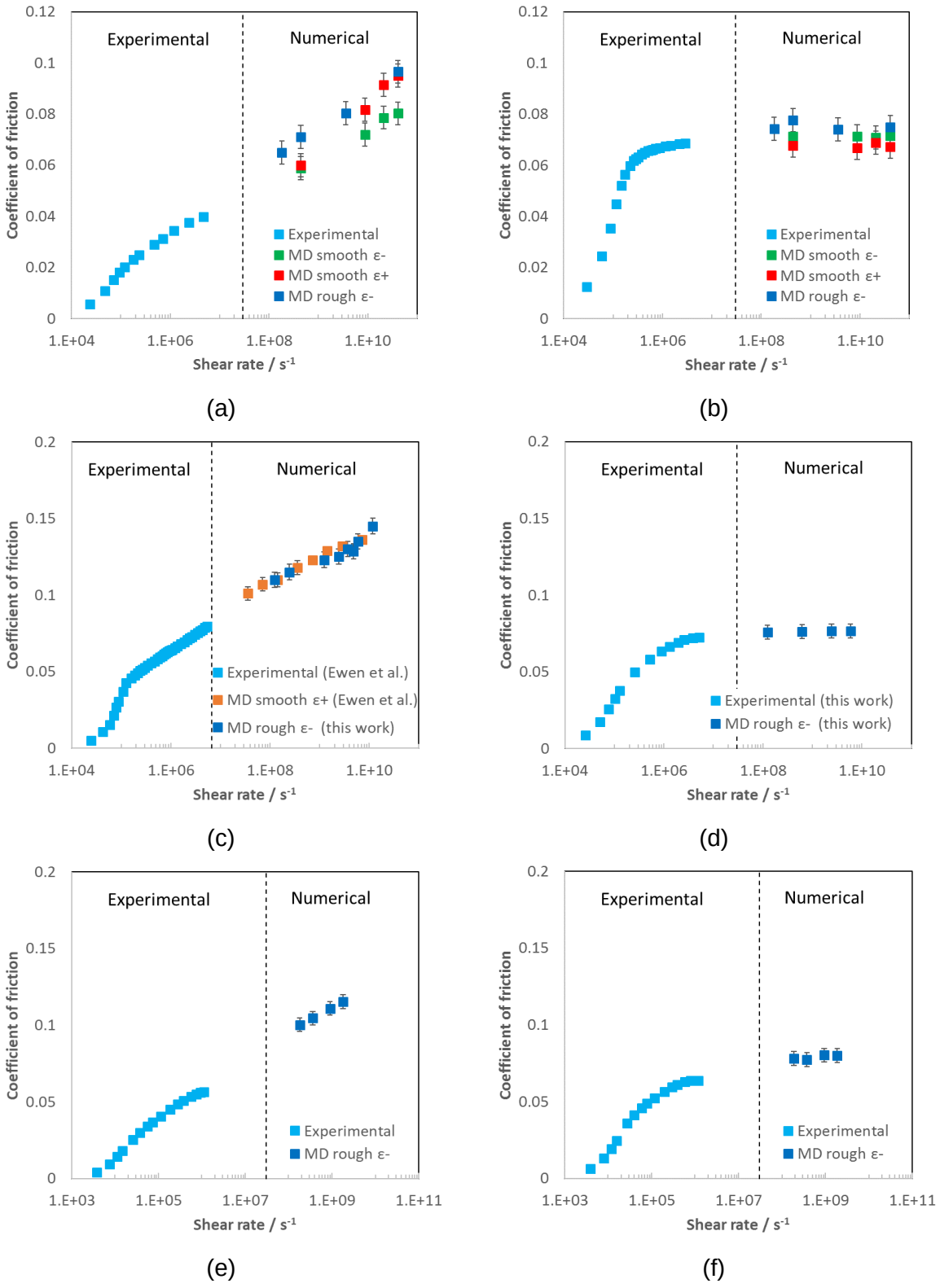

Figure IV.7. Coefficient of friction versus shear rate for BB at 313 K and (a) 0.5 GPa and (b) 2 GPa, for SQ at (c) 353 K and 2 GPa, and (d) 313 K and 1.2 GPa, and NPE at 300 K and (e) 0.8 GPa and (f) 1.4 GPa. For figure (c), experimental and numerical data with smooth surfaces come from [10]. For figures (d), (e) and (f), new experimental measurements following the procedure in [36] are confronted to numerical data. In all the plots, the vertical dashed line marks the separation between experimental (left) and MD (right) results.

It should also be noted that for each boundary condition applied to the BB system, different velocity and density profiles were measured even though they all converge towards similar values of friction. It suggests no apparent connection between flow and friction behavior. Indeed, flow behavior originates from the confinement conditions encountered in the contact (pressure and temperature) as well as from the characteristics of the solid confining walls (roughness and wettability). The friction value, however, is independent of the choice of the solid surfaces, and thus of the flow regime, as long as the film thickness is big enough.

In Figure IV.7.a and in Figure IV.7.b, BB friction measurements from experimental data measured by Ndiaye et al. [36] are compared to NEMD simulation data of 13 nm thick film systems of the same fluid submitted to 313 K and both to 0.5 and 2 GPa. Previous experimental and NEMD simulation friction data are also available for SQ at 353 K and 2 GPa (Figure IV.7.c) [10]. They are compared to new simulation data of SQ confined between rough surfaces. In addition, friction behavior for SQ at 313 K and 1.2 GPa is investigated (Figure IV.7.d). The analysis is finally completed by directly comparing data for the NPE mixture for both experiments and simulation with rough surfaces in Figure IV.7.e and Figure IV.7.f. All new experimental data originate from P. Vergne at LaMCoS and have been provided following the procedure detailed in [36]. The experimental pressures for the six cases correspond to the averaged pressures in the contact region. For all six cases presented, coefficients of friction calculated from MD are in good accordance with experiments, even though the time and length scales differ by several orders of magnitude. A similar outcome was reached by [10] for traction fluids and for a linear alkane.

With regards to the LSS behavior, the plateau regime is correctly quantitatively predicted from NEMD simulations of confined BB once the melting pressure of the fluid (according to the phase diagram in Figure III.10) is surpassed. This correlation between physical state and friction response is successfully reproduced for SQ and for the NPE mixture, when shearing under solid-like conditions, called supercooled state in Figure III.10. Indeed, it should be noted that for SQ submitted to 2 GPa and 353 K, no plateau regime is expected as the fluid is supposed to be in a liquid state (see Figure III.10), an aspect that was not considered beforehand in [10]. Thus, for the molecular structures studied in this Chapter, it can be concluded that both the LSS and the phase transition are two strongly interconnected concepts, even if no direct causality between both phenomena is proven. In addition to this, the sensitivity of the fluid to both pressure and temperature could also be significantly affected by its deformation (shearing), so that the LSS response may originate from a more sophisticated mechanism, possibility related to its dynamic behavior. This last notion will be revisited in the next Chapter. Moreover, this would lead friction maps such as [45, 46, 47] (derived from confined NEMD simulations using smooth surfaces) to be restrained to very particular cases, with no direct significant influence on macroscopic phenomena.

Finally, it can be concluded that the plateau behavior of confined fluids under EHD conditions and the phase transition are interrelated concepts. There is substantial evidence proving that for every fluid there is a given pressure and temperature combination for which it undergoes a phase transition from a liquid to a solid-like state. When in the liquid state, the fluid molecules have enough liberty to respond and to adapt to the generated stresses, so that friction can evolve with increasing shear rates. This would be evidenced by phenomena like shear thinning. At higher rates, the LSS is reached.

IV.5. Conclusion

In this Chapter, a series of NEMD simulations of confined benzyl benzoate, squalane, and a binary mixture of neopolyol esters have been presented, where flow and friction have been studied with respect to different confining surfaces of various natures. The results have highlighted the strong impact of the confining walls on the flowing mechanisms. Indeed, if either the geometry or the physical nature of the surfaces is slightly modified, the resulting flow profile can be a homogeneous Couette profile or present localized wall-slip or locking. Flow was then explained by a continuous competition between interactions occurring at the bulk of the fluid and at the solid/fluid interface, deriving in shear being concentrated at the weakest interface. Surprisingly, friction appeared to be unaffected by the different flow profiles. Consequently, it was shown that no direct link could be established between friction measurements and the phenomenology associated with flow during shearing.

A second aspect of interest investigated in this Chapter is related to the simulated film thickness. The size of the MD model has a strong impact on the measured friction value when the thickness becomes very low (less than a few nm). It is only after a critical value of film thickness that the coefficient of friction reaches a constant value and becomes independent with the size of the simulated system. This last value of friction is taken to be the most representative for full film lubrication.

Finally, the coefficient of friction calculated from numerical simulation was directly compared to new and already existing friction data. Despite the different ranges of shear rates tested, the results show an excellent agreement between both sets of data. It evidenced the influence of pressure and temperature (or the physical state) on the response of the fluid on friction. Indeed, under nominal liquid conditions, the coefficient of friction increased continuously with shear rate while, when submitted to nominal solid-like conditions, the response in friction was saturated, leading to a plateau regime present in both experiments and simulation. The results highlight the strong correlation between the friction response of the fluid and its physical state. In addition, the friction results were independent on the choice of surfaces, for which different flow profiles were observed. It can thus be concluded that the LSS phenomenon is uncorrelated to the flow behavior of the confined fluid.

Chapter V

Molecular origin of the limiting shear stress

Chapter V
Molecular origin of the limiting shear stress

In the previous Chapter, a Molecular Dynamics model of three confined molecular fluids has been constructed and analyzed for various operating conditions. In particular, a limiting shear stress has been reached for the three fluids when high pressure (or low temperature) and high shear rates were simultaneously applied. This event raises some questions with respect to the mechanisms by which energy is dissipated when this regime is active, as a saturation in friction implies a limit in the capabilities of the fluid to dissipate heat. Temperature is also closely related to the kinetics of the atoms of the fluid. In this Chapter, two parameters (the fluctuation of velocity and the mean squared displacement) are reviewed aiming to describe the relationship existing between the friction response during shearing and the mobility of the molecules conforming the lubricants in order to elucidate the physical mechanisms behind the LSS. At last, a new theoretical approach to predict friction including the ultimate response of the fluid under severe conditions is proposed.

V.1. Temperature analysis

V.1.1. Energy balance

The molecular interactions governing the system are conservative, i.e. any additional quantity of energy added to the molecular model needs to be evacuated in the same amount. In particular, for the systems of interest treated in this work, energy is generally added mechanically through a compressive load and during the shearing of the confined fluid and dissipated as heat. Hence, heat dissipation will be one of the main focus points of this Chapter. Molecular Dynamics simulations employ thermostats in order to regulate the excess energy in the system. The thermostat in particular allows to directly couple the simulated molecules to the fictive molecules of the heat bath, leading to the control of the kinetic energy of the system. For homogeneous systems, like bulk solids or liquids, the control of temperature is done homogeneously with several algorithms, the oldest (and probably the simplest) one being the velocity-rescaling algorithm [12]. With the velocity-rescaling algorithm, temperature is controlled by scaling up or down the velocities of the particles at fixed intervals. Since then, more sophisticated and advanced methods have been created, as the Nosé-Hoover [174, 12, 219] or the Langevin algorithm [31], which let temperature evolve gradually in the system. However, when working with lubricated contacts at the nanoscale, some problems emerge. These are primarily related to the non-homogeneous nature of the lubricant film, where the solid/fluid interface and nanoscale phenomena play an important role. Additionally, when shear acts upon the fluid, viscous shear heating emerges, which has to be evacuated out of the fluid through the confining solid surfaces [32]. Consequently, a series of energetic transformations emerge within the lubricant film, and a characteristic velocity and temperature gradient develop. The latter is only possible if the thermostating algorithm does not act directly on the fluid molecules [32, 34].

The analysis of the different energy fluxes encountered in the study of nanoscale lubricated contacts will shed light on the contact dynamics on two aspects. First, it will allow to

verify the validity of the integration method and, secondly, it will allow to better understand the path the energy follows in lubricated contacts at the atomic scale, thus elucidating the origin and the nature of friction.

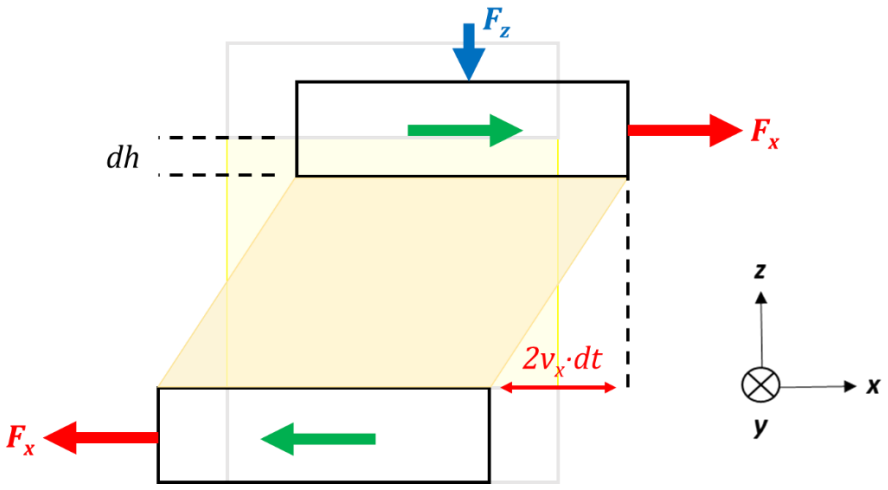

(a) Input of energy: compression and shear

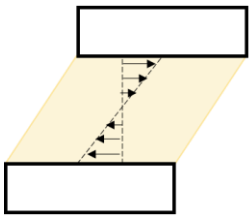

(b) Absorption
Shear is transmitted to the lubricant.

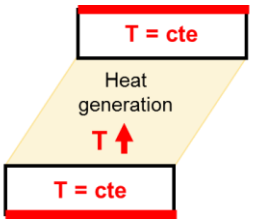

(c) Transformation
Heat builds up within the lubricant film.

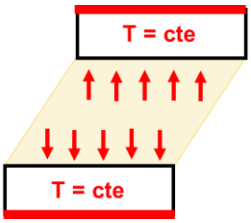

(d) Dissipation
Heat is transported to the surfaces and evacuated.

Figure V.1. Schematic representation of the path the energy follows in a system formed by a lubricant (yellow) confined between two parallel solid plates (white), starting from when it is input into the system as mechanical energy (compression and shear) until it is evacuated out of the system as heat. In (a), a representation of the normal and the tangential distances traversed during a single time step are given, which are used to calculate the input energy following equation (V.1). The energy is then absorbed by the lubricant in (b) and transformed into heat inside the confined fluid in (c). It finally is (d) dissipated by the thermostat through the solid surfaces. Adapted from Berro [22].

In MD simulations, the path followed by the energy during the shearing of a confined fluid is given in Figure V.1 and is composed of three different steps. Energy is first added to the system through the compression and the relative motion of the confining surface. The energy is thus absorbed by the lubricant as mechanical energy and transformed during the shearing process into viscous heat. This transformation entrains an increase in the global fluid

temperature and the generation of a temperature gradient across the film with the thermostated surfaces. It finally results in the dissipation through the confining solid surfaces of the thermal energy.

In real lubricated contacts, the fluid also transports energy towards the contact outlet, but this phenomenon is not seen in the MD simulations involving periodic boundary conditions. Eventually, in real experimental systems, aside from the energy dissipation mechanisms by the thermostats described in this section, there are other important dissipation mechanisms that may appear in the system, such as convection in the inlet or outlet of the contact, and radiation. However, because of the periodicity of the boundary conditions in MD simulations, all of the mechanical energy that enters the system is directly transformed into heat and later on dissipated.

The energy imputed to the system is of mechanical nature and can be calculated as the sum of the work of the normal forces (compression of the fluid) and tangential forces (shearing) so that:

$$dE_{in} = -F_z \cdot dh + 2F_x \cdot u_x \cdot dt \tag{V.1}$$

In (V.1), dE_{in} is the input mechanical energy during a time step duration dt. F_z represents the compressive contact load, and F_x the force acting on the solid surfaces needed in order to maintain steady state sliding with the velocity u_x. The latter is also opposed to the frictional force transmitted from the lubricant molecules to the confining solid surfaces. As for dh, it symbolizes the variation in film thickness during one time step due to this normal load. In this equation, the negative sign on the normal force contribution assumes the compression of the fluid, which leads to the sign of the work being positive.

From equation (V.1), the input energy flux φ_{in} can be inferred by dividing the input mechanical work dE_{in} over the area of contact S:

$$\varphi_{in} = \frac{1}{S}\frac{dE_{in}}{dt} = \frac{1}{S}\left(-F_z \cdot \frac{dh}{dt} + 2F_x \cdot u_x\right) \tag{V.2}$$

On the other hand, the output flux φ_{out}, which will be of thermal nature, can be calculated from the dissipated energy E_{out} by the thermostats from both surfaces over a time step dt as:

$$\varphi_{out} = \frac{1}{S}\frac{dE_{out}}{dt} \tag{V.3}$$

In the atomistic model it is assumed that there is no storage of energy, meaning that the following expression is valid:

$$\varphi_{in} = \varphi_{out} \tag{V.4}$$

which, assuming a steady position of the upper surface, can otherwise be expressed as:

$$\frac{1}{S}\frac{dE_{out}}{dt} = \frac{2F_x \cdot u_x}{S} \quad \text{(V.5)}$$

In other words, equation (V.5) shows the strong relationship between the dissipated energy and the friction force generated in the contact.

The MD model used in this section is the one reported in the previous chapter, where the fluid molecules appear confined between two parallel solid plates. With respect to the choice of surfaces, only the case of α-Fe[100] surfaces is considered, where roughness has been randomly assigned following the same algorithm as before. In between these plates, fluid molecules (BB, SQ or NPE) have been placed creating a film thickness of around 13 nm at the highest pressure. The simulation runs in a similar fashion as previously presented, with an initial equilibration step to minimize the potential energy in the system, followed by a compression and a shearing step for which different pressure, temperature, and wall sliding speeds are imposed. The analysis presented here only focuses on the steady shear phase.

V.1.2. Thermostating algorithms

The preferred method to control heat dissipation in simulations of confined films under shear is known as the sliding boundary thermostat (SBT) method [34, 32, 33, 156]. Here, the excess heat generated during sliding is dissipated through the surface only. The thermostat is not applied directly to the fluid system but rather on the solid surfaces, whose temperature is held fixed. Indeed, some authors have found transport properties like the viscosity to be altered when the thermostat is applied to the fluid [32]. In reality, when sliding at elevated rates, the confined fluid builds up heat leading to a particular temperature field across the film thickness, thus modifying the local lubricant properties as well as global friction in the contact. That is why, as shown in Figure II.6, the thermostat here only applies on a part of the solid surfaces. In this section, boundary thermostating and its influence on the heat dissipation mechanisms during shearing is discussed.

Three thermostating algorithms are tested, namely the velocity-rescaling, the Nosé-Hoover, and the Langevin thermostats. For additional information on these algorithms, see Appendix B.

In the velocity-rescaling algorithm, Newton's equations of motion are not modified with the addition of new terms. The algorithm equilibrates the system at regular intervals to a specific temperature by periodically rescaling the atomic velocities up or down such that the target temperature is achieved. Hence, the global temperature of the surface is controlled, and a temperature gradient may still occur across the surface. With respect to the Nosé-Hoover algorithm, a dynamical variable is added to Newton's equation of motion. This new variable, whose physical meaning is that of friction, slows down or accelerates the surface particles until the target value is reached. This algorithm allows for a smoother temperature control than the velocity-rescaling algorithm, as now no abrupt rescales are performed. Finally, the Langevin algorithm controls temperature on a per-atom basis by adding both a frictional and a random force to the already existing conservative forces acting on each specific atom. The frictional force is proportional to the velocity of the surface atom while the random force accounts for the collisions of the original surface atoms with imaginary particles from the heat bath.

Confined NEMD simulations were conducted on BB submitted to 2 GPa of pressure, a nominal temperature of 313 K, and to different shear rate values. The thickness of the film was about 13 nm, which assures independence of the friction value to the dimensions of the system (see Figure IV.6). The efficiency of the three previously presented thermostating algorithms was tested. For the velocity-rescaling algorithm, three different time intervals (noted τ_R) between consecutive rescales were considered (50 fs, 100 fs and 200 fs), while for both the Nosé-Hoover and the Langevin algorithms a damping coefficient of 100 fs was fixed. The results of these simulations are given in Figure V.2.

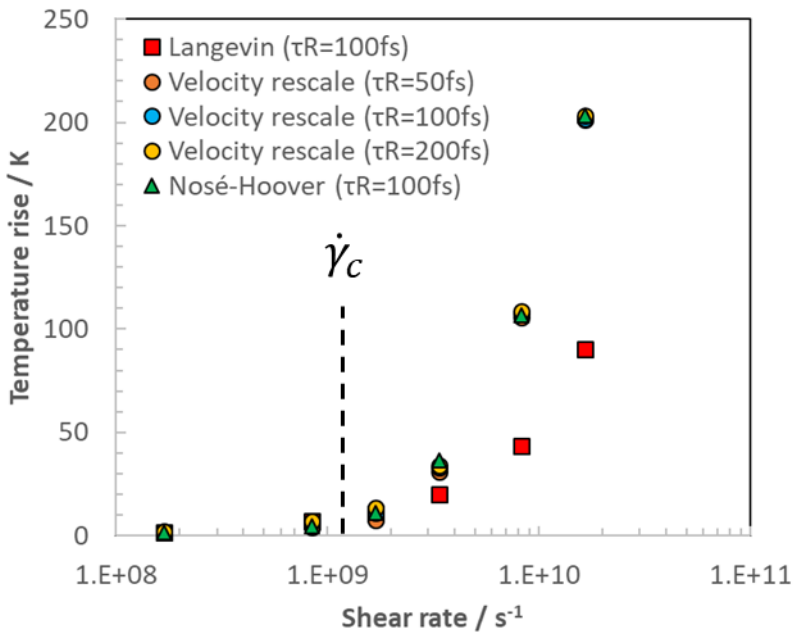

Figure V.2. Temperature increase of a 13nm-thick film of confined benzyl benzoate between two rough α-Fe[100] surfaces at 2 GPa and at nominal 313 K, as a function of the apparent shear rate. Different thermostating methods are compared. In the diagram, τ_R stands for the time interval between consecutive rescales.

In Figure V.2, the temperature increase experienced across the film thickness for the five different thermostating configurations after reaching the stationary state are plotted against the effective shear rate. Shearing was performed for 10 ns during each simulation run. For shear rates below $2.10^9\ s^{-1}$, almost no viscous shear heating appears within the film, having all the thermostats a similar dissipative response. This result is surprising, as the energy is dissipated in very different ways in each case (see Appendix B). Above this shear rate value, the rise of temperature inside the fluid film diverges. On the one hand, the velocity-rescaling and the Nosé-Hoover algorithms give similar values of lubricant heating. However, when the Langevin algorithm evacuates the excess heat, the temperature rise is about 50% less than for the other thermostating methods for the highest simulated shear rates. Consequently, Figure V.2 would suggest a lesser influence of the Langevin algorithm on the shear stress for shear rates above the critical value. As it was already reported by Berro et al. [35], the choice of the thermostating method will influence how the confined fluid will heat up and the value of

the shear stress that will be measured at the solid/fluid interface, specially above a critical shear rate $\dot{\gamma}_c$, close to 10^9 s^{-1}.

An explanation as to why such a different behavior is obtained between the Langevin thermostating algorithm on one side and the velocity-rescaling and the Nosé-Hoover thermostating algorithms on the other side can be given based on how energy is transferred from the affected group of atoms of the confining surfaces and the heat bath. Indeed, while the velocity-rescaling and the Nosé-Hoover algorithms act on the group atoms "globally", the Langevin algorithm does it on each atom individually. Thus, with the latter method, no temperature gradient can be generated in the thermostated region, which leads to a faster dissipation of energy through the surfaces. In other words, the rate at which heat is generated in the contact is higher than the rate at which the thermostat can dissipate energy, and this effect is less predominant for the Langevin algorithm.

In conclusion, it becomes patent how much the thermostating algorithm can influence the friction response of a confined lubricant while shearing. A critical shear rate value $\dot{\gamma}_c \sim 10^9 s^{-1}$, can be identified below which no significant thermal effects are observed. As the shear rate is increased, the response between temperature-control algorithms diverges, giving the highest thermal dissipation for the Langevin thermostat with the parameters employed, and leading to a less important impact of temperature on friction. Hence, the choice of this thermostat is validated.

V.1.3. Shear heating

Several authors attribute thermostating methods to have a significant impact on the overall global fluid temperature when the lubricant is susceptible of heating up [35, 48]. Eventually, the thermostat is just one aspect that needs to be examined when considering heating, the other aspect being the type of fluid that is confined during the simulation. Furthermore, the existence of a shear rate threshold above which viscous shear heating appears has already been observed for many molecular systems [35, 48]. Although there has been an effort to establish a universal law for the prediction of heating inside the fluid, no successful progress has been made yet [35], as viscous hearing depends on the type of fluid used. Classically, only Lennard-Jones fluids have been considered [46, 45, 47], as well as simple n-alkane-like fluids [35, 48]. However, in this work more complex molecular systems with more degrees of freedom are used.

Simulations using BB, SQ and NPE have been conducted with randomly rough α-Fe[100] surfaces at a wide variety of sliding speeds, giving shear rates ranging from 10^8 s^{-1} up to around 10^{11} s^{-1}. As for the pressure and temperature conditions employed, two cases have been studied for each fluid based on the thermodynamic conditions specified in Chapter IV, which resulted either in a nominal solid-like state or in a liquid-like state for each lubricant, leading to the apparition of a plateau regime or just a shear-thinning regime, respectively. Hereon forward, the Langevin algorithm with a damping coefficient of 100 fs is used for all subsequent simulations to control temperature in the contact.

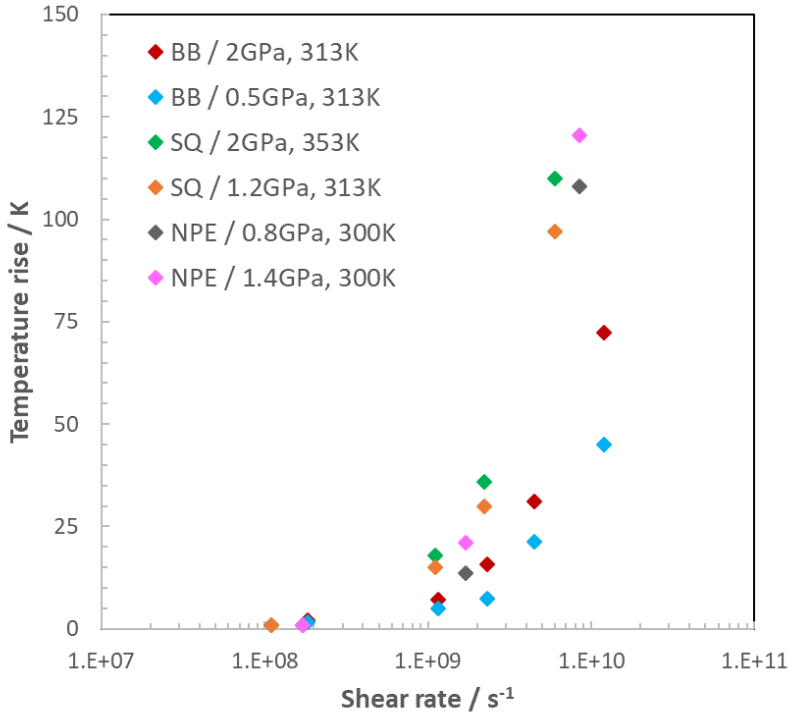

Figure V.3. Temperature increase inside a confined BB, SQ and NPE film between two rough α-Fe[100] surfaces, and at different pressure and temperature conditions, accounting for liquid or solid-like thermodynamic conditions. The Langevin thermostat with a damping coefficient of 100 fs is used.

The results for the temperature increase within the lubricant film are presented in Figure V.3, where a critical shear rate marking the onset of shear heating is visible. However, the starting point of viscous heating and its magnitude appear to be strongly dependent on the nature of the fluid. Indeed, lubricants such as SQ presenting alkane-like structures are usually more sensitive to temperature than traction-like fluids like BB. Temperatures increase by a factor two to four times higher in SQ than in BB, depending on the operating conditions. The thermal behavior of the NPE fluid resembles SQ the most, even though the fluid composition is completely distinct.

The results given in Figure V.3 are also consistent with the Archard equation [220]:

$$\Delta\bar{T}_{total} = \Delta\bar{T}_s + \Delta\bar{T}_f = \left(\frac{1}{(2\pi\lambda_s\rho_s c_s)^2}\, t_i^{0.5} h + \frac{1}{b\lambda_f} h^2\right)\bar{\tau}\dot{\gamma} \qquad \text{(V.6)}$$

where $\Delta\bar{T}_s$ is the temperature increase in the solid surfaces, and $\Delta\bar{T}_f$ the temperature increase in the fluid. For the surfaces, λ_s, ρ_s, and c_s are the thermal conductivity, the density and the heat capacity respectively, t_i is the transit time of the surfaces across the contact and h the lubricant film thickness. As for the confined lubricant, λ_f is the fluid's thermal conductivity and b a parameter characterizing the generation of heat. Shear heating, as presented in Figure V.3, increases linearly with the rate, which is predicted by the Archard equation [220]. In previous NEMD simulations of confined n-hexane [35], a linear increase of $\Delta\bar{T}_f$ with the shear

rate has also been observed using similar thermostating strategies, for which the onset of viscous heating oscillated around 9.1x10^{10} s^{-1}. However, film thicknesses and shear stresses were inferior (2.5 nm and around 59 MPa, respectively) from the values registered in the current simulations, hence why the confined fluids treated in this section start to heat at lower rates. These results manifest that it is not possible to calculate a universal critical shear rate at which shear heating will occur in NEMD simulations, since this will depend on both geometric (h) as well as on material properties (λ_f, $\bar{\tau}$) of the lubricant, as shown in (V.6).

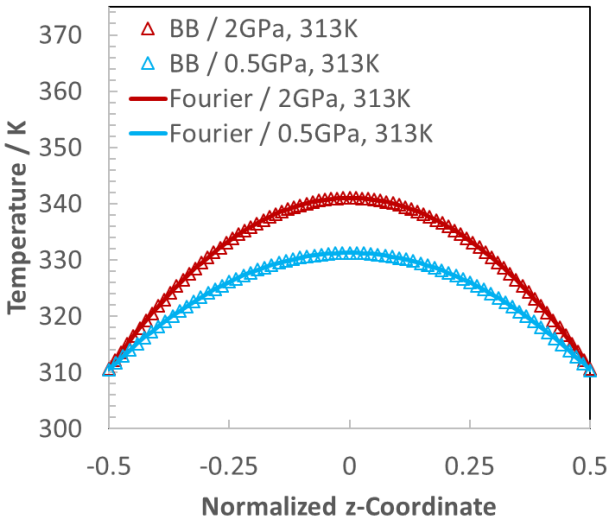

Figure V.4. Spatially averaged temperature profiles for BB at 313 K and 0.5 GPa and 2 GPa, for a shear rate of about 5x10^{9} s^{-1}, compared to their respective fit with the Fourier equation. The z-coordinate has been normalized as z/h.

The spatial temperature distribution across the film thickness can also be determined in a similar fashion to the density and the velocity values by calculating the local temperature in the cross-flow z-direction. The temperature does not distribute uniformly across the film, developing a temperature gradient inside the contact. An example is given in Figure V.4, where the temperature profile for BB at 313 K and 0.5 GPa and 2 GPa is plotted. The profiles are obtained at the stationary state, after shearing for 10 ns at about 10^{9} s^{-1}. This phenomenon is expected because the temperature has only been fixed on a limited region of the confining solid surfaces far from the solid/fluid interface, leaving the temperature to evolve freely inside the fluid during shearing. Additional temperature profiles are presented in Appendix C for BB, SQ and NPE.

The gradients of temperature from Figure V.4 can be best described by using the Fourier law of heat conduction [221]:

$$\varphi_{out} = -\lambda_f \frac{dT}{dz} \tag{V.7}$$

Combined (V.7) with (V.5), and substituting u_x by $u_x = {\dot{\gamma} z}/{2}$, and F_x by $F_x = \tau_{xy} S$, it results in:

$$dT = -\frac{\tau_{xy}\dot{\gamma}}{\lambda_f} z dz \tag{V.8}$$

After integration it results in:

$$T = -\frac{\tau_{xy}\dot{\gamma}}{2\lambda_f} z^2 + T_{s-f} \tag{V.9}$$

with z being the distance from the center of the fluid film, and T_{s-f} the temperature at the solid/fluid interface, typically equal to the imposed wall temperature for the current systems studied, since thermal slip was not observed. NEMD results from Figure V.4 evidence the excellent agreement between numerical data and the Fourier law, which predicts the temperature to evolve quadratically with space. Specifically, for shear rates below 10^9 s^{-1}, simulations can be considered isothermal, since there is a negligible increase in the fluid temperature, usually of less than about 10 K. Moreover, the effect of viscous shear heating appears to be more critical when the fluid is submitted to higher pressures (or lower temperature), higher shear rates, and also depending on the nature of the fluid. BB, for instance, is a fluid with a high capacity to dissipate heat and experiences a lower increase of its temperature with respect SQ and NPE when high shear rates apply. When BB is submitted to 2 GPa, 313 K and a shear rate of 10^9 s^{-1}, the registered shear stress is about $\tau_{xy} = C_f P = 152\ MPa$ (see Figure IV.7.b). Under the same pressure and shear rate conditions, but with 323 K, the new shear stress calculated from NEMD simulations is $\tau = C_f P = 147\ MPa$. This means that an increase in temperature of ΔT = 10 K under the tested operational conditions implies a decrease in shear stress of $\Delta\tau_{xy} = 5\ MPa$, and thus a variation in viscosity of $\Delta\eta(\Delta T = 10K) = {\Delta\tau_{xy}}/{\dot{\gamma}} = 5\ mPa.s$ for a shear rate of 10^9 s^{-1}. This drop of viscosity alone cannot explain the apparition of the LSS friction plateau, and additional more sophisticated mechanisms are expected to take place.

V.2. Structure and orientation of confined molecular systems

The radial distribution function (RDF) can give information on the structure of the fluid molecules when they are submitted to high pressures or strong confinement. The RDF is a function that states the probability density of finding an atom at a randomly chosen point at a distance r away from the central atom. It is one of the most effective and popular techniques used to characterize the structural features of liquids, as well as amorphous or crystalline solids. It can be expressed as:

$$RDF(r) = \frac{V}{N^2}\langle \sum_{i=1}^{N} \frac{n(r)}{4\pi r^2 \Delta r} \rangle \tag{V.10}$$

with V the volume of the fluid system, N the total number of atoms contained in said system, and $n(r)$ the number of atoms around a central atom within the range $[r, r+dr]$. $\langle \dots \rangle$ is the ensemble average.

Figure V.5 represents the RDF function for the three tested molecular fluids. The RDF was calculated for the aromatic carbons of the BB molecule, for the methyl-carbon atoms in SQ, and for the central carbon atoms in the NPE mixture. It shows that the intramolecular bond lengths are well preserved with the increase of pressure, which is indicated by the first three peaks for BB and the first peak of the RDF for SQ. Pressure also increases the packing of the molecular sample (e.g. BB has its fourth peak increased in Figure V.5.a and SQ its second peak in Figure V.5.b). The phase transition reported in the three different phase diagrams (see Figure III.10) is not translated here as a sharp transition in the structure of the fluids, but rather as a gradual change in the disposition of molecules. This event has already been reported by Washizu et al. [172]. It also becomes clear the little influence confinement and shear between the two rough ε^- plates have on fluid structuration when compared with the equilibrium bulk counterpart.

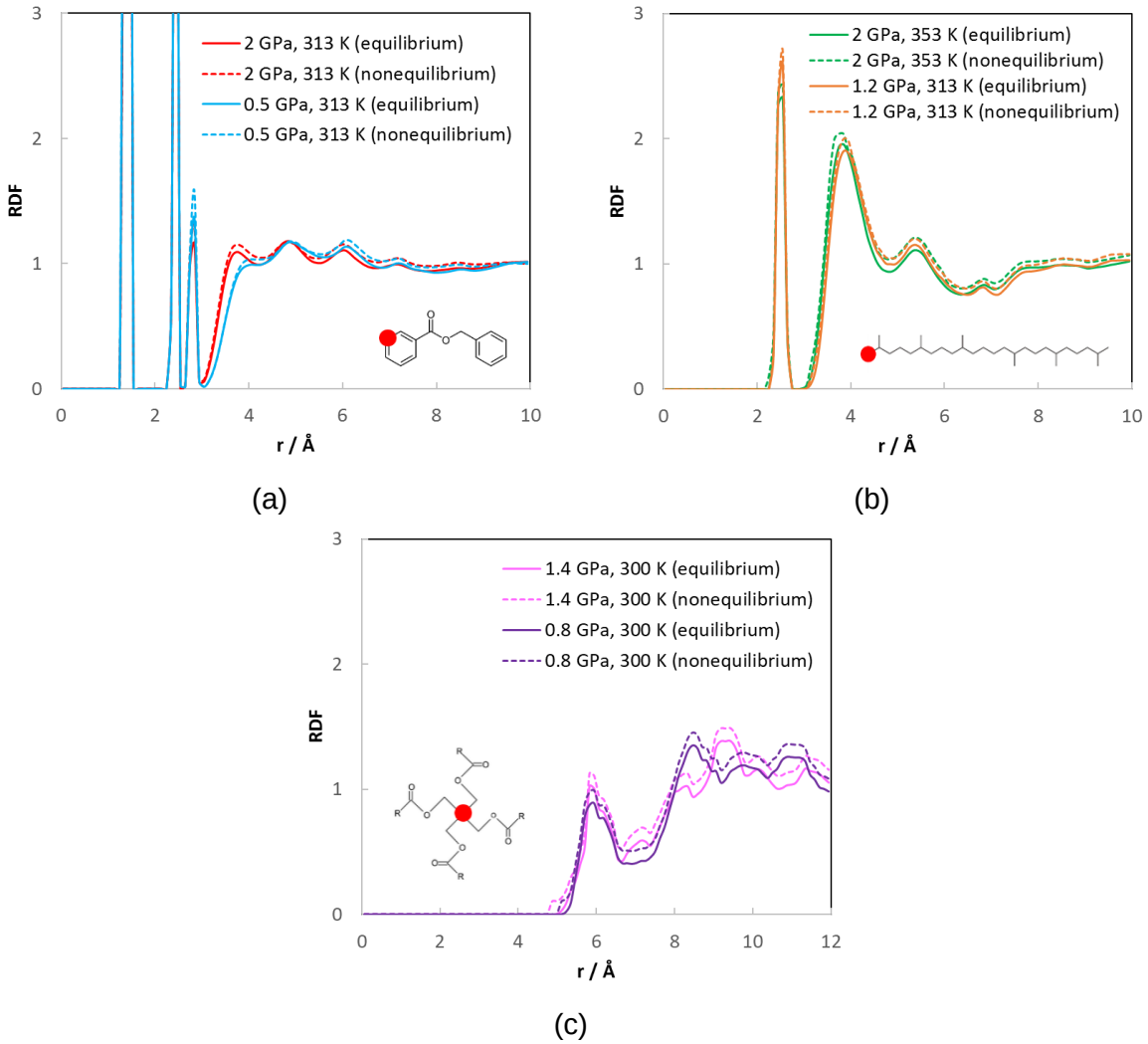

Figure V.5. Radial distribution function of (a) the aromatic carbon atoms of BB at 313 K and at two pressures, (b) the methyl-carbon atoms of squalane at various pressures and temperatures, and (c) the central carbon atom of the PEC molecules of the NPE mixture at 300 K and at two pressures. The diagrams compare bulk and confined simulations of the fluids using rough ε^- surfaces with shearing at about 10^9 s^{-1}.

Orientation is also thought to be of influence in the friction behavior of confined fluids. Indeed, the non-linear behavior of the friction response of lubricants is typically associated with the orientation of molecules in the contact [133]. In this work, the order parameter S_θ is used to describe orientation, which is expressed as:

$$S_\theta = \frac{\langle c\,\mathrm{os}^2\,\theta - 1\rangle}{3} \tag{V.11}$$

where θ represents the angle between the vector normal to the solid confining surface and a characteristic vector specific to the fluid molecule defining its orientation. The definition of the characteristic vector for each fluid molecule is represented in Figure V.6 and Figure V.7 alongside the order parameter S_θ, plotted following different criteria.

In Figure V.6 and Figure V.7, the orientation parameter S_θ is shown for BB, for SQ and for NPE under confinement. For all the fluids, the impact of the physical state is studied by comparing the orientation of the fluid molecules in both nominal liquid and solid-like conditions. All fluid molecules are studied between two parallel rough ε^- plates, but in particular, for BB (see Figure V.6), the influence of the surface nature is also shown by representing the variation of S_θ with smooth ε^- and smooth ε^+ plates too. The order parameter S_θ varies from -0.5 to 1, meaning that $S_\theta = -0.5$ implies fluid molecules to be parallel to the solid surface, and $S_\theta = 0$ for fluid molecules to be perpendicular to it. When $S_\theta = 1$, the fluid system is considered isotropic i.e. the structure is close to a crystal.

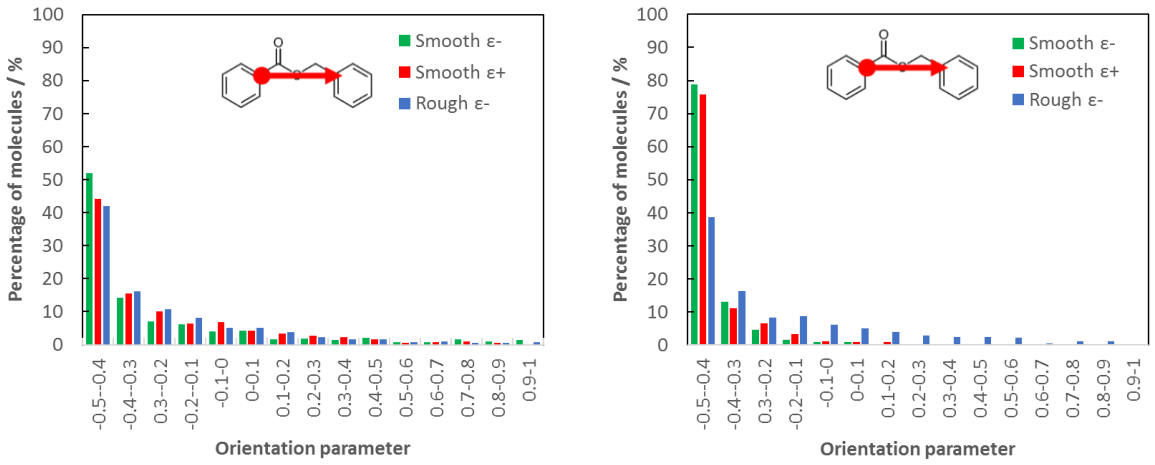

(a) (b)

Figure V.6. Orientation parameter S_θ for BB in (a) a nominal liquid state (0.5 GPa, 313 K), and (b) in a nominal solid-like state (2 GPa, 313 K) for different confining surfaces sheared at about 10^9 s^{-1}.

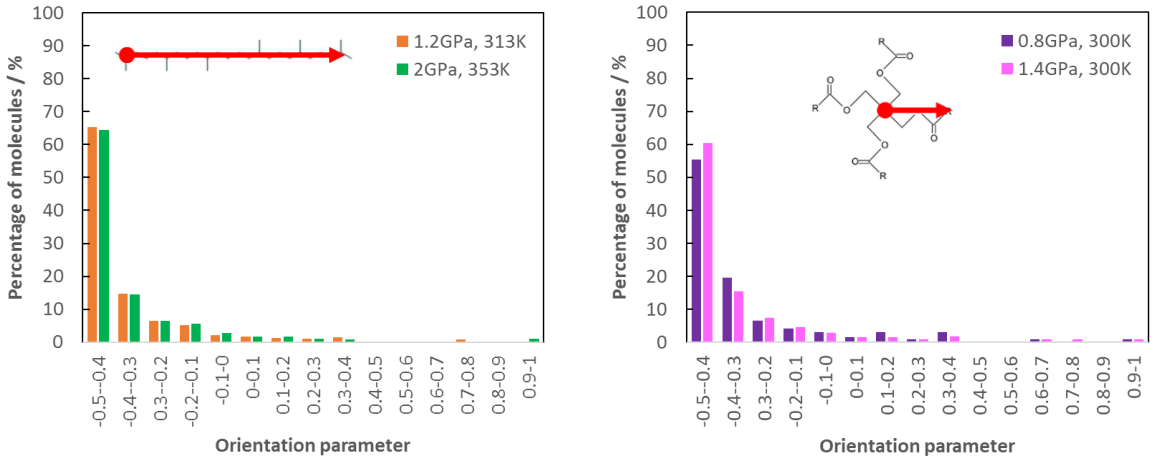

(a) (b)

Figure V.7. Orientation parameter S_θ for (a) SQ and (b) NPE for conditions where a solid like-state (1.2 GPa, 313 K for SQ, and 1.4 GPa, 300 K for NPE) and a liquid-like state (2 GPa, 353 K for SQ and 0.8 GPa, 300 K for NPE) is expected, for systems considering rough surfaces. All the systems are sheared at about 10^9 s^{-1}.

In Figure V.6, for BB, the type of surface does not play a major role at lower pressures, where the orientation of the fluid molecules is mostly parallel to every type of confining walls. As pressure is increased, the impact of the surface nature on the molecular orientation becomes crucial, where smooth surfaces promote more molecules to orient themselves parallel to the solid walls than rough surfaces do. Indeed, the orientation of the fluid molecules is affected by both confinement and the type of surface used. While rough surfaces lead to disordered structures across the film thickness, smooth surfaces promote layering, especially close to the confining walls and to a lesser extent the farther from the solid/fluid interface. However, in Figure V.6.a and Figure V.7, it becomes evident that even with rough surfaces, at least 40% of the molecules are oriented parallel to the surface, possibly hinting shear-thinning.

The nature of the fluid molecules should also be an important factor determining molecular orientation in the contact: BB molecules are small and bulky compared to SQ, which are long and flexible. NPE, on the other hand, is a special case, as it corresponds to a mixture of two similar molecules whose sole difference is the length of the radical alkane chains. For rough surfaces, the change of the thermodynamic state of the fluids has no impact on its orientation.

V.3. Molecular mobility

In the following sections, two parameters are discussed to account for the dynamics of the fluid molecules. These are the velocity fluctuation and the mean squared displacement respectively.

V.3.1. Velocity fluctuation

The motion of fluid molecules was discussed in the previous Chapter through the different velocity profiles of BB, SQ, and NPE. Couette-like velocity profiles were observed with rough surfaces at any given pressure whereas for smooth surfaces a transition to non-Newtonian regimes was obtained at high pressure values. The transition to non-linear flow regimes suggested an increase of the interatomic interactions of molecules once pressures reached severe values. A deeper understanding of the mechanisms affecting flow, and thus friction, is obtained in this section with the introduction of the velocity fluctuation [172]. The velocity fluctuation $\widetilde{u_i}$ of a particle i in a given direction is here defined as:

$$\widetilde{u_i}(z) = \langle u_i(z,t) - \bar{u}_i(z) \rangle^2 \qquad \text{(V.12)}$$

where $u_i(t)$ is the velocity of the particle i at the time t for a given direction and $\bar{u}_i(z)$ is the average velocity of the same particle in time for the same direction. The difference between the atomic velocities and their average velocity is time-averaged over the whole simulation run and squared, so that the velocity fluctuation, as expressed by equation (V.12), is equivalent to the statistical variation of the velocity experimented by the fluid during steady state shearing.

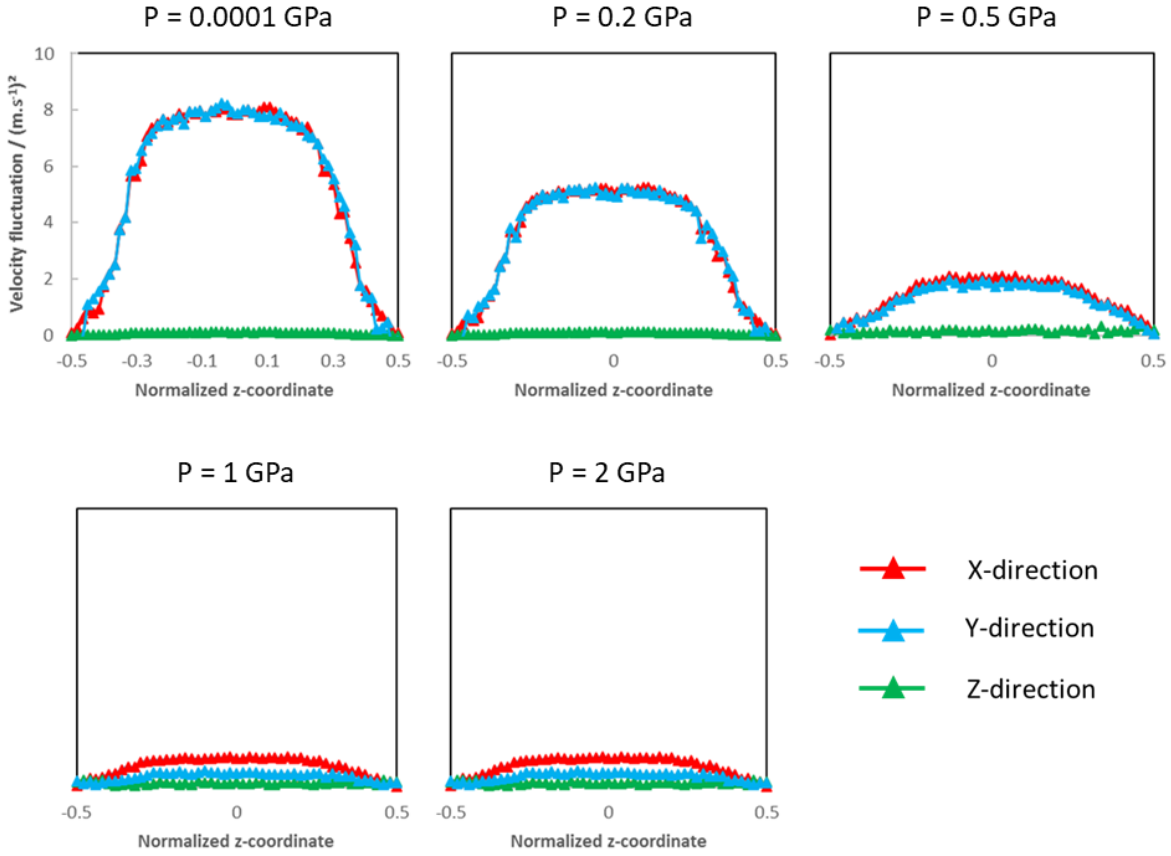

Figure V.8. Influence of pressure on the fluctuation of velocity for BB at 313 K and a shear rate of 10^8 s^{-1}.

The velocity fluctuation for BB at 313 K is presented in Figure V.8, where the difference in motion in the three directions of space is clearly shown for different pressures and when a

shear rate of 10^8 s^{-1} is applied. The choice of the shear rate is to ensure no shear heating takes place, as Figure V.3 shows insignificant temperature increases in the fluid for shear rates below 10^9 s^{-1}. At low pressures (pressures below the transition value of 0.65 GPa, as seen in Figure III.10), the fluctuation curves in the x- and y- direction (planes parallel to the confining solid walls) are almost identical, while the fluctuation in the z-direction (normal to the solid walls) is nearly equal to zero. Indeed, the fluctuations in this latter direction are suppressed stronger than in the x- and y-direction, probably owing to confinement. The results also imply consistency with the Eyring model for shear flow [123]: the high fluctuation in velocity only in planes parallel to confinement indicate that flow originates as a succession of different planes sliding against each other in the imposed direction of shear. Molecules are thus bounded to move within these planes, unable to move from plane to plane (low velocity fluctuation following the z-direction).

The velocity fluctuation of the fluid molecules gradually changes as pressure is increased. The fluctuation is suppressed in the three directions of space, with a higher impact in the x- and y-directions. However, the velocity fluctuation of molecules is stronger reduced in the transversal direction y to flow, as indicated in Figure V.8. At very high pressures, the fluctuation is reduced by four with respect to lower pressures. The physical meaning behind these results can be found with respect to the state at which the confined fluid is. As pressure is increased in the molecular system, the fluid undergoes a transition to a solid-like state, where velocity fluctuation is strongly reduced and molecules are theorized to be placed in semi-fixed positions in space [164]. However, shear is imposed in the x-direction, which forces the particles to move to a lesser degree in the direction of flow, hence the difference in velocity fluctuations between the x- and y-directions with increasing pressure. The results from Figure V.8 are consistent with NEMD simulations of short n-alkanes performed by Washizu et al. [172]. Finally, a reduction of the velocity fluctuation of the fluid molecules at high pressures (and thus the suppression of the degrees of freedom of the system) also indicate a possible inability of the system to respond to solicitations. Thus, if certain operating conditions are to be met (high pressure, low temperature, high shear rates), then the fluid would macroscopically reflect its limit behavior of motion into a limit behavior in friction.

V.3.2. Mean squared displacement

The friction behavior of a given fluid, and thus the thermal agitation of its atoms, is also closely related to the diffusive behavior of the molecules conforming said fluid [35]. In order to quantify the average diffusive behavior of the lubricant molecules, the conventional approach is to define the mean squared displacement (MSD) of the fluid particles. The MSD measures the average squared distance described from the trajectories of the diffusing particles in terms of distance from their initial position [12]. It is expressed for any direction as:

$$MSD = \frac{1}{N}\sum_{i=1}^{N}\langle|r_i(t) - r_i(0)|^2\rangle \tag{V.13}$$

where N depicts the number of fluid molecules in the system, and $|r_i(t) - r_i(0)|$ is the distance travelled by a molecule i over a time interval t. In the same expression, $r_i(t)$ would thus represent the position of a specific molecule i at a time t, and $r_i(0)$ the position of the same

molecule at the initial time step taken as the reference time. The ⟨…⟩ is the ensemble average over space and time for the whole set of particles of the system.

From the definition given by formula (V.13), a series of different dynamic regimes of the fluid can be quantified, resulting from the various interactions between the particles during time. At very short timescales, the inertia of the particles becomes significant, leading to an inertia-dominated regime known as ballistic (see Figure V.9). In this regime, the molecules, after receiving an impulse from the surrounding particles, move in straight lines with constant velocity before colliding with neighboring fluid molecules, slowing them down and randomizing their motion [49]. The MSD has here a quadratic dependence with time (a slope of two on a log-log plot) [50]. It follows at intermediate times a caging regime, characterized by a plateau regime in the MSD vs time plot. The molecules randomly collide against each other and become temporarily trapped in cages formed by their nearest neighbors, restricting their mobility and their rearrangements. Moreover, under these circumstances the fluid behaves solid-like. The movement thus becomes collaborative until enough energy is acquired to overcome the energy barriers associated with the cage-breaking transition and diffuse. Even though the fluid is not subjected to direct motion, a molecule will tend to not remain indefinitely in the vicinity of its current position, but rather change its location with time. The characteristic time at which molecules start diffusing at long timescales is known as the relaxation time t_{rel}. In Figure V.9, the relaxation time is represented as the passage from the caging to the diffusive regime. The MSD in this last dynamic regime shows an upturn, turning to diffusive motion. It increases nearly linearly with time (a slope of unity on a log-log plot), being directly proportional to the diffusion coefficient (the rate at which molecules diffuse) and to the viscosity of the fluid [50]. The fluid behaves like a liquid under these premises.

The regimes described in Figure V.9 allow characterizing the macroscopic flow behavior of the base oil and are, amongst other, suspected to depend on shear and on the confining conditions the fluid molecules are subjected to, hinting towards a possible link with the limiting shear stress phenomenon.

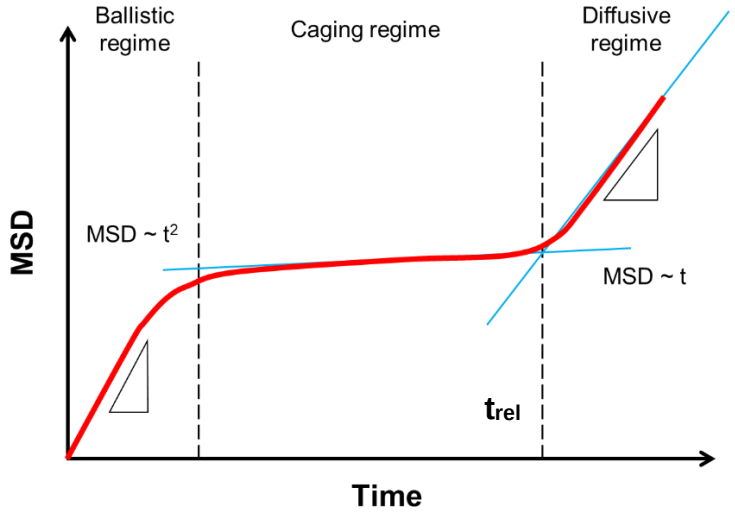

Figure V.9. Representation of the mean squared displacement and the dynamic regimes that appear with time: the ballistic regime at short times, the caging regime at intermediate times, and the diffusive regime at long times. The relaxation time t_{rel} marks the transition from caging to diffusive regime, determined from the intersection of the two regimes (blue lines).

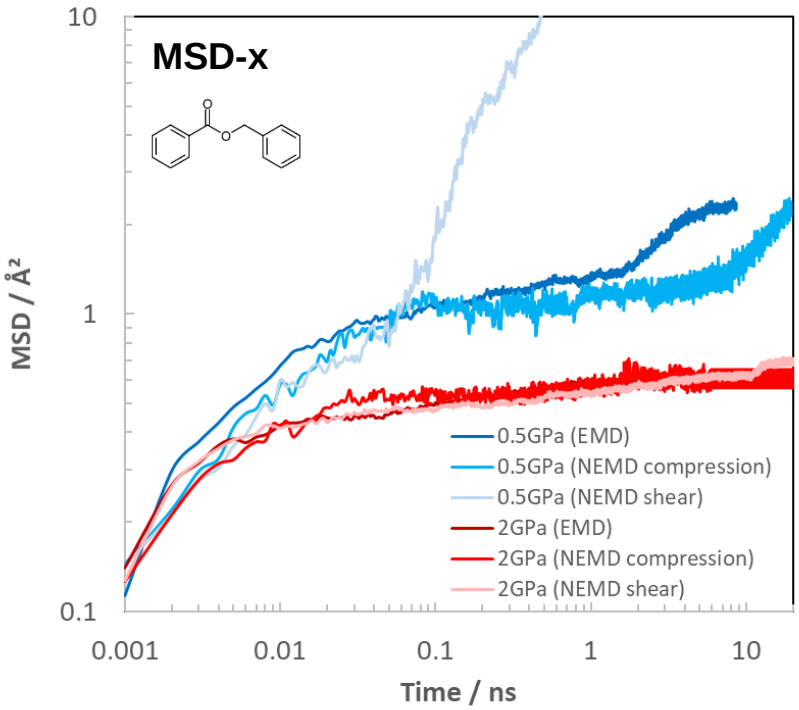

(a)

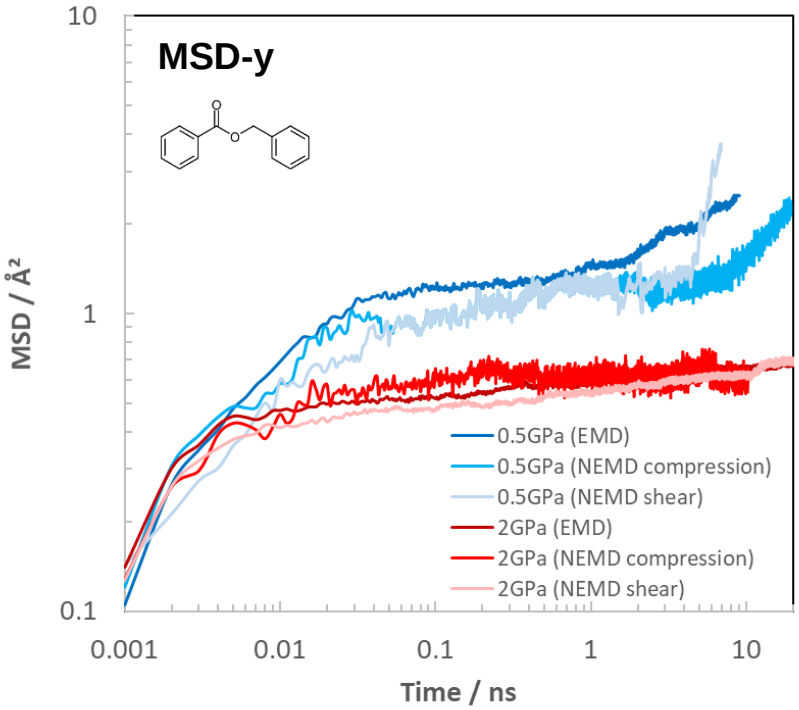

(b)

Figure V.10. Mean squared displacement for bulk and confined NEMD simulations of BB at 313 K at either 0.5 GPa or 2 GPa. Different boundary conditions are considered: no confinement (static bulk fluid), static confinement, and shear under confinement. In (a) the x-component of the MSD, and in (b) the y-component of the MSD are represented.

The MSD parameter for BB at 313 K is plotted against time in Figure V.10. In this figure, a load below (0.5 GPa) and a load above (2 GPa) the transition pressure at a temperature of 313 K is considered, as well as different boundary conditions (static bulk systems, static compression of fluid molecules under confinement, and confined shear). They are separated into the x- and y-direction.

The thermodynamic and operational conditions that are considered in the analysis of the MSD (pressure, temperature, confinement, and shear) are all interconnected and influence the dynamics of the fluid, either by reducing the mobility or by altering the relaxation response of the fluid system. First, for bulk BB molecular systems (see Figure V.10) at 0.5 GPa, the MSD plot undergoes the three previously-described dynamic regimes, starting with ballistic motion at low times (< 0.003 ns), and escaping caging at around t_{rel} = 1 ns, at which point the molecules begin to diffuse. On the contrary, if the pressure is increased to 2 GPa, once the caging regime is into effect, no diffusion of the molecules is accomplished during the duration of the simulation. Indeed, pressure (as stated in Chapter IV) determines the physical state of the lubricant, which consequently defines the rheological properties of the fluid. At 313 K and 2 GPa, the bulk BB system is expected to present solid-like characteristics, i.e. large viscosity values and high relaxation times. Furthermore, the cohesion of the molecules in the system is increased with pressure, accompanied by a dramatic change in the motion of particles. This translates into slowed-down dynamics by the presence of a plateau in the MSD versus time plot, from which the molecules are unable to escape during the whole simulation run. When this occurs, the time need for BB molecules to respond to any kind of solicitation goes towards infinity.

If the fluid is then confined between two parallel rough plates, under the same pressure and temperature conditions as before, while no shear is applied, little to no variation in the motion of the BB molecules is observed with respect to its bulk counterpart (see Figure V.10), with the representation of similar values of MSD, and with the presence of the same dynamic regimes.

The last variable that is analyzed with respect to its influence on the MSD curves is shear. For this last scenario, the systems consider both rough iron surfaces and a shear rate of approximately 10^8 s^{-1}. The latter value of shear rate comes from the very low viscous shear heating response of BB predicted in Figure V.3. In general, all the fluids tested in this work experience negligible viscous shear heating ($\Delta T \sim 1$ K) for shear rates of the order of 10^8 s^{-1}. By performing simulations under these assumptions, if any phenomena are to occur with respect to the molecular mobility of the confined lubricant, it would only be of mechanical nature, as temperature would not play a significant role in the dynamic response of the fluid.

The observed response of BB being sheared under nominal solid-like conditions at 313K and 2 GPa resembles its static counterpart, where both the confined compression and the confined shear curves perfectly match each other and are nearly superimposed. Nevertheless, at lower pressures, the fluid submitted to shear also shows a similar behavior to the compression scenario, but with an almost immediate passage from ballistic motion to diffusive motion in the x-direction. This is due to the energy being added to the system by imposing shear on the confining walls. In the y-direction, the relaxation time matches the value found in the bulk case and in the confined compression case. Consequently, the energetic barrier is lowered i.e. the energy needed to diffuse the molecules, and thus the fluid system

exits the caging regime at lower times. In other words, the added energy to the fluid system implies a much easier escape of the BB molecules from their neighbors, leading to diffusion at lower relaxation times.

The influence of the physical state of the fluid on its dynamics is critical, as for high pressures the high cohesion impedes molecular diffusion to occur even if energy is added to the system through shearing. Mobility is also reduced with respect to lower pressures. Caging would here be associated with the ultimate response in friction of the lubricant and would macroscopically manifest itself through the LSS plateau in friction tests. For instance, for BB submitted to 313 K and 2 GPa, the relaxation time is so high (over 20 ns) that even if the shear rate value is high (here at 10^8 s^{-1}), diffusion will not take place, and a LSS behavior will be observed. In addition, it should be worth mentioning the impact of thermal effects to the study of molecular mobility by MD simulations. Indeed, BB has a critical shear rate around 10^9 s^{-1} above which temperature increases at low pressure (see Figure V.3). Consequently, simulations are restrained to a small frame of possible shear rate values before viscous shear heating occurs, implying that, eventually, LSS could possibly happen at shear rates above the value of 10^9 s^{-1} for BB at 313 K and 0.5 GPa. However, because of the shear heating of the fluid in the contact, diffusion would be promoted and no LSS would be perceived in the simulations.

A similar analysis for the molecular mobility of SQ and NPE as presented in this section is given in Appendix D.

V.4. A theoretical approach to explain the appearance of LSS based on the activation energy

The different existing friction models proposed in literature are mostly empirical and are still open to debate, as they sometimes fail to describe the physical phenomena that occur when pressure and shear rate become very high [89]. Among these models, the exponential law [89] or the Carreau law [89] for the prediction of shear stress and their variants have gained increasing popularity in recent years. A notable exception is the model proposed by Eyring [89, 123], based on the physical concept of the activation energy. This model assumes that diffusion and viscous shear flow are thermally activated. In other words, it supports the idea that molecules, based on their thermal motion, are able to jump to adjacent energy minima by overcoming a free energy barrier. At equilibrium, motion is isotropic, without any privileged direction, as seen in Figure V.10 for bulk systems at equilibrium and for confined systems under static conditions. Indeed, for both scenarios, the MSD parameter of BB in the x- and y-directions is seen to present similar values.

The concept of activation energy, first developed by Arrhenius [123], allows to express the diffusion as:

$$D = D_0 \, e^{-E_a/k_B T} \tag{V.14}$$

where D is the diffusion coefficient, D_0 is a pre-exponential factor, k_B the Boltzmann constant, and T the temperature. E_a is in this equation the activation energy, accounting for the potential energy barrier. It is agreed that this expression only holds in the diffusive regime.

A good estimation of the activation energy can be acquired with equilibrium MD simulations through the MSD parameter for different temperature and pressure conditions. Indeed, at a fixed temperature and pressure, the coefficient of diffusion D is proportional to the slope of the MSD [12] versus time plot when in the diffusive regime, and is equal to:

$$D = \lim_{t\to\infty} \frac{1}{6}\frac{1}{dt} MSD \tag{V.15}$$

On another note, (V.14) shows that the logarithmic value of the diffusion coefficient D is proportional to the inverse of the temperature:

$$\ln D \sim f\left(\frac{1}{T}\right) \tag{V.16}$$

so that if $\ln D$ is plotted against $1/T$, then the slope of the plot would be directly related to the activation energy as follows:

$$E_a = slope \cdot k_B \tag{V.17}$$

A series of EMD simulations of bulk BB have been performed under different temperature and pressure conditions, ranging from 300 to 2000 K and from 0.0001 to 2 GPa, respectively. The diffusion coefficient D, calculated from the slope of the MSD at long times is represented as a function of the inverse of temperature in Figure V.11. The slopes of the $\ln D$ versus $1/T$ plot are negative for any given pressure i.e. the lower the temperature, the less agitation the fluid molecules have. For more details on how these curves are obtained, see Appendix D. A similar analysis for SQ is developed in Appendix E.

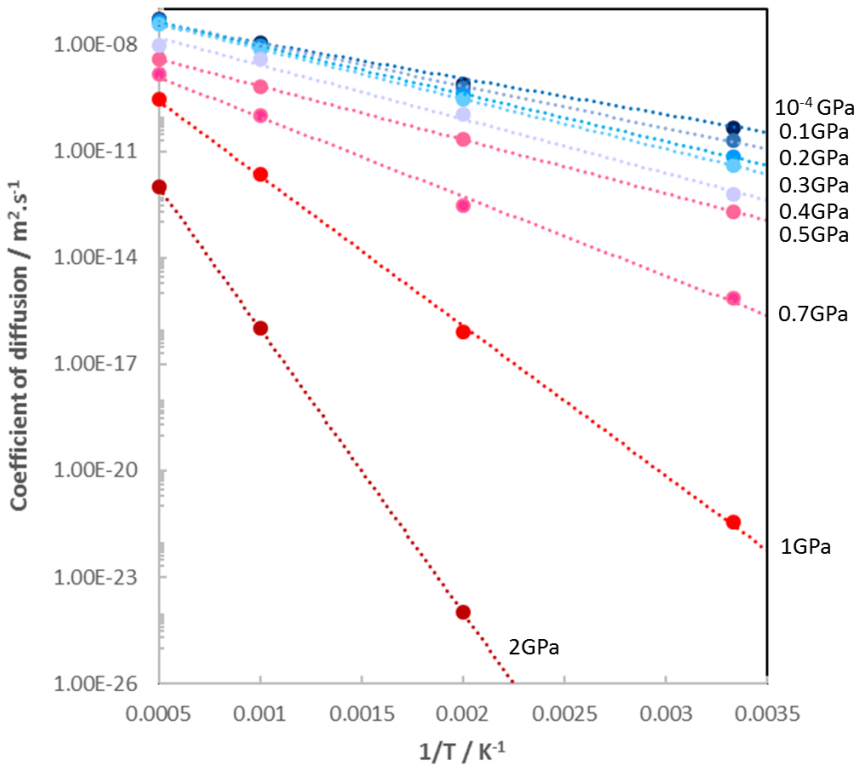

Figure V.11. Evolution of the coefficient of diffusion of BB as a function of the inverse of temperature for different pressures. The coefficient of diffusion for each pressure and temperature state has been calculated from the diffusive regime of the MSD vs. time plot, from EMD simulations. See Appendix D for details.

The diffusion coefficient can only be calculated in the diffusive regime. Each curve in Figure V.11 results in a unique activation energy value characteristic of a fixed pressure for the range of temperatures studied. An estimation of this activation energy can be derived by applying (V.17) to the different curves. The pressure dependence of the activation energy of BB is represented in Figure V.12.

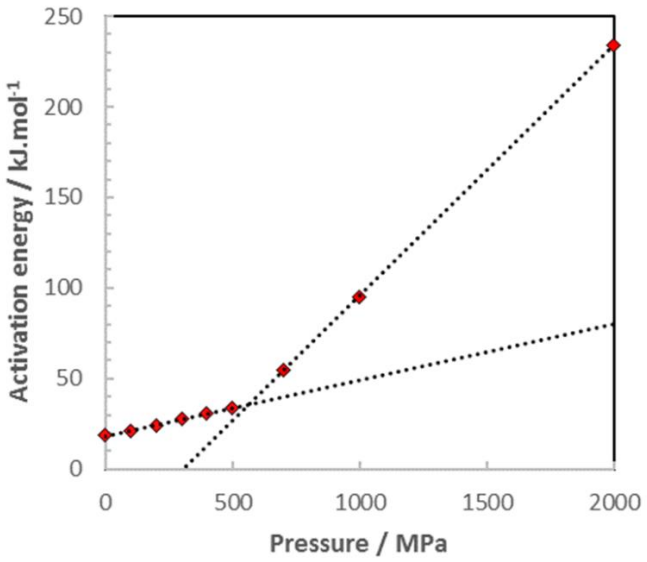

Figure V.12. Evolution of the activation energy of BB as a function of pressure. The red points represent each one of the activation energies calculated from the curve slopes from the lnD versus 1/T plots. The dashed lines, on the other hand, evidence the linear dependence of E_a with pressure, differentiating two separate regimes.

Interestingly enough, the figure shows the activation energy to increase linearly with pressure, a behavior that is already predicted in literature and explained by the expression [222]:

$$E_a = E_{a0} + P \cdot V_a \tag{V.18}$$

with E_{a0} the activation energy at low pressure, which does not explicitly depend on the temperature of the system. P is the applied pressure, and V_a a parameter known as the activation volume [11]. Surprisingly, the activation volume does not depend on the temperature, on the range of studied temperatures, even for squalane (see Appendix E) and contrary to the analysis developed in [11].

In addition to this, the activation energy presents an inflection point close to 0.5 GPa for BB, beyond which the activation energy sharply increases with pressure. Practically, when BB goes from 0.5 GPa to 2 GPa, the activation energy is multiplied by a factor 6.95.

On the other hand, diffusion is linked to the relaxation time [223] by:

$$t_{rel} = \frac{d^2}{D} \tag{V.19}$$

where d is the size of the BB molecule.

Inserting (V.14) into (V.19) leads to:

$$t_{rel} \propto e^{\frac{E_a(P)}{k_B T}} \quad \text{(V.20)}$$

From 0.5 GPa to 2 GPa, t_{rel} is multiplied by a factor $e^{6.95} \sim 1000$, reaching the order of the microsencond. This would explain why in Figure V.10, at 2 GPa and for the applied shear rate, the diffusive regime was never attained with MD simulations.

From this analysis, we have determined that pressure controls the activation energy. The activation energy E_a not only defines diffusion, but also determines the relaxation time of the fluid. In other words, if pressure is increased, so does the activation energy and, consequently, the relaxation time. From here, a characteristic shear rate can be calculated from the relaxation time t_{rel} as $\dot{\gamma}_{rel} = {t_{rel}}^{-1}$. Thus, if the fluid is submitted to a faster shear rate than $\dot{\gamma}_{rel}$, then the fluid molecules do not have enough time to respond to the stresses that are generated and relax, leading to a limiting value of the shear stress. On the contrary, if the applied shear rate is lower than $\dot{\gamma}_{rel}$, then a steady increase of the shear stress with the shear rate is expected.

V.5. Conclusion

In this Chapter, focus has been set on the mechanisms for energy dissipation during shearing. Friction being directly related to the ability of the system to evacuate heat out of the contact, the LSS phenomenon has been assumed to be directly dependent on the transport phenomena of molecules, that is, its dynamics. The first aspect investigated in this Chapter is related to temperature. Fluids, when submitted to EHD conditions, are very sensitive to the applied operating conditions and usually experience an increase in temperature once a critical shear rate is applied. Viscous shear heating depends on the nature of the fluid, but also on other parameters like the pressure. The thermostating algorithms used for the NEMD simulations also play an important role in heat dissipation, with the Langevin algorithm having the least influence on viscous shear heating. Thus, the choice of using this thermostat in the NEMD models of this work was validated, for a range of shear rates where the least possible shear heating is expected.

Structure and orientation of the fluid molecules do not have a significant impact for the range of pressures and shear rates studied. The study was made at moderate shear rates so as not to interfere with the fluid global temperature, avoiding shear heating of the fluid. Then, the dynamics of the fluids were put into test thanks to both the fluctuation of velocity and to the mean squared displacement parameter. The fluctuation of velocity, for instance, marked the influence of pressure on the flowing fluid system. It manifested a significant reduction of the molecular motion with the change of the operating conditions, going from a system best described by a succession of molecules sliding against each other when shearing under nominal liquid conditions, to a system where the degrees of freedom are reduced to just one (in the direction of flow) when solid-like conditions are in place. This was later on observed by the mean squared displacement parameter for EMD and NEMD simulations. The results evidenced the passage of the fluid molecules through three different dynamic regimes depending on their ability to move, namely a ballistic regime, a caging regime, and a final diffusive regime at long times. It was found that, in the onset of a transition to a solid-like state, the dynamics of the fluid slowed down. Relaxation times thus significantly increased, and the

molecules remained in the caging regime, losing the ability to respond fast enough to solicitations. A fluid-like motion was hence not ensured. Consequently, friction saturates to a limit value, which is what is known as the limiting shear stress phenomenon [30].

Finally, a theoretical approach was proposed to characterize the appearance of LSS based on concept of the activation energy. Based on an Arrhenius law, diffusion is expected to depend exponentially on an activation energy. It was shown that, in the diffusive regime, the activation energy is sharply dependent on the applied pressure. Consequently, the relaxation time of the fluid increases following the same trend. At high pressure and high shear rate (which corresponds to a small shearing time), the lubricant molecules do not have time to respond to the applied shear. This process is correlated with the caging regime observed in the mobility analysis. Under these conditions, a limiting shear stress appears.

Conclusions and perspectives

Conclusions and perspectives

Conclusions

Friction accounts for one of the main dissipation mechanisms in mechanical systems, where two contacting bodies move in relative motion. Some of the technical solutions considered to reduce energy dissipation at the level of the contact concern the use of a lubricant of a specific nature and rheology. Typically, a lubricant ensures the power transmission between the two moving touching bodies, often operating in the elastohydrodynamic regime, such as for gears, cam-follower systems, or roller bearings. This regime leads to very high pressures (a few gigapascals) and severe shear rates, which results in very thin film thicknesses (some tens to hundreds of nanometers). Under these extreme conditions of pressure and shear rate, the shear stress may reach a plateau value (a phenomenon called LSS) linked to the ultimate friction response of the confined lubricant. In this plateau regime, which appears beyond a critical shear rate, the shear stress becomes shear-independent, and hence energy losses are limited. Consequently, a good understanding of how to predict and control this plateau regime would allow to greatly improve the performance of industrial mechanical systems. However, not much is yet understood with respect to the physical mechanisms that originate this ultimate response in friction of lubricants.

A series of hypotheses have been proposed in literature to explain this phenomenon (a liquid-to-solid state transition of the lubricant, wall slip, or shear banding amongst others), but tribologists are still unable to reach consensus on the matter. Indeed, the inability to perform friction measurements simultaneously to in-situ observations of flow behavior, coupled to the many local phenomena acting on the contact level over a large range of scales, lead altogether to an extremely complex response of the lubricated contact (**Chapter I**). Thus, the LSS problem requires a multiphysics and multiscale approach. In recent years, Molecular Dynamics simulations have gained popularity because they are able to easily access local parameters, which are otherwise impossible to obtain by experimentation alone (**Chapter II**). In this work, they were used to study the rheology, the transport properties, as well as the friction response of two model lubricants (benzyl benzoate and squalane) and an aero-type industrial base oil.

In **Chapter III**, a full picture of the physical state of the three fluids was obtained at equilibrium with the development of a phase diagram for each lubricant. The diagrams were then used to determine liquid or solid-like thermodynamic operating conditions. The physical state of the lubricants during shearing was investigated in **Chapter IV**. Different boundary conditions at the solid surfaces were implemented onto the MD model to account for roughness or wettability. The lubricant molecules displayed a distinct flow response with respect to the applied operating and boundary conditions during shearing, presenting either non-linear velocity distributions (for smooth surfaces with strong or low interfacial adhesion energy) or Couette-like velocity profiles (for low adhesion energy rough surfaces). Furthermore, the plateau friction regime emerged naturally when the fluid molecules were submitted to solid-like thermodynamic conditions, independently to the flow response of the lubricant during shearing. This crucial result was compared both qualitatively and quantitatively to experimental measurements, with a very good match despite the different ranges of film thicknesses and shear rate considered in experiments and simulations. Moreover, the velocity gradient

developed during shearing arose as a direct consequence of the imposed conditions at the solid/liquid interface, with shear originating at the weakest interface (close to the confining walls or inside the fluid film, depending on the simulation details).

Friction being directly related to the thermal agitation of atoms, a plateau in friction implies a limit to the ability of the fluids to dissipate heat. However, even though this limit in friction was obtained under nominal solid-like conditions, the viscosity values that were derived from the velocity distributions of lubricant systems confined between rough surfaces were too low to assume glassy mechanics (<< 1 Pa.s). This question was further investigated in **Chapter V**. With rough surfaces, no particular orientation or ordering of the lubricant molecules across the contact film thickness was found when going from a liquid-like to a solid-like state. The dynamic response of BB in particular was studied by observing the influence of pressure on the fluctuations in velocity and on the mean squared displacement of the fluid molecules. Both parameters evidenced slowed-down dynamics with increasing pressure, with the restriction of the degrees of freedom of the molecules once a solid-like state was reached. By suppressing the degrees of freedom of the fluid, the molecules tended to form cages with neighboring molecules, no longer having the ability to respond fast enough to solicitations. However, even though the caging regime could be overcome by injecting a sufficiently high energy to the system by shearing, the potential activation barrier energy needed to exit the cages, and thus the relaxation time of the lubricant, increases rapidly with pressure, hence the absence of diffusion even at the very high shear rates encountered in MD simulations. The macroscopic response to this phenomenon is thus observed as a limit value in friction when the fluid is sheared under severe pressure and shear rate conditions.

This analysis asserts the universality of the limiting shear stress behavior as a material-inherent property, appearing as a consequence of slowed-down dynamics once the lubricant transitions to a solid-like state. On the other hand, increasing shear rate above a critical value would generate thermal thinning, impeding to measure LSS, but rather a friction decrease. The results presented in this thesis can help industrial manufacturers to better understand the friction response of lubricants when severe pressure and shear rate conditions apply. With the concept of LSS now based on physical phenomena, a new perspective to develop predictive friction laws respectful to the thermodynamics of confined fluids at the EHD lubrication regime is at hand. This opens the door to a better quantification of friction and energy losses in lubricated systems involving concentrated contacts, such as rolling element bearings or gears. To achieve this, a change of scale is required to adapt the molecular aspects identified in this work to models based on continuum mechanics, better suited (in both space and time scales) for the direct comparison with experimental friction data.

Perspectives

Some perspectives of this work and further investigations are discussed hereon.

- <u>New perspective for a predictive friction law based on molecular mobility</u>

This work has presented simulation friction results for three test fluids (BB, SQ, and NPE) in very good agreement with experimental data. It has been demonstrated the important role of the activation energy in the appearance of the friction plateau at high pressure and high

shear rates, strongly correlated to a liquid-to-solid phase transition. Further research on this matter can be envisaged in order to complete the analysis on the role of the activation energy [11], as this parameter would also be affected by the imposed shear rate, an aspect that has not yet been studied here. By further developing this approach, a better understanding of the origin of friction can be reached [173] and new predictive friction laws could be derived based on the molecular mobility concept.

- Simulations at larger scales

The flow and friction behavior of confined lubricants was investigated in this work through atomistic simulations. Eventually, these kinds of simulations present some major limitations, especially regarding the spatial and time scales, restraining most simulations to a few nanometer-thick boxes and some tens of nanoseconds respectively [22]. The extension of the analysis presented in this work to larger scales would immediately allow to first overcome the constraints associated to atomistic simulations, and also to simulate for more complex and larger systems [79]. Here, both discrete (coarse graining) and continuum (finite element analysis) techniques can be envisaged [224].

- In-situ characterization of lubricants

Reproducing the operational conditions encountered in typical elastohydrodynamic lubricated contacts during experiments is a very complex and demanding task, as pressure and temperature need to be controlled in every moment of the experience [8]. Additionally, performing simultaneous measurements of friction and flow behavior of highly confined liquids is still today an open field with many unanswered questions, in spite of the many advances made during the last two decades [225]. Particle tracking, for example, has seen an increase in popularity as it constitutes an effective and non-invasive approach to characterize dynamic thin-film flows [218].

- Investigations of the phase transition

In this work, the crucial influence of the physical state of the fluid on its friction behavior has become patent. Hence, numerical analysis of the EHD contact would nourish from experimentation [155, 226, 227]. Indeed, the project would benefit from coupling spectroscopy and friction measurements in order to investigate simultaneously the frictional behavior and the possible changes experienced in the microstructure of the lubricant [8], evidencing either local or global phase transitions throughout the contact region [173]. The results would then be correlated to the onset of LSS and further support the results and predictions from atomistic simulations.

Appendix A
Phase diagrams based on EMD simulations

The diagrams in this Appendix aim to illustrate the process of elaboration of a phase diagram based on EMD simulations of the fluids introduced in Chapter III. Each black triangle in Figure III.10 corresponds to one EMD simulation, where the corresponding pressure and temperature values equal to the point where an inflexion in the volume vs temperature plot is observed at constant pressure. An example of these kinds of results is given in Figure A.1.

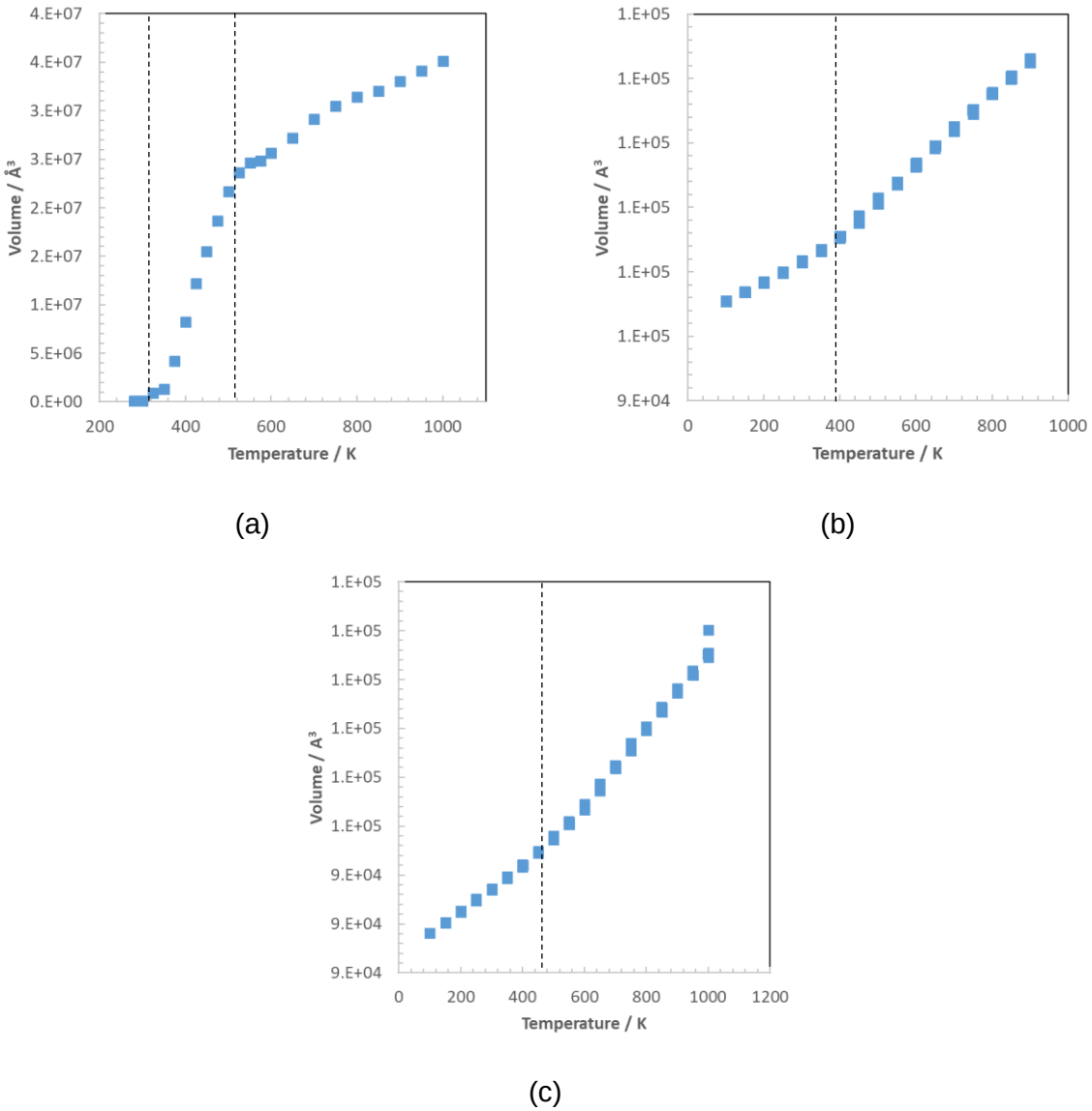

Figure A.1. The evolution of the system's volume with temperature at constant pressure for (a) BB at 0.0001 GPa, (b) SQ at 2 GPa, and (c) NPE at 5 GPa. The dashed lines mark the transitions from one state to another.

Appendix B
Temperature-control algorithms

Classical molecular dynamics requires solving Newton's equations of motion on a system of molecules that are constantly interacting with purely conservative forces. Thus, systems are placed in the NVE (micro-canonical) thermodynamic ensemble, where the number of particles, the volume, as well as the total energy of the system are kept constant. However, experiments often consider a constant temperature instead of the constant energy condition of the NVE ensemble. Several algorithms have been developed in order to cope with this problem, allowing to control the temperature of the molecular system during the simulation run [12, 219].

Temperature is treated in classical MD simulations as the time average of an "instantaneous" temperature, which is often referred to as the kinetic temperature because of its close relation to the total kinetic energy by thermal vibrations E_k. The kinetic temperature $T(t)$ at an instant t is given by:

$$E_k = \sum_{i=1}^{N} \frac{|p_i|^2}{2m_i} = \frac{k_B T(t)}{2}(3N - N_c) \tag{B.1}$$

where N is the total number of atoms in the system, p_i and m_i the linear momentum and the mass of an atom i respectively, and N_c the number of constraints, so that $(3N - N_c)$ represents the number of degrees of freedom. k_B is the Boltzmann constant.

The kinetic temperature $T(t)$ is controlled by a series of algorithms: the velocity-rescaling algorithm, the Nosé-Hoover algorithm, and the Langevin algorithm. They are classically used in MD simulations and are presented in the following sections. More details about thermostating methods are given in references.

B.1. Velocity-rescaling

The velocity-rescaling algorithm is the simplest thermostating method for controlling the temperature in MD simulations. It consists in scaling the atomic velocities at constant time intervals so that the global kinetic temperature of the thermostated region $T(t)$ reaches the target temperature T_t [12]. In order to do so, the atomic velocities are multiplied by a factor $\tilde{\lambda}$, meaning that the kinetic energy is multiplied by $\tilde{\lambda}^2$. Consequently, the rescaling factor is related to the instantaneous kinetic temperature and to the target temperature by:

$$\tilde{\lambda} = \sqrt{\frac{T(t)}{T_t}} \tag{B.2}$$

The dissipated (or added) energy to the system by the thermostat is given by:

$$\Delta E = E_k\left(\tilde{\lambda}^2 - 1\right) \tag{B.3}$$

where E_k is the total kinetic energy of the atoms in the thermostated group, calculated by (B.1).

With this thermostating algorithm, all atomic velocities are rescaled by a same quantity. Therefore, heat is removed from the system in a homogeneous manner, even though some atoms may present larger deviations from the target temperature. In addition to this, the velocity-rescaling algorithm controls the temperature in a "brutal" way. Indeed, temperature does not fluctuate as it is expected from the NVT (canonical) thermodynamic ensemble. A solution of this problem was proposed by Nosé, and later developed by Hoover, with the creation of a new alternative temperature-control algorithm.

B.2. Nosé-Hoover algorithm

The concept behind the Nosé-Hoover thermostat is to integrate the external heat bath into the thermostated group of atoms [12, 219, 174]. The extended system thus contains the real molecules and the heat bath, which are coupled with the addition of an artificial degree of freedom $\tilde{s}$, related to an artificial thermal inertia Q_b and to an artificial velocity $\dot{\tilde{s}}$. The magnitude Q_b determines the coupling between both systems, and $\tilde{s}$ is a scaling parameter for the time dt. It results:

$$d\tilde{t} = \tilde{s}dt \tag{B.4}$$

where $d\tilde{t}$ is the time for the extended system (real molecules and heat bath).

The coordinates *r* and *s* are identical in the real and in the extended system. However, their velocities depend on $\tilde{s}$, leading to:

$$\dot{\tilde{r}} = \frac{\dot{r}}{\tilde{s}}$$
$$\dot{\tilde{s}} = \frac{\dot{s}}{\tilde{s}} \tag{B.5}$$

The Nosé equations of motion are written as follows in the extended system:

$$\ddot{\tilde{r}}_i = \frac{\tilde{F}_i}{m_i\tilde{s}^2} - \frac{2\dot{\tilde{s}}\dot{\tilde{r}}_i}{\tilde{s}} \tag{B.6}$$

$$\ddot{\tilde{s}} = \frac{1}{Q_b\tilde{s}}\left(\sum_i m_i\tilde{s}^2\dot{\tilde{r}}^2 - \left(N_{dof}+1\right)k_BT_0\right) \tag{B.7}$$

In the formula (B.7), N_{dof} corresponds to the degrees of freedom, which are a function of the molecular constraints of the system. The Nosé equations of motion can also be rewritten in terms of the real system variables by defining $= \dot{s}/_S$:

$$\ddot{r}_i = \frac{F_i}{m_i} - \gamma r_i \tag{B.8}$$

$$\dot{\gamma} = \frac{-k_B N_{dof}}{Q_b} T(t) \left(\frac{N_{dof}+1}{N_{dof}} \frac{T_0}{T(t)} - 1 \right) \tag{B.9}$$

The choice of Q_b determines to what extend the real molecular system and the heat bath are coupled. If Q_b is very large ($Q_b \to \infty$), then the coupling is very weak and little energy is exchanged between both systems. The equations (B.6) and (B.7) would then give the NVE thermodynamic ensemble trajectories. On the contrary, if Q_b is very small ($Q_b \to 0$), a tight coupling is used, and high frequency temperature oscillations are susceptible to occur.

A more intuitive choice of the coupling parameter Q_b can be made through the relaxation time τ_{NH}, defined as:

$$\tau_{NH} = \sqrt{\frac{Q_b}{k_B N_{dof} T_0}} \tag{B.10}$$

The expression (C.7) then becomes:

$$\dot{\gamma} = \frac{-1}{\tau_{NH}^2} \frac{T(t)}{T_0} \left(\frac{N_{dof}+1}{N_{dof}} \frac{T_0}{T(t)} - 1 \right) \tag{B.11}$$

The relaxation time has time units and equals roughly to the time needed for the system to thermally relax. From (B.10) it can be derived that large values of τ_{NH} result in slow transfers of temperature between the real molecular system and the heat bath, while for lower values of τ_{NH} this transfer is done more rapidly. The choice of τ_{NH} is done by trial and error. In practice, a value around 100 fs ensures the correct canonical thermodynamic integration [12]. With respect to the velocity-rescaling algorithm, the temperature evolves more smoothly with the Nosé-Hoover thermostat. For both methods, the heat transfer depends on the ratio of the instantaneous kinetic temperature $T(t)$ and the target temperature T_t.

B.3. Langevin algorithm

The Langevin thermostat uses Brownian dynamics in order to solve the 3D Langevin equations [31]. These equations of motion are modified to include two additional terms: a friction force and a random force, both of them acting independently on all the atoms in the thermostated group. The friction force represents the resistance of the atom to the surrounding medium. On the other hand, the random force accounts for the random collisions occurring between the atoms in the real system and the heat bath. The new equations of motion, considering the intermolecular force F_c, the friction force F_f, and the random force F_r is equal to:

$$\ddot{r}_i = \frac{F_t}{m_i} \tag{B.12}$$

$$F_t = F_c + F_f + F_r \tag{B.13}$$

The friction force acting on each individual atom is calculated as:

$$F_f = \left(\frac{m_i}{\tau_L}\right)\dot{r}_i \tag{B.14}$$

where τ_L is a damping time. It roughly represents the time necessary for the system to relax with time. The random force, according to the fluctuation-dissipation theorem, is equal to:

$$F_r \propto \sqrt{\frac{k_B T_0 m_i}{dt\tau_L}} \tag{B.15}$$

With respect to the previously presented methods, the Langevin thermostat presents the advantage of treating each atom individually, removing heat locally from where it is needed. As a result, there is no risk of developing a temperature gradient in the thermostated group.

Appendix C
Heat conduction in confined fluids

In NEMD simulations of confined lubricants subjected to shear, a viscous heat flux is generated. The purpose of this Appendix is to present two equivalent approaches for the determination of the thermal conductivity of fluids: either by directly applying the Fourier law after the calculation of the heat flux, or by fitting equation (V.8) derived from the Fourier law to the induced temperature profile across the film.

C.1. Thermal conductivity

Understanding how the thermal conductivity of confined fluids behaves under different pressure and temperature conditions is important in order to fully understand and predict temperature changes inside the contact. In this first section, two methods are presented to estimate the thermal conductivity λ_f of a fluid from NEMD simulations. The first method is based on the energy balance introduced in Chapter V. For instance, when a lubricated system is sheared, a viscous heat flux is generated that needs to be evacuated through the solid confining surfaces (see equation (V.3)). The temperature then follows a gradient across the film thickness, best explained by the Fourier law [228]:

$$\varphi_{out} = -\lambda_f \frac{dT}{dz} \tag{C.1}$$

The thermal conductivity can then be easily obtained by comparing equations (V.3) and (C.1). Furthermore, a similar outcome can be obtained by fitting equation (V.8) to the temperature profile across the contact. Some temperature profiles for BB, SQ, and NPE at different pressure and temperature conditions exposed to various shear rates are represented in Figure C.1. Indeed, both approaches are equivalent, as the two are based on the Fourier law of heat conduction, either in its derivative form (taking as an input the dissipated heat flux), or in its developed form (the input is then the temperature profile).

Figure C.2 shows the thermal conductivity of BB, SQ, and NPE for nominal liquid and solid-like state conditions over a wide range of shear rates. It evidences how little the shear rate has an impact on the thermal conductivity value, being nearly constant over the range of rates simulated. The average value of thermal conductivity is presented in Table C.1.

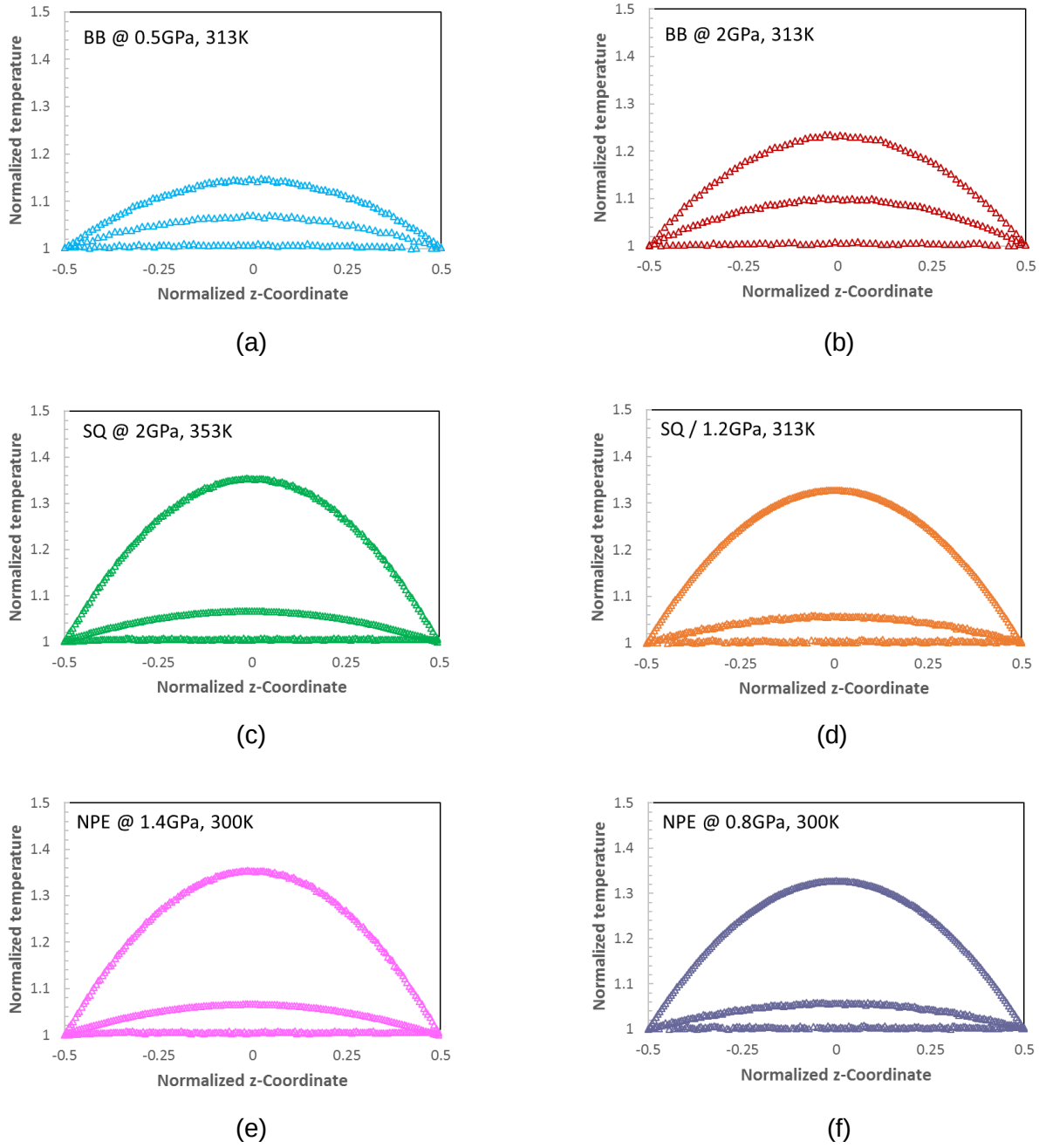

Figure C1. Spatially averaged temperature profiles for (a) BB, (b) SQ and (c) NPE at different pressure and temperature conditions and for different shear rates (10^8 s^{-1}, 5 x 10^9 s^{-1} and 10^{10} s^{-1}). In all the profiles, both the z-coordinate and the temperature have been normalized to z/h and T/T_w respectively, in order to facilitate comparison between systems. T_w is the temperature imposed at the wall, and h the total film thickness equal to 10-13 nm. The temperature profiles in the left column correspond to systems submitted to liquid thermodynamic conditions, while in the right column solid-like thermodynamic conditions favoring LSS apparition are applied.

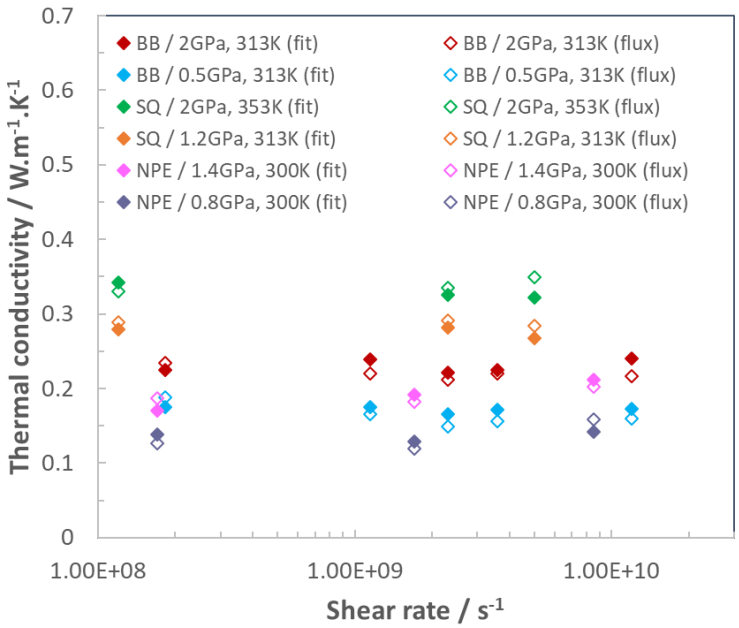

Figure C.2. Variation of the thermal conductivity λ_f of BB, SQ, and NPE for different pressure and temperature conditions. The thermal conductivity has been determined by either considering the dissipated energy flux and equation (C.1) (unfilled symbols), or by fitting (V.8) to the temperature profile (filled symbols).

Table C.1. Average values of the thermal conductivity for the three tested fluid under different pressure and temperature conditions.

Fluid	Pressure / GPa	Temperature / K	λ_f / W.(m.K)$^{-1}$
BB	0.5	313	0.1721
	2	313	0.2344
SQ	1.2	313	0.2789
	2	353	0.3341
NPE	0.8	300	0.1349
	1.4	300	0.1902

C.2. Validation of the thermal conductivity of squalane by empirical models

There is not much data available for the thermal properties of highly confined lubricants at elevated pressure, hence the need to use empirical models to extrapolate low pressure data to higher pressures. From the three simulated fluids in this work, only the thermal conductivity

of squalane has been experimentally measured. The thermal conductivity λ_f of squalane is expressed as:

$$\lambda_f = C\kappa^{-s} \tag{C.2}$$

with:

$$\kappa = \left(\frac{V}{V_R}\right)\left[1 + A\left(\frac{T}{T_R}\right)\left(\frac{V}{V_R}\right)^{-q}\right] \tag{C.3}$$

The meaning, as well as the numerical value for each parameter, is given in Table C.2, and are supplied by [229, 230].

A modified version of the Tait equation of state is used to model the temperature and pressure dependence of volume for squalane. It is written for the volume relative to the volume at ambient pressure as:

$$\frac{V}{V_0} = 1 - \frac{1}{1 + K'_0}\ln\left[1 + \frac{p}{K_0}(1 + K'_0)\right] \tag{C.4}$$

where:

$$K_0 = K_{00}e^{-\beta_k T} \tag{C.5}$$

The volume at ambient pressure relative to the ambient pressure volume at the reference temperature, T_R, is assumed to vary with temperature as:

$$\frac{V}{V_R} = 1 + a_v(T - T_R) \tag{C.6}$$

In a similar fashion, the thermal conductivity of BB can be estimated at ambient pressure with the following formula [231]:

$$\log \lambda_f = x_1 + x_2\left(\frac{T}{x_3}\right)^{\frac{2}{7}} \tag{C.7}$$

where x_1 is equal to -1.7335, x_2 is 0.9898, and x_3 is 820. Formula (C.7) can later be used to fit simulation data with the Tait equation of state (C.2), but with a new set of coefficients, as presented in Table C.2.

Table C.2. Parameters for the Tait equation of state for the determination of the thermal conductivity of benzyl benzoate and squalane [229, 230].

Parameter	Nomenclature	Value BB	Value SQ
Thermal conductivity / W.(m.K)$^{-1}$	λ_f		
Pressure / Pa	p		
Temperature / K	T		
Parameter in the conductivity function / W.(m.K)$^{-1}$	C	0.143	0.074
Dimensionless conductivity scaling parameter	κ	0.804	0.748
Exponent in the conductivity scaling model	s	1.7	4.5
Coefficient in the dimensionless conductivity scaling parameter	A	0.001	-0.115
Coefficient in the dimensionless conductivity scaling parameter	q	14	2
Isothermal bulk modulus at p=0 / Pa	K_0	2.02 x 10^9	1.19 x 10^9
Pressure rate of change of isothermal bulk modulus at p=0	K'_0	10.44	11.74
K_0 at absolute temperature / Pa	K_{00}	1.37 x 10^{10}	8.66 x 10^9
Temperature coefficient of K_0 / K^{-1}	β_k	6.11 x 10^{-3}	6.33 x 10^{-3}
Thermal expansivity defined for volume linear with temperature / K^{-1}	a_v	7.47 x 10^{-4}	8.36 x 10^{-4}

The thermal conductivity of squalane coming from NEMD simulations has been directly compared to the Tait equation of state parametrized for the same fluid [229, 230] for two different conditions: at 1.2 GPa and 313 K, where LSS was present, and for 2 GPa and 353 K, where LSS was not observed. Regarding benzyl benzoate, NEMD simulations at 313 K and 0.5 GPa and 2 GPa are considered, where either shear thinning or LSS is present respectively. The final thermal conductivity value that is used to compare to the Tait equation of state model is obtained by averaging the values of conductivity calculated from the temperature profile and from the Fourier law fit. The results are presented in Table C.3. The results show the very good agreement with experiments and the validity of the MD model.

Table C.3. Comparison between simulated and extrapolated thermal conductivity data of benzyl benzoate and squalane for two different operating conditions.

Fluid	Pressure / GPa	Temperature / K	$\lambda_{f,MD}$ / W.(m.K)$^{-1}$	$\lambda_{f,Tait}$ / W.(m.K)$^{-1}$	Relative error / %
BB	0.5	313	0.1722	0.1677	2.68
	2	313	0.2318	0.2069	12.03
SQ	1.2	313	0.2789	0.2739	1.81
	2	353	0.3341	0.3369	-0.82

Appendix D
Mean squared displacement of fluids

The data presented in this Appendix aims to complete the results of mobility from Chapter V. In the first section, the MSD of SQ and the NPE mixture for liquid and solid-like conditions is shown for both bulk and confined situations. In the second section, additional MSD curves of bulk BB are introduced. They are used to create Figure V.8.

D.1. Mean squared displacement of squalane (SQ) and neopolyol ester mixture (NPE)

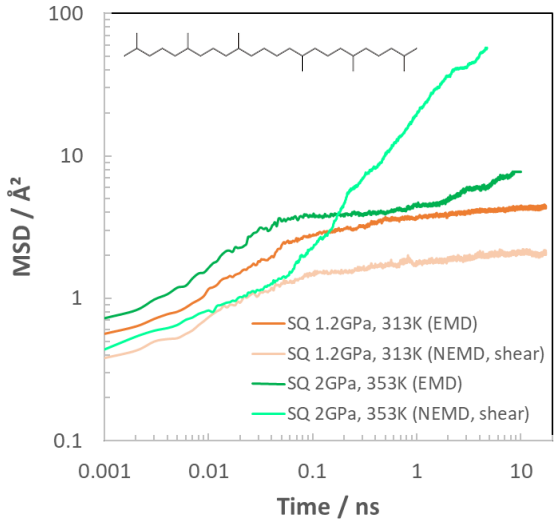

(a)

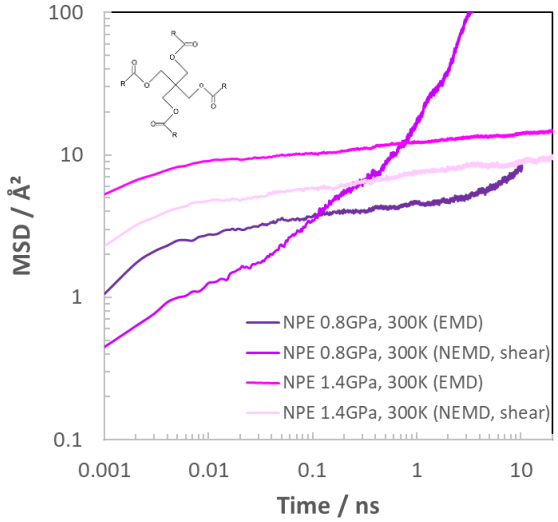

(b)

Figure D.1. The total MSD against time for (a) SQ and (b) NPE, for bulk and confined NEMD simulations submitted to a shear rate of 10^8 s^{-1}.

In Figure D.1, the global MSD for SQ and for NPE is represented against time for solid-like and for liquid thermodynamic conditions. A gap between equilibrium and nonequilibrium data is present. This gap corresponds to the restriction of movement in the z-direction due to confinement. For solid-like states (SQ at 1.2 GPa and 31 3K, and NPE at 1.4 GPa and 300 K), the fluid is in the caging regime, unable to overcome the potential energy barrier needed to escape from the influence of the neighboring molecules. Under these circumstances, LSS is present during shearing. For liquid conditions (SQ at 2GPa and 353K, and NPE at 0.8 GPa and 300 K), the molecules can escape from the cages and diffuse at long times. No LSS is measured here.

D.2. Mean squared displacement of benzyl benzoate at equilibrium

In this section, some of the MSD curves used to create Figure V.8 from Chapter V are shown. From these figures, the coefficient of diffusion is calculated at long times from the slope of the MSD in the diffusive regime with formula (V.14).

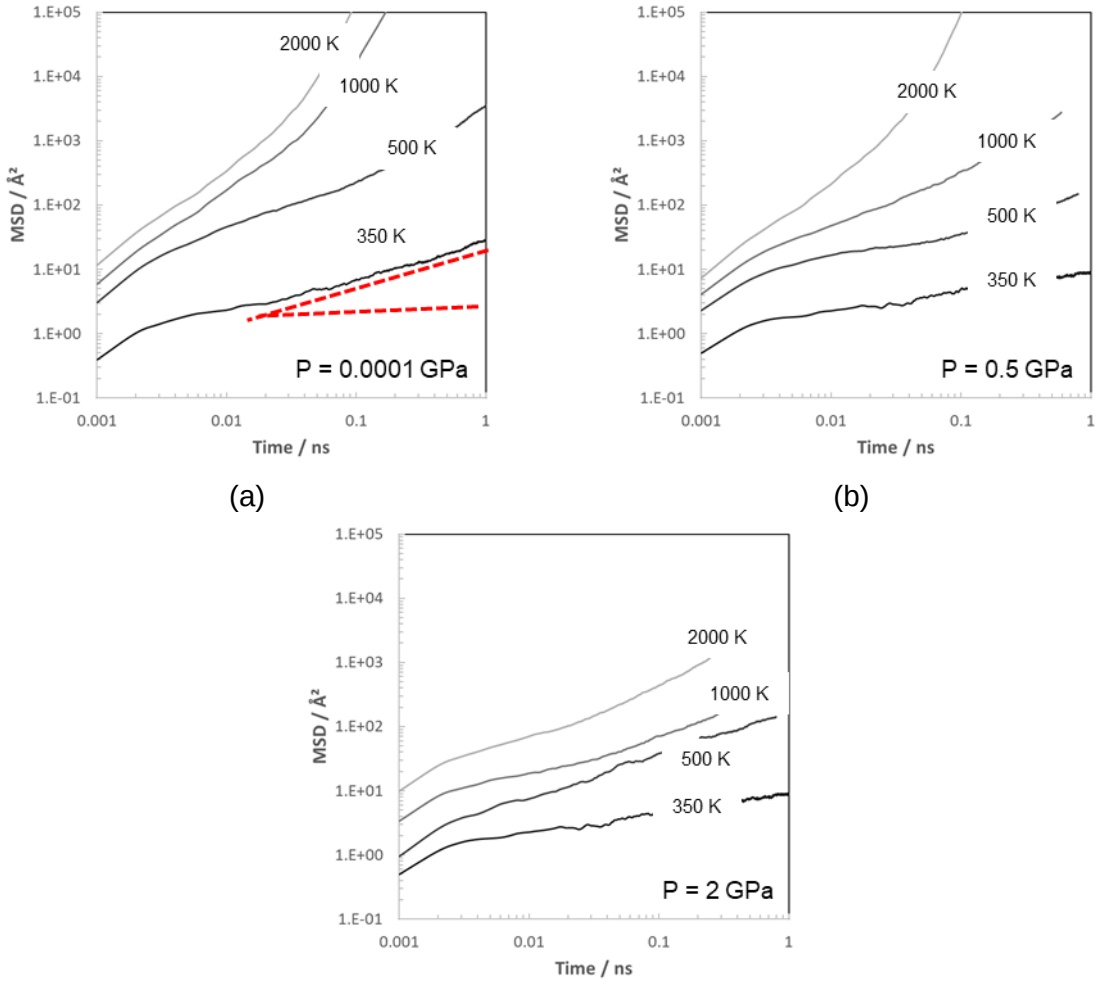

(a) (b)

(c)

Figure D.2. MSD against time for static bulk BB systems at (a) ambient pressure, (b) 0.5 GPa, and (c) 2 GPa, and at three different temperatures: 350 K, 500 K, 1000 K, and 2000 K. In (a), a representation of how the slope in the diffusive regime is determined is presented.

Appendix E
Activation energy of squalane

The data presented in this Appendix aims to complete the results of the activation energy from Chapter V. The analysis is here extended to squalane by performing EMD simulations on bulk systems of this molecule under static conditions, for different values of pressure and temperature. From these simulations, the coefficient of diffusion can be derived from the MSD. In Figure E.1, the coefficient of diffusion is plotted as a function of the inverse of temperature for four different pressures.

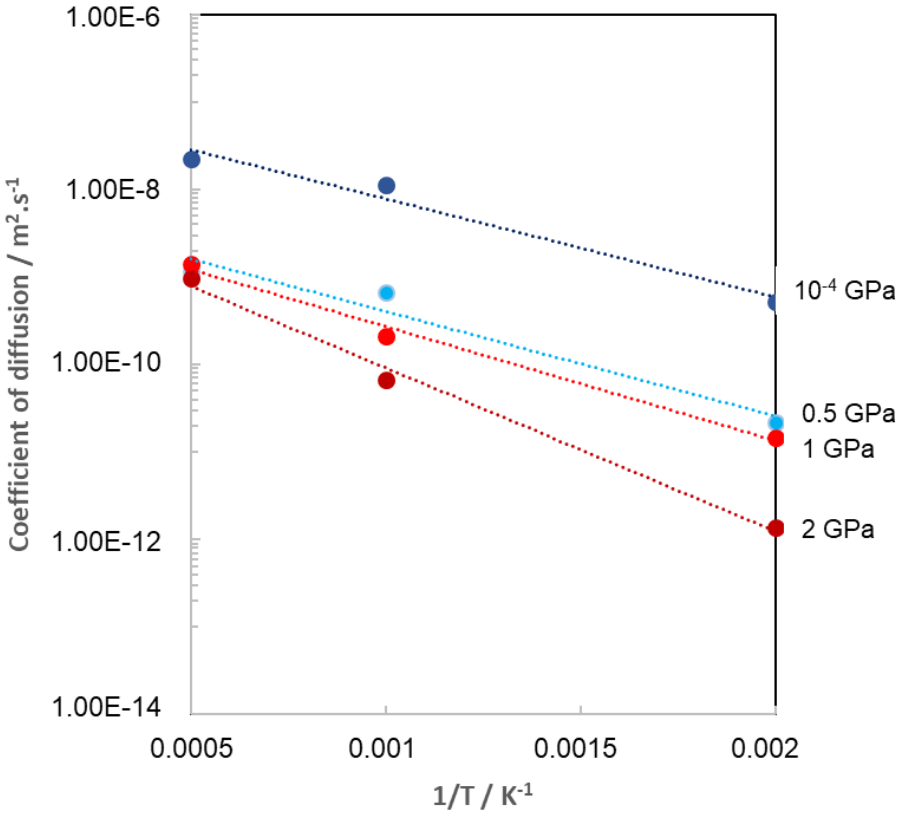

Figure E.1. Evolution of the coefficient of diffusion of SQ as a function of the inverse of temperature for different pressures. The coefficient of diffusion for each pressure and temperature state has been calculated from the diffusive regime of the MSD vs. time plot, from EMD simulations.

From Figure E.1, the activation energy can be calculated for each pressure and for the specific range of temperatures simulated following equation (V.17). The results are given in Figure E.2, where the activation energy for squalane is seen to evolve linearly with increasing pressures following equation (V.18), similarly to benzyl benzoate. As shown previously for the case of benzyl benzoate, the activation volume does not depend here on the temperature for the range of temperatures considered.

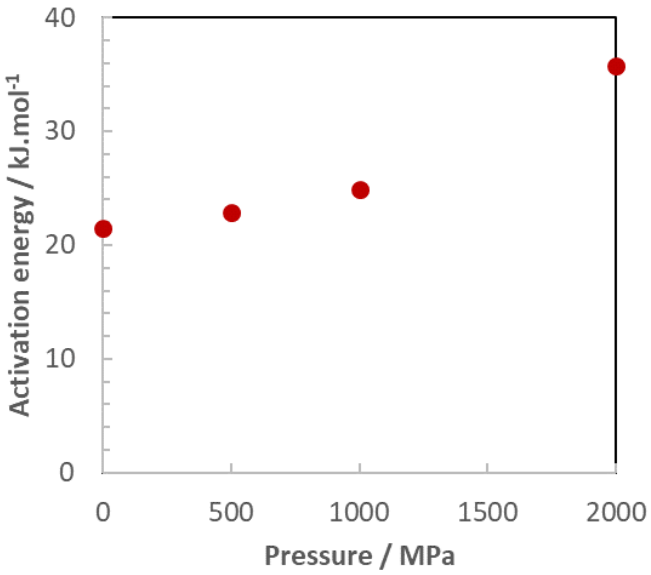

Figure E.2. Evolution of the activation energy of SQ as a function of pressure. The red points represent each one of the activation energies calculated from the curve slopes from the lnD versus 1/T plots. The activation energy E_a follows a linear trend with pressure.

Bibliography

[1] J.-D. Wheeler, P. Vergne, N. Fillot and D. Philippon, "On the relevance of analytical film thickness EHD equations for isothermal point contacts: Qualitative or quantitative predictions?," *Friction,* vol. 4, no. 4, pp. 369-379, 2016.

[2] S. Bair, Kotzalas and M., "The contribution of roller compliance to elastohydrodynamic traction," *Tribol. Trans.,* vol. 49, no. 2, pp. 218-224, 2006.

[3] S. Bair, High pressure rheology for quantitative elastohydrodynamics. Vol. 54, Elsevier, 2007.

[4] F. W. Smith, "Lubricant behavior in concentrated contact systems - the Castor oil-steel system," *Wear,* vol. 2, no. 4, pp. 250-263, 1959.

[5] F. W. Smith, "The effect of temperature in concentrated contact lubrication," *ASLE Trans.,* vol. 5, no. 1, pp. 142-148, 1962.

[6] B. O. Jacobson, Rheology and elastohydrodynamic lubrication, New York: Elsevier, 1991.

[7] S. Bair, "Shear strength measurements of lubricants at high pressure," *J. Lubr. Technol.,* vol. 101, pp. 252-257, 1979.

[8] S. Ndiaye, Ultimate behavior of confined fluids under very high pressure and shear stress. PhD thesis, Lyon: INSA Lyon, 2017.

[9] S. Bair and W. O. Winer, "The high shear stress rheology of liquid lubricants at pressures of 2 to 200 MPa," *J. Tribol. ,* vol. 112, no. 2, pp. 246-252, 1990.

[10] J. P. Ewen, C. Gattinoni, J. Zhang, D. M. Heyes, H. A. Spikes and D. Dini, "On the effect of confined fluid molecular structure on nonequilibrium phase behaviour and friction," *Phys. Chem. Chem. Phys.,* vol. 19, no. 27, p. 17883, 2017.

[11] V. Jadhao and M. O. Robbins, "Probing large viscosities in glass-formers with nonequilibrium simulations," *PNAS,* vol. 114, no. 30, pp. 7952-7957, 2017.

[12] M. P. Allen and D. J. Tildesley, Computer simulation of liquids, Oxford University Press, 1989.

[13] A. I. Jewett, Z. Zhuoyun and J.-E. Shea, "Moltemplate: a course-grained model assembly tool," *Biophys.,* vol. 104, p. 169a, 2012.

[14] S. Plimpton, "Fast Parallel Algorithms for Short-Range Molecular Dynamics for the United States Department of Energy under Contract DE.ACO4-76DPOO789," *J. Comput. Phys.,* vol. 117, pp. 1-19, 1993.

[15] K. Pluhackova, H. Morhenn, L. Lautner, W. Lohstroh, K. S. Nemkovski, T. Unruh and R. A. Bockmann, "Extension of the LOPLS-AA Force Field for Alcohols, Esters, and

Monoolein Bilayers and its Validation by Neutron Scattering Experiments," *J. Phys. Chem. B,* vol. 119, no. 49, p. 15287–15299, 2015.

[16] S. W. Siu, K. Pluhackova and R. A. Bockmann, "Optimization of the OPLS-AA force field for long hydrocarbons," *J. Chem.Theory Comput.,* vol. 8, no. 4, p. 1459–1470, 2012.

[17] W. L. Jorgensen, D. S. Maxwell and J. Tirado-Rives, "Development and Testing of the OPLS All-Atom Force Field on Conformational Energetics and Properties of Organic Liquids," *J. Am. Chem. Soc.,* vol. 118, no. 45, p. 11225, 1996.

[18] J. Ewen and S. Echeverri-Restrepo, "LAMMPS_builder," [Online].

[19] A. Hjorth, "The Atomic Simulation Environment - A Python library for working with atoms," *J. Phys.: Condens. Matter,* vol. 29, p. 273002, 2017.

[20] P. A. Thompson and M. O. Robbins, "Shear flow near solids: Epitaxial order and flow boundary conditions," *Phys. Rev. A,* vol. 41, no. 12, pp. 6830-6837, 1990.

[21] C. Trozzi and G. Ciccotti, "Stationary nonequilibrium states by molecular dynamics. II. Newton's law," *Phys. Rev. A,* vol. 29, pp. 915-925, 1984.

[22] H. Berro, A molecular dynamics approach to nano-scale lubrication. PhD thesis, Lyon: INSA Lyon, 2010.

[23] A. Jabbarzadeh and R. I. Tanner, "Thin lubricant films confined between crystalline surfaces: Gold versus mica," *Tribol. Int.,* vol. 44, pp. 711-719, 2011.

[24] D. Savio, N. Fillot, P. Vergne and M. Zaccheddu, "A model for wall slip prediction of confined n-alkanes: effect of wallfluid interaction versus fluid resistance," *Tribol. Lett.,* vol. 46, no. 1, pp. 11-22, 2012.

[25] H. Berro, N. Fillot and P. Vergne, "Molecular dynamics simulation of surface energy and ZDDP effects on friction in nano-scale lubricated contacts," *Trib. Int.,* vol. 43, pp. 1811-1822, 2010.

[26] S. Foiles, M. Baskes and M. Daw, "Embedded-Atom-Method functions for the FCC metals Cu, Ag, Au, Ni, Pd, Pt, and their alloys," *Phys. Rev. B,* vol. 33, no. 12, pp. 7983-7991, 1986.

[27] M. I. Mendelev, S. Han, D. J. Srolovitz, G. J. Ackland, D. Y. Sun and M. Asta, "Development of new interatomic potentials appropriate for crystalline and liquid iron," *Philos. Mag.,* vol. 83, no. 35, pp. 3977-3994, 2003.

[28] L. Zhao, L. Liu and H. Sun, "Semi-ionic model for metal oxides and their interfaces with organic molecules," *J. Phys. Chem. C,* vol. 111, no. 28, pp. 10610-10617, 2007.

[29] J. Cao and A. E. Likhtman, "Shear banding in molecular dynamics of polymer melts," *Phys. Rev. Lett.,* vol. 10, no. 2, p. 028302, 2012.

[30] C. R. Evans and K. L. Johnson, "The rheological properties of elastohydrodynamic lubricants," *Proc. Inst. Mech. Eng., Part C,* vol. 200, no. 5, pp. 303-312, 1986.

[31] T. Schneider and E. Stoll, "Molecular-dynamics study of a three-dimensional one-component model for distortive phase transitions," *Phys. Rev. B,* vol. 17, no. 3, p. 1321, 1978.

[32] R. Khare, J. de Pablo and A. Yethiraj, "Molecular simulation and continuum mechanics study of simple fluids in non-isothermal planar couette flows," *J. Chem. Phys.,* vol. 107, no. 7, pp. 2589-2596, 1997.

[33] A. Martini, Y. Liu, R. Snurr and Q. Wang, "Molecular dynamics characterization of thin film viscosity for EHL simulation," *Tribol. Lett.,* vol. 21, no. 3, pp. 217-225, 2006.

[34] S. Y. Liem, D. Brown and J. H. R. Clarke, "Inverstigation of the homogeneous-shear nonequilibrium-molecular-dynamics method," *Phys. Rev. A,* vol. 45, no. 6, pp. 3706-3713, 1992.

[35] H. Berro, N. Fillot, P. Vergne, T. Tokumasu, T. Ohara and G. Kikugawa, "Energy dissipation in non-isothermal molecular dynamics simulations of confined liquids under shear," *J. Chem. Phys.,* vol. 135, no. 13, p. 134708, 2011.

[36] S. Ndiaye, L. Martinie, D. Philippon, N. Devaux and P. Vergne, "A quantitative friction-based approach of the limiting shear stress pressure and temperature dependence," *Tribol. Lett.,* vol. 65, no. 4, p. 149, 2017.

[37] S. Bair, C. McCabe and P. Cummings, "Calculation of viscous EHL traction for squalane using molecular simulation and rheometry," *Tribol. Lett.,* vol. 13, no. 4, pp. 251-254, 2002.

[38] S. Bair, "The viscosity at the glass transition of a liquid lubricant," *Friction,* vol. 7, no. 1, pp. 86-91, 2019.

[39] J. Donnelly, L. Drewes, R. Johnson, W. Munslow, K. Knap and G. Sovocool, "Purity and heat fusion data for environmental standards as determined by differential scanning calorimetry," *Thermochim. Acta,* vol. 167, no. 2, p. 155, 1990.

[40] "Final report on the safety assessment of squalane and squalene," *Int. J. Toxicol.,* vol. 1, no. 2, pp. 37-56, 1982.

[41] D. Savio, N. Fillot and P. Vergne, "A molecular dynamics study of the transition from ultra-thin film lubrication toward local film breakdown," *Trib. Lett.,* vol. 50, pp. 207-220, 2013.

[42] J. Gao, W. D. Luedtke and U. Landman, "Structure, solvation forces and shear of molecular films in a rough nano-confinement," *Trib. Lett.,* vol. 9, pp. 3-13, 2000.

[43] B. N. J. Persson, V. N. Samoilov, S. Zilberman and A. Nitzan, "Phenomenology of squeezing and sliding of molecularly thin Xe, CH4 and C16H34 lubrication films between smooth and rough curved solid surfaces with long-range elasticity," *J. Chem. Phys. ,* vol. 117, no. 8, p. 3897, 2002.

[44] J. Gao, W. D. Luedtke, D. Gourdon, M. Ruths, J. N. Iraelachvili and U. Landman, "Frictional forces and Amontons' law: from the molecular to the macroscopic scale," *J. Phys. Chem. B,* vol. 108, no. 11, pp. 3410-3425, 2004.

[45] C. Gattinoni, D. M. Heyes, C. D. Lorenz and D. Dini, "Traction and nonequilibrium phase bejavior of confined sheared liquids at high pressure," *Phys. Rev. E,* vol. 88, p. 052406, 2013.

[46] D. M. Heyes, E. R. Smith, D. Dini, H. A. Spikes and T. A. Zaki, "Pressure dependence of confined liquid behavior subjected to boundary-driven shear," *J. Chem. Phys.,* vol. 136, no. 13, p. 134705, 2012.

[47] S. Mackowiak, D. Heyes, D. Dini and A. Branka, "Non-equilibrium phase behavior and friction of confined molecular films under shear: A non-equilibrium molecular dynamics study," *J. Chem. Phys.,* vol. 145, no. 16, p. 164704, 2016.

[48] J. P. Ewen, H. Gao, M. H. Müser and D. Dini, "Shear heating, flow, and friction of confined molecular fluids at high pressure," *Phys. Chem. Chem. Phys.,* vol. 21, pp. 5813-5823, 2019.

[49] R. Huang, I. Chavez, K. M. Taute, B. Lukic, S. Jeney, M. G. Raizen and E.-L. Florin, "Direct observation of the full transition from ballistic to diffusive Brownian motion in a liquid," *Nature Phys.,* vol. 7, pp. 576-580, 2011.

[50] A. Einstein, "Zur theorie der Brownschen Bewegung," *Ann. Phys. ,* vol. 324, pp. 371-381, 1906.

[51] S. Boyde, "Green lubricants. Environmental benefits and impacts of lubricants," *Green. Chem.,* vol. 4, no. 4, pp. 293-307, 2002.

[52] K. Holmberg, P. Andersson and A. Erdmir, "Global enery consumption due to friction in passenger cars," *Tribol. Int.,* vol. 47, pp. 221-234, 2012.

[53] K. Holmberg, P. Kivikytö-Reponen, P. Härkisaari, K. Valtonen and A. Erdemir, "Global energy consumption due to friction and wear in the mining industry," *Tribol. Int.,* vol. 115, no. 4, pp. 116-139, 2017.

[54] M. Charlotte, Physico-chemistry, high pressure rheology and film-forming capacity of polymer-base oil solutions in EHL. PhD thesis, Lyon: INSA Lyon, 2014.

[55] GVR, "Bearings market size, share & trends analysis report by product (ball, roller), by application (automotive, agriculture, electrical, mining & construction, railway & aerospace), and segment forectas, 2019-205," Grand View Research, March 2019. [Online]. Available: http://www.grandviewresearch.com/industry-analysis/bearings-market.

[56] D. Dowson, History of tribology, London: Longman, 1979.

[57] G. Amontons, "De la resistance causeé dans les machines," *Memoires de l'Academie Royal des Sciences,* pp. 275-282, 1699.

[58] C. A. Coulomb, Mémoires relatifs à la physique, 1784.

[59] B. Tower, "First report on friction experiments (friction of lubricated bearings)," *Proc. Instn. Mech. Engrs.,* pp. 632-659, 1883.

[60] A. S. Szeri, Fluid film lubrication: theory and design, Cambridge University Press, 2005.

[61] O. Reynolds, "On the theory of lubrication and its application to Mr. Beauchamp Tower's Experiments, including an experimental determination of the viscosity of olive oil," *Proc. R. Soc. London,* vol. 40, no. 242-245, pp. 191-203, 1886.

[62] R. Stribeck, "Die wesentlichen Eigenschaften der Gleit- und Rollenlager," *Z. Deut. Ing.,* vol. 46, pp. 1241-1348, 1902.

[63] H. Hertz, "Über die Berührung fester elastischer Körper," *Journal für die reine und angewandte Mathematik,* vol. 92, pp. 156-171, 1881.

[64] C. Barus, "Isothermal, isopiestics and isometrics relative to viscosity," *Am. J. Sci.,* vol. 45, pp. 87-96, 1893.

[65] C. J. A. Roelands, Correlational aspects of the viscosity-temperature-pressure relationship of lubrication oil. PhD thesis, Technische Hogeschool Delft, 1966.

[66] M. L. Williams, R. F. Landel and J. D. Ferry, "The temperature dependence of relaxation mecanisms in amorphous polymers and other glass-forming liquids," *J. Am. Chem. Soc.,* vol. 77, no. 14, pp. 3701-3707, 1955.

[67] H. S. Cheng and B. Sternlicht, "A numerical solution for the pressure, temperature, and film thickness between two infinitely long, lubricated rolling and sliding cylinders, under heavy loads," *J. Basic Eng.,* vol. 87, no. 3, pp. 695-704, 1965.

[68] D. Dowson and G. R. Higginson, Elastohydrodynamic Lubrication, the fundamentals of roller and gear lubrication, Pergamon Press, 1966.

[69] A. Ertel, "Hydrodynamic lubrication based on new principles," *Akad. SSR Prikadnaya Mathematica i Mekhanika,* vol. 2, pp. 41-52, 1939.

[70] A. N. Grubin and I. E. Vinogradova, Investigation of the contact of machine components, Central Scientific Research Institute for Technology and Mechanical Engineering Moscow, 1949.

[71] S. Bair, "A rough shear-thinning correction for EHD film thickness," *STLE Trib. Trans.,* vol. 47, pp. 361-365, 2004.

[72] H. S. Cheng, "A refined solution to the thermal-elastohydrodynamic lubrication of rolling and sliding cylinders," *J. Basic Eng.,* vol. 8, pp. 397-410, 1965.

[73] T. Doki-Thonn, N. Fillot, G. E. Morales-Espejel, M. Querry, D. Philippon, N. Devaux and P. Vergne, "A dual experimental/numerical approach for film thickness anlysis in TEHL spinning skewing circular contacts," *Tribol. Lett.,* vol. 50, no. 1, pp. 115-126, 2013.

[74] V. Bruyere, N. Fillot, G. E. Morales-Espejel and P. Vergne, "Computational fluid dynamics and full elasticity model for slidinf line thermal elastohydrodynamic contacts," *Tribol. Int.,* vol. 46, no. 1, pp. 3-13, 2012.

[75] W. Habchi, P. Vergne, S. Bair, O. Andersson, D. Eyheramendy and G. E. Moreales-Espejel, "Influence of pressure and temperature dependence of thermal properties of a lubricant on the behavior of circular TEHD contacts," *Tribol. Int.,* vol. 43, pp. 1842-1850, 2010.

[76] W. Habchi and J. Issa, "Fast and reduced full-system finite element solution of EHL problems: line contacts," *Adv. Eng. Soft.,* vol. 56, pp. 51-62, 2013.

[77] H. P. Evans and G. Hughes, "Evaluation of deflection in semi-infinite bodies by a differential method," *Proc. IMechE Part C J. Mech. Eng. Sci.,* vol. 214, no. 4, pp. 563-584, 2000.

[78] C. H. Veneer and A. A. Lubrecht, Multi-level methods in lubrication, Elsevier, 2000.

[79] D. Savio, Nanoscale phenomena in lubrication: from atomistic simulations to their integration into continuous models. PhD thesis, Lyon: INSA Lyon - Karlsruher Institut für Technologie , 2013.

[80] D. Zhu and Q. J. Wang, "On the l ratio range of mixed lubrication," *Proc. Inst. Mech. Eng. Part J J. Eng. Trib.,* vol. 226, no. 12, pp. 1010-1022, 2012.

[81] H. A. Spikes, "Mixed lubrication - an overview," *Lub. Sci.,* vol. 9, no. 3, pp. 221-253, 1997.

[82] H. A. Spikes and A. V. Olver, "Basics of mixed lubrication," *Lub. Sci.,* vol. 16, no. 1, pp. 1-28, 2003.

[83] K. L. Johnson, J. A. Greenwood and S. Y. Poon, "A simple theory os asperity contact in elastohydro-dynamic lubrication," *Wear,* vol. 19, no. 1, pp. 91-108, 1972.

[84] H. A. Spikes, "Sixty years of EHL," *Lub. Sci.,* vol. 18, no. 4, pp. 265-291, 2006.

[85] D. Dowson and G. R. Higginson, "A numerical solution to the leasto-hydrodynamic problem," *Mech. Eng. Sci.,* vol. 1, no. 1, pp. 6-15, 1959.

[86] W. Habchi, P. E. D. Vergne and G. E. Morales-Espejel, "Numerical investigation of the use of machine low-viscosity working fluids as lubricants in elastohydrodynamic lubricated point contacts," *Proc. IMechE. Part J J. Eng. Tribol.,* vol. 225, pp. 165-477, 2011.

[87] S. Bair, "Rheology and high-pressure models for quantitative elastohydrodynamics," *Proc. Inst. Mech. Eng. Part J,* vol. 223, pp. 617-628, 2009.

[88] S. Bair and O. Winer, "A rheological model for elastohydrodynamic contacts based on primary laboratory data," *J. Lubr. Technol.,* vol. 101, no. 3, pp. 258-164, 1979.

[89] S. Bair, "Actual Eyring models for thixotropy and shear-thinning: experimental validation and application to EHD," *Trans. ASME,* vol. 126, pp. 728-732, 2004.

[90] N. F. Bader, Traction in EHL-contacts: the influence of local fluid rheology and temperatures. PhD thesis, Hannover: Gottfried Wilhelm Leibniz Universität Hannover, 2018.

[91] R. I. Tanner, Engineering Rheology, OUP Oxford, 2000.

[92] I. J. Gruntfest, "Apparent departures from Newtonian behavior in liquids caused by viscous heating," *Trans. Soc. Rheol.,* vol. 9, no. 1, pp. 425-441, 1965.

[93] S. Bair, F. Qureshi and W. O. Winer, "Observations of shear localization in liquid lubricants under pressure," *J. Tribol. ,* vol. 115, no. ", pp. 507-513, 1993.

[94] K. L. Johnson and J. L. Tevaarwerk, "Shear behavior of elastohydrodynamic oil films," *Proceedings of the Royal Society of London A: Mathematical, Physical and Engineering Sciences,* vol. 356, no. 1687, pp. 215-236, 1977.

[95] A. Dyson, "Friction traction and lubricant rheology in elastohydrodynamic lubrication," *Philos. Trans. R. Soc. London A Math. Phys. Eng. Sci. ,* vol. 266, no. 1170, pp. 1-33, 1970.

[96] M. A. Plint, "Third paper: traction in elastohydrodynamic contacts," *Proc. Inst. Mech. Eng. ,* vol. 182, no. 1, pp. 300-306, 1967.

[97] M. Alsaad, S. Bair, D. M. Sanbonr and W. O. Winer, "Glass transition in lubricants: its relation to elastohydrodynamic lubrication (EHD)," *J. Tribol. ,* vol. 100, no. 3, pp. 404-416, 1978.

[98] S. Bair, C. Mary, N. Bouscharain and P. Vergne, "An improved Yasutomi correlation for viscosity at high pressure," *Proc. Inst. Mech. Eng. Part J J. Eng. Tribol.,* vol. 227, no. 9, pp. 1056-1060, 2013.

[99] S. Butler and P. Harrowell, "Simulation of the coexistence of a shearing liquid and a strained crystal," *J. Chem. Phys.,* vol. 118, no. 9, pp. 4115-4126, 2003.

[100] R. G. Horn and J. N. Israelachvili, "Direct measurement of structural forces between two surfaces in nonpolar liquid," *J. Chem. Phys.,* vol. 75, pp. 1400-1411, 1981.

[101] J. Gao, W. D. Luedtke and U. Landman, "Layering transitions and dynamics of confined fluid films," *Phys. Rev. Lett.,* vol. 79, no. 4, p. 705, 1997.

[102] J. Gao, W. D. Luedtke and U. Landman, "Structure and solvation forces in confined films: linear and branched alkanes," *J. Chem. Phys.,* vol. 106, no. 10, pp. 4309-4318, 1997.

[103] A. Ponjavic, M. Chennaoui and J. S. S. Wong, "Through-thickness velocity profile measurements in an elastohydrodynamic contact," *Tribol. Lett.,* vol. 50, no. 2, pp. 261-277, 2013.

[104] K. L. Johnson and R. Cameron, "Fourth paper: shear behavior of elastohydrodynamic oil films at high rolling contact pressures," *Proc. Inst. Mech. Eng.,* vol. 182, no. 1, pp. 307-330, 1967.

[105] K. L. Johnson and A. D. Roberts, "Observations of viscoelastic behavior of an elastohydrodynamic lubricant film," *Proceedings of the Royal Society of London A: Mathematical, Physical and Engineering Sciences,* vol. 337, no. 1609, pp. 217-242, 1974.

[106] N. Ohno, N. Kuwano and F. Hirano, "Effect of bulk modulus of solidfiied oils under high pressure on tractional behavior," *Japanese H. Tribol.,* vol. 38, no. 10, pp. 1361-1372, 1993.

[107] A. J. Barlow, G. Harrison, J. B. Irving, M. G. Kim, J. Lamb and W. C. Pursley, "The effect of pressure on the viscoelastic properties of liquids," *Proceedings of the Royal Society of London A: Mathematical, Physical and Engineering Sciences,* vol. 327, no. 1570, pp. 403-412, 1972.

[108] B. J. Briscoe and D. Tabor, "Rheology of thin organic films," *ASLE Trans.,* vol. 17, no. 3, pp. 158-165, 1974.

[109] V. S. J. Craig, C. Neto and D. R. M. Williams, "Shear-dependent boundary slip in an aqueous Newtonian liquid," *Phys. Rev. Lett.,* vol. 87, no. 5, p. 54504, 2001.

[110] Y. Zhu and S. Granick, "Mimit of the hydrdynamic no-slip condition," *Phys. Rev. Lett.,* vol. 88, no. 10, p. 106102, 2002.

[111] P. A. Thompson and S. M. Troian, "A general boundary condition for liquid flow at solid surfaces," *Nature,* vol. 389, no. 6649, pp. 360-362, 1997.

[112] E. Schnell, "Slippage of water over nonwettable surfaces," *J. Appl. Phys.,* vol. 27, no. 10, pp. 1149-1152, 1956.

[113] R. Pit, H. Hervet and L. Léger, "Direct experimental evidence of slip in hexadecane: solid interfaces," *Phys. Rev. Lett.,* vol. 85, no. 5, pp. 980-983, 2000.

[114] H. Hervet and L. Léger, "Flow with slip at the wall: from simple to complex fluids," *Comptes Rendus Phys.,* vol. 4, no. 2, pp. 241-249, 2003.

[115] C. W. Wu, P. Zhou and G. J. Ma, "Squeeze fluid film of spherical hydrophobic surfaces with wall slip," *Tribol. Int.,* vol. 39, no. 9, pp. 863-872, 2006.

[116] K. L. Johnson and J. G. Higginson, "A non-Newtonian effect of sliding in micro-EHL," *Wear,* vol. 128, no. 3, pp. 249-264, 1988.

[117] X. M. Li, F. Guo and P. L. Wong, "Shear rate and pressure ffects on boundary slippage in highly stresses contacts," *Tribol. Int.,* vol. 59, pp. 147-153, 2013.

[118] Y. Zhu and S. Granick, "Rate-dependent slip of Newtonian liquid at smooth surfaces," *Phys. Rev. Lett.,* vol. 87, no. 9, p. 96105, 2001.

[119] P. L. Wong, X. M. Li and F. Guo, "Evidence of lubricant slip on steel surface in EHL contact," *Tribol. Int.,* vol. 61, pp. 116-119, 2013.

[120] J. Richmond, O. Nilsson and O. Sandberg, "Thermal properties of some lubricants under high pressure," *J. Appl. Phys.,* vol. 56, no. 7, pp. 2065-2067, 1984.

[121] Y. Zhang and K. T. Ramesh, "On the compressibility of a glass-forming lubricant: experiments and molecular modeling," *J. Mech. Phys. Solids,* vol. 46, no. 10, pp. 1699-1722, 1998.

[122] M. Kaneta, H. Nishikawa and K. Kameishi, "Observation of wall slip in elastohydrodynamic lubrication," *J. Tribol.,* vol. 112, no. 3, pp. 447-452, 1990.

[123] H. Eyring, "Viscosity, plasticity, and diffusion as examples of absolute reaction rates," *J. Chem. Phys.,* vol. 4, pp. 283-291, 1936.

[124] P. B. Bowden and J. A. Jukes, "The plastic flow of isotropic polymers," *J. Mat. Sci.,* vol. 7, pp. 52-63, 1972.

[125] L. Chang, "On the shear bands and shear localizations in elastohydrodynamic lubrication film," *J. Tribol.,* vol. 127, no. 1, p. 245, 2005.

[126] S. Bair and C. McCabe, "A study of mechanical shear bands in liquids at high pressure," *Tribol. Int.,* vol. 37, no. 10, pp. 783-789, 2004.

[127] B. O. Jacobson, "An experimental determination of the solidification velocity for mineral oils," *ASLE Trans.,* vol. 17, no. 4, pp. 190-294, 1974.

[128] P. Sperka, I. Krupta and M. Hartl, "Evidence of plug flow in rolling-sliding elastohydrodynamic contact," *Tribol. Lett.,* vol. 2, no. 54, pp. 151-160, 2014.

[129] A. Ponjavic, L. Mare and J. S. S. Wong, "Effect of pressrue on the flow behavior of polybutene," *J. Polym. Sci. Part B Polym. Phys.,* vol. 52, no. 10, pp. 708-715, 2014.

[130] N. Metropolis and S. Ulam, "The Monte Carlo method," *J. Am. Stat. Assoc.,* vol. 44, pp. 335-341, 1949.

[131] N. Metropolis, A. W. Rosenbluth, M. N. T. A. H. Rosenbluth and E. Teller, "Equation of state calculations by fast computing machines," *J. Chem. Phys.,* vol. 21, pp. 1087-1092, 1953.

[132] S. A. Serebrinsky, "Physical time scale in kinetic Monte Carlo simulations of continuous-time Markov chains," *Phys. Rev. E ,* vol. 83, p. 037701, 2011.

[133] A. Jabbarzadeh, J. D. Atkinson and R. I. Tanner, "Nanorheology of molecularly thin films of n-hexadecane in Couette shear flow by molecular dynamics simulation," *J. Non-Newt. Fluid Mech.,* vol. 77, pp. 53-78, 1998.

[134] N. Voeltzel, P. Vergne, N. Fillot, N. Bouscharain and L. Joly, "Rheology of ionic liquid with variable Carreau exponent: a full picture by molecular simulation with experimental contribution," *Trib. Lett. ,* vol. 64, p. 25, 2016.

[135] G. P. Morriss, P. J. Daivis and D. J. Evans, "The rheology of normal alkanes: Decane and Eicosane," *J. Chem. Phys. ,* vol. 94, pp. 7420-7433, 1991.

[136] J. D. Weeks, D. Chandler and H. C. Andersen, "Role of repulsive forces in determining the equilibrium structure of simple liquids," *J. Chem. Phys. ,* vol. 54, pp. 5237-5247, 1971.

[137] R. Khare, J. de Pablo and A. Yethiraj, "Rheological, thermodynamic, and structural bodies of linear and branched alkanes under shear," *J. Chem. Phys. ,* vol. 107, pp. 6956-6964, 1997.

[138] J. D. Moore, S. T. Cui, H. D. Cochran and P. T. Cummings, "Rheology of lubricant basestocks: a molecular dynamics study of C-30 isomers," *J. Chem. Phys.,* vol. 113, pp. 8833-8840, 2000.

[139] C. McCabe, S. T. Cui and P. T. Cummings, "Characterizing the viscosity-temperature dependence of lubricants by molecular simulation," *Fluid Phase Equilib. ,* vol. 183, pp. 363-370, 2001.

[140] C. McCabe, S. T. Cui, P. A. Gordon and R. B. Saeger, "Examining the rheology of 9-octylheptadecane to giga-pascal pressures," *J. Chem. Phys.,* vol. 114, pp. 1887-1891, 2001.

[141] S. T. Cui, P. T. Cummings, H. D. Cochran, J. D. Moore and S. A. Gupta, "Nonequilibrium molecular dynamics simulation of the rheology of linear and branched alkanes," *Int. J. Thermophys. ,* vol. 1998, pp. 449-459, 1998.

[142] J. I. Siepmann, S. Karaboni and B. Smit, "Simulating the critical rbehavior of complex fluids," *Nature,* vol. 365, pp. 330-332, 1993.

[143] M. S. Green, "Markov random processes at the statistical mechanics of time-dependent phenomena. II. Irreversible processes in fluids," *J. Chem. Phys.,* vol. 22, pp. 398-413, 1954.

[144] R. Kubo, "Statistical-mechanical theory of irreversible processes. I. General theory and simple applications to magnetic conduction problems," *J. Phys. Soc. Jpn.,* vol. 12, pp. 570-586, 1975.

[145] S. Bair, C. McCabe and P. T. Cummings, "Comparison of nonequilibrium molecular dynamics with experimental measurements in the nonlinear shear-thinning regime," *Phys. Rev. Lett.,* vol. 88, p. 58302, 2002.

[146] K. P. Travis, B. D. Todd and D. J. Evans, "Departure from Navier-Stokes hydrodynamics in confined liquids," *Phys. Rev. E,* vol. 55, pp. 4288-4295, 1997.

[147] I. Bitsanis, J. J. Magda, M. Tirrell and H. T. Davis, "Molecular dynamics of flow in micropores," *J. Chem. Phys.,* vol. 87, pp. 1733-1750, 1987.

[148] W. T. Ashurst and W. G. Hoover, "Dense-fluid shear viscosity via nonequilibirium molecular dynamics," *Phys. Rev. A,* vol. 11, pp. 658-678, 1975.

[149] I. Bitsanis, S. A. Somers, H. T. Davis and M. Tirrell, "Microscopic dynamics of flow in molecularly narrow pores," *J. Chem. Phys.,* vol. 93, pp. 3427-3431, 1990.

[150] J. J. Magda, M. Tirrell and H. T. Davis, "Molecular dynamics of narrow, liquid-filled pores," *J. Chem. Phys.,* vol. 83, pp. 1888-1901, 1985.

[151] Coulomb, Premier mémoire sur l'électricité et le magnétisme, Histoire de l'Académie Royale des Sciences , 1785.

[152] F. F. Abraham, "The interfacial density profile of a Lennard-Jones fluid in contact with a (100) Lennard-Jones wall and its relationship to idealized fluid/wall systems: A Monte Carlo simulation," *J. Chem. Phys.,* vol. 68, pp. 3713-3716, 1978.

[153] I. K. Snook and W. Van Megen, "Solvation forces in simple dense fluids. I," *J. Chem. Phys.,* vol. 72, pp. 2907-2913, 1980.

[154] P. A. Thompson and M. O. Robbins, "Epitaxial order and flow boundary conditions," *Phys. Rev. A,* vol. 41, p. 6830, 1990.

[155] A. Jabbarzadeh, P. Harrowell and R. I. Tanner, "Crystal bridge formation marks the transition to rigidity in athin lubrication film," *Phys. Rev. Lett.,* vol. 96, p. 206102, 2006.

[156] R. Balasundaram, S. Jiang and J. Belak, "Structural and rheological properties of n-decane confined between graphite surfaces," *Chem. Eng. J,* vol. 74, pp. 117-127, 1999.

[157] A. Jabbarzadeh, P. Harrowell and R. I. Tanner, "Low friction lubrication between amorphous walls: Unraveling the contributions of surface roughness and in-plane disorder," *J. Chem. Phys.,* vol. 125, p. 034703, 2006.

[158] U. Heinbuch and J. Fischer, "Liquid flow in pores: Slip, no-slip, or multi-layer sticking," *Phys. Rev. A,* vol. 40, p. 1144, 1989.

[159] S. A. Somers and H. T. Davis, "Microscopic dynamics of fluids confined between smooth and atomically structured solid surfaces," *J. Chem. Phys.,* vol. 96, pp. 5389-5407, 1992.

[160] N. Voeltzel, A. Giuliani, N. Fillot, P. Vergne and L. Joly, "Nanolubrication by ionic liquids: molecular dynamics simulations reveal an anomalous effective rheology," *Phys. Chem. Chem. Phys.,* vol. 17, pp. 23226-23235, 2015.

[161] R. Singh, J. Monk and F. R. Hung, "Heterogeneity in the dynamics of the ionic liquid [bmim+][pf6-] confined in a slit nanopore," *J. Phys. Chem. C,* vol. 115, pp. 16544-16554, 2011.

[162] S. Granick, "Motions and relaxations of confined liquids," *Science,* vol. 253, pp. 1374-1379, 1991.

[163] J. Klein and E. Kumacheva, "Simple liquids confined to molecularly thin layers. I. Confinement-induced liquid-to-solid phase transitions," *J. Chem. Phys.,* vol. 108, pp. 6996-7009, 1998.

[164] P. A. Thompson, G. S. Grest and M. O. Robbins, "Phase transition and universal dynamics in confined films," *Phys. Rev. Lett.,* vol. 68, p. 3448, 1992.

[165] H. Docherty and P. T. Cummings, "Direct evidence for fluid-solid transition of nanoconfined fluids," *Soft Matter,* vol. 6, pp. 1640-1643, 2010.

[166] A. Jabbarzadeh, J. D. Atkinson and R. I. Tanner, "The effect of branching on slip and rheological properties of lubricants in molecular dynamics simulation of Couette shear flow," *Tribol. Int.,* vol. 35, pp. 35-46, 2002.

[167] A. Jabbarzadeh, J. D. Atkinson and R. I. Tanner, "Effect of the wall roughness on slip and rheological properties of hexadecane in molecular dynamics simulation of Couette shear flow between two sinusoidal walls," *Phys. Rev. E,* vol. 61, p. 690, 2000.

[168] N. Fillot, H. Berro and P. Vergne, "From continuous to molecular scale in modeling elastohydrodynamic lubrication: nanoscale surface slip effects on film thickness and friction," *Tribol. Lett.,* vol. 43, pp. 257-266, 2011.

[169] A. Jabbarzadeh, J. D. Atkinson and R. I. Tanner, "Wall slip in the molecular dynamics simulation of thin films of hexadecane," *J. Chem. Phys.,* vol. 110, pp. 2612-2620, 1999.

[170] A. Martini, H.-Y. Hsu, N. A. Patankar and S. Lichter, "Slip at high shear rates," *Phys. Rev. Lett.,* vol. 100, p. 20601, 2008.

[171] A. Vadakkepatt, Y. L. Dong, S. Lichter and A. Martini, "Effect of molecular structure on slip," *Phys. Rev. E,* vol. 84, p. 11, 2011.

[172] H. Washizu, T. Ohmori and A. Suzuki, "Molecular origin of limiting shear stress of elastohydrodynamic lubricaiton oil film studied by molecular dynamics," *Chem. Phys. Lett.,* vol. 678, pp. 1-4, 2017.

[173] L. Martinie and P. Vergne, "Lubrication at extreme conditions: a discussion about the limiting shear stress concept," *Trib. Lett.,* vol. 63, no. 2, p. 21, 2016.

[174] S. Nosé, "A unified formulation of the constact temperature molecular dynamics methods," *J. Chem. Phys,* vol. 81, pp. 511-519, 1984.

[175] X. Yong and L. T. Zhang, "Thermostats and thermostat strategies for molecular dynamics simulations of nanofluidics," *J. Chem. Phys. ,* vol. 138, p. 084503, 2013.

[176] Bernardi, S., B. D. Todd and D. J. Searles, "Thermostating highly confined fluids," *J. Chem. Phys. ,* vol. 132, p. 244706, 2010.

[177] C. Gattinoni, S. Mackowiak, D. M. Heyes, A. C. Branka and D. Dini, "Boundary-controlled barostats for slab geometries in molecular dynamics simulations," *Phys. Rev. E,* vol. 90, p. 13, 2014.

[178] S. Bair and W. O. Winer, "A new high-pressure, high-shear viscometer and results for lubricants," *Tribol. Trans.,* vol. 36, no. 4, pp. 721-725, 1993.

[179] F. Varnik, L. Bocquet, J.-L. Barrat and L. Berthier, "Shear-localization in a model glass," *Phys. Rev. Lett.,* vol. 90, p. 095702, 2003.

[180] A. V. Mokshin and J. L. Barrat, "Shear-induced crystallization of an amorphous system," *Phys. Rev. E,* vol. 77, no. 2, p. 021505, 2008.

[181] S. Yamada, "General shear-thinning dynamics of confined fluids," *Trib. Lett.,* vol. 13, no. 3, pp. 207-220, 2013.

[182] J. P. Ewen, D. M. Heyes and D. Dini, "Advances in nonequilibrium molecular dynamics simulations of lubricants and additives," *Friction,* pp. 1-38, 2018.

[183] E. T. Thostenson, Z. Ren and T.-W. Chou, "Advances in the science and technology of carbon nanotubes and their composites: a review," *Compos. Sci. Technol.,* vol. 61, pp. 1899-1912, 2001.

[184] W. F. van Gunsteren and H. .. C. Berendsen, "Computer simulation of molecular dynamics: Methodology, applications and perspectives in chemistry," *Angew. Chem. Int.,* vol. 29, pp. 992-1023, 1990.

[185] R. Car and M. Parrinello, "Unified approach for molecular dynamics and density-functional theory," *Phys. Rev. Lett.,* vol. 55, p. 2471, 1985.

[186] K. Binder, Monte Carlo and molecular dynamics simulations in polymer science, Oxford University Press, 1995.

[187] R. O. Dror, R. M. Dirks, J. P. Grossman, H. Xu and D. E. Shaw, "Biomolecular simulation: A computational microscope for molecular biology," *Annu. Rev. Biophys.,* vol. 41, pp. 429-452, 2012.

[188] J. D. Durrant and J. A. McCammon, "Molecular dynamics simulations and drug discovery," *BMC Biol.,* vol. 28, no. 9, pp. 1-9, 2011.

[189] M. Karplus and J. McCammon, "Molecular dynamics simulations of biomolecules," *Nat. Struct. Mol. Biol.,* vol. 9, pp. 646-652, 2002.

[190] M. Karplus and G. Petsko, "Molecular dynamics simulations in biology," *Nature,* vol. 347, pp. 631-639, 1990.

[191] J. Klimes, D. R. Bowler and A. Michaelides, "Chemical accuracy for the van der Waals density functional," *J. Phys. Cond. Matt.,* vol. 22, p. 022201, 2010.

[192] W. Jorgensen and J. Tirado-Rives, "The OPLS forcefield for proteins, energy minimizations for crystals of cyclic peptides and crambin," *J. Am. Chem. Soc.,* vol. 110, p. 1657–1723, 1988.

[193] W. Cornell, P. Cieplak, C. Bayly, I. Gould, K. Merz, D. Ferguson, D. Spellmeyer, T. Fox, J. Caldwell and P. Kollman, "A second generation force field for the simulation of proteins, nucleic acids and organic molecules," *J. Am. Chem. Soc.,* no. 117, pp. 5179-5197, 1995.

[194] K. A. Maerzke and J. I. Siepman, "Transferable potentials for phase quilibria-coarse-grain description for linear alkanes," *J. Phys. Chem. B,* vol. 115, pp. 3452-3465, 2011.

[195] R. Hockney and J. Eastwood, Computer simulation using particles, crc Press, 1988.

[196] D. Alfè and M. Gillan, "First-principle calculation of transport coefficients," *Phys. Rev. Lett.,* vol. 81, pp. 5161-5164, 1998.

[197] F. Müller-Plathe, "Reversing the perturbation of nonequilibrium molecular dynamics: An easy way to calculate the viscosity of fluids," *Phys. Rev. E,* vol. 59, pp. 4894-4898, 1999.

[198] A. Jabbarzadeh, J. Atkinson and R. Tanner, "Rheological properties of thin liquid films by molecular dynamics simulations," *Journal of Non-Newtonian Fluid Mechanics,* vol. 69, no. 2-3, pp. 169-193, 1997.

[199] A. T. J. Hayward, "Compressibility equations for liquids: a comparative study," *Brit. Jour. Appl. Phys.,* vol. 18, no. 7, p. 965, 1967.

[200] H. Hoang and G. Galliero, "Local viscosity of a fluid confined in a narrow pore," *Phys. Rev. E,* vol. 86, p. 021202, 2012.

[201] V. Anghel and R. P. S. H. A. Glovnea, "Friction and film-forming behavior of five traction fluids," *Lubr. Sci.,* vol. 21, no. 1, pp. 13-32, 2006.

[202] H. Hata and T. Tsubouchi, "Molecular structures of traction fluids in relation to traction properties," *Trib. Lett.,* vol. 5, pp. 69-74, 1998.

[203] S. Gunsel, S. Korcek, M. Smeeth and H. Spikes, "The elastohydrodynamic firction and film forming properties of lubricant base oils," *Tribol. Trans.,* vol. 42, no. 3, pp. 559-569, 1999.

[204] C. Low, H. Voon Lee and S. Bee Abd Hamid, "atalytic upgrading of bio oil model, compound into polyol ester via green alginante catalized esterification rection," *Proc. Saf. Env. Protec.,* vol. 111, pp. 160-169, 2017.

[205] J. J. Segovia, O. Fandino, E. R. Lopez, L. Lugo and M. C. F. J. Martin, "Automated densimetric system: measurements and uncertainties for compressed fluids," *J. Chem. Thermo.,* vol. 41, no. 5, pp. 632-638, 2009.

[206] O. Fandino, "Volumetric behaviour of the environmentally compatible lubricants pentaerythritol tetraheptanoate and pentaerythritol tetranoate at high pressures," *Green Chem.,* vol. 7, no. 11, pp. 775-783, 2005.

[207] O. Fandino, M. J. P. Comunas, L. Lugo, E. R. Lopew and J. Fernandez, "Density measurements under pressure for mixtures of pentaerythritol ester lubricants. Analysis of a density-viscosity relationship," *J. Chem. Eng. Data,* vol. 52, no. 4, pp. 1429-1436, 2007.

[208] N. Bouscharain, "Charactérisation de l'huile Nycobase 5750," INSA Lyon, 2018.

[209] K. A. G. Schmidt, D. Pagnutti, M. D. Curran, A. Singh, J. P. M. Trusler, G. C. Maitland and M. McBride-Wright, "New experimental data and reference models for the viscosity and density of squalane," *J. Chem. Eng. Data,* vol. 60, no. 1, pp. 137-150, 2014.

[210] M. Alsaad, D. M. Sanborn and W. O. Winer, "Glass transition in lubricants: its relation to elastohydrodynamic lubrication (EHD)," *J. Lubr. Technol.,* vol. 19, no. 1, pp. 404-416, 1978.

[211] A. Porras-Vazquez, L. Martinie, P. Vergne and N. Fillot, "Independence between friction and velocity distribution in fluids subjected to severe shearing and confinement," *Phys. Chem. Chem. Phys.,* vol. 20, no. 43, pp. 27280-27293, 2018.

[212] J. P. Ewen, S. Echeverri-Restrepo, N. Morgan and D. Dini, "Nonequilibrium molecular dynamics simulations of stearic acid adsorbed on iron surfaces with nanoscale roughness," *Tribol. Int. ,* vol. 107, pp. 264-273, 2016.

[213] S. Bair and W. Winer, "The high pressure high shear stress rheology of liquid lubricants," *J. Tribol.,* vol. 114, no. 1, pp. 1-9, 1992.

[214] B. Gecim and W. O. Winer, "Lubricant limiting shear stress effect on EHD film thickness," *J. Lubr. Technol.,* vol. 102, no. 2, pp. 213-220, 1980.

[215] P. Sperka, I. Krupka and M. Hartl, "Lubricant flow in thin-film elastohydrodynamic contact under extreme conditions," *Friction,* vol. 4, no. 4, pp. 380-390, 2016.

[216] A. Jabbarzadeh, P. Harrowell and R. I. Tanner, "The structural origin of the complex rheology in thin dodecane films: three routes to low friction," *Tribol. Int.,* vol. 40, no. 10-12, pp. 1474-1486, 2007.

[217] S. Bair, "Measurements of real non-Newtonian response for liquid lubricants under moderate pressures," *Proc. Inst. Mech. Eng. Part J,* vol. 20, no. 3, pp. 223-233, 2015.

[218] S. M. B. Albahrani, T. Seoudi, D. Philippon, L. Lafarge, P. Reiss, H. Hajjaji, G. Erard-Guillot, M. Querry, J.-M. Bluet and P. Vergne, "Quantum dots to probe temperature and pressure in highly confined liquids," *RSC Adv.,* vol. 8, no. 41, pp. 22897-22908, 2018.

[219] P. H. Hünenberg, "Thermostat algorithms for molecular dynamics simulations," *Adv. Polym. Sci.,* vol. 173, pp. 105-149, 2005.

[220] J. Archard, "Temperature of rubbing surfaces," *Wear,* vol. 2, pp. 438-455, 1959.

[221] B. Y. Cao, "Nonequilibrium molecular dynamics of the thermal conductivity based on an improved relaxation scheme," *J. Chem. Phys.,* vol. 129, p. 074106, 2008.

[222] B. Grocholski and R. Jeanloz, "High-pressure and -temperature viscosity measurements of methanol and 4:1 methanol:ethanol solution," *J. Chem. Phys.,* vol. 123, p. 204503, 2005.

[223] N. Voeltzel, Molecular simulation of an ionic liquid as lubricant: from bulk rheology to nanoconfinement. PhD thesis, Lyon: INSA Lyon, 2016.

[224] W. Habchi, A full-system finite element approach to elastohydrodynamic lubrication problems: application to ultra-low-viscosity fluids. PhD thesis, Lyon: INSA Lyon, 2008.

[225] B. Bhushan, J. N. Israelachvili and U. Landman, "Nanotribology: friction, wear, and lubrication at the atomic scale," *Nature,* vol. 307, pp. 607-616, 1995.

[226] M. L. Gee, P. M. McGuiggan, J. N. Israelachvili and A. M. Homola, "Liquid to solid-like transitions of molecularly thin films under shear," *J. Chem. Phys.,* vol. 93, pp. 1895-1906, 1990.

[227] J. Van Alsten and S. Granick, "Molecular tribometry of ultrathin liquid films," *Phys. Rev. Lett.,* vol. 61, pp. 2570-2573, 1988.

[228] E. R. G. Eckert, Heat and mass transfer, New York: MCGraw-Hill, 1959.

[229] M. Björling, W. Habchi, S. Bair, R. Larsson and P. Marklund, "Towards the true prediction of EHL friction," *Trib. Int.,* vol. 66, pp. 19-26, 2013.

[230] S. Bair, "Reference liquids for quantitative elastohydrodynamics: selection and rheological characterization," *Trib. Lett.,* vol. 22, no. 2, pp. 197-206, 2006.

[231] Handbook of thermal conductivity, Volume 3. Organic compounds C8 to C28., Ed. Carl. L. Yaws, 1995.

Publications and conferences

Publication:
Porras-Vazquez, A., Martinie, L., Vergne, P., Fillot, N. (2018).
Title: Independence between friction and velocity distribution in fluids subjected to severe shearing and confinement. Physical Chemistry Chemical Physics. 2018, 20 (43), pp 27280-27293.
DOI: 10.1039/C8CP04620D

Oral presentations:

- 6th World Tribology Congress, Beijing, China 17-22 Sept. 2017.
  Title: A Molecular Dynamics study of the limiting shear stress phenomenon in an EHD contact. A. Porras-Vazquez, L. Martinie, P. Vergne, N. Fillot.

- 45th Leeds-Lyon Symposium on Tribology, Leeds, England 4-7 Sept. 2018.
  Title: A numerical analysis of the behavior of confined fluids under high shear and high stress: seeking the origins of the limiting shear stress phenomenon. A. Porras-Vazquez, L. Martinie, N. Fillot, P. Vergne, G. Morales-Espejel.

- 9th Multiscale Materials Modeling, Osaka, Japan 28 Oct. – 2 Nov. 2018.
  Title: Ultimate response of confined fluids under extreme conditions: a molecular dynamics analysis. A. Porras-Vazquez, L. Martinie, P. Vergne, N. Fillot.

Poster presentations:

- TriboUK, London, England 27-28 Apr. 2017.
  Title: Limiting shear stress in EHD contacts: a Molecular Dynamics approach. A. Porras-Vazquez, L. Martinie, N. Fillot.

- Beilstein Nanotechnology Symposium, Potsdam, Germany 2-4 Oct. 2018.
  Title: Understanding the limiting shear stress phenomenon in confined molecular fluids: a Molecular Dynamics analysis. A. Porras-Vazquez, L. Martinie, N. Fillot, G. Morales-Espejel, P. Vergne.

FOLIO ADMINISTRATIF

THESE DE L'UNIVERSITE DE LYON OPEREE AU SEIN DE L'INSA LYON

NOM : PORRAS VAZQUEZ DATE de SOUTENANCE : 29/10/2019

Prénoms : Alejandro

TITRE : A molecular approach to the ultimate friction response of confined fluids

NATURE : Doctorat Numéro d'ordre : 2019LYSEI087

Ecole doctorale : Mécanique, Energétique, Génie Civil, Acoustique

Spécialité : Génie Mécanique

RESUME :
Afin de contrôler les pertes d'énergie dans les systèmes mécaniques, un film mince de lubrifiant est souvent introduit entre les solides en contact. Les contacts lubrifiés ponctuels fonctionnent en régime élastohydrodynamique, caractérisé par des pressions élevées (de l'ordre du GPa) et des épaisseurs de film minces (de l'ordre de 100 nanomètres). A des taux de cisaillement élevés, le fluide peut présenter une contrainte de cisaillement limite dont l'origine physique est encore incertaine. Actuellement, les modèles empiriques disponibles pour la prédiction du frottement ne décrivent pas la réponse ultime des lubrifiants dans ces conditions sévères. De plus, l'analyse expérimentale in-situ est très difficile à réaliser en raison du confinement et des fortes pressions. Ainsi, dans cette thèse, le problème est abordé sous l'angle de la modélisation à l'échelle atomique. Le comportement en cisaillement de trois de fluides (un fluide de traction, un lubrifiant modèle et un lubrifiant industriel pour le secteur aérospatial) est analysé par simulation Dynamique Moléculaire. Les résultats numériques sont ensuite comparés qualitativement et quantitativement à des essais expérimentaux. La réponse en frottement est indépendante du profile de vitesse dans l'épaisseur du confinement, ce dernier apparaissant plutôt comme une conséquence des conditions limites aux surfaces. Le régime de frottement limite apparaît naturellement lorsque le lubrifiant est soumis à des conditions thermodynamiques caractéristiques d'un état solide. Dans ce cas, la dynamique des molécules est fortement ralentie. L'énergie d'activation augmente rapidement avec la pression, de sorte que la diffusion devient négligeable à forte pression, même aux taux de cisaillement sévères imposés dans les simulations Dynamique Moléculaire. La réponse macroscopique à ce phénomène est donc une saturation de la valeur du frottement. Ce travail s'achève en jetant les bases d'une modélisation qui pourra permettre la prédiction du frottement lubrifié sous conditions sévères.

MOTS-CLÉS : Lubrification Elastohydrodynamique, Dynamique Moléculaire, Contrainte Limite Tangentielle, Transition de Phase, Mobilité Moléculaire.

Laboratoire (s) de recherche : Laboratoire de Mécanique des Contacts et des Structures

Directeur de thèse : Dr. Nicolas Fillot, Dr. Laetitia Martinie

Président de jury :

Composition du jury :
- Prof. Ashlie Martini (Rapporteure)
- Prof. Guillaume Galliero (Rapporteur)
- Prof. Laurent Joly (Examinateur)
- Dr. Kirsten Martens (Examinatrice)
- Dr. Laetitia Martinie (Co-directrice)
- Dr. Nicolas Fillot (Directeur)